UNIVERSITY OF SOUTHAMPTON

FACULTY OF ENGINEERING AND THE ENVIRONMENT

Modelling the combined effects of creep and frictional heating in the development of landslides

by

Sujeevan Vinayagamoorthy

Thesis for the degree of Doctor of Philosophy

May 2014

UNIVERSITY OF SOUTHAMPTON

ABSTRACT

FACULTY OF ENGINEERING AND THE ENVIRONMENT

Thesis for the degree of Doctor of Philosophy

MODELLING THE COMBINED EFFECTS OF CREEP AND FRICTIONAL HEATING IN THE DEVELOPMENT OF LANDSLIDES

By: Sujeevan Vinayagamoorthy

In this work, different thermo-poro mechanical models for large scale landslides were developed to predict the transition between the creep and the catastrophic phases of a landslide.

First, a refinement was made of an existing thermo-poro-mechanical landslide model, including a realistic formulation for the dynamics of the moving slide. The model equations were then solved by using an unconditionally stable numerical scheme and the results were compared with a similar existing model and data available from landslide case studies. It was found that the refined model gave different predictions for the slide's acceleration and velocity which however were only marginally so in the time window of realistic run-out distances.

Secondly, a thermo-poro-mechanical model for landslides was developed based on rate process theory. The model was initially used in an attempt to back-analyse a real landslide case. It was subsequently used to explore factors that influence the transition from an initial phase of creep to a final catastrophic phase. It was found that a threshold initial velocity separates the creep and collapse regimes, beyond which frictional heating leads to the final failure.

A different thermo-poro-mechanical model for landslides based on a constitutive theory that combines a thermo-plasticity model with a creep model for soils was also developed. The model was initially used in an attempt to back analyse a real landslide. It is able to predict a transition between the creep and collapse phases. Thermal diffusivity of the shear band material plays a major role on the predicted duration of the creep phase.

Finally a landslide model based on Perzyna's visco-plasticity theory was also developed. It was found that the extremely low velocity predicted during the creep phase leads to insignificant heat dissipation inside the shearband making the prediction of thermal pressurization and collapse impossible with this model.

Table of contents

List of Figures

List of Tables

Declaration of Authorship

I, SUJEEVAN VINAYAGAMOORTHY declare that this thesis and the work presented in it are my own and has been generated by me as the result of my own original research.

MODELLING THE COMBINED EFFECTS OF CREEP AND FRICTIONAL HEATING IN THE DEVELOPMENT OF LANDSLIDES

I confirm that:

1. This work was done wholly or mainly while in candidature for a research degree at this University;
2. Where any part of this thesis has previously been submitted for a degree or any other qualification at this University or any other institution, this has been clearly stated;
3. Where I have consulted the published work of others, this is always clearly attributed;
4. Where I have quoted from the work of others, the source is always given. With the exception of such quotations, this thesis is entirely my own work;
5. I have acknowledged all main sources of help;
6. Where the thesis is based on work done by myself jointly with others, I have made clear exactly what was done by others and what I have contributed myself;
7. Parts of this work have been published as:

S.Vinayagamoorthy and A.Zervos (2014). *The influence of shear heating on the development of creeping landslides*. *In:* XII International IAEG Congress, Torino, 2014 (accepted)

Signed :……………………………………………………………………………………….

Date:………………………………………………………………………………………….

Acknowledgements

This PhD thesis is an output of a robust research study for which many people have contributed and given valuable support. I would like to express my gratitude to the following people for their precious help, support and advice.

I pay homage to my supervisor Dr. Antonis Zervos, for making this research overall possible. He has been a tremendous mentor for me over the last three and half years. His invaluable supervision, motivation, encouragement as well as his painstaking effort in proof reading draft thesis are greatly appreciated. His unflinching courage and conviction always inspire me.

I would like to thank Dr. Jeff Priest for his valuable feedback on my 9-month and 18-month reports.

I am also indebted to Prof. Athula Kulathilaka for his motivation and support given to me for pursuing research in Geotechnics.

I take this opportunity to sincerely acknowledge the Faculty of Engineering and the Environment, University of Southampton for funding my PhD research.

I gratefully acknowledge Dr. Manolis Veveakis and Dr Francesco Cecinato for their encouragement and valuable discussions during my participation in the ALERT workshop in 2011 and 2012.

I would like to thank my mother (Mrs. Lalithambikai Vinayagamoorthy) and brothers (Rajeevan, Myooran and Nirooban) for their moral support, care and love. They have cherished me in every moment in my life and supported me in needs.

I would also like to thank Neha, for her support during my crucial moments, especially for proof reading drafts and making diagrams.

I am also thankful to Dr. Clive Wiggan for proof reading my draft thesis.

I am very grateful to my friends who made my Southampton-life more joyful. Specially, Aingaa, Sinthu, Gayan and ‘Ammadios’ group gave me an ideal environment to complete this research successfully on time.

Last but not least, I would like to pay high regards to my older Sri Lankan friends, who cherished me continuously from the distance. Besides this, several people have knowingly and unknowingly helped me for the successful completion of my PhD.

List of Notations

General symbols

A	total area of particle assembly
a	area of contact circle
a_1	rate of static friction coefficient
a_2	rate of static friction coefficient
a_c	thermal expansion coefficient of soil skeleton
a_f	activation frequency
a_m	thermal expansion coefficient of soil-water mixture
a_s	thermal expansion coefficient of solid particles
a_w	thermal expansion coefficient of pure water
B_i	heat equation coefficient
C_α	secondary compression coefficient
C_c	compression index
C_f	thermal constant of soil-water mixture
C_i	heat equation coefficient
C_r	recompression index
$\boldsymbol{C}^{\boldsymbol{Te}}$	stress independent thermo elastic tensor
C'	viscoplastic parameter
c	soil compressibility
c_v	consolidation coefficient
c_w	water compressibility
D	resultant driving force
$\overline{D}$	Singh-Mitchell creep coefficient (measure of deviator stress)
D_w	dissipated work within shearband
D_i	non-linear thermal diffusivity
D_p	plastic dissipation
D_t	time dependent dissipation

D_{vp}	viscoplastic dissipation
$\boldsymbol{D^{me}}$	standard elasticity matrix
$\boldsymbol{D^{te}}$	thermal tensor
E	experimental activation energy
E^*	equivalent elastic moduli of soils particle
e	void ratio
F	overstress function
F_f	applied force between two soil particles
F_1, F_2, F_3	heat equation coefficients
F_a, F_b	temperature dependent rate process coefficients
f	yield locus
$\bar{f}$	applied shear force on a flow unit
f_p	dynamic loading surface/dynamic yield function/viscoplastic potential
f_y	static yield locus
G	shear modulus
g	plastic potential
$\tilde{g}$	thermal friction sensitivity
H	sliding block thickness
h	Planck's constant
I_p	second moment of area
$j(\rho C)_m$	thermal constant of soil water mixture
K	bulk modulus
$\bar{K}$	Ter-Stepanian's proportionality factor
K_c	Taylor's friction circle correction factor
K_q	ratio between volumetric and distortional strain rates
k	Boltzmann's constant
k_{Fm}	Fourier's thermal conductivity of soil water mixture
k_{Fs}	Fourier's thermal conductivity of soil granules

k_{Fw}	Fourier’s thermal conductivity of water
k_w	Darcy permeability coefficient
L	lifetime of inter particle bonds
M	critical state parameter
M_{drv}	driving moment
M_{res}	resisting moment
M^*	stress ration at critical state
m	Singh-Mitchell creep parameter
m'	viscoplastic parameter
N	Avogadro’s number
n	porosity
n	number of particles per unit length
P	normal stress applied on particle assembly
p'	mean effective stress
p'_c	preconsolidation stress
$(p'_c)_{Hu}$	Hueckel’s Preconsolidation stress
p'_{cy}	size of static yield locus
p_d	excess pore pressure at the interface between shearband and failure slide
q	deviatoric stress
q_{ult}	ultimate failure strength
R	universal gas constant
R_f	radius of failure circle
R_D	radius of friction circle
r	degree of plasticisation
S	number of bonds per unit area
S_{ij}	deviatoric stress tensor
S_1	proportionality factor for number of bonds
T_v	dimensionless time factor

t	time
t_c	creep duration
t_d	deviatoric age of soils
t_v	volumetric age of soils
T	absolute temperature (K)
U_0	free activation energy
v_d	slide velocity
v_t	slide velocity at creeping phase
v_v	viscoplastic creep velocity
v	specific volume
W	block weight
W^{vp}	viscoplastic work
Y_i	diffusion coefficient
Z_b	shear band thickness
z	depth
α	thermal expansion coefficient
$\bar{\alpha}$	Singh-Mitchell creep parameter
α_2	opening angle of the part of the failure surface below the phreatic surface
β	plastic compressibility modulus
$\tilde{\beta}$	compressibility modulus
β_s	plastic contraction coefficient
β_s'	volumetric expansion coefficient
Γ	specific volume intercept of critical state line
γ	rate of thermal softening
γ_d	shear distortion
γ_s	unit weight the soil
γ_w	unit weight of the water
$\dot{\gamma}$	shear strain rate

$\boldsymbol{\delta}$	Kronecker delta
ε	total strain
ε_a	axial strain
ε_{ij}	strain components
$\varepsilon_1, \varepsilon_2, \varepsilon_3$	principal strain components
ζ	over consolidation ratio
η_{ij}	stress ration tensor
θ	temperature (℃)
θ_d	angular displacement
κ	slope of unloading-reloading line
κ_m	thermal diffusivity of soil water mixture
λ	slope of isotropic compression line
λ_l	distance between successive equilibrium points of two flow units
$\dot{\lambda}$	plastic multiplier
λ_m	thermal pressurisation coefficient
$\hat{\mu}$	Vardoulakis's evolution law of friction coefficient
μ_{cs}	Veveakis's evolution law of friction coefficient
μ_p	peak friction coefficient
μ_r	evolution law of residual friction coefficient
μ_{rs}	static residual friction coefficient
μ_{rd}	dynamic residual friction coefficient
ν	poisson ratio
ρ	density of the failure mass
ρ_w	density of the pore fluid
$\boldsymbol{\sigma}$	stress vector
σ_i	principal stress vector
σ_{ij}	stress components
σ'_n	effective normal stress

$\sigma_1, \sigma_2, \sigma_3$	principal stress components
τ	shear stress
τ_{ult}	ultimate shear strength
Φ	rate sensitivity coefficient
ϕ	viscous nucleus
ϕ	soil particle size
φ_F	incipient friction angle
φ_m	mobilised friction angle
ψ	slope angle
ψ_α	secondary compression index
$\widetilde{\omega}$	secondary compressibility modulus

Abbreviations

CSL	critical state line
MCC	modified cam clay
NCL	normal consolidation line
OCR	over consolidation ratio
URL	unloading reloading line

Subscripts

iso	isotropic mechanism
dev	deviatoric mechanism
0	initial state
i	reference value
ref	at reference state
new	new geometry values

Superscripts

e	elastic
ep	elasto plastic

me	mechanical elastic
p	plastic
t	time dependent
te	thermo elastic
tep	thermal elasto plastic
tp	thermoplastic
vp	viscoplastic

Chapter 1: Introduction

1.1 Background

Large scale landslides are a common geotechnical hazard in many parts of the world. They may occur in land or under the sea and are a severe danger to human life. There are many examples that can be quoted as evidence. In 1963, the Vajont Slide that occurred in Italy moved 2.7 x 10^8 m^3 of rock mass into an artificial lake and as a result killed 2600 people. In 1999, the Jiufengershan slide occurred in Taiwan. It was triggered by the Chi-Chi earthquake and killed 2400 people. In 1998, a submarine landslide caused the Sissano Tsunami which killed 2000 people and left 12,000 people homeless.

Many events such as earthquakes, sudden changes in pore pressure, and dissociation of gas hydrates have been proposed by many authors as causes of initiating large scale landslides. However, the mechanisms due to which a slide acquires extremely high velocity leading to catastrophic failure are not clearly understood yet. Frictional heating was identified as a possible cause of the unexpected velocity and the long run-outs of some large scale landslides (Anderson, 1980, Habib, 1975, Vardoulakis, 2000, Vardoulakis, 2002a, Veveakis et al., 2007, Voight and Faust, 1982). Rapid movement of the slide occurs due to build-up of pore water pressure. Build-up of pore water pressure is explained by expansion of water due to frictional heat production (Baldi et al., 1988, Hueckel and Baldi, 1990, Hueckel and Pellegrini, 1991, Modaressi and Laloui, 1997). Furthermore, the elastic domain of the soil will shrink due to heating and its friction angle may decrease. These phenomena lead to declining shear resistance at the slipping plane.

Very few landslide models exist in the literature that take into account the effect of frictional heating. However, these models are one-dimensional, with simple constitutive relations for the soil and they were used to back analyse particular landslides cases only. Recently, an improved thermo-poro-mechanical model for landslides was developed incorporating a realistic constitutive assumption of soils (Cecinato, 2009, Cecinato and Zervos, 2008, Cecinato and Zervos, 2012, Cecinato et al., 2011, Cecinato et al., 2008). Using this model, the investigators provided insights on the role of frictional heating, establishing that in the idealised case of an infinite slope, permeability of the soil and the thickness of the sliding mass dominate the development of catastrophic velocities.

Despite these developments, the thermo-poro-mechanics of catastrophic landslides is still not understood comprehensively because most of the above mentioned models cover only the final stage of failure, when catastrophic movement is involved. However, large-scale landslides may exhibit a creeping phase, possibly followed by catastrophic failure. An example of a landslide that exhibited such behaviour was the Vaiont landslide that occurred in Italy, 1963, where the final phase of catastrophic collapse was preceded by several months of creep (Müller, 1964).

This thesis is concerned with developing models that include both the frictional heating and the creep-like movement of landslides. Therefore, the above model will be improved by incorporating the more realistic time dependency behaviour of soils to cover the creep like criteria of movements in this research.

1.2 Aims and objectives

The aim of the research is to investigate the impact of frictional heating in the lifetime of catastrophic landslides in slopes of different in-situ conditions.

The individual objectives are;

- A critical review of existing models of landslides, and of the thermo-mechanical and creep behaviour of soils to determine the range of in-situ conditions and relevant parameters.
- The development of advanced thermo-poro-mechanical models of the slip zone of a landslide, allowing for both the stage of creep-like slope movement and an eventual stage of catastrophic collapse.
- Numerical implementation and validation of each model through some back analysis of a well-documented catastrophic landslide case history
- A parametric study to systematically investigate the in-situ conditions that are critical in making a slope prone to catastrophic failure, with particular emphasis on the lifetime of the resulting landslide.

1.3 Layout of the thesis

A literature review is presented in Chapter 2. A brief description and classification of landslides is first given to provide the context of this research (Section 2.1). Then a critical review of a range of constitutive relations (thermo-plasticity of soils, creep behaviour) that can be used to model soil behaviour in the context of landslides is provided (Sections 2.3 & 2.4). Finally, existing models of large scale landslides are presented and critically discussed in Section 2.5.

Chapter 3 presents a refined thermo-poro-mechanical model of landslides, developed by including a realistic formulation for the dynamics of the moving slide in an existing model. The model equations are then solved by using an unconditionally stable numerical scheme and the results are compared with a similar existing model and data available for Vaiont case study. Subsequently, a parametric study is carried out to investigate the influence of shape and size of the failing mass on the development of the landslide.

A different thermo-poro-mechanical model for landslides is presented in Chapter 4. The behaviour of the clay is modelled using rate process theory, which is a general theory quantifying time-dependent soil deformation on the basis of micromechanical considerations. The model is then validated through the back-analysis of Vaiont case after generalizing to a uniform infinite slope. Also, the model is used to explore factors that influence the transition from an initial phase of creep to a final catastrophic phase.

Chapter 5 presents a thermo-poro-mechanical model for landslides based on a refined constitutive theory that combines a thermo-plasticity model with a creep model for soils. Subsequently, the governing equations for the landslide model are developed and discretised, and model is used in an attempt to back analyse the Vaiont case landslide.

In Chapter 6, a landslide model based on Perzyna's viscoplasticity theory is presented. First a modification to classical visco-plastic theory is presented to include temperature effects. Then the landslide equations are modified consistently with the new thermo-viscoplastic model. Like previous chapters, validation of model is attempted thorough a back-analysis of the Vaiont case landslide. A parametric study is also carried out to investigate the behaviour of the model.

In Chapter 7, conclusions from this research are outlined alongside with recommendations for future research on this subject.

Chapter 2: Literature review

In this chapter, a brief description and classification of landslides is first given to provide the context of this work. Afterwards, the Vaiont landslide case history is introduced in details. This case history is used to validate the models presented in the following chapters. Then a number of constitutive relations that can be used to model soil behaviour in the context of landslides are reviewed. The constitutive models considered here can be divided into two broad categories, i.e. those concerned with the thermo-plasticity of soils and those aimed at modelling creep. Finally, existing models of large scale landslides are presented and critically discussed.

2.1 Classification of landslides

In general, landslides may occur on land (sub-aerial landslides) or under the sea (submarine landslides). Both types of landslides are identified as one of the major geologic hazards in the world. Several studies on landslides and their mechanisms are available in the literature. Here, it is only focused on a selection of material that is most relevant to the objectives of this research.

Varnes (1978) classified landslides based on the materials involved and the mode of movement. Other classification systems that have been proposed incorporate other aspects of landslides such as the rate of movement and the water, air or ice contents of the sliding mass (Cruden and Varnes, 1996, Dikau, 1996, Hungr et al., 2001, Hutchinson, 1989, Sidle and Ochiai, 2006). The most accepted categories of landslides are listed below (Varnes, 1978):

a) **Slides**: This type of failure occurs when a weak zone of a slope separates the sliding material from more stable underlying materials. Slides can be further divided into two types: translational slides and rotational slides. In translational sliding, the landslide mass moves along a roughly planar surface. Usually, rapid deformation takes place during translational sliding (Cruden and Varnes, 1996).

Rotational sliding on the other hand takes place on a curved sliding surface (e.g. cylindrical or circular).

b) **Falls:** Falls are characterised by free movement of mass through air, bouncing or rolling. Fall landslides are always extremely rapid. Separation of mass occurs in falls due to the existence of fractures, joints and bedding planes.

c) **Topples:** A landslide is classified as topple, when the soil or rock mass rotates forward in a very steep slope about a point below the centre of gravity of the failing mass.

d) **Flows**: Flows can be further divided into five categories: debris flows, debris avalanches, earth flows, mudflows and creeping flows. A ‘debris flow’ may consist of a combination of loose soil, rock, organic matter, air and water. A mixture of these materials mobilizes downward on a slope like slurry. Debris flows are mainly caused by a sudden supply of surface water, rapid snow melt and heavy rainfall that erodes the loose soil and rock particles on steep slopes.

   A ‘debris avalanche’ is a variant of debris flow when the debris movement is extremely rapid.

   An ‘earthflow’ is another type of debris flow where the materials of the slope become liquid and start to flow downward by forming a basin at the head of the slope. This failure occurs on reasonably steep slopes that contain fine grain materials or clay bearing rocks, and is characterised by the “hourglass” shape that the flowing mass assumes.

   A ‘mudflow’ is a particular type of earthflow where the material contains at least 50% sand-, silt-, and clay sized particles that allow it to flow down when wet enough. Mudflows and debris flows are often referred to as mudslides.

   A ‘creeping flow’ is a slow, steady downward movement of a slope mass that contains soils or rock. Creep is caused by a constant applied shear stress, lower than the shear strength of the moving mass. This amount of stress is enough to cause permanent deformation but not enough to trigger shear failure at the sliding plane. Generally, three types of creep can be identified. (1) Seasonal creep, where movement is within the depth of soil affected by seasonal changes in soil moisture and temperature. (2) Continuous creep, where shear stress continuously increases and but doesn’t exceeds the strength of the materials and (3) progressive creep, where slopes reach the point of failure like other types of mass movements.

e) **Lateral Spreads**: This type of landslides occurs usually on very gentle or flat slopes. Unlike natural slope failures, the mass will spread laterally. Liquefaction is the main cause of this type of mobilization of soil mass.

All the above types of landslides are depicted in Figure 1.

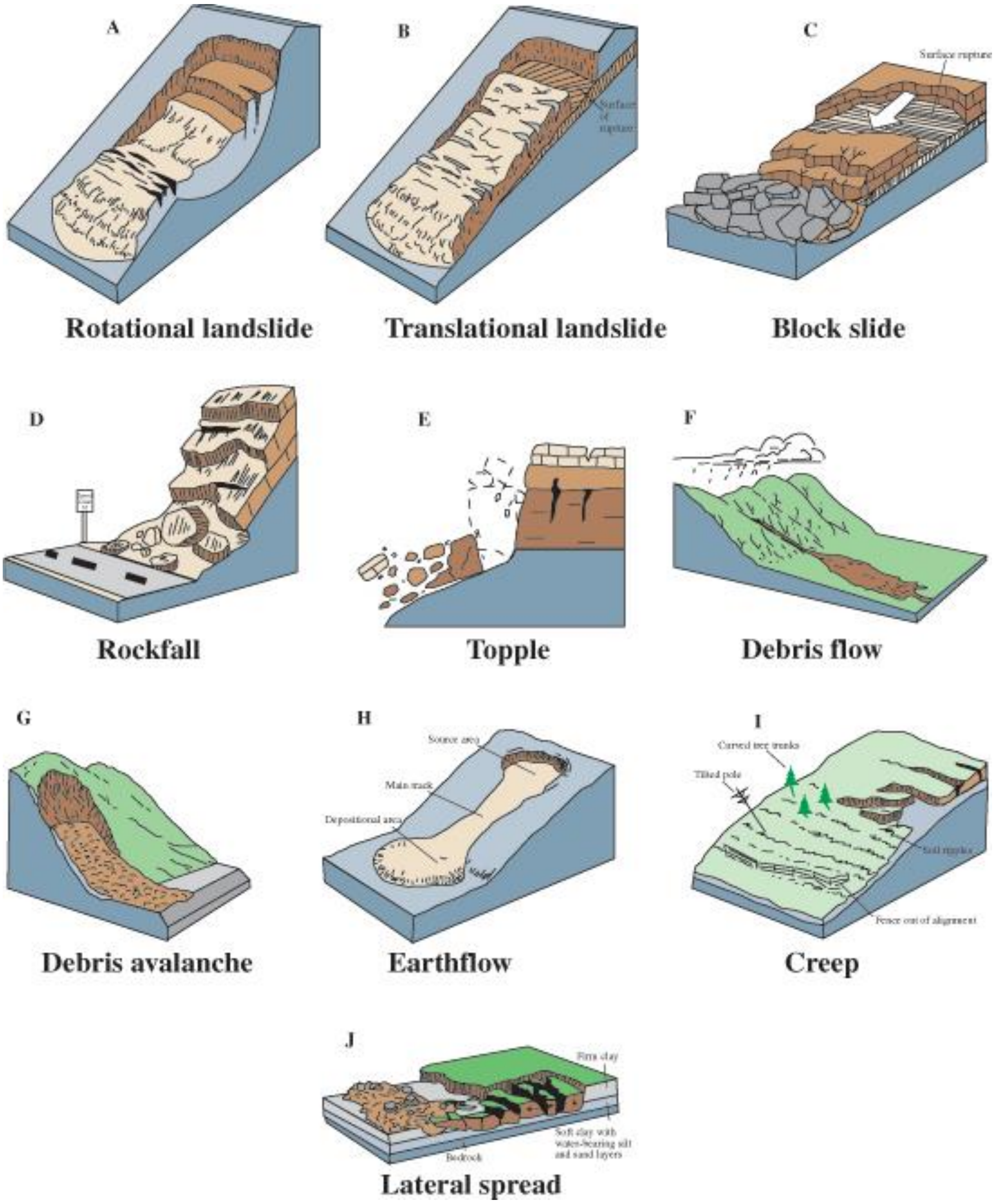

Figure 1: Graphical illustration of major types of landslides (Varnes, 1978)

2.2 Vaiont case history

2.2.1 Overview

Well documented in the literature is the case of the Vaiont landslide, which occurred in northern Italy on 9th October 1963. The landslide was preceded by 3 years of creep that ended with the final collapse of the rock mass.

Approximately, 2.7×10^8 m^3 of rock was moved from the northern flank of the Mount Toc in to an artificial reservoir of about 1.5×10^8 m^3 impounding the east-west trending Vaiont deep gorge (Figure 3). Nearly 250 m thickness of mass slipped about 400-450 m with the final slip rate of 25-30 m/s. The reservoir filling (4.7×10^7 m^3) produced a giant wave that propagated towards down the valley, overflowed the dam and killed more than 2000 people after destroying village of Longarone. (Anderson, 1980, Hendron and Patton, 1985).

Site excavation for the Vaiont dam project began in 1956 in Mountain Toc, Italy and the construction was completed in 1961. The main purpose of this project was to provide hydroelectric power for the rapidly-expanding northern cities of Milan, Turin and Modena. It is the world's highest thin arch dam measuring 262 m high, 27 m thick at the base, 3.4 m at the crest, with a chord of 160 m, and a reservoir volume of 115 million m^3.

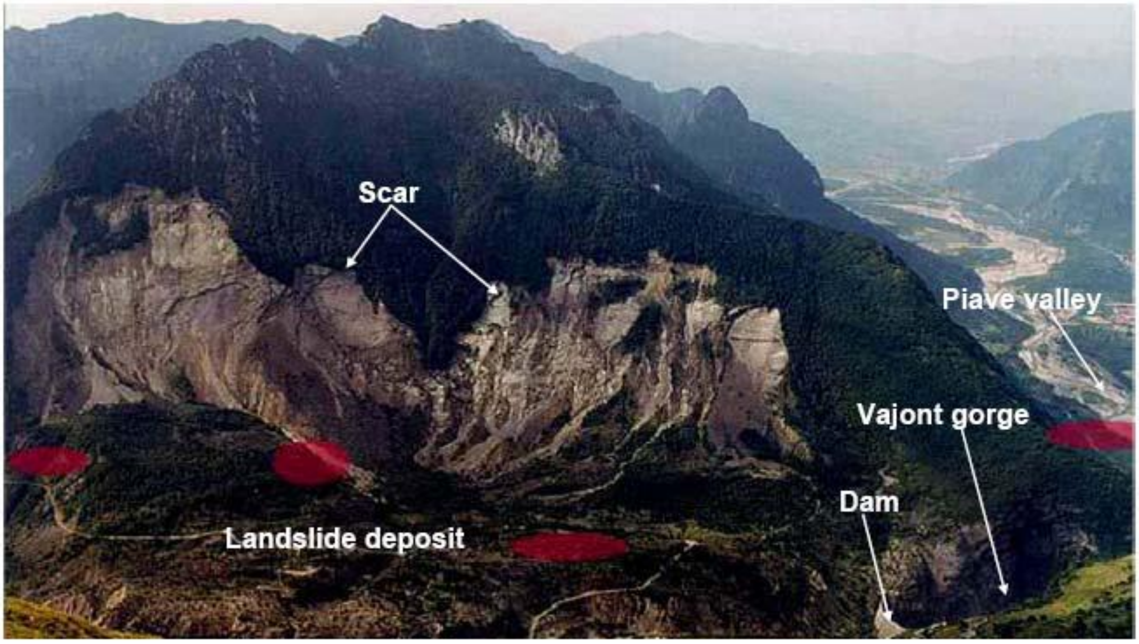

Figure 2: Overview of the Vaiont valley after disaster, photo from Schrefler and Sanavia (2005) and reproduced from Cecinato (2009)

2.2.2 Geology of the Vaiont slide

The Vaiont slide has been the interest of numerous investigations due to its social and legal implications. A detailed geological study has been reported in Hendron and Parton (1985), however, most relevant aspects for this thesis are summarised below.

The Vaiont river flows from east to west, which cuts a large syncline structure which folds Jurassic and Cretaceous strata (Figure 3). The syncline created an "open chair" and eventually defined the geometry of the failure surface.

The sliding area consists a succession of limestones and marls. The slide occurred at the top limestone strata with the thickness greater than 0.5m. The failure surface consisted of

0.05-0.3m thick strata of limestone and marl with clay-rich layers in between. The failure slip was confined in 0.5-17.5cm thick continuous clay-rich layers (Figure 4).

Hendron and Patton (1985) proposed two representative cross-sections (Sections 2 and 5), which are used for the stability analysis by many authors (Figure 5). These cross sections are located upstream of the dam position at 400 m and 600 m distances. In this research Section 5 is chosen to investigate the proposed models.

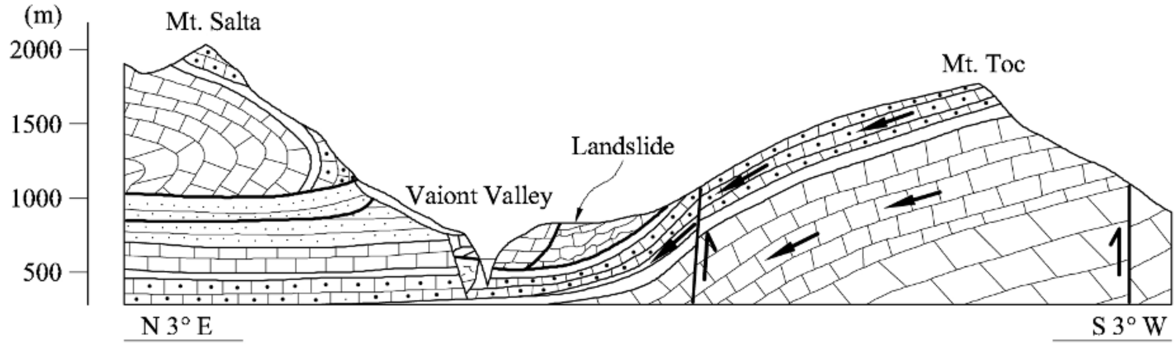

Figure 3: North (Monte Toc) to south (Monte Salta) section showing the general layout of the syncline, the Vaiont gorge and the position of the ancient landslide (after Semenza and Ghirotti, 2000).

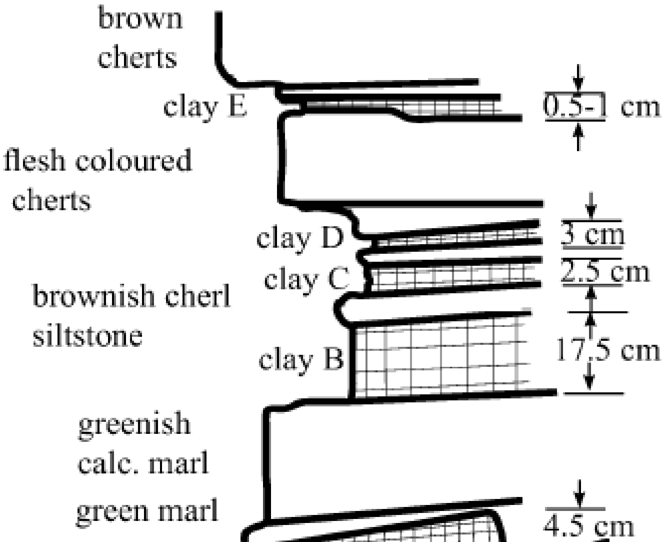

Figure 4: Stratigraphy of the rocks of the Vaiont sliding surface, the thickness is given at right hand side.

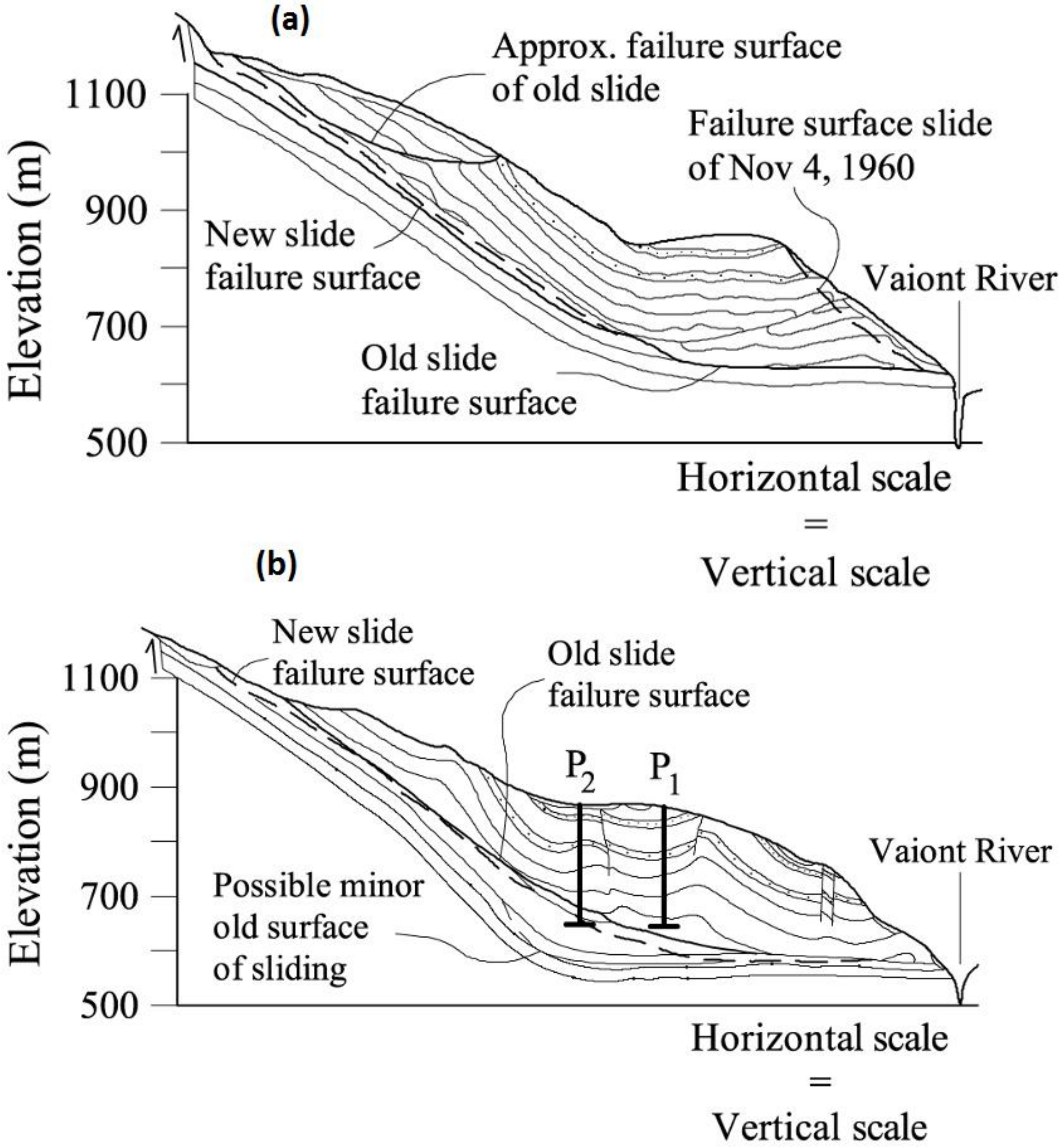

Figure 5: Two representative cross-sections of the landslide: (a) Section 2; (b) Section 5 (see the location in Figure 6) (After Hendron and Patton, 1985)

2.2.3 Events leading to the landslide

Under the supervision of an expert in rock mechanics (L.Müller-Salzburg), dedicated geological surveys were carried out since 1958. During the construction between 1958 and 1959, a prehistoric slide was identified which caught the concern of the experts. However, engineers concluded that deep-seated landslides were highly unlikely because the three test borings carried out (Figure 6) did not reveal weak zones (Müller, 1964, Müller, 1968).

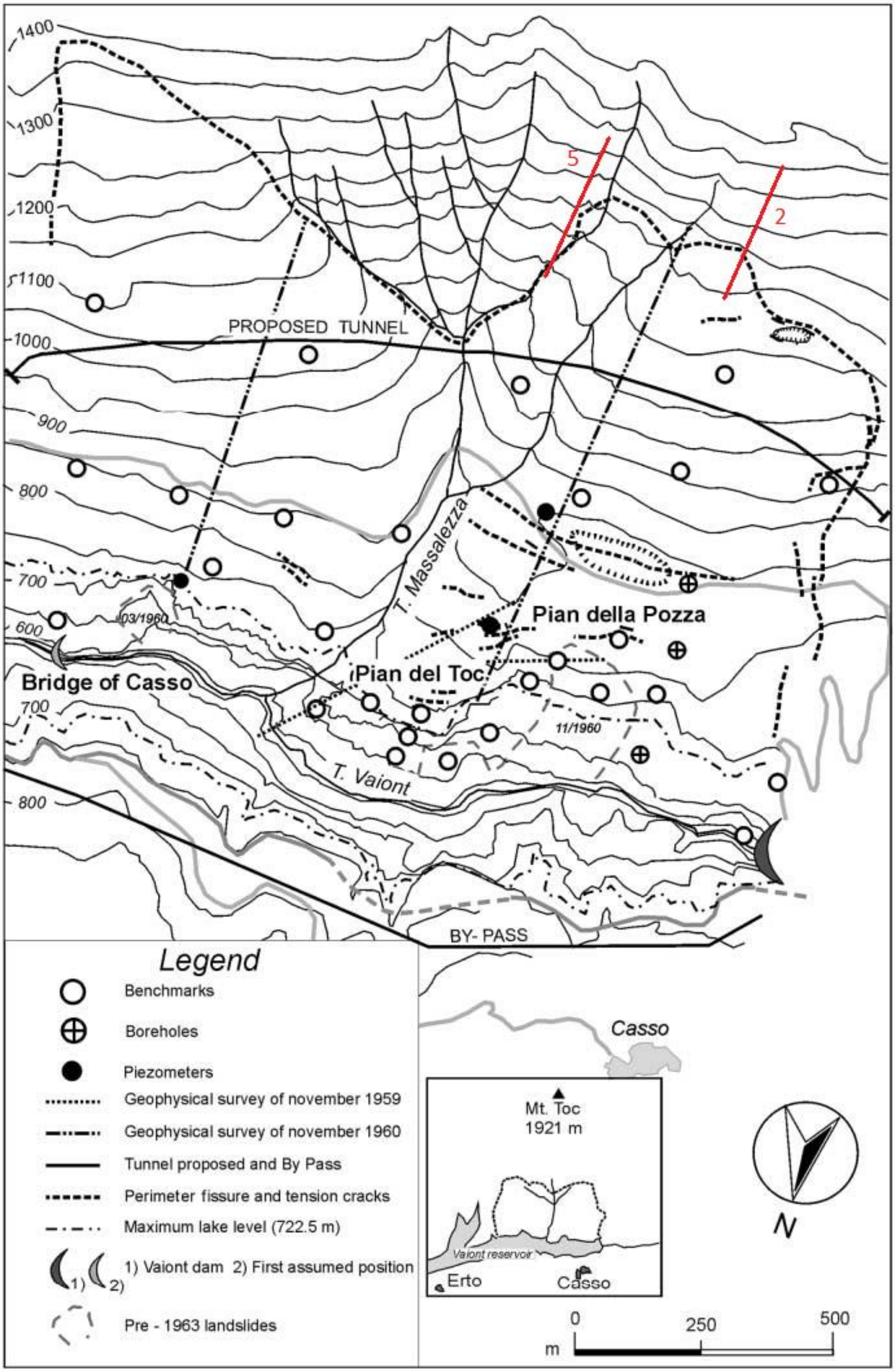

Figure 6: Location map of the Vaiont dam and reservoir (Semenza and Ghirotti, 2000)

The first filling of the reservoir started in February 1960 before the completion of the dam in September 1960. A first crack in the bank was observed when the reservoir level reached 130m above the river level by March 1960. While continuing the filling of the reservoir, inspectors began to monitor the bank movements along with the other necessary measurements such as rainfall (Figure 7).

In October 1960, the bank movement rapidly increased to 3.5cm/day when reservoir level reached 170m. At the same time, a continuous M shape crack, as shown in Figure 6, with 1m width and 2.5 km long was observed which suggested that a very large landslide had been mobilised.

On 4th November 1960, approximately 700,000 m^3 of landslide slid in to the lake in the course of 10 minutes with the reservoir level at 180m. In response to the slide, the reservoir level was reduced back to 135m. Consequently, the bank movement rate reduced from 8cm/day to 1mm/day. By this time, the landslide had already moved by a distance of approximately 1m (Figure 8). The following remedies were proposed by the engineers to stabilise the bank.

- Draining the failure mass to prevent or reduce water infiltration
- Removing millions of cubic meters of material from the mass
- Grouting the sliding mass, especially along the failure surface, and
- Building an earthen buttress at the foot of the slide.

However, all of these measures were found to be impractical and the designers decided to control the landslide movement only by controlling the reservoir water level. Therefore, the drainage tunnels were constructed to control the rate of landslide movement. In addition, four standpipe piezometers were installed between July and October 1961 to record the groundwater table elevation (Figure 6).

The reservoir level was again raised to 185 m on February 1962 and to 235m on November 1962. During this filling the movement rate did not increase substantially, however it reached 1.2 cm/day at the end of the filling. Therefore, the reservoir level was lowered back to 185m over a period of four months. Initially, the velocity remained the same but in December 1962 it started decreasing.

By April 1963, when the reservoir level was at 185m, the movement rate was effectively zero. On the basis of all the above, the designers considered that the landslide movement can be controlled by the reservoir elevation. Between April and May 1963, the reservoir level was again increased rapidly to 231 m and a slight increase in the rate of movement (always less than 0.3cm/day) is observed. In mid-July the reservoir level was brought to 240 m and some further increase in velocity was observed to 0.5cm/day. The level was maintained till mid-August during which time the velocity increased to 0.8 cm/day. The reservoir level was increased another 5m at the end of August and as a consequence, the velocity increased to 3.5cm/day at some parts. In late September, the reservoir level was slowly lowered to bring down the movement under control. However, no reduction in velocity was observed while the reservoir level was brought down to 235 m. On October 9, up to 30 cm/day of velocity was recorded before the catastrophic failure occurred at 22:38 GMT (Figure 9).

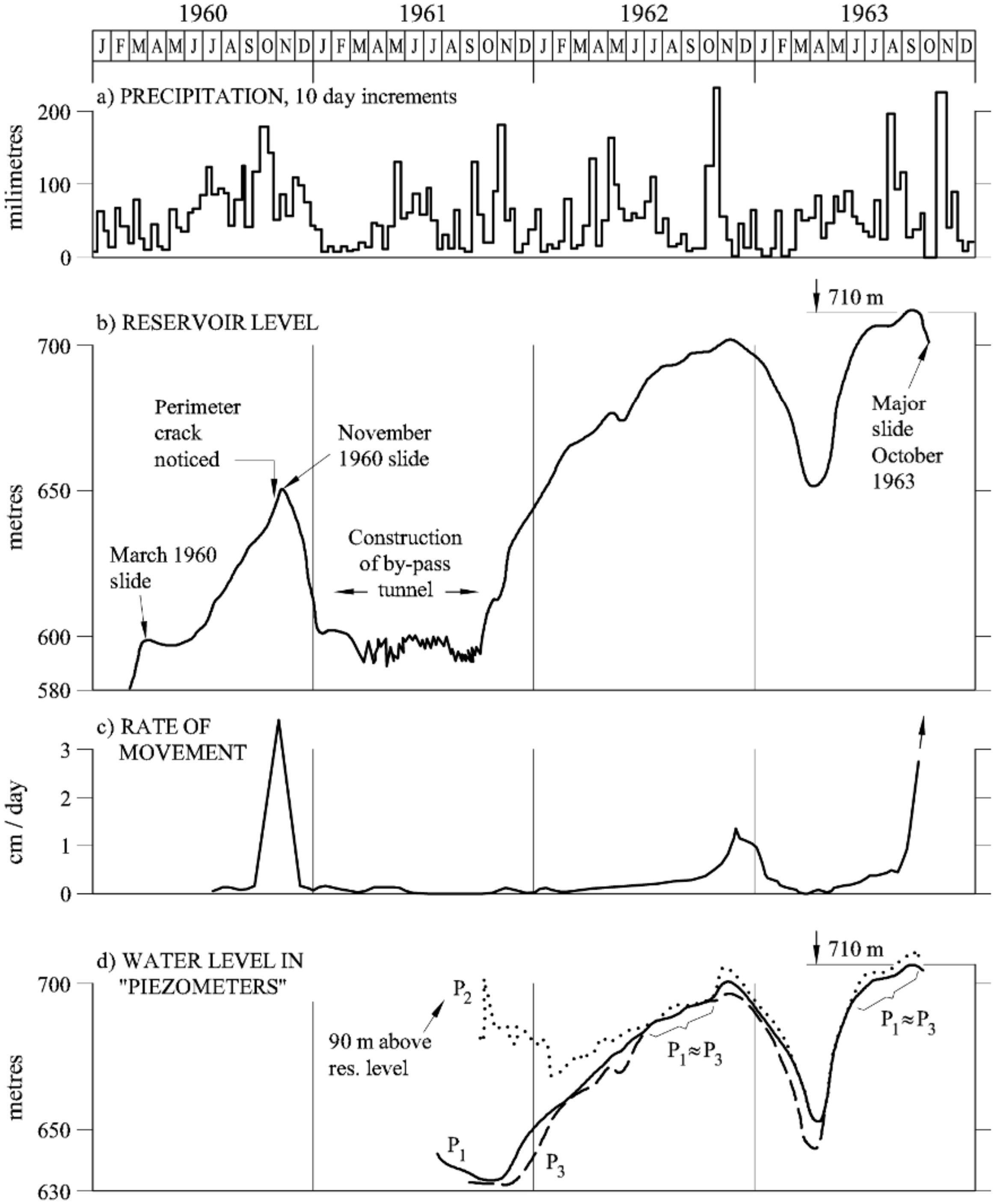

Figure 7: Time histories of precipitation, changes of the water elevation in the reservoir, movement rates before slide on October 9, 1963; and piezometer measurements (after Muller 1964).

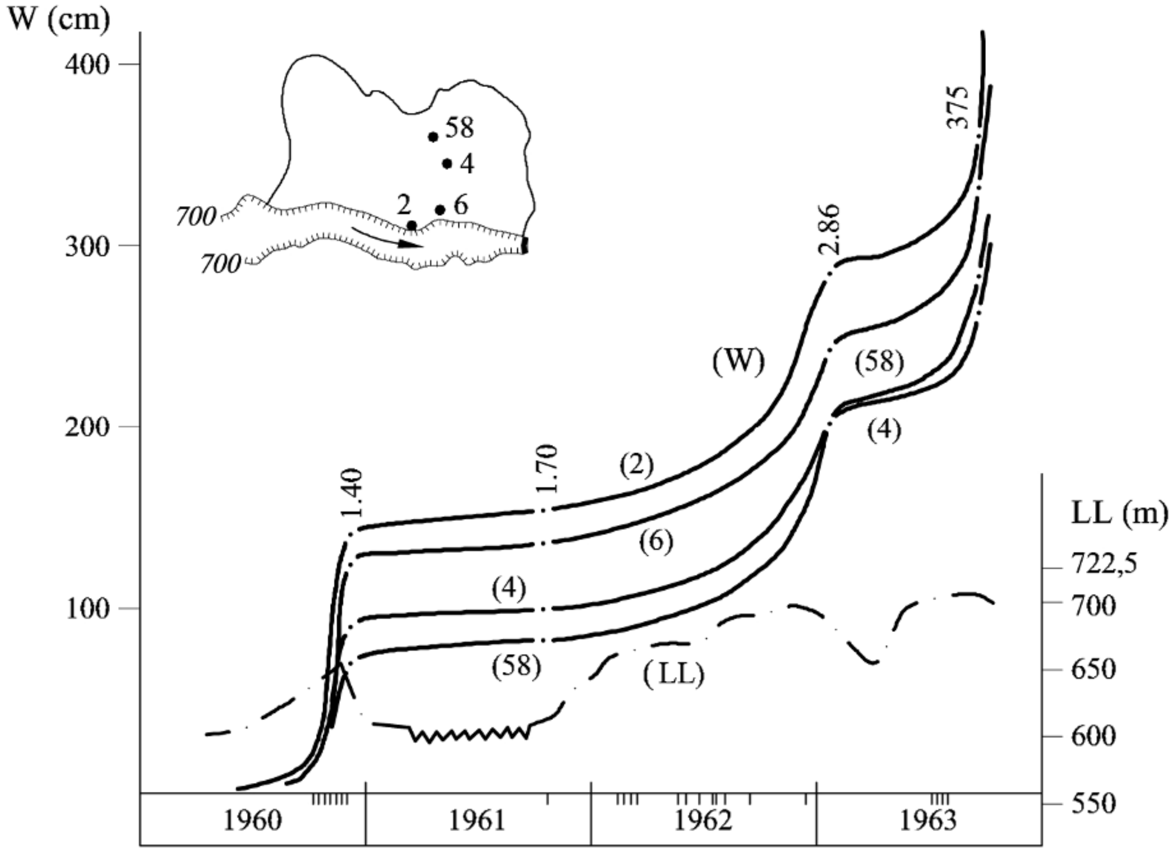

Figure 8: Accumulated displacements of surface markers (W) in the period 1960−1963 and its correlation with reservoir elevation (LL). Seismic events are marked in the time scale (reproduced from Alonso et al. (2010))

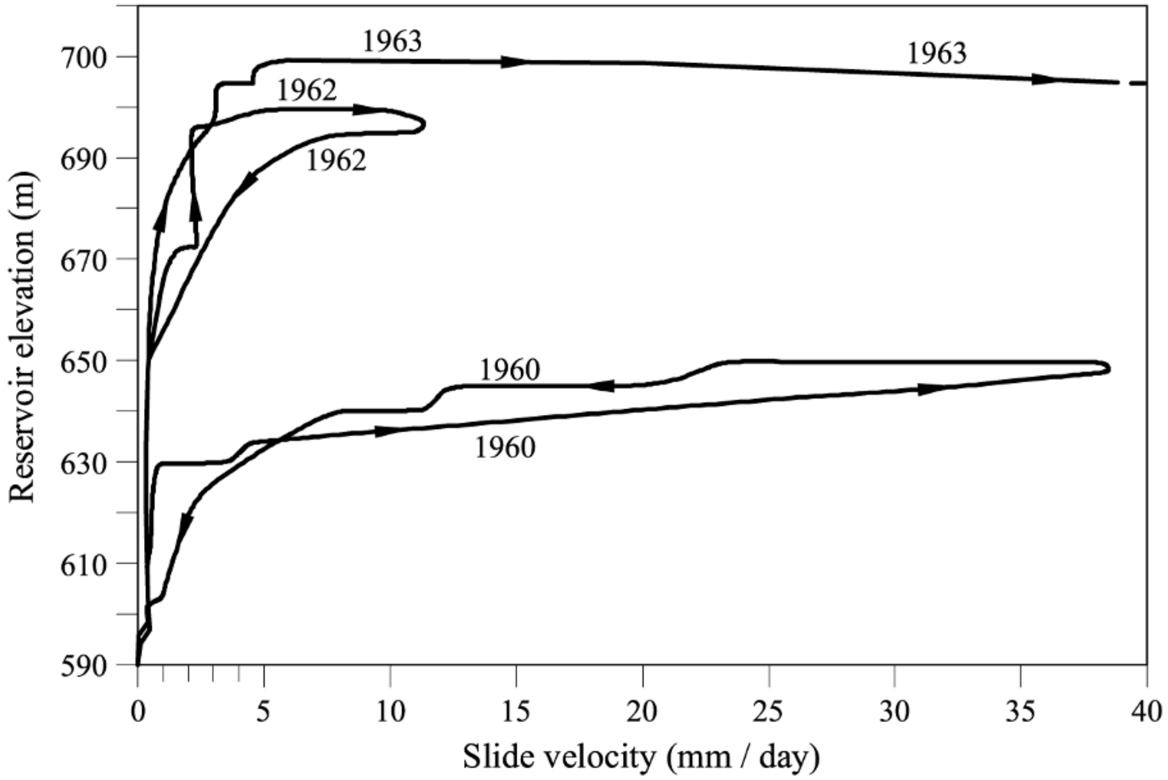

Figure 9: Relationship between water level in the reservoir and sliding velocity (courtesy of G. Fernández) (reproduced Alonso et al. (2010))

2.2.4 Hypothesis for the instability of the slope and the failure

Müller (1964, 1968) formulated a hypothesis that the movements were due to the effect of the saturation of the materials which, for the first time, were inundated by water. The belief that this phenomenon was the main cause of the observed instability led to the decision to gradually raise the lake level once again from April 1963. Müller’s hypothesis was confirmed by the insignificant increase in the slide velocity till July 1963 although the reservoir level was increased significantly (Figure 7).

Hendron and Patton (1985) suggested that a continuous impermeable layer is formed due to the pre-existing failure surface and, as a result, it created two aquifers in the slope. Precipitation and snow melt in the hydro-geological basin fed the lower confined aquifer. After a large spring thaw or prolonged rainfall, the water level in the lower aquifer may have gradually reached much higher values than in the upper aquifer. Therefore, the shear resistance along the failure surface would have decreased significantly, which leads the instability of the mass.

Despite these all hypothesis, many authors suggested that the frictional heat generated during the movement could have caused a distinct decrease in the shear resistance of the material in the failure surface (Habib, 1975, Sultan et al., 2002, Vardoulakis, 2002a, b) . The potential role of frictional heating in the rapid failure of the Vaiont slide is discussed in Section 2.2.6 in detail.

2.2.5 Material properties

Hendron and Patton (1985) performed a detailed investigation to identify the geotechnical properties of the sliding surface. As mentioned earlier, the slip was concentrated in clay-rich layer. Samples of these clays were tested in different laboratories and found to be high plastic and the plasticity plot is given in Figure 10. Liquid limits were found to be well in excess of 50%.

Ring shear experiments by Tika and Hutchinson (1999) on Vaiont slide material showed that it exhibits velocity and displacement friction softening and reaches a residual value (Figure 11 and Figure 12). Vardoulakis (2002a) proposed a hyperbolic function for the mobilized friction angle as follows;

$$\hat{\mu} = \mu_r + \left(\mu_p - \mu_r\right)\frac{1}{1 + a_1\left(\frac{x_d}{Z_b}\right)} \qquad 2.1$$

where;

$$\mu_r = \mu_{rd} + (\mu_{rs} - \mu_{rd})\frac{1}{1 + a_2\left(\frac{v_d}{Z_b}\right)} \qquad 2.2$$

In the above equations, D_b is the shear band thickness, while x_d and v_d are displacement and velocity respectively. The thickness dependent strain and strain rate can be written as $\gamma = \frac{x_d}{Z_b}$ and $\dot{\gamma} = \frac{v_d}{Z_b}$ The other parameters present in the equation are;

μ_{rs}, μ_{rd} – Static and dynamic residual friction coefficient (limiting values) ($\mu_{rs} = 0.18, \mu_{rd} = 0.077$)

μ_p – Initial (peak) friction coefficient $\left(\mu_p = 0.577\right)$

a_1, a_2 – Parameters that control how rapidly the friction coefficient decreases with displacement and velocity respectively. ($a_1 = 0.114, a_2 = 0.103s$)

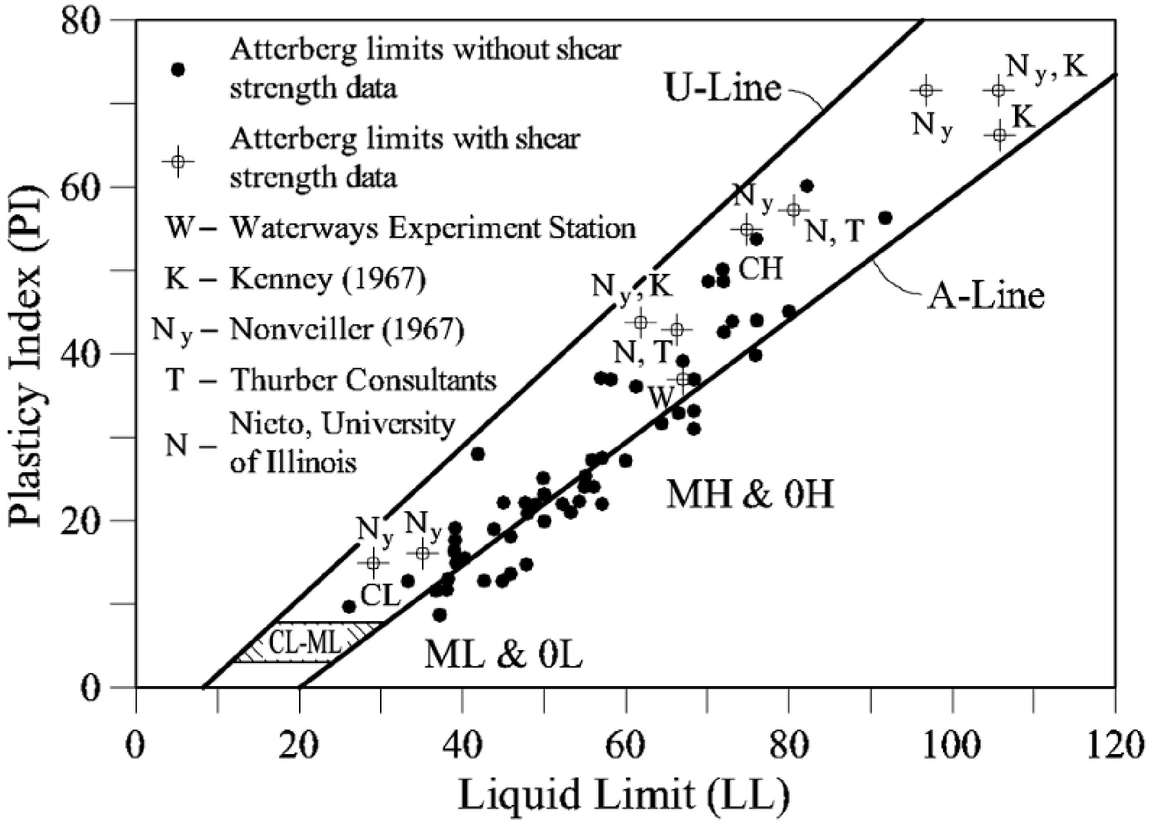

Figure 10: Plasticity of clay samples from the Vaiont sliding surface (Hendron and Patton, 1985).

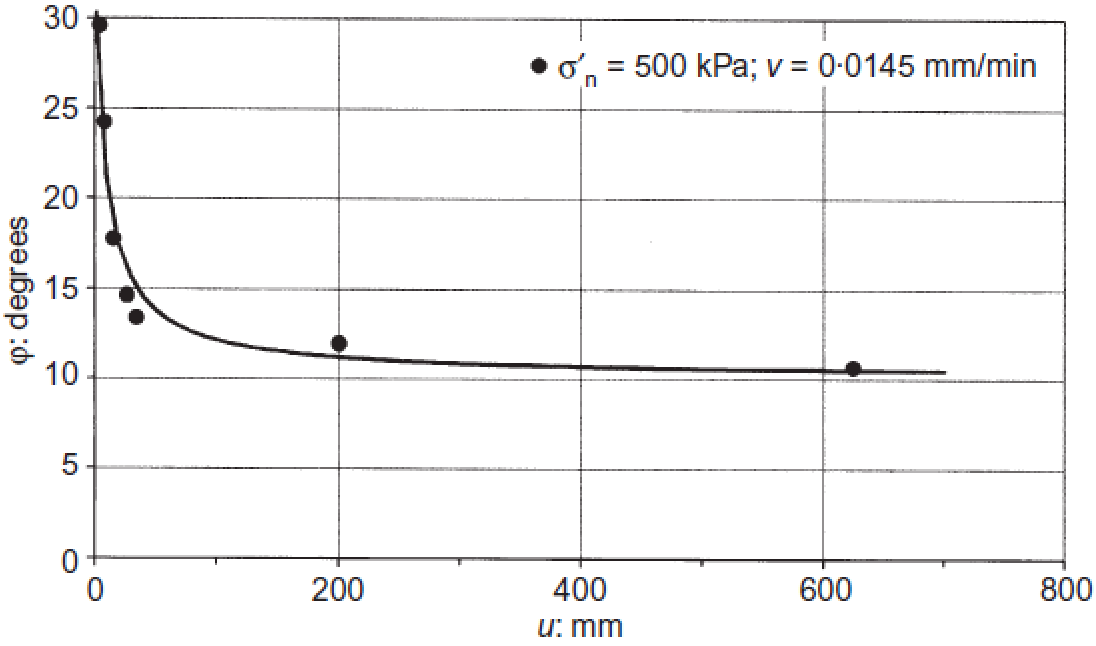

Figure 11: Displacement softening data from ring shear tests (Tika and Hutchinson, 1999) and hyperbola law (Vardoulakis, 2002a)

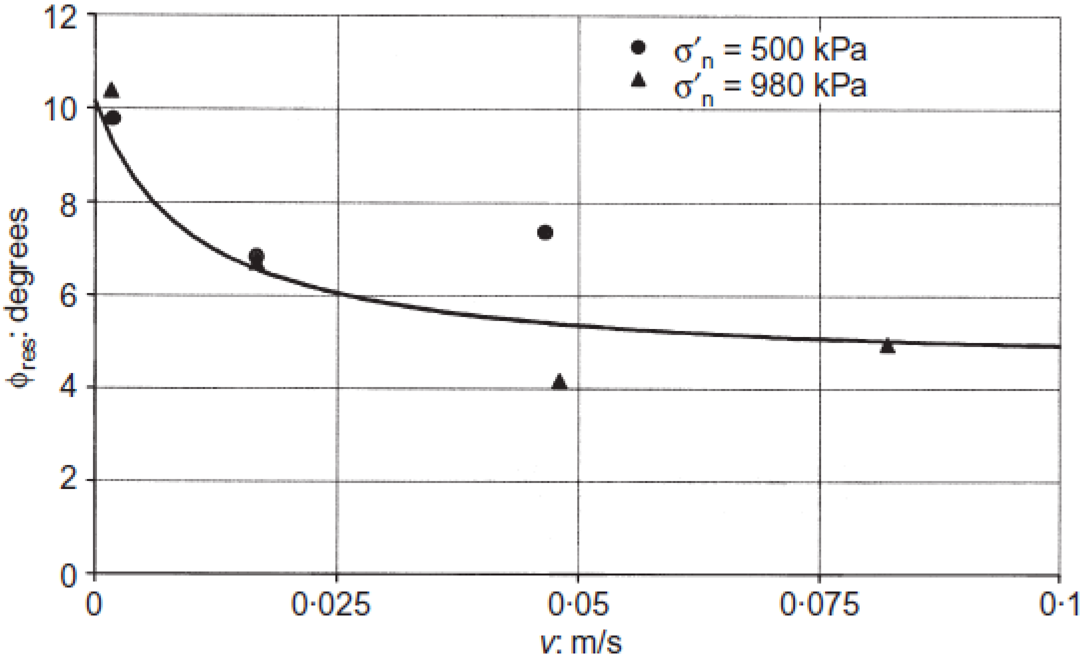

Figure 12: Velocity softening data from ring shear tests (Tika and Hutchinson, 1999) and hyperbola law (Vardoulakis, 2002a)

2.2.6 Potential role of frictional heating

It has been proposed by many authors that frictional heating of the slip zone plays a major role on the failure of large landslides. Firstly, Habib (1975) proposed a mechanism of pressurization due to vaporization of pore water because of frictional heating to explain the reduction in the strength of rockslides, notably in the Vaiont landslide. De Blasio and Elverhoi (2008), Erismann (1979) and Gaziev (1984) described rockslides by using a concept called “self-lubrication”; it is explained as either crushing in to fine grains or even melting of rock particles the shear zone, leading to loss of shear strength. Voight and Faust (1982) hypothesised pore water pressure increase due to heating to explain the catastrophic evolution of large landslides. Moreover,Chang et al. (2005a), Chang et al. (2005b) developed a block-on-slope thermo-mechanical model that includes thermal pressurization to back analyse the 1999 Jiufengershan landslide in Taiwan.

A number of thermo-poro-mechanical models for catastrophic landslides were developed and successfully back analysed the Vaiont slide taking into consideration of frictional heat generation and build-up of pore water pressure inside the failure zone (Cecinato, 2009, Cecinato et al., 2011, Pinyol and Alonso, 2010, Vardoulakis, 2002a). All these considered the final collapse stage only. Veveakis et al. (2007) presented a physically base landslide model to predict the transition between the creep and the catastrophic phase of Vaiont slide incorporating the fictional heating effects.

2.3 Review of thermo-plastic constitutive models for soil

In this section, some existing constitutive models of thermo-plasticity of soils are presented. When frictional heating is considered such constitutive relations are necessary for determining the mechanical behaviour of soil as a function of temperature. In the following models for elasto-plastic and thermo-elastoplastic behaviour of soils are presented.

2.3.1 Elasto-plasticity of soils

The elasto-plastic behaviour of a soil can be described using a yield surface is defined as function of (effective) stresses. If the stress state remains within the yield surface, then deformation is fully elastic. When the stress state reaches the yield surface, plastic deformation will start to occur. Depending on the type of model, the yield surface can either remain fixed (perfect plasticity) or evolve (hardening plasticity).

Modified Cam-Clay is a particular model used to describe the elasto plasticity of soils. The yield surface of Modified Cam Clay is defined as a function of mean effective stress *(p')*, deviatoric stress *(q)* and preconsolidation stress(p_c') and has elliptical shape (Roscoe and Burland, 1968). The size of the yield surface is given by the preconsolidation stress. The change in size of the yield surface is described through a hardening relationship defining the variation of the preconsolidation stress with volumetric plastic strain. The yield surface expands with the compactive volumetric strain (hardening) and shrinks with dilative volumetric strain (softening).

A ‘critical state’ is said to have been reached when shearing of the soil can continue without further change in stress or volumetric strain. Therefore, at the onset of the critical state;

$$\frac{\partial p'}{\partial \gamma_d} = \frac{\partial q}{\partial \gamma_d} = \frac{\partial v}{\partial \gamma_d} = 0 \tag{2.3}$$

In the above, $\gamma_d$is the shear distortion, v is the specific volume. Critical states correspond to failure. For a given soil, all critical state fall on a unique line called the Critical State Line (CSL) is defined by the following equations in (p', q, v) space.

$$\begin{gathered} q = Mp' \\ v = \Gamma - \lambda \ln(p') \end{gathered} \tag{2.4}$$

where M, Γ & λ are soil parameters determined from experiments.

2.3.2 Hueckel’s constitutive model

Based on experimental test of soils at different temperatures, Hueckel developed a modification on the critical state soil model. First, modification was done for the drained conditions (Hueckel and Baldi, 1990, Hueckel and Peano, 1987) (Figure 13). Subsequently, undrained failure was also interpreted with the inclusion of changes to pore water pressure due to temperature variations (Baldi et al., 1988, Hueckel and Pellegrini, 1991) (Figure 14).

The volumetric and deviatoric thermo elastic strain in terms of triaxial notation can be written as follows (Hueckel and Peano, 1987);

$$\varepsilon_v^{te} = \frac{K}{1 + e_0} \ln \frac{p'}{p'_0} - \alpha \Delta\theta \tag{2.5}$$

$$\varepsilon_q^{te} = \frac{1}{3G}(q - q_0) \tag{2.6}$$

where

$p' = \dfrac{\sigma'_1 + 2\sigma'_3}{3}$

$q = \sigma'_1 - \sigma'_3$,

K = bulk modulus of the soil at the reference temperature,

G = shear modulus at the reference temperature,

p'_0, q_0 = reference values of p' and q

α = thermal expansion coefficient of soil.

Non-linear changes in soil compressibility and the effect of secondary compression are ignored. The elliptical yield locus was derived as;

$$f = \left(\left\{\frac{2p'}{(p_c')_{Hu}\left(\varepsilon_v^{tp}, \Delta\theta\right)} - 1\right\}^2 + \frac{4q^2}{\left[M(p_c')_{Hu}\left(\varepsilon_v^{tp}, \Delta\theta\right)\right]^2} - 1\right) \qquad 2.7$$

In the above equation, the apparent preconsolidation stress $(p_c')_{Hu}$ is a function of volumetric strain and temperature and is given as

$$(p_c')_{Hu} = \left[\bar{a} \exp\left\{\frac{1}{\lambda - K_T}\left(e_1 + (1+e_0)\varepsilon_v^{tp}\right)\right\} + a_1 \Delta\theta + a_2 \text{ sign } (\Delta\theta)\Delta\theta^2\right] \qquad 2.8$$

where $K_T = \frac{K}{1+e_0} + (\alpha_1 + \alpha_1 \Delta\theta)\Delta\theta$

ε_v^{tp} - volumetric thermo plastic strain

$\Delta\theta$ – change in temperature

λ - slope of the isotropic normal-compression line

$\bar{a}$ – coefficient with the dimension of pressure

a_1, a_2 - coefficients of thermal sensitivity of the yield surface.

e_0, e_1 - reference void ratio

At yielding, the total strain rate is obtained by adding the elastic and plastic strain rates (Hueckel and Pellegrini, 1991)

$$\dot{\varepsilon}_v = \dot{\varepsilon}_v^{te} + \dot{\varepsilon}_v^{tp} \qquad 2.9$$

$$\dot{\varepsilon}_q = \dot{\varepsilon}_q^{te} + \dot{\varepsilon}_q^{tp} \qquad 2.10$$

The plastic strain rate can be obtained from the flow rule as follows;

$$\dot{\varepsilon}^p = \dot{\lambda}\frac{\partial g}{\partial \boldsymbol{\sigma}} \qquad 2.11$$

$\dot{\lambda}$ is a scalar valued plastic multiplier and g is the plastic potential which is also a function of $p', q, p_c'\left(\varepsilon_v^p, \Delta\theta\right)$. The plastic multiplier $\dot{\lambda}$ is obtained from the consistency condition, stating that during yielding the stress state should lie on the evolving yield surface. Therefore, the consistency condition is expressed as;

$$\dot{f} = \frac{\partial f}{\partial p'}\dot{p}' + \frac{\partial f}{\partial q}\dot{q} + \frac{\partial f}{\partial \theta}\dot{\theta} + \frac{\partial f}{\partial \varepsilon_v^{tp}}\dot{\varepsilon}_v^{tp} = 0 \qquad 2.12$$

Furthermore, Hueckel and Borsetto (1990) proposed two different plastic multipliers $\left(\dot{\lambda}_v, \dot{\lambda}_q\right)$ in order to find out the volumetric and deviatoric plastic strain rate with single plastic potential function. So that;

$$\dot{\varepsilon}_v^{tp} = \dot{\lambda}_v \frac{\partial g}{\partial p'} \qquad 2.13$$

$$\dot{\varepsilon}_v^{tp} = \dot{\lambda}_q \frac{\partial g}{\partial q} \qquad 2.14$$

Substituting the equation 2.12 into flow rule function 2.13, the volumetric plastic multiplier can be found as

$$\dot{\lambda}_v = \frac{\frac{\partial f}{\partial p'}\dot{p}' + \frac{\partial f}{\partial q}\dot{q} + \frac{\partial f}{\partial \theta}\dot{\theta}}{\widetilde{H}}, \quad \widetilde{H} = \frac{\partial f}{\partial \varepsilon_v^{tp}}\frac{\partial g}{\partial p'} \qquad 2.15$$

Similarly, the deviatoric plastic multiplier is given as;

$$\dot{\lambda}_q = \dot{\lambda}_v + \frac{f_1}{\widetilde{H}}\dot{\theta}, \qquad f_1 = \frac{\partial f}{\partial \theta} + f_{1T}\left(p', q, (p_c')_{Hu}(\varepsilon_v^p, \Delta\theta)\right) \qquad 2.16$$

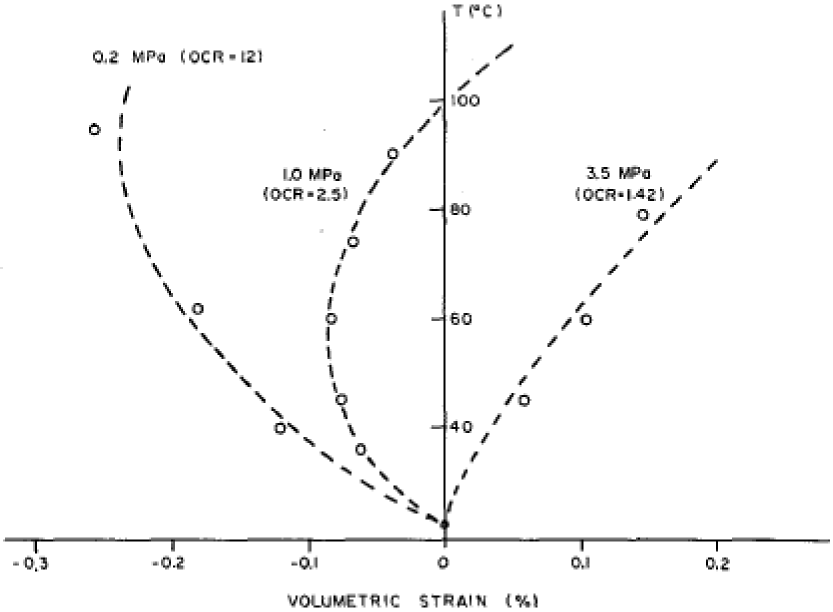

Figure 13: Drained heating tests at constant effective stress at various OCR – Remolded Pontida Clay (Hueckel and Baldi, 1990)

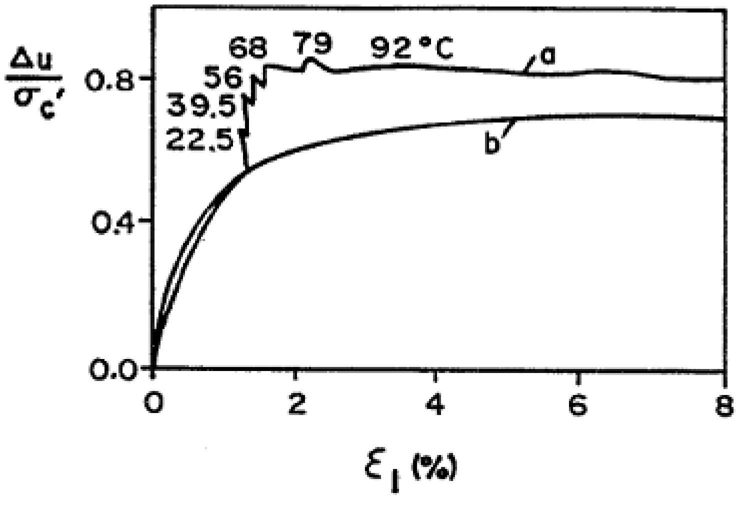

Figure 14: Undrained heating test on Pontida Clay , water pressure vs axial strain (Hueckel and Pellegrini, 1991)

2.3.3 Laloui’s constitutive model

Based on experimental results from triaxial tests with temperature control, Laloui and co-workers developed a thermoplastic constitutive relation describing separately the isotropic and deviatoric mechanisms of deformations (Laloui and Cekerevac, 2003, 2008, Laloui and Francois, 2009, Laloui et al., 2008, Modaressi and Laloui, 1997).

The total strain rate, accounting also for the influence of temperature, can be split into thermo-elastic and thermo-plastic components; in tensor form:

$$\dot{\varepsilon}_{ij} = \dot{\varepsilon}_{ij}^{te} + \dot{\varepsilon}_{ij}^{tp} \tag{2.17}$$

The volumetric thermo-elastic strain is a combination of a reversible thermal strain and a reversible mechanical strain component.

$$\dot{\varepsilon}_{v}^{te} = \frac{\dot{p}'}{K} - \beta_s'\dot{\theta} \ , \tag{2.18}$$

where β_s' is the volumetric expansion coefficient of the solid skeleton. It was found that the thermal expansion coefficient is a function of temperature and the OCR (ξ) as below (Laloui and Francois, 2009).

$$\beta_s' = (\beta_{s0}' + \zeta\Delta\theta)\zeta \tag{2.19}$$

The parameter ζ defines the non-linear dependency to the temperature. β_{s0}' is the value of β_s' at reference temperature, normally taken as the ambient temperature.

The deviatoric (purely mechanical) component is given as

$$\dot{\varepsilon}_{d}^{e} = \frac{\dot{q}}{3G} \tag{2.20}$$

The elastic bulk and shear moduli are given as

$$K = K_{ref}\left(\frac{p'}{p'_{ref}}\right)^{n} , \qquad G = G_{ref}\left(\frac{p'}{p'_{ref}}\right)^{n} \tag{2.21}$$

K_{ref}, G_{ref} are the values of the moduli at the reference pressure p'_{ref}.

Laloui and Francois (2009) proposed that the total plastic strain increment is a linear combination of two irreversible processes an isotropic and a deviatoric one. Therefore, the plastic strain is decomposed as follows;

$$\dot{\varepsilon}_{ij}^{tp} = \sum_{k=1}^{2} \dot{\varepsilon}_{ij}^{tp} = \dot{\varepsilon}_{ij,iso}^{tp} + \dot{\varepsilon}_{ij,dev}^{tp} \tag{2.22}$$

Each process is described using a flow rule. Laloui and Francois (2009) proposed two separate yield surfaces corresponding to the isotropic and the deviatoric mechanisms respectively. The yield function for the isotropic mechanisms is denoted by f_{iso} (Figure 15) and describes the influence of temperature on the apparent preconsolidation pressure on the (p', θ) plane. The yield function for deviatoric mechanisms is denoted by f_{dev} and coincides with that of the original Cam-Clay constitutive model. f_{iso}, f_{dev} and the way they are coupled is shown in Figure 16. A general form of flow rule to describe the isotropic and the deviatoric process can be written as;

$$\dot{\varepsilon}_{ij}^{tp} = \sum_{k=1}^{2} \lambda_k^p \frac{\partial g_k}{\partial \sigma'_{ij}} \qquad 2.23$$

where, g_k is the plastic potential corresponding to each mechanism, and λ_k^p is the respective plastic multiplier. $k = iso$ for the isotropic mechanisms and $k = dev$ for the deviatoric one

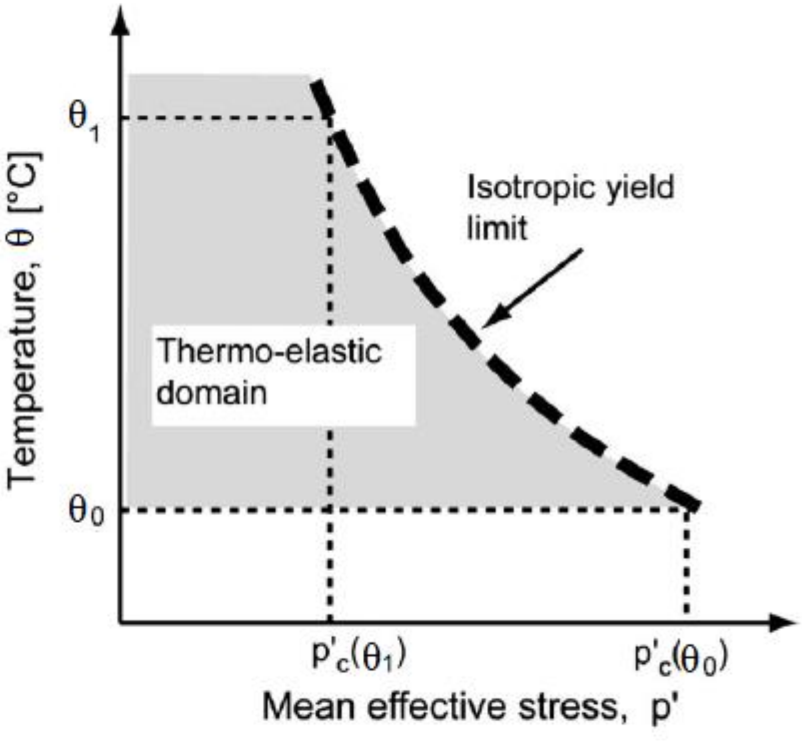

Figure 15: Isotropic thermoplastic yield limit (Laloui and Francois, 2009)

2.3.3.1 The isotropic mechanism

The isotropic yield function is given as; (Figure 15)

$$f_{iso} = p' - (p'_c)(\varepsilon_v^p, \theta) r_{iso} \qquad 2.24$$

where, p'_c the apparent preconsolidation pressure that depends on ε_v^p, θ. r_{iso} is the degree of plastification through which the progressive evolution of the yield function is taken in to account as illustrated in Figure 17. The apparent preconsolidation is given by (Laloui and Cekerevac, 2003);

$$(p'_c) = p'_{c0T0}\left[1 - \gamma \log\left(\frac{\theta}{\theta_0}\right)\right]\exp\left(\beta \varepsilon_v^p\right) \qquad 2.25$$

where γ is a material parameter, p'_{c0T0} is the initial apparent preconsolidation at ambient temperature and β is the plastic compressibility modulus. Finally, substituting the above equation into isotropic yield function, the latter is expressed as

$$f_{iso} = p' - p'_{c0T0}\left[1 - \gamma \log\left(\frac{\theta}{\theta_0}\right)\right]\exp\left(\beta \varepsilon_v^p\right) r_{iso} \qquad 2.26$$

The associative flow rule for isotropic mechanism gives

$$\dot{\varepsilon}_v^{tp} = \lambda_{iso}^p \frac{\partial g_{iso}}{\partial p'} = \lambda_{iso}^p \frac{\partial f_{iso}}{\partial p'} = \lambda_{iso}^p \qquad 2.27$$

2.3.3.2 The deviatoric mechanism

The proposed deviatoric yield function is an extension of the original Cam-Clay model.

$$f_{dev} = q - Mp'\left(1 - \ln\frac{p'\vartheta}{(p'_c)}\right) r_{dev} = 0 \qquad 2.28$$

r_{dev} is again the degree of plastification but in the deviatoric mechanism. ϑ represents the distance between the critical state line at ambient temperature and the isotropic consolidation curve for a given temperature. M is the critical state parameter which varies with temperature as follows;

$$M = M_0 - \tilde{g}(\theta - \theta_0) \qquad 2.29$$

M_0 is the critical state parameter (CSM) at ambient temperature θ_0. The thermal friction sensitivity parameter $\tilde{g}$, which gives the rate of friction softening due to temperature, is calculated using available experimental data (Laloui, 2001). By examining the behaviour of different soils shown in Figure 18, it can be concluded that the value of $\tilde{g}$ falls in the range of $10^{-3} \leq \tilde{g} \leq 10^{-2}$.

By combining the above equations, the deviatoric yield function becomes;

$$f_{dev} = q - r_{dev}p'[M_0 - \tilde{g}(\theta - \theta_0)]\left\{1 - \ln\left(\frac{p'\vartheta}{p'_{c0T0}\left[1 - \gamma \log\left(\frac{\theta}{\theta_0}\right)\right]\exp\left(\beta \varepsilon_v^p\right)}\right)\right\} = 0 \qquad 2.30$$

By applying the associative deviatoric flow rule, it was found that the deviatoric mechanics contributes to both volumetric and deviatoric strain rates as shown below.

$$\dot{\varepsilon}_{v,d}^p = \lambda_{dev}^p \frac{\partial g_{dev}}{\partial p'} = \lambda_{dev}^p \frac{\partial f_{dev}}{\partial p'} = \lambda_{dev}^p \frac{1}{Mp'}\left(M - \frac{q}{p'}\right) \qquad 2.31$$

$$\dot{\varepsilon}_d^p = \lambda_{dev}^p \frac{\partial g_{dev}}{\partial q} = \lambda_{dev}^p \frac{\partial f_{dev}}{\partial q} = \lambda_{dev}^p \frac{1}{Mp'} \tag{2.32}$$

Finally, Laloui and Francois (2009) coupled the above mechanisms using the hardening variable ε_v^p . As shown above, the increment in ε_v^p results from both mechanisms. Therefore, the total volumetric strain rate is the sum.

$$\dot{\varepsilon}_v^p = \lambda_{iso}^p \frac{\partial g_{iso}}{\partial p'} + \lambda_{dev}^p \frac{\partial g_{dev}}{\partial p'} \tag{2.33}$$

Laloui's model is validated through the experiments on Bangkok clay carried out by Laloui and Francois (2009). The numerical simulations and the experimental results for various cases are illustrated in Figure 19 and Figure 20.

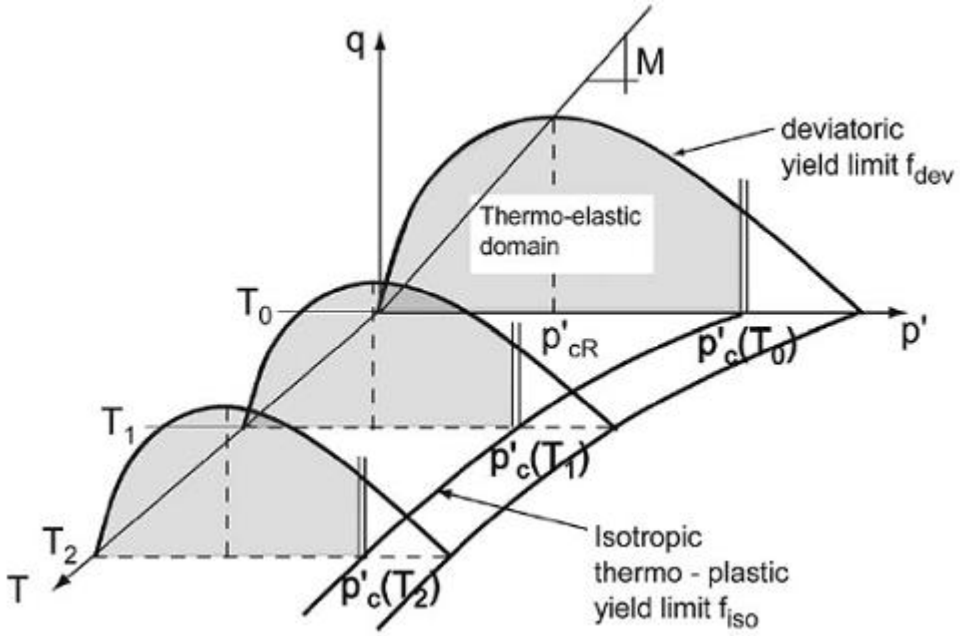

Figure 16: The coupled thermo-plastic yield limit (Laloui and Francois, 2009)

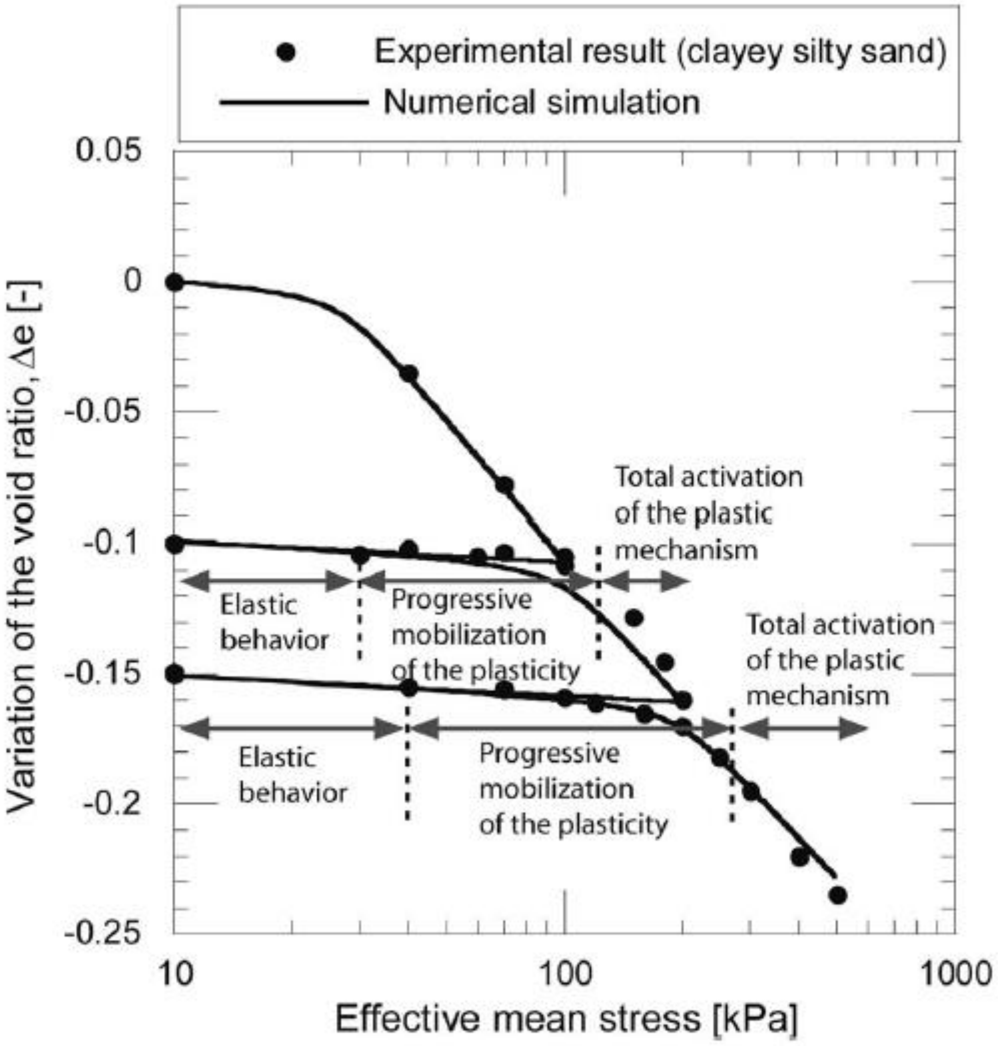

Figure 17: Isotropic Compression test: Comparison of experimental results and the numerical simulation (Laloui and Francois, 2009)

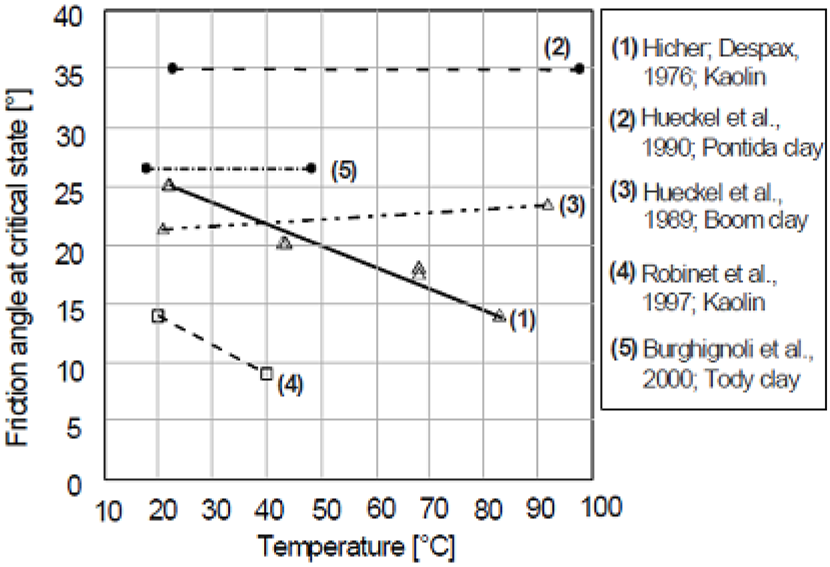

Figure 18: Experimental results for thermal friction sensitivity

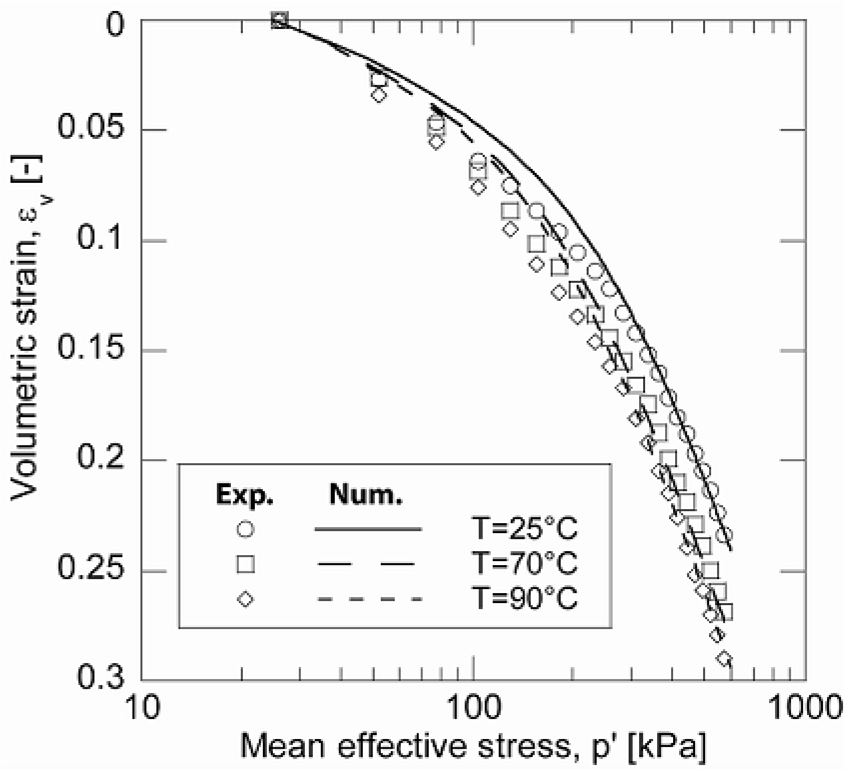

Figure 19: Numerical simulations of isotropic compression tests of Bangkok clay at three different temperatures (Reproduced from Laloui and Cekerevac (2003))

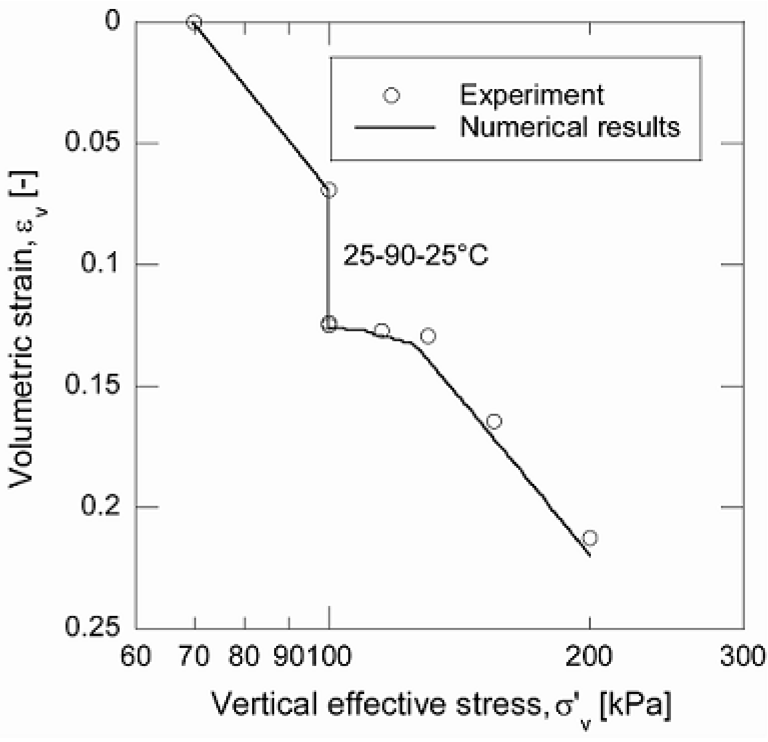

Figure 20: Numerical simulations of a combined thermo-mechanical oedometric path of Bangkok clay. Comparison with experimental results (Reproduced from Laloui and Cekerevac (2003))

2.3.4 Cecinato’s thermo-mechanical constitutive model

Cecinato (2009), Cecinato et al. (2011) and Cecinato and Zervos (2012) proposed an improved constitutive model by modifying Laloui’s model. Rather than using the original Cam-Clay model to describe the deviatoric yield, Cecinato suggested using the Modified Cam Clay (MCC) model which has advantages when it becomes to numerical implementation.

Cecinato divided the total strain rate in to three different components.

$$\dot{\boldsymbol{\varepsilon}} = \dot{\boldsymbol{\varepsilon}}^{me} + \dot{\boldsymbol{\varepsilon}}^{te} + \dot{\boldsymbol{\varepsilon}}^{p} \tag{2.34}$$

where superscripts $me,\ te$,and p denote mechanical elastic, thermo elastic and plastic parts.

2.3.4.1 Thermo-elasticity

The thermo elastic strain rate $\dot{\boldsymbol{\varepsilon}}^{te}$ is proportional to temperature rate $\dot{\theta}$.

$$\dot{\boldsymbol{\varepsilon}}^{te} \propto \dot{\theta} \tag{2.35}$$

Hooke’s law then gives

$$\dot{\boldsymbol{\sigma}} = \boldsymbol{D^{me}}\dot{\boldsymbol{\varepsilon}} + \boldsymbol{D^{te}}\dot{\theta} \tag{2.36}$$

where $\boldsymbol{D^{me}}$ is the standard fourth-order tensor of elastic moduli, $\boldsymbol{D^{te}}$ is here called the thermal tensor and is given as

$$\boldsymbol{D^{te}} = -\beta_s' K \boldsymbol{\delta} \tag{2.37}$$

where, β_s' is the volumetric expansion coefficient of the solid skeleton, $\boldsymbol{\delta}$ is the *Kronecker delta* and K is the stress dependent bulk modulus. The thermo-elastic stress-strain relations can be written as;

$$\dot{\boldsymbol{\sigma}} = \left(K - \frac{2}{3}G\right)\boldsymbol{\delta}\dot{\boldsymbol{\varepsilon}}^{me} + 2G\dot{\boldsymbol{\varepsilon}}^{me} - \beta_s K \boldsymbol{\delta}\dot{\theta} \tag{2.38}$$

where, G is stress dependent shear modulus.

2.3.4.2 Thermo-plasticity

The plastic strain rate can be obtained through the (in general non associative) flow rule.

$$\dot{\boldsymbol{\varepsilon}}^{p} = \dot{\lambda}\frac{\partial g}{\partial \boldsymbol{\sigma}} \tag{2.39}$$

where g is the plastic potential.

From the consistency condition and the flow rule the plastic multiplier is calculated as,

$$\dot{\lambda} = \frac{f_{\sigma}\boldsymbol{D}^{me}\dot{\boldsymbol{\varepsilon}} + (f_{\theta} + 2\boldsymbol{D}^{te}f_{\sigma})\dot{\theta}}{f_{\sigma}\boldsymbol{D}^{me}g_{\sigma} - f_{\varepsilon_v^p}g_{p'}} \tag{2.40}$$

where $f_a = \dfrac{df}{da}$ and $g_a = \dfrac{dg}{da}$

The MCC yield function is;

$$f = q^2 - M^2 p'(p'_c - p') \tag{2.41}$$

Substituting the equation for the apparent preconsolidation pressure (Equation 2.25) and the thermal-friction sensitivity (Equation 2.29) from Laloui's model onto the above MCC equation, the final yield function becomes

$$f = q^2 - p'[M_0 - \tilde{g}(\theta - \theta_0)]^2 \left\{ p'_{c0T0} \left[1 - \gamma\, log\left(\frac{\theta}{\theta_0}\right) \right] \exp\left(\beta \varepsilon_v^p\right) - p' \right\} \tag{2.42}$$

The above deviatoric yield function was coupled with Laloui's isotropic yield function (2.26). The resultant shape of yield function in (p', q, θ) space is shown in Figure 21.

Combining both the thermo-elasticity and the thermo-plasticity, the general form of thermo-elasto-plastic stress-strain rate equation becomes

$$\dot{\boldsymbol{\sigma}} = \boldsymbol{D}^{me}\left(\dot{\boldsymbol{\varepsilon}} - \dot{\lambda}\frac{\partial g}{\partial \boldsymbol{\sigma}}\right) + (\boldsymbol{D}^{te} - \boldsymbol{C}^{te})\dot{\theta} \tag{2.43}$$

where $\boldsymbol{C}^{te} = \dfrac{1}{3}\beta'_s\boldsymbol{\delta}$

The model was validated thorough the experimental data from Laloui and Cekerevac (2003) as given in Figure 22.

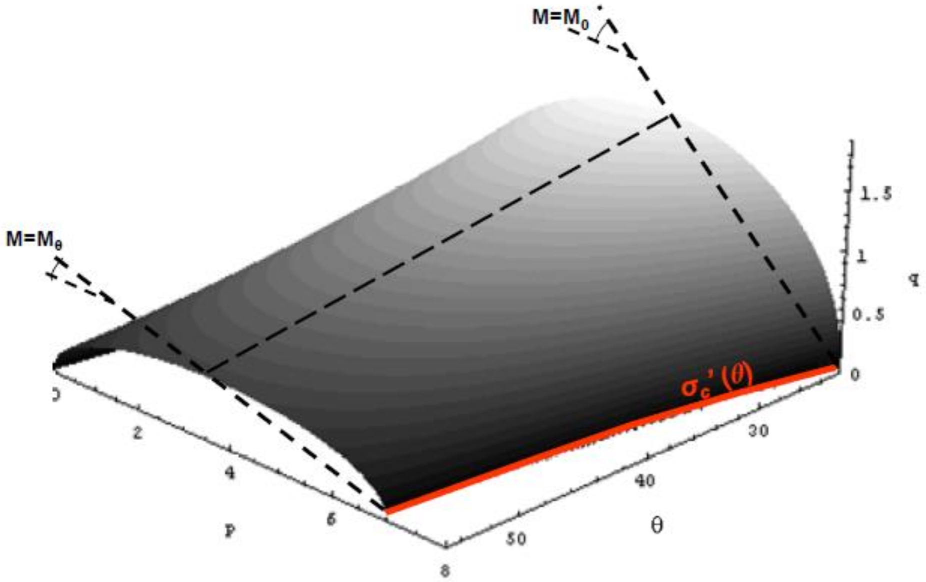

Figure 21: Qualitative shape of the thermo-plastic yield locus at critical state (Cecinato, 2009)

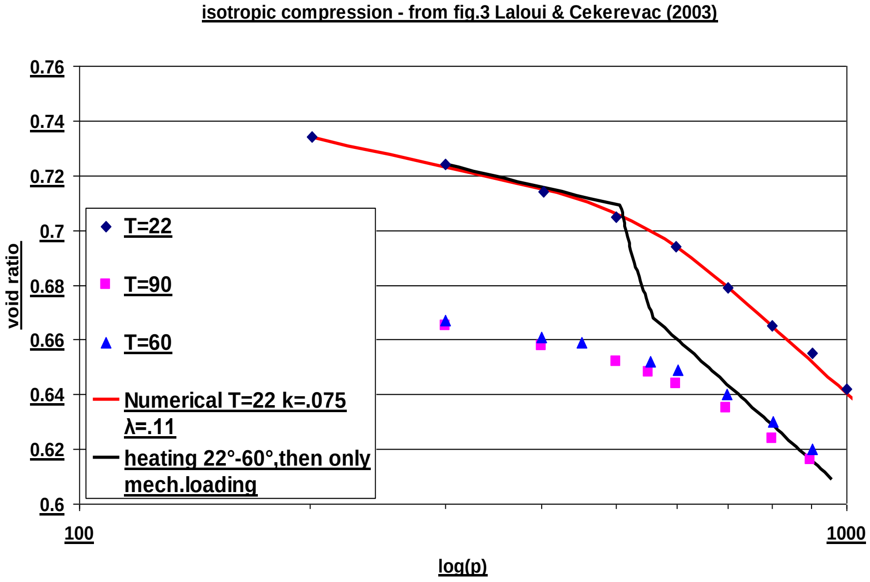

Figure 22: Validation of Cecinato's model through experimental data from Laloui and Cekerevac (2003) (reproduced from Cecinato (2009))

2.3.5 Robinet's model

Robinet et al. (1996) developed a thermo-mechanical constitutive model based on Hueckel's model. This model considered the existence of a threshold temperature. Above the threshold temperature, both irreversible and reversible dilative strains occur as temperature increases. Below the threshold temperature, only reversible strains occur. Therefore, an isotropic yield surface was introduced based on the concept of threshold temperature in order to calculate the reversible and irreversible thermal strain. In addition, a different hardening rule was adopted to ensure that no change in the yield locus takes place while cooling.

For the deviatoric part, MCC was adopted and was coupled with the above isotropic yield function. Validation of Robinet's model through some experimental data is given in Figure 23

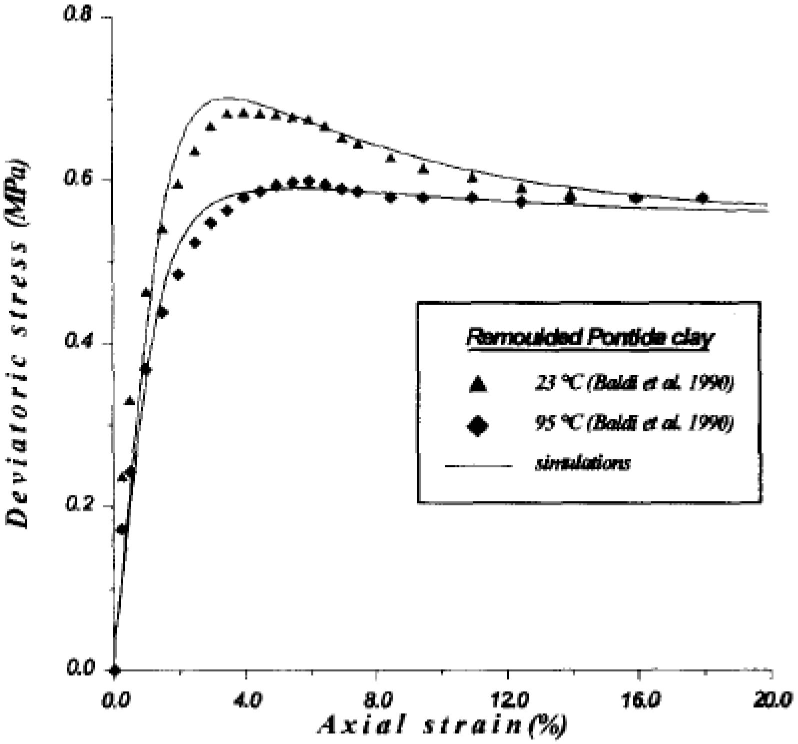

Figure 23: Numerical simulation and experiments of two axial drained paths of over consolidated state (Robinet et al., 1996)

2.3.6 Sultan's model

Cui et al. (2000), Delage et al. (2000) and Sultan et al. (2002) developed a thermo-mechanical model for saturated clays based on experimental results from triaxial tests under temperature control. The effect of overconsolidation ratio on the volumetric strain induced due to heating was investigated experimentally. Findings from this study were used to modify the existing models proposed by Hueckel and Borsetto (1990) for saturated clays in order to include the effects of over consolidation ratio.

Hueckel proposed that, irreversible thermal contraction occurs only on highly over consolidated specimens. Unlike Hueckel's model, Cui et al. (2000) observed experimentally that, there can be irreversible thermal contraction for low values of OCR. A new plastic mechanism called "thermal yield" (TY) was introduced by using an additional yield locus. Then the TY yield locus was coupled with Hueckel's hardening law to express more realistically the hardening behaviour of soil. Modified Cam clay was adopted for the deviatoric part. Validation of Sultan's model through some experimental data is given in Figure 24.

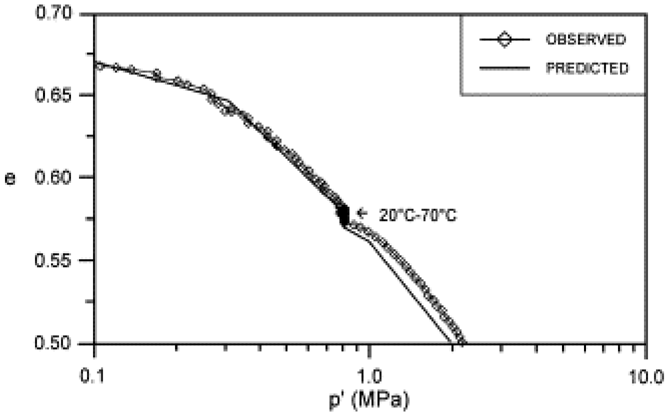

Figure 24: Thermal overconsolidation of the boom clay: comparison between predicted and observed results (Sultan et al., 2002)

2.3.7 The mechanism of thermal pressurisation

In the context of landslide, the thermal pressurization phenomena can be explained as follows;

When the slide starts, the heat is produced due to friction within the slip surface due to the dissipated work. The soil strength reduces as velocity and displacement increases (Tika and Hutchinson, 1999). At the same time, thermo plastic collapse occurs due to temperature rise as explained in Laloui and Francois (2009). Furthermore, temperature rise facilitate the generation of pore water pressure due to thermal expansion of water. As a consequence, the effective stress at the slip surface is reduced due to rising of pore water pressure. The resistance to sliding is reduced which lead the collapse.

Thermal pressurisation has been extensively studied, especially when it occurs in rock leading to shear failure or hydraulic fracturing (Rice, 2006). Sulem et al. (2007) and Wibberley and Shimamoto (2005) studied about the thermal collapse of clay materials in fault zones. Vardoulakis (2002a, 2002b) has studied thermal pressurisation in clayey gouges with application to the dynamic behaviour of rapid landslides. Many experimental evidence of thermal pressurisation mechanism can be found in the literature notably, Baldi et al. (1988) Campanella and Mitchell (1968) Ghabezloo and Sulem (2009) Sultan et al. (2002).

Many attempt has been made to measure or calculate an average value for the key parameter, pressurisation coefficient λ_m, that gives the pore pressure increase due to a unit temperature increase under undrained and isochoric conditions (at constant specific volume). This can be given in terms of the thermal expansion coefficient (α) and the compressibility coefficient (c) as Vardoulakis (2002a)

$$\lambda_m = \left.\frac{\partial p}{\partial \theta}\right|_{\substack{vol=const \\ undrained}} = \frac{\alpha}{c} \tag{2.44}$$

where $\alpha = \alpha_m - \alpha_c$; α_m and α_c are the thermal expansion coefficients of the soil water mixture and soil skeleton respectively.

Experimental evidence shows that normally consolidated soil exhibits volume contraction under drained heating. (Hueckel and Baldi, 1990, Laloui and Cekerevac, 2003, Laloui and Francois, 2009). This is explained as the result of an internal mechanism of microstructural collapse, due to changes in water absorption by clay particles (Campanella and Mitchell, 1968).

Several authors found that normally consolidated soil exhibits volume reduction during heating , while over-consolidated soil shows elastic expansion at the initial stage of heating and plastic contraction with subsequent heating (Baldi et al., 1988, Laloui and Cekerevac, 2003, Modaressi and Laloui, 1997, Sultan et al., 2002). Volume change due to heating for different OCRs can be plotted as in Figure 25. Under a heating/cooling cycle, volume changes for different values of OCR are shown in Figure 26. For increasing OCR, a transition temperature was identified at which plastic contraction starts from dilative elastic behaviour.

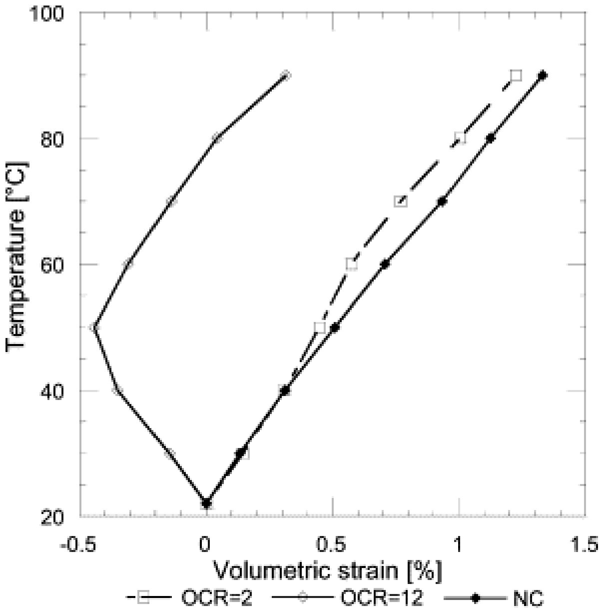

Figure 25: Experimentally observed thermal volume change of the CM clay (Kaolin) (Laloui and Cekerevac, 2003)

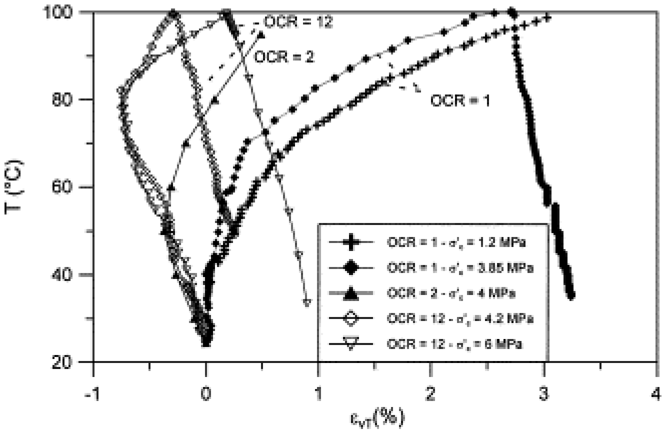

Figure 26: Thermal volumetric changes of Boom clay samples at different OCR values.

Based on the above experiments carried out in Boom clay, four major trends of thermal volume changes were identified as listed below (Sultan et al., 2002)

- The plastic contraction of normally consolidated samples is independent of the mean effective stress applied.
- The thermal contraction increases when OCR is decreased, leading to pure contraction for normally consolidated soil.
- The slope of the volumetric strain versus temperature (i.e. thermo-elastic expansion coefficient) in the cooling stage is independent of the applied mean effective stress.
- The temperature at which the transition between thermal expansion and contraction occurs decreases with OCR.

For clay, Campanella and Mitchell (1968) found λ_m = 0.01 MPa/°C, Vardoulakis (2002a) proposed λ_m = 0.06 MPa/°C while Sulem et al. (2007) suggested λ_m = 0.1 MPa/°C. For sandstone, Campanella and Mitchell (1968) proposed λ_m = 0.05 MPa/°C while Rice (2006) estimated λ_m = 0.92 MPa/°C for a 7 km deep fault in rock with intact walls.

2.3.8 Discussion on thermo plasticity on soils

All constitutive models of thermo plasticity of soils have some common characteristics as well as some drawbacks. Hueckel's model is the first comprehensive model which is suitable for numerical implementations. This model was improved by Sultan, Robinet and co-workers by incorporating a new volumetric mechanism. Moreover, Hueckel's model concentrated more on describing volumetric deformation, which is not as important in a landslide context as shear deformation.

A different model was proposed by Laloui and co-workers to describe the deformation of soils due to thermal loading. The main drawback of Laloui's model is that for the deviatoric mechanism the original Cam Clay yield function was used which, due to its non-smooth character, may cause problem in a numerical implementation. Also, this model is more complex as it contains two separate mechanisms for isotropic and deviatoric.

Cecinato (2009) modified Laloui’s model by adopting the Modified Cam Clay model instead which is smooth and does not suffer from this problem. Although all the above models take the temperature into account none includes the time dependent behaviour of soils present even in isothermal conditions.

In the following section, a critical review on time dependent behaviour of soils (creep) is made, with the intention of improving the existing thermo-plasticity models of soil so that, they cover temperature as well as time-dependent behaviour.

2.4 Review of constitutive models of time-dependent behaviour of soil

In this section, existing models that deal with time dependent behaviour of soils are reviewed. Creep of soils has been investigated in the laboratory by researchers and is defined as the progressive, irrecoverable deformation of a soil element under a state of constant effective stress (Hyde and Brown, 1976, Kuwano and Jardine, 2002, Murayama et al., 1984).

In general, the entire process of shear creep of a soil can be divided into three stages: primary, secondary and tertiary creep (Augustesen et al., 2004). Experimental evidence shows that during the primary creep stage the shear strain rate decreases with time. Then, during the secondary stage the rate remains constant and finally during the tertiary stage it increases with time. Failure due to what is called creep rupture is possible during the tertiary stage (Figure 27). Many authors proposed models for secondary creep only (Bjerrum, 1967, Borja and Kavazanjian, 1985, Kavazanjian and Mitchell, 1977, Singh and Mitchell, 1968), although several models for all three stages of creep including rupture have also been proposed (Feda, 1989, Kuhn and Mitchell, 1993, Mitchell et al., 1968, Ter-Stepanian, 1975).

Feda (1989) describes that the structural hardening, i.e. particle re-orientation, is responsible for the primary creep whereas structural softening, i.e. particle disorienting, is for tertiary creep. The balancing of both softening and hardening occur during secondary creep. In the context of landslides, the primary and secondary creep can be used to explain the prolonged slow movement whereas, the tertiary creep can be used to explain the eventual catastrophic failure.

In some soils one-dimensional compression continues under constant loading even after excess pore pressure has dissipated, i.e. after primary consolidation has ceased - this is called secondary compression or volumetric creep (Lo, 1961, Mesri, 1973). The secondary compression coefficient C_α is used to describe the magnitude of the volumetric creep as follows (Figure 28);

$$\Delta e = C_\alpha \Delta \log(t) \qquad 2.45$$

where Δe change in void ratio and $\Delta \log(t)$ is the change of logarithmic time. The temperature dependence on volumetric creep strain rate in explained in Section 5.8.1 in detail.

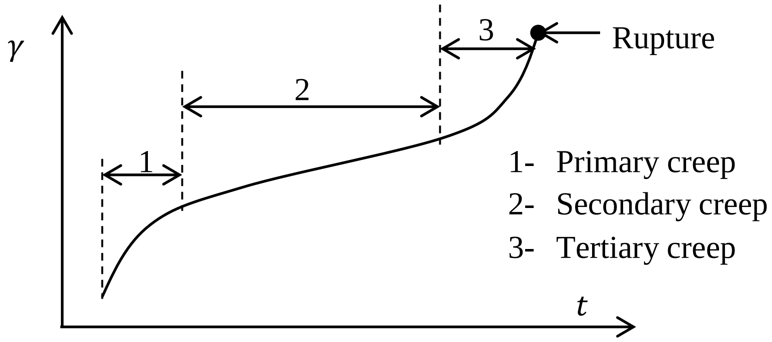

Figure 27: Three stages of creep of soil under constant effective stress

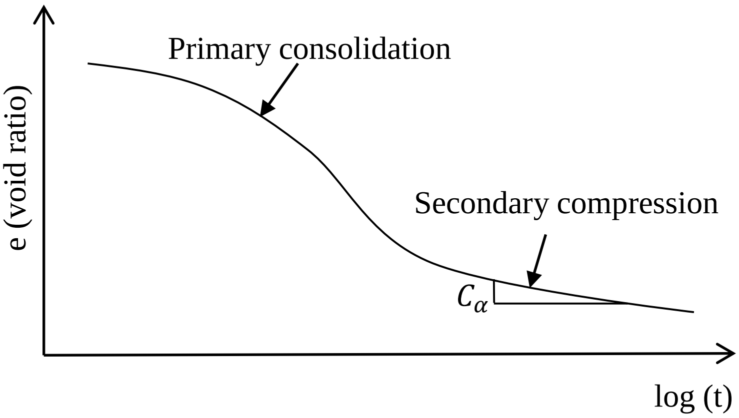

Figure 28: primary and secondary consolidation in *e vs log(t)* plot for soils

2.4.1 Bjerrum’s model for volumetric creep

Bjerrum (1967) proposed that the total volume change occurring in clay has two main components as defined below (Figure 29b).

a) An ‘instant compression’ which occurs simultaneously with the increase in effective pressure and causes a reduction in void ratio until an equilibrium value is reached at which the structure effectively supports the applied pressure.

b) A ‘delayed compression’ representing the reduction in volume at constant effective stress.

These two components are contrary to the well-known expressions, ‘primary’ and ‘secondary’ compression Figure 29a.

Assuming that the behaviour of soil is governed by a single void ratio *e vs log p′* curve, it is not possible to capture the delayed compression of soils. To overcome this problem, Bjerrum (1967) introduced a system of *e vs log p′* lines called time lines as shown in Figure 30. Timelines are defined as “lines of constant duration of loading”. Each timeline represents the compression behaviour after a particular duration of sustained loading. For example, if applied stress is increased at an interval of 24h, the corresponding *e vs log p′* line is called 1-day time line (Bjerrum, 1967).

Figure 30 illustrates the development of delayed compression under constant stress with time (path A–B). It also should be mentioned that, during delayed compression, void ratio decreases passing through the successive timelines as shown in Figure 30. Also, the soil becomes over consolidated with time as the apparent preconsolidation stress , $\sigma'_{z,pc}$, increases (point C in Figure 30).

Bjerrum’s model of secondary compression is a relatively simple one that quantitatively captures some aspects of soil creep although it is only concerned with the volumetric component.

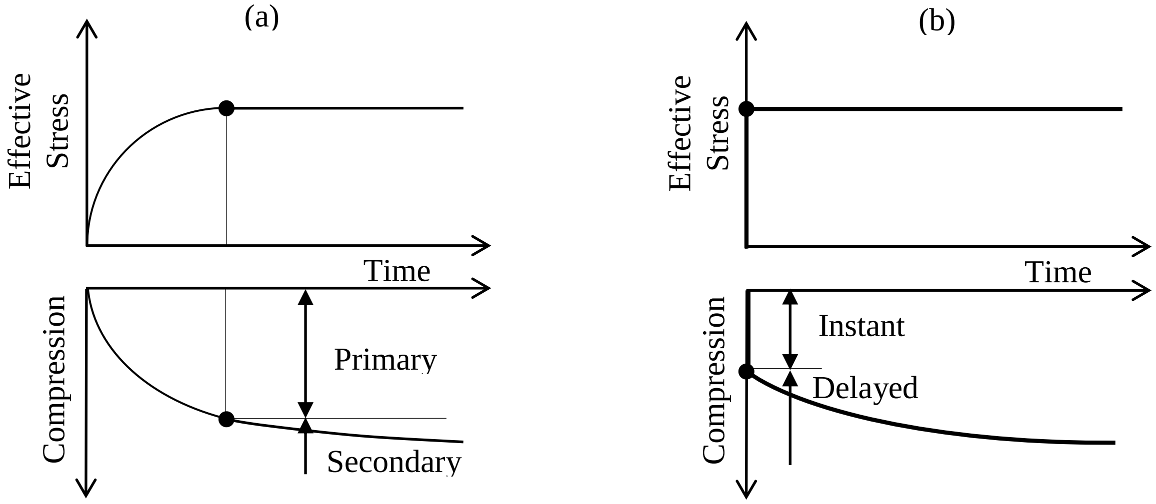

Figure 29: (a) Concept of primary and secondary compression (b) Concept of instant and delayed compression proposed by Bjerrum (1967)

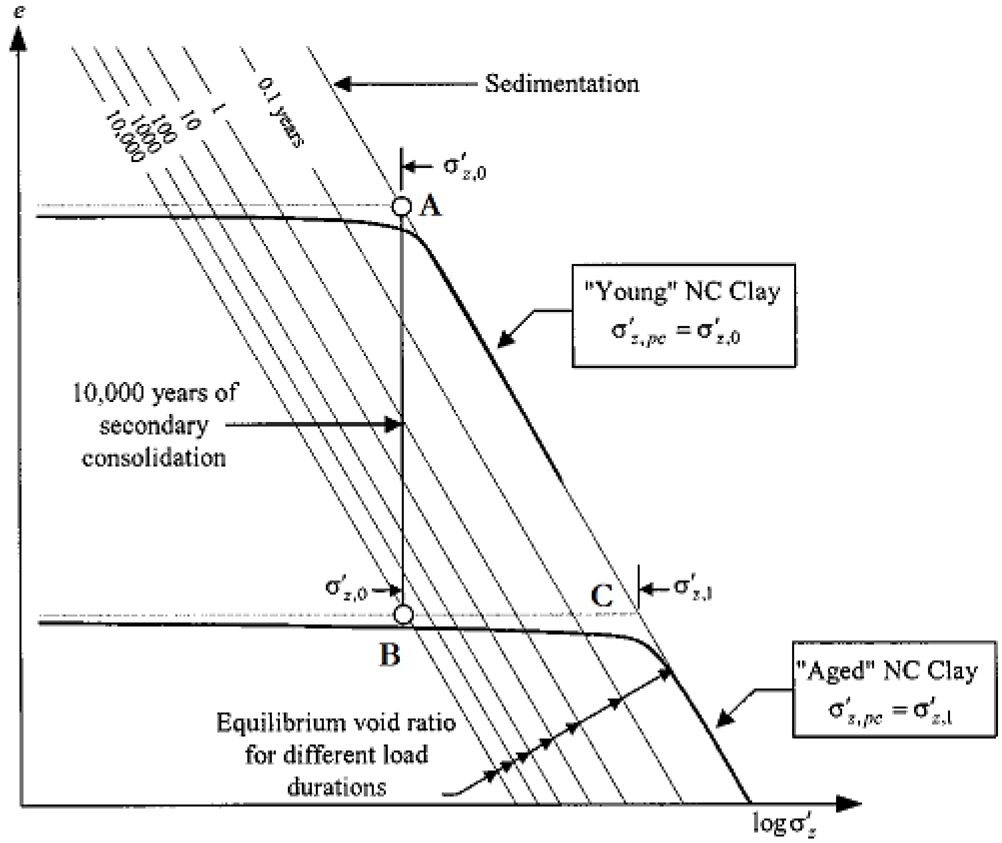

Figure 30: Proposed timelines in e vs log p plot (modified from Bjerrum (1967))

2.4.2 Singh and Mitchell model

From the experimental studies carried out by Mitchell and Campanella (1964), it was clearly understood that the time dependent response of a soil depends on various factors such as soil type, soil structure, stress history, drainage conditions and type of loading among others.

Singh and Mitchell (1968) proposed a general stress–strain-time equation with parameters based on drained and undrained triaxial creep tests (Figure 31 and Figure 32). Their model focused on the creep behaviour of clays subjected to stresses in the range of 30% - 90% of the initial strength. The axial strain rate – time relationship in this model is;

$$\dot{\varepsilon}_a = A\, e^{\bar{\alpha}\bar{D}} \left(\frac{t_i}{t}\right)^m \tag{2.46}$$

where $\bar{\alpha} = \alpha q_{max}$ and $\bar{D} = q/q_{max}$. A is a parameter that represents the composition, structure and the stress history of the soil, α indicates the stress intensity effect on the creep rate q indicates the deviatoric stress applied on specimen, t is the time t_i is a reference time. Finally, the parameter m controls the strain rate with time and has a key role: If $m >$ 1; the axial creep strain reaches an asymptotic value over time and if $m \leq 1$; the creep strain increases infinitely with time (Figure 33a).

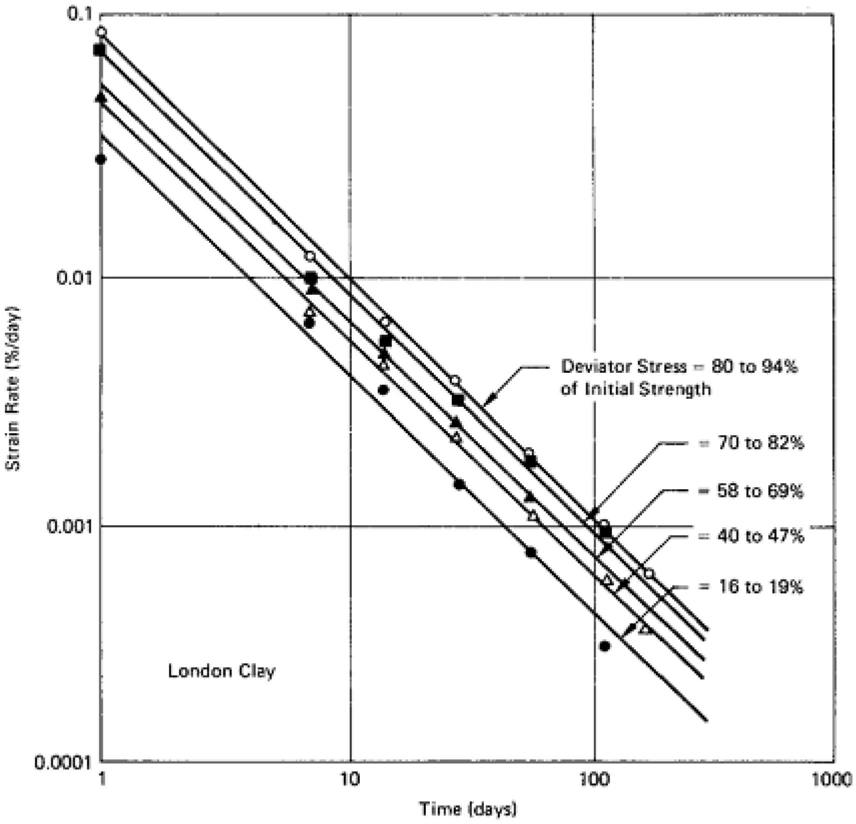

Figure 31: Strain rate vs. time relationships during drained creep of London clay (data from Bishop (1966)).

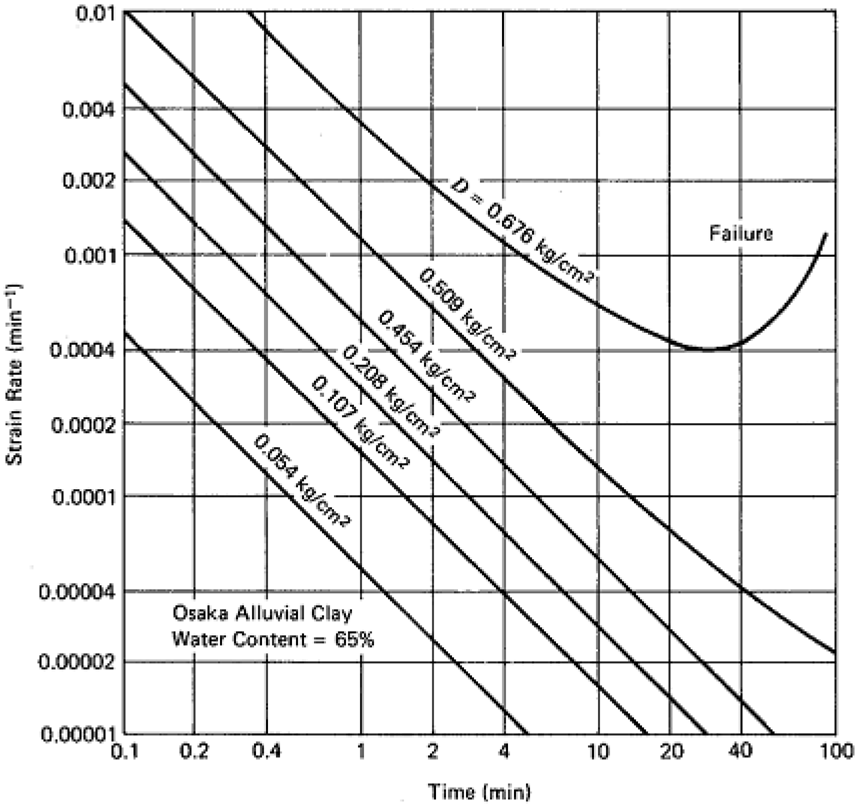

Figure 32: Strain rate vs. time relationships during undrained creep of Osaka alluvial clay (data from Murayama and Shibata (1958)).

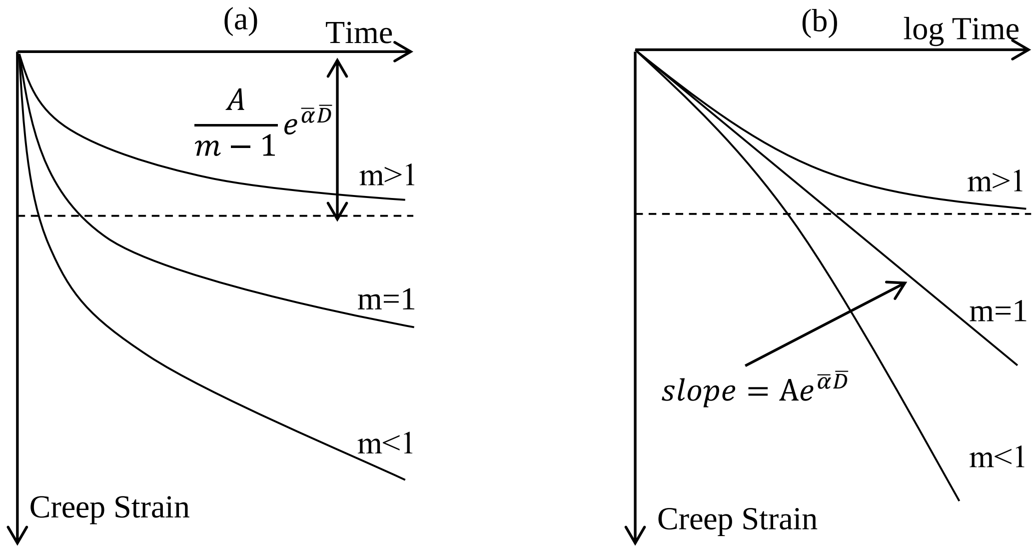

Figure 33: Creep curves predicted from Singh-Mitchell Creep equation for different m values. (a) strain vs time and (b) strain vs log time

2.4.3 Kavazanjian and Mitchell model

Kavazanjian and Mitchell (1977) proposed a different constitutive model for the time dependent behaviour of soil in the form of a general stress- strain-time relationship.

This model was separately formulated for the volumetric and deviatoric components. Both components are assumed to have instantaneous and delayed strains as defined in Bjerrum (1967). Kavazanjian and Mitchell (1977) derived the volumetric part of the strain from the concept of logarithmic secondary compression law and the deviatoric part from the Singh-Mitchell model. Even though the Singh-Mitchell model quantifies the axial strain in triaxial conditions, Kavazanjian and Mitchell (1977), proposed an indirect method for calculating the deviatoric strain from axial strain.

Borja and Kavazanjian (1985) expanded this model further to calculate creep strains by employing the normality rule on the modified Cam Clay yield surface. To achieve this, the total strain was decomposed into three parts as follows;

$$\dot{\boldsymbol{\varepsilon}} = \dot{\boldsymbol{\varepsilon}}^e + \dot{\boldsymbol{\varepsilon}}^p + \dot{\boldsymbol{\varepsilon}}^t \tag{2.47}$$

where superscripts e and p denote time-independent elastic and plastic components respectively and t denotes the time-dependent component, which is irreversible. Borja and Kavazanjian (1985) proposed that the preconsolidation pressure p_c increases due to two mechanisms. The first one is due to the strain hardening. The second one is due to aging of soil as proposed by Bjerrum (1967). The expression for $\dot{p}_c$ (rate of preconsolidation pressure) is given as (Borja and Kavazanjian, 1985);

$$\dot{p}_c = \left(\frac{1+e}{\lambda-\kappa}\right) p_c \dot{\boldsymbol{\varepsilon}}_v^p + \left(\frac{\psi}{\lambda-\kappa}\right)\left(\frac{p_c}{t}\right) \qquad \text{where}\,, \psi_\alpha = \frac{C_\propto}{\ln 10} \qquad 2.48$$

where $C_\propto$ is the coefficient of secondary compression (Equation 2.45), e is the void ratio, λ is the slope of the normal consolidation line, κ is the slope of unloading-reloading line, $\dot{\boldsymbol{\varepsilon}}_v^p$ is the volumetric strain rate and t is the time.

Borja and Kavazanjian (1985) validated their model against data from drained triaxial compression test on Weald Clay as shown in Figure 34.

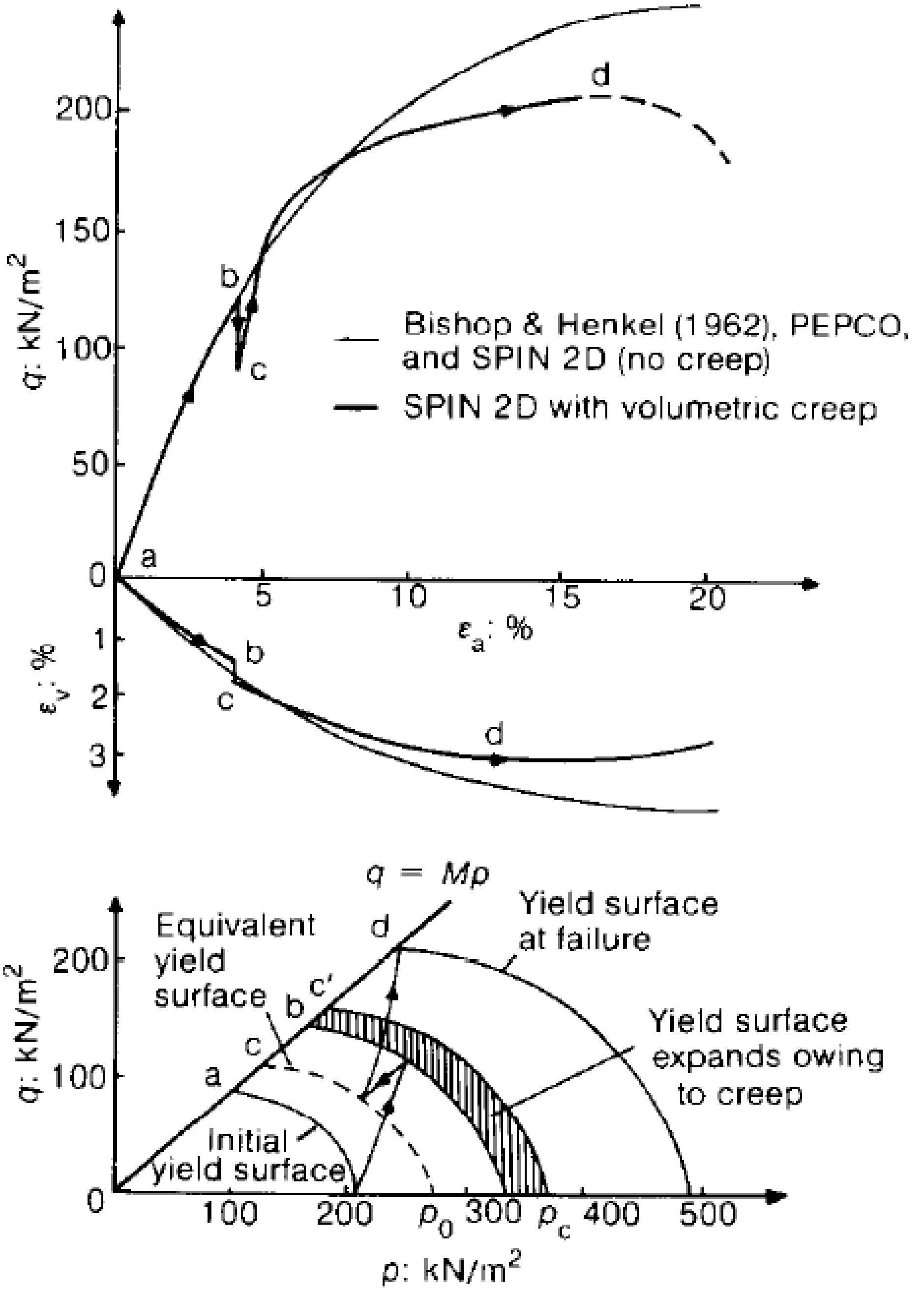

Figure 34: Comparison of numerical simulations (SPIN 2D) and drained triaxial test on Weald Clay (Borja and Kavazanjian, 1985)

Overall, the model proposed by Kavazanjian and Mitchell (1977) and Borja and Kavazanjian (1985) can be considered as a comprehensive model for the creep of soils as it describes both the volumetric and the deviatoric creep strain components.

2.4.4 Creep model with strain rate effects

Many studies showed that strain rate also influences the stress-strain behaviour of soil. This can be demonstrated using the direct shear test carried out at different shearing velocity. Each velocity will give a different stress strain behaviour (Di Benedetto et al., 2002, Leroueil et al., 1985, Mateši and Vucetic, 2003, Vaid and Campanella, 1977).

Leroueil et al. (1985), investigated the relationship between stress (σ_z'), axial strain(ε_a), and strain rate $(\dot{\varepsilon}_a)$ on many natural clays. Constant rate of strain tests (CRS) were carried out for five types of natural clays selected from different sites (Smith and Wahls, 1969, Wissa et al., 1971). Using the experimental results, as shown in Figure 35, Leroueil et al. (1985) suggested a possible framework between σ_z', ε_a and $\dot{\varepsilon}_a$ can be described by two general functions.

The first one gives the preconsolidation pressure as a function of strain rate as follows

$$\sigma_{z,pc}' = f(\dot{\varepsilon}_a\,) \tag{2.49}$$

The second one represents the normalized stress-strain relationship

$$\frac{\sigma_z'}{\sigma_{z,pc}'} = g(\varepsilon_a) \tag{2.50}$$

The above two equations (2.49 and 2.50) can be explained using Figure 36. The normalized stress-strain curve varies for clays depends on the types structures of the clays.

For a given soil, a unique normalised stress-strain relation can be written from one dimensional consolidation as follows,

$$\varepsilon_a = \frac{C_r}{1+e_0}\ln\left(\frac{\sigma_{z,pc}'}{\sigma_{z,o}'}\right) + \frac{C_c}{1+e_0}\ln\left(\frac{\sigma_z'}{\sigma_{z,pc}'}\right) \tag{2.51}$$

In the above, C_c & C_r are the compression and the recompression index of the soils, e_0 is the initial void ratio and $\sigma_{z,o}'$ is the initial vertical stress. There is no closed-form expression for f, in Equation 2.49, recommended by Leroueil et al. (1985). But later, Leroueil et al. (1996), suggested a linear relationship for the preconsolidation pressure ($f(\dot{\varepsilon}_z)$ in Equation 2.49) as follows;

$$\sigma_{z,pc}' = A + \left(\frac{1}{m'}\right)(\dot{\varepsilon}_z) \tag{2.52}$$

where *m'* and *A* are constants. Therefore, it is possible to derive a general stress-strain-strain rate equation after substituting Equation 2.52 into Equation 2.51.

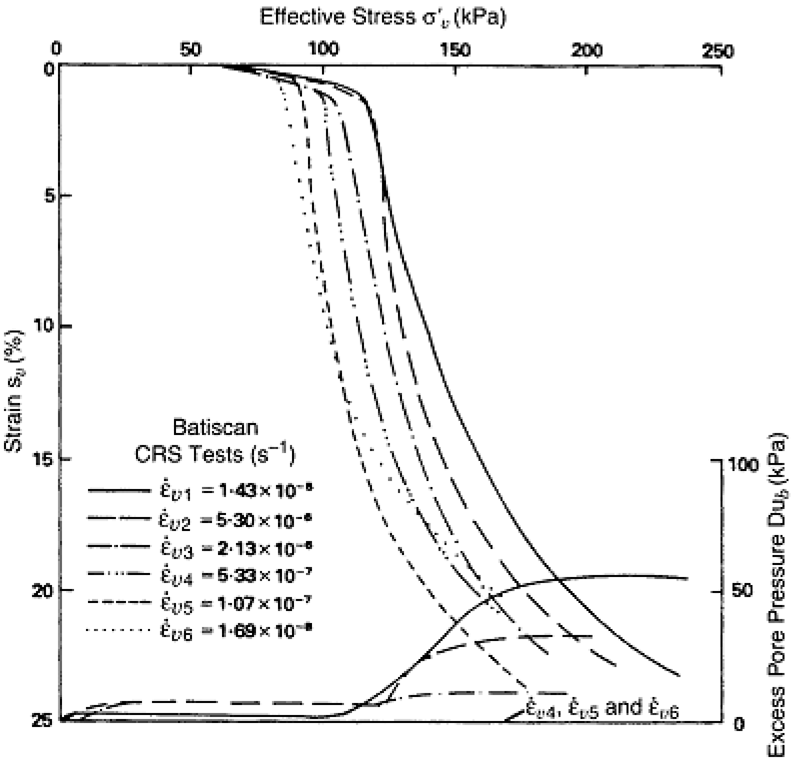

Figure 35: Rate dependency on one-dimensional compression characteristics of Batiscan clay (After Leroueil et al. (1985))

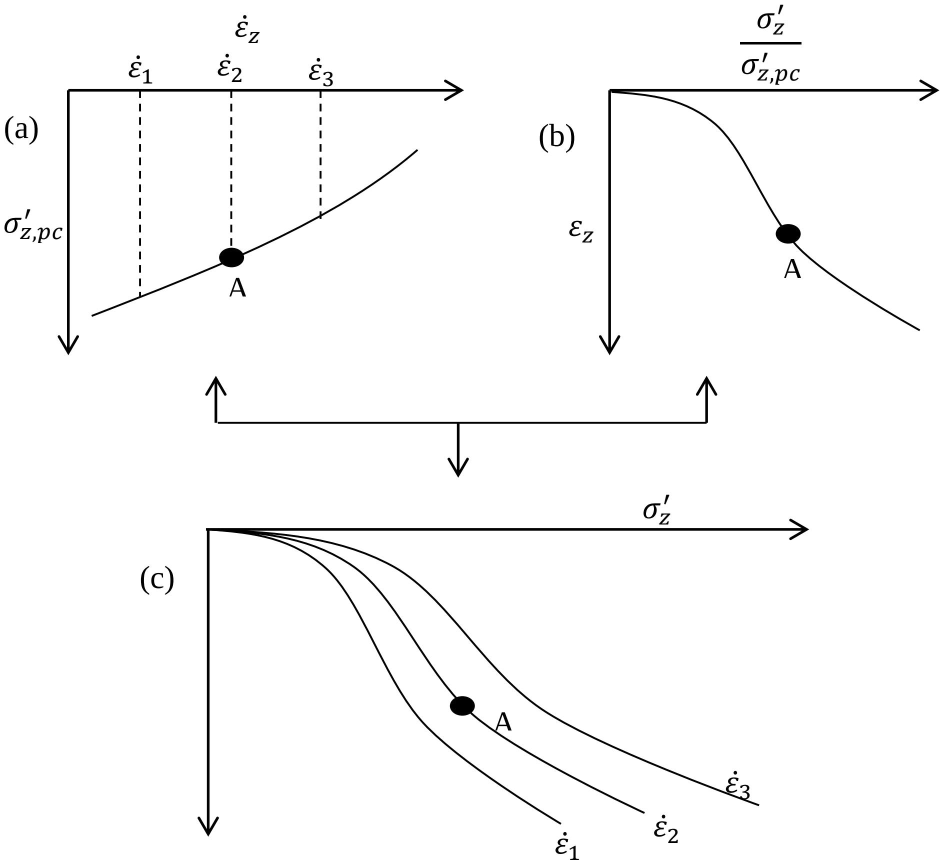

Figure 36: Stress–strain–strain-rate relationship for the strain rate approach: (a) normalized variation of the preconsolidation pressure with the strain rate (b) normalized effective stress–strain relation (c) experimental curves obtained at different strain rates (Leroueil et al., 1985)

2.4.5 Soil creep as a rate process

Many authors described creep of soil using rate process theory (Feda, 1989, Kuhn and Mitchell, 1993, Kwok and Bolton, 2010, Mitchell et al., 1968, Ter-Stepanian, 1975). Rate process theory is applicable to various materials such as polymer, asphalt, minerals etc. (Eyring, 1936)

Rate process theory describes creep by considering on the movement of flow units such as atoms, molecules or particles. The movement of flow units is opposed by an energy barrier called activation energy which keeps a flow unit in an equilibrium position. If enough additional energy to exceed the activation energy is applied to the flow unit by an external source, it will move and cause deformation. This energy source can have different forms (e.g. a heat source or an applied stress). The complete description of rate process theory and application to the creep of soils will be discussed in Sections 4.1, 4.2 and 4.3.

2.4.6 Soil Creep models with the influence of temperature

Temperature also affects the creep behaviour soils. Some experimental studies were carried out by Campanella and Mitchell (1968) to predict the effects of temperature. In this experiment, a conventional triaxial creep test was carried out with step increments of temperature. Typical results from test for most samples are shown in Figure 37. Using this experimental results, Mitchell et al. (1968) proposed the following equation.

$$E = \frac{2.3 \times R \times T_2 \times T_1}{(T_2 - T_1)} \log_{10} \frac{\dot{\varepsilon}_2 T_1}{\dot{\varepsilon}_1 T_2} \qquad 2.53$$

where, E is called activation energy is a constant for a given soil will be discussed in Section 4.3.1 in detail. $\dot{\varepsilon}_1$ and $\dot{\varepsilon}_2$ are the strain rate values at the values of absolute temperature T_1 and T_2 respectively. R is the gas constant.

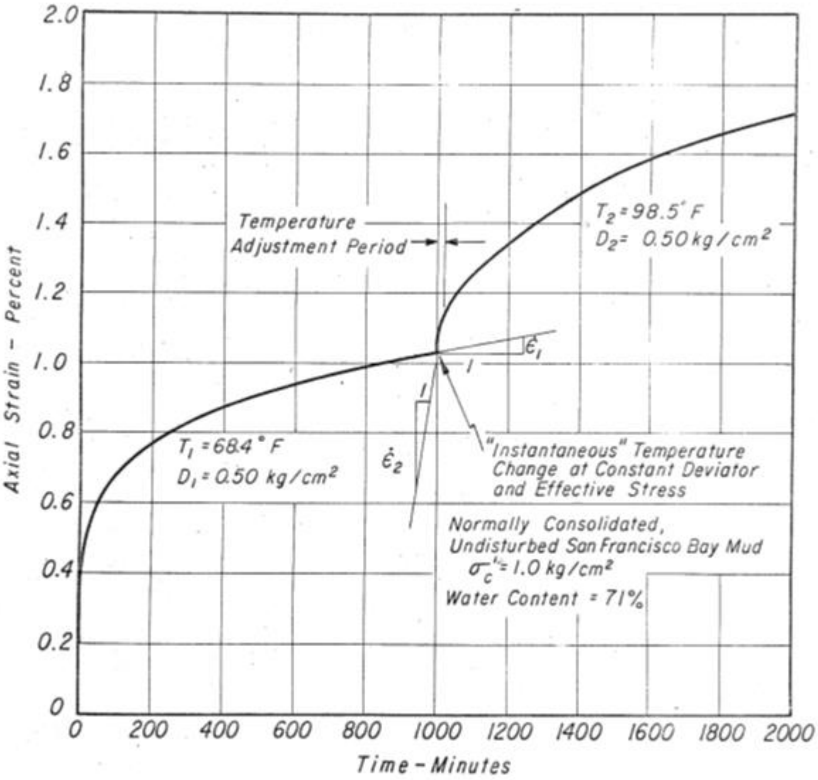

Figure 37: Typical results of triaxial creep test with step increment of temperature (Campanella and Mitchell, 1968)

2.4.7 Feda's creep model

Feda (1989) attempted interpreting the results of ring shear experiments (Figure 38) on the basis of rate process theory. Moreover, inclusion of primary and tertiary creep was also attempted in this model which will be more relevant in the context of landslides.

From the basic consideration of rate process theory shear strain rate can be written in the following form (Feda, 1989);

$$\dot{\gamma} = \frac{2kT}{h} \exp\left(\frac{\tau\lambda_l}{2SkT} - \frac{U_0}{RT}\right) \qquad 2.54$$

k = Boltzmann’s constant, 1.38×10^{-23}J/K

h = Plank’s Constant 6.62×10^{-34}J s

R = Universal gas constant, 8.31 J/ (mol K)

T = Absolute temperature, K

λ_l = Distance between successive equilibrium points of two flow units

U_0= Activation Energy, which is a measure of bonding strength, J/mol

τ = Applied shear stress

S = Number of bond/m^2

Feda (1989) modelled the shear creep of soil by combining the rate process theory and observations made from ring shear experiments for different specimen of soil.

With some substitutions, Feda (1989) modified the shear strain equation as follows;

$$\dot{\gamma} = D\, exp\, \alpha_d \tau_f \left(\frac{\tau}{\tau_f}\right) \qquad 2.55$$

τ_f - Long term strength (tertiary creep occurs at $\tau \rightarrow \tau_f$)

$$D = \frac{2kT}{h} exp\left(-\frac{U_0}{RT}\right)$$

$$\alpha_d = \frac{\lambda_l}{2SkT}$$

In isothermal conditions, the term D is constant, so that shear strain rate, in Equation 2.55, becomes constant with constant applied shear stress. Therefore, it is possible to model only secondary creep in isothermal condition. In order to include primary creep, where strain rate decreases with time, Feda (1989) proposed to consider D as time dependent as follows;

$$D(t) = D\left(\frac{t_i}{t}\right)^n \qquad 2.56$$

where t_i, is a reference time, t is the natural time and $n > 0$ is an exponent determines the rate of shear strain rate. Now it is possible to predict the primary creep by using rate process theory.

Furthermore, from the experimental data (ring shear test), it was found that, α_d obeys the following equation.

$$\alpha_d \tau_f = a_d + b_d \left(\frac{t}{t_i}\right) \qquad 2.57$$

The stage of creep can be obtained by using the following conditions;

If $b_d > 0$;

Soil is in primary creep. During this stage, the soil exhibits strain hardening behaviour, therefore the strain rate diminishes with time.

If $b_d = 0$;

Soil is in secondary creep. During this stage, the soil can be thought of both strain hardening and strain softening at the same rate therefore the strain rate remains constant with time.

If $b_d > 0$;

Soil is in tertiary creep, during this stage soil exhibits strain softening behaviour. Therefore the strain rate increases with time and the soil will eventually fail.

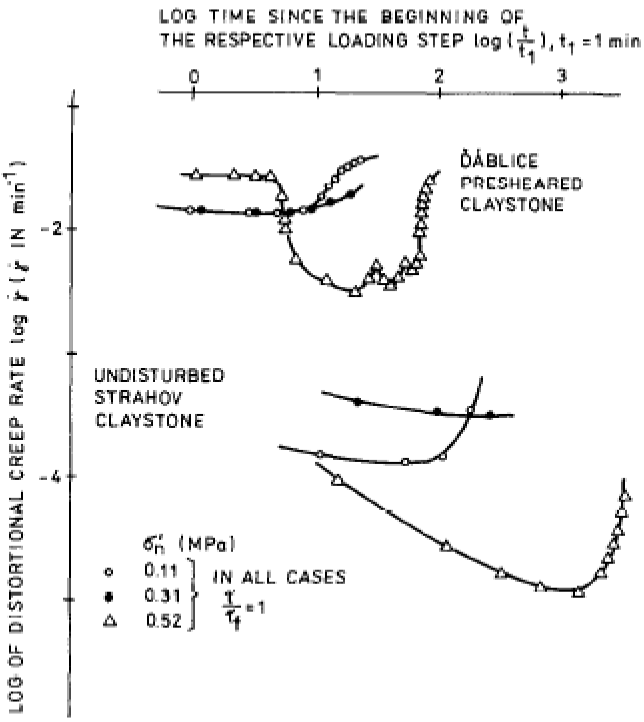

Figure 38: Results of ring shear creep test on different soils (Feda, 1989)

2.4.8 Ter-Stepanian's model

Ter-Stepanian (1975) also presented a model of shear creep of clay based on rate process theory and experimental results (Figure 39) . It is based on the following assumptions.

- The external forces applied to a soil specimen are transferred to the particle contacts, and each contact force can be resolved in to a normal (r_i) and a tangential (f_i) component. It is assumed that the shear strain rate of the soil specimen is proportional to 'structure deformability', defined as the ratio between vectorial sum of tangential $(F = \sum f_i)$ and normal $(R = \sum r_i)$ forces.

- Each inter-particle contact contains several bonds, which break due to the applied shear stress. Therefore the lifetime (L) of the interparticle bonds depends on the applied shear stress (Bjerrum, 1973).
- During primary creep, the strain rate reduces due to reorientation of particles arrangement, (i.e. soil structure becomes more regular). So that, L is directly proportional to time but during tertiary creep, the particles become more de-oriented and L is inversely proportional to time.

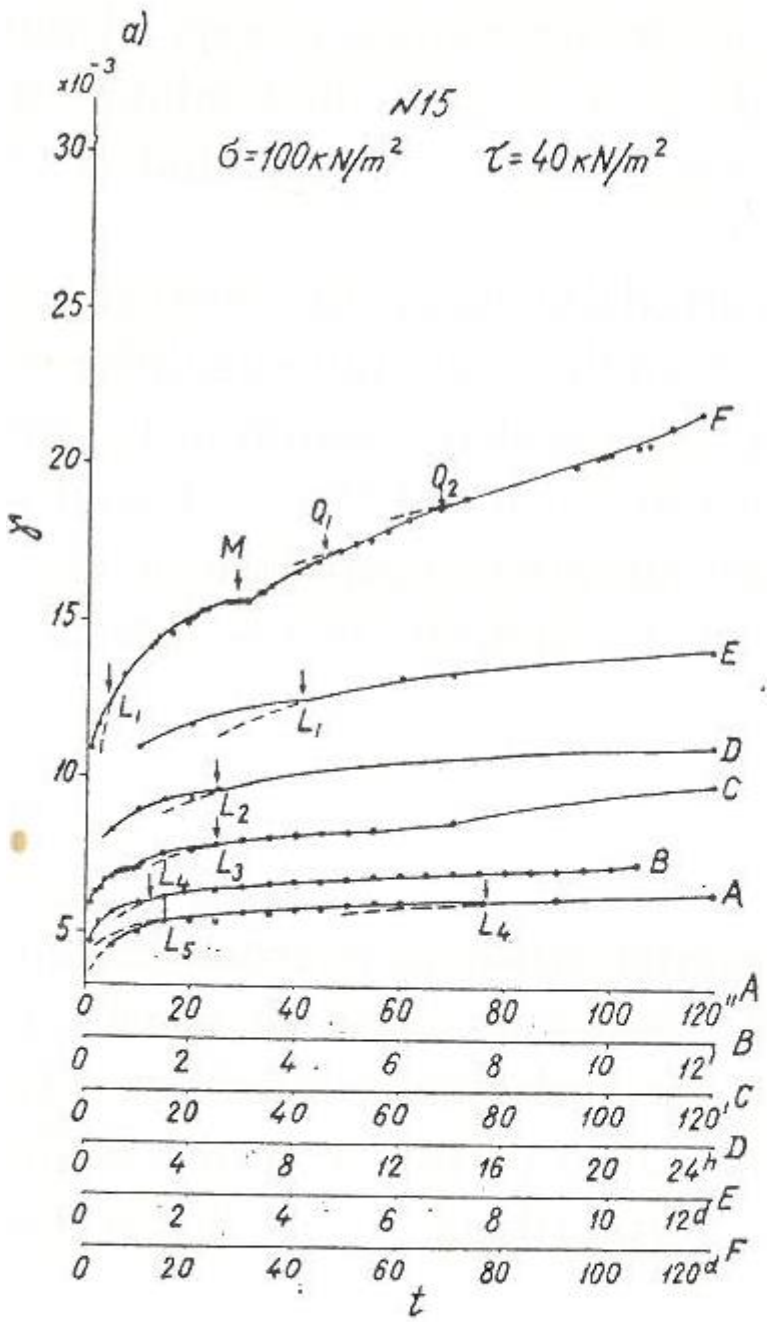

Figure 39: Results of ring shear creep test on Sissian Pliocene diatomaceous deposits

With these assumptions, the following strain rate equation for was proposed for primary creep.

$$\dot{\gamma} = a\left(\frac{\tau - \tau_p}{\zeta}\right)\frac{1}{t} \tag{2.58}$$

Similarly, during the tertiary creep strain rate becomes;

$$\dot{\gamma} = a\left(\frac{\tau - \tau_p}{\zeta}\right)\frac{t}{(t_0)^2} \tag{2.59}$$

In Equations 2.58 & 2.59, ζ is a constant and a is a coefficient that depends on structure deformability (F/R). The coefficient a is;

$$a = \overline{K}\left(\frac{F}{R}\right)\frac{kT}{h}\exp\left(\frac{-U_0}{RT}\right)\exp\left(\frac{\lambda_l f_0}{2kT}\right) \tag{2.60}$$

where, $\overline{K}$ is the coefficient of proportionality with dimension of time and f_0 is the average tangential force per flow unit i.e. molecule in the soil. In this model, f_0 was assumed constant for a given soil, and independent of external applied forces.

2.4.9 Visco-plasticity of soils

The concept of visco-plasticity was introduced and developed by Perzyna; it is also referred to as overstress theory (Olszak and Perzyna, 1966a, b, Perzyna, 1962a, Perzyna, 1962b, 1966). A key assumption in Perzyna's overstress theory is that viscous effects are negligible in the elastic region, i.e., no viscous strains occur within the static yield surface, which corresponds to the traditional yield surface associated with time independent plasticity (Figure 40). In other words, the elastic strains are time independent whereas the inelastic strains are time dependent. The total strain rate is additively composed of the elastic and viscoplastic strain rates:

$$\dot{\varepsilon} = \dot{\varepsilon}^{e} + \dot{\varepsilon}^{vp} \tag{2.61}$$

In the theory of elasto-visco-plasticity, the inelastic strain rate represents the viscous and plastic effects combined. The elastic strain rate is assumed to obey the generalized Hooke's law. The static yield function denoted by f_y separates the elastic and inelastic strain regime. f_y is consistent with the classical concept of an elasto plastic yield function. If the stress point lies inside the static yield locus, elastic deformation takes place while if it is outside, viscoplastic strain would be expected to occur. In contrast to elasto-plastic theory, in viscoplastic theory, stress states are allowed to go outside the static yield locus and it is then that viscoplastic strains occur. The overstress function F determines the magnitude of viscoplastic strain and is defined such that $F > 0, F < 0, F = 0$ when the stress state P is outside, within or on f_y respectively. While the viscoplastic strain-rate is assumed to obey the following non-associated flow rule:

$$\dot{\varepsilon}_{ij}^{vp} = \gamma\phi(F)\,\frac{\partial g}{\partial \sigma'_{ij}} \qquad 2.62$$

where γ is the fluidity parameter, ϕ is the viscous nucleus, F is the overstress function, g is the potential function and σ'_{ij} is the effective stress state.

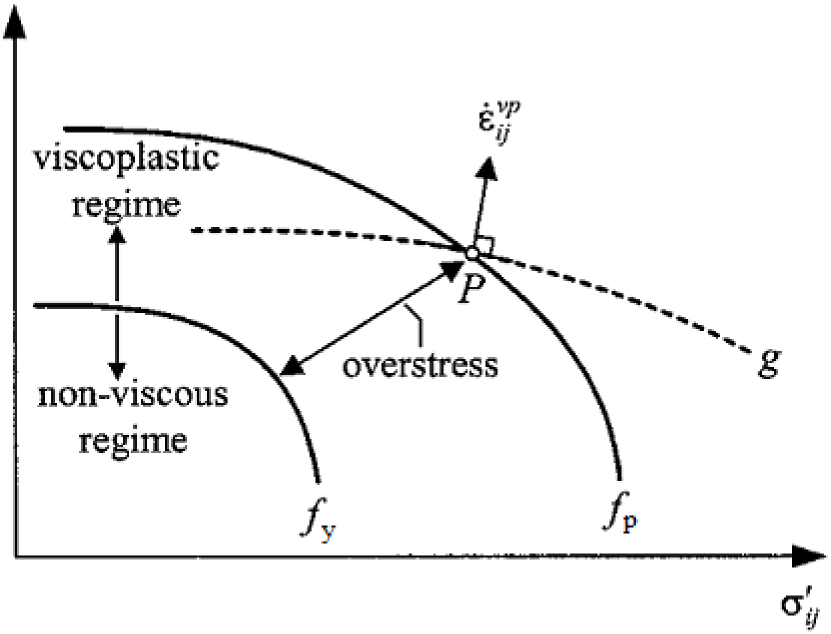

Figure 40: Stress state P is part of the dynamic yield surface f_p and overstress F is defined as the distance between P and the static yield surface f_y Furthermore, the viscoplastic strain rate vector is perpendicular to the plastic potential surface g

The over stress function is a function of viscoplasitc work $W^{vp}$and the current stress state σ'_{ij} which can be written as

$$F\left(W^{vp}, \sigma'_{ij}\right) = \frac{f_p\left(W^{vp}, \sigma'_{ij}\right)}{\kappa_s(W^{vp})} - 1 \qquad 2.63$$

where

$$W^{vp} = \int_0^{\dot{\varepsilon}_{ij}^{vp}} \sigma'_{ij}\dot{\varepsilon}_{ij}^{vp}$$

and the function f_p describes the dynamic loading surface on which the current stress point P is located (Figure 40) and κ_s is the hardening parameter. Therefore, the following constraints are applied to the viscous nucleus ϕ according to the key assumption of flow rule applied to the dynamic yield function.

$$\langle\phi(F)\rangle = \begin{cases} 0 & \text{for } F \leq 0 \\ \phi(F) & \text{for } F > 0 \end{cases} \qquad 2.64$$

The above constraints can be considered as loading criteria for inelastic deformation. The direction of viscoplastic strain is assumed normal to the dynamic yield function f_p.

2.4.10 Discussion

The models reported above take different approaches for describing the creep behaviour of soils. Secondary compression law is the first methodology used to calculate the long-term settlement of soils under constant loading. However, this method can be used to calculate the volumetric creep only. Bjerrum's model is more advanced, in that total strain is decomposed as instant (primary) and delayed (secondary). Again however, only volumetric strain can be calculated by using this model.

The Singh and Mitchel model can capture both volumetric and shear creep of soils. However tertiary creep cannot be simulated, because the strain rate is considered to either decreases or remain constant with time. The Kavazanjian and Mitchell model is a more advanced and comprehensive model, as it describes the both volumetric and deviatoric creep behaviour of soils. One further advantage is that it used the widely uses the Modified Cam Clay yield surface.

Viscoplasticity is widely used currently to describe the time dependent behaviour of soil. The one advantage is that, by using this, both the creep (constant stress rate) and the relaxation process (constant strain rate) can be simulated. In viscoplastic models, the stress point should be outside the static yield locus in order to create creep strain. However, soil may undergo deformation under constant stress even though the stress state is in elastic region. This particular behaviour cannot be predicted by a viscoplastic model. Another disadvantage is that it lacks the ability to predict the tertiary creep.

Feda's and Ter-Stepanian's models were derived based on rate process theory and some experimental results. Both have some common characteristics;

- Both models focused mainly on shear creep of soil and ring shear tests were carried out to support them.
- In both cases, time dependent coefficients were used to capture the different stages (primary, secondary and tertiary) of creep.
- Even though the basic equation for rate process theory contains temperature as a parameter both models were proposed for isothermal conditions.

In conclusion, most creep models in the literature consider isothermal conditions. A model considering both creep and temperature dependent soil behaviour is still lacking.

2.5 Review of existing models of large scale landslides

There are many models available in the literature that deal with large scale landslides. Some selected models, which include frictional heating, are reviewed here and a discussion is made on the advantages and disadvantages of each model.

It has been proposed that frictional heating of the slip zone plays a major role on the failure of landslides. Firstly, Habib (1975) proposed a mechanism of vaporization of pore water pressure due to frictional heating to explain the reduction in the strength of rockslides in the Vaiont landslide. De Blasio and Elverhoi (2008), Erismann (1979) and Gaziev (1984) described the concept of "self-lubrication", where rock particles crushed the in to fine grains or even melted in the shear zone, leading to loss of shear strength.

2.5.1 Vardoulakis's dynamic thermo-poro-mechanical model

Vardoulakis (2002a) presented a comprehensive landslide model by using a thermo-poro-mechanics approach. In this model, heat generation due to friction, pore pressure build up due to the production of heat and loss of shear strength due to thermoplastic collapse of the soil skeleton were taken into account to determine the evolution of a landslide during the time window of catastrophic acceleration of the sliding mass, but before the sliding mass starts break into pieces. It considers a rock mass sliding on a thin clay layer (shear band); the motion of the mass and the deformation of the shear band is derived using energy, mass and momentum balance. The geometry of the problem is divided into two sections. The first one is a long thin shear band with thickness of Z_b. Pore pressure *u (z,t)*, temperature *θ (z,t)*, and the velocity *v (z,t)* inside the shear band are functions of time *t* and depth *z* . Furthermore, it was considered that, all deformation and heat production take place inside this thin shear band. The second section of the geometry is the sliding mass on top of the shear band (Figure 41).

The shear band thickness plays a major role on the shear strain, strain rate, heat generation and diffusion of heat and pore water pressure. Vardoulakis selected the shear band thickness of 1.4mm based on experimental observations (Morgenstern and Tchalenko, 1967, Tika and Hutchinson, 1999).

In the shear band, temperature increases due to frictional heating and pore water pressure rises due to thermal pressurization. This set of soil behaviour will allow rapid loss of shear strength; ultimately leading to catastrophic failure. From a constitutive model point of view, it was assumed that, the soil inside the shear band follows with the Mohr-Coulomb failure law (Figure 42). Some material strain and strain rate softening also were taken in to consideration (Tika and Hutchinson, 1999).

A set of three governing equations were derived in order to calculate the pore water pressure, temperature and the velocity/displacement profiles.

The first equation is the heat diffusion-production equation, and is an energy balance equation as follows;

$$\frac{\partial \theta}{\partial t} = \kappa_m \frac{\partial^2 \theta}{\partial z^2} + \hat{\mu}(\gamma, \dot{\gamma}) \left(\frac{|\sigma'_{n0} + u(z,t)|}{j(\rho C)_m} \right) \dot{\gamma} \qquad 2.65$$

The first term on the RHS of Equation 2.65 accounts for heat diffusion and the second is heat generation. Other parameters are defined are defined below;

κ_m= Kelvin’s coefficient of thermal diffusivity of the soil–water mixture

$\hat{\mu}(\gamma, \dot{\gamma})\ |\sigma'_{n0} + u(z,t)|\dot{\gamma} = D$, is the dissipation term, equal to the plastic work done inside the shear band,

$\hat{\mu}(\gamma, \dot{\gamma})$ is the strain and strain rate dependent friction coefficient,

$j(\rho C)_m = C_f$ is the thermal constant of the soil water mixture

The second equation is the pore water pressure equation, derived from mass balance together with Darcy’s law as follows;

$$\frac{\partial u}{\partial t} = \frac{\partial}{\partial z}\left(c_v(\theta) \frac{\partial u}{\partial z} \right) + \lambda_m \frac{\partial \theta}{\partial t} \qquad 2.66$$

where c_v is the temperature dependent consolidation coefficient and λ_m is the temperature and pore pressure dependent pressurization coefficient. The first term on the RHS of Equation 2.66 accounts for pore water pressure diffusion and the second term for generation of excess pore water pressure due to thermal pressurization.

The third equation is the dynamics equation derived from the momentum balance of the material inside the shear band. The velocity profile inside the shear band is described as follows;

$$\frac{\partial v}{\partial t} = \frac{1}{\rho}\left[-\hat{\mu}(\gamma, \dot{\gamma}) \frac{\partial u}{\partial z} + H|\sigma'_{n0} + u(z,t)| \frac{\partial^2 u}{\partial z^2} \right] \qquad 2.67$$

where $H = \frac{\partial \hat{\mu}}{\partial \dot{\gamma}}$ is called as frictional rate sensitivity. After integration of Equation 2.67,

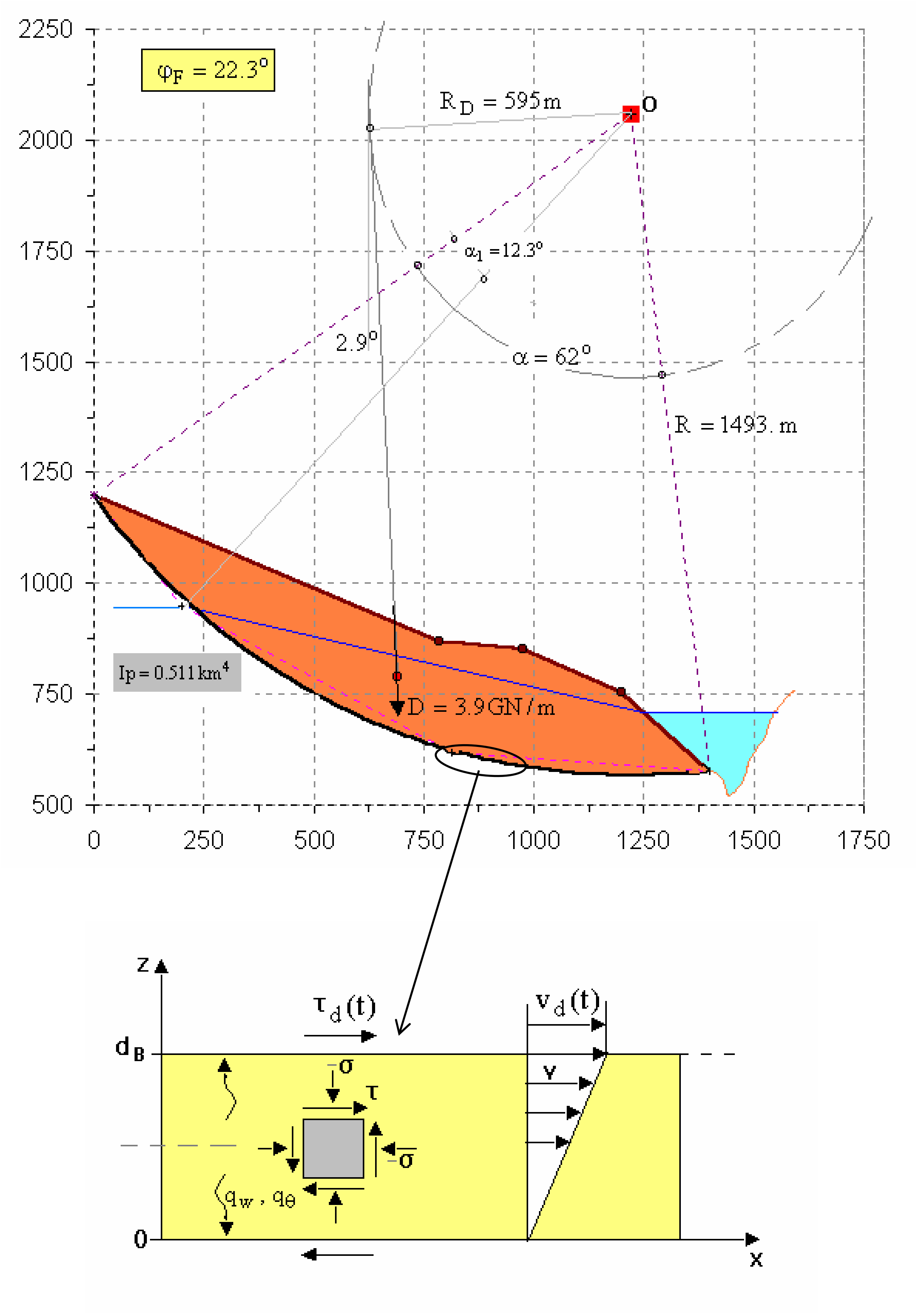

Figure 41: “Section 5” of Vaiont Landslides and enlarged shear band (After Vardoulakis (2002a))

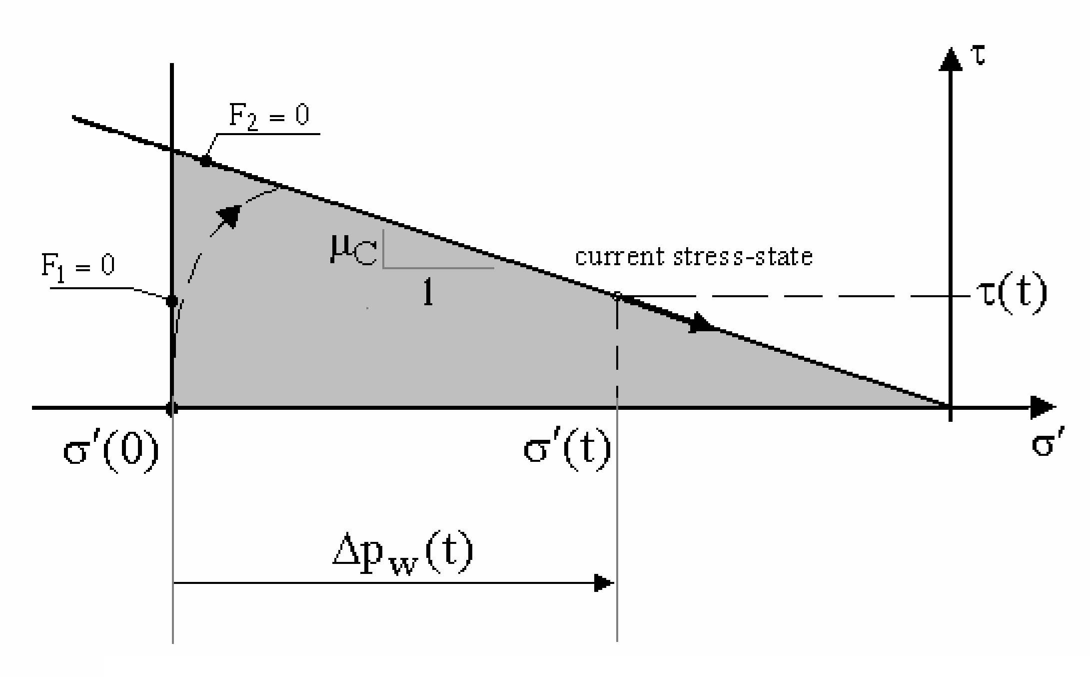

Figure 42: Scheme of constitutive model (Vardoulakis 2002)

Vardoulakis (2002a) found that the resulting spatial velocity profile is close to linear form, so that following equation is adopted instead of equation 2.67.

$$v = v_d(t)\left(\frac{z}{Z_b}\right) \tag{2.68}$$

where z is the spatial coordinate inside the shear band, Z_b is the thickness of the shear band. $v_d(t)$ is the velocity at the upper boundary of the shearband which coincides with the velocity of the sliding mass and is governed by;

$$\frac{dv_d}{dt} = R\omega_0^2\left(A(\mu_m) + \frac{u_d(t)}{p_c(\mu_m)}\right) \tag{2.69}$$

where ω_0^2 & R are constants depending on the geometry, A and p_c are model parameters, and are functions of mobilised friction coefficient and u_d is the excess pore water pressure at the interphase between the shear band and sliding mass.

This model was applied to back analyse the Vaiont landslide, successfully reproducing its catastrophic acceleration phase.

2.5.2 Cecinato's model

Cecinato (2009), Cecinato et al. (2011) and Cecinato and Zervos (2012) improved Vardoulakis's model by incorporating some additional aspects. First, a more realistic constitutive approach was adopted than in Vardoulakis's model based on thermo-plasticity and covering wider range of thermal behaviour of soil. As Modified Cam-Clay is used in Cecinato's thermo-plasticity constitutive model, a superposition of thermal softening was made in the critical state parameter *(M)* in addition to the Vardoulakis's assumption of displacement and velocity softening. Final expression for M yields as:

$$M(\gamma,\dot{\gamma},\theta) = \widehat{M}(\gamma,\dot{\gamma}) - \tilde{g}(\theta - \theta_{ref}) \tag{2.70}$$

where θ is the temperature, θ_{ref} is the reference temperature and $\tilde{g}$ is thermal sensitivity.

Vardoulakis (2002a) used the Mohr-Coulomb failure law in constitutive point of view which is temperature independent. Therefore, the pressurization coefficient λ_m is proposed based on the available experimental evident. However, Cecinato developed a thermo-plasticity constitutive model that can capture the thermal behaviour of soils (Section 2.3.4). Therefore an expression for λ_m is derived which is consistent with the proposed thermo plasticity framework which is given by;

$$\lambda_m = \frac{\lambda - \kappa}{\lambda c}\left\{\frac{\gamma\kappa}{(1+e)\theta\left(1 - \gamma\log\left(\frac{\theta}{\theta_0}\right)\right)} - 2\beta_s\right\} \tag{2.71}$$

In the above, λ is the slope of the normal consolidation line, κ is the slope of the unloading-reloading line, c is the compressibility of soils, γ is a material parameter defining the rate of decrease of preconsolidation stress with θ. θ is the temperature and θ_0 is reference temperature normally taken as ambient temperature.

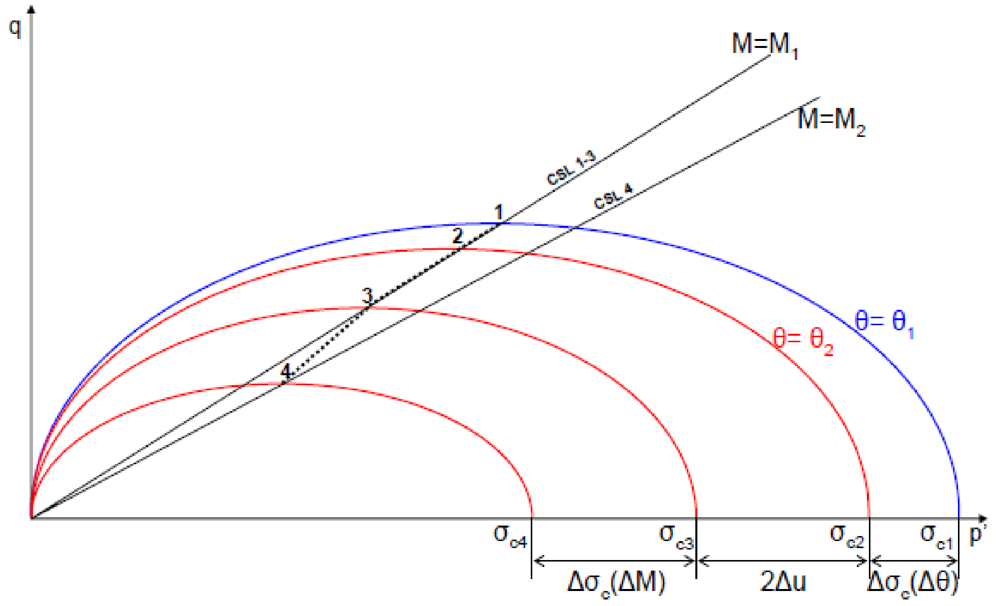

Figure 43: Effective stress path of material point inside the shear band (Cecinato, 2009)

Cecinato (2009), Cecinato et al. (2011) and Cecinato and Zervos (2012) assumed that the stress lies at critical state. The stress path during entire process of a landslide illustrated in

Figure 43; path 1 to 2 occurs due to thermal softening (2.25), path 2-3 occurs due to existences of excess pore water pressure, which reduces by $2\Delta u$ in preconsolidation pressure and path 3-4 occurs due to frictional softening where M reduces according to thermal friction sensitivity equation. But, all processes actually occur at the same time.

Using this model, Cecinato (2009) was also able to reproduce the catastrophic phase of the Vaiont Slide. Cecinato’s findings further show that, thermal friction softening is less important as a destabilising mechanism than the strain and strain rate softening for the development of catastrophic acceleration, also that thermal pressurization will cause thicker sliding masses to accelerate faster.

2.5.3 Thermo-poro-mechanics of creeping landslides (Veveakis et al, 2007)

Veveakis et al. (2007) presented a physically based landslide model with the inclusion of a creeping phase. This model also was finally applied to the Vaiont landslide for validation. As confirmed from the geological data, the Vaiont landslide was preceded by 3 years of creep and ended with the catastrophic collapse of a rock mass with velocity of about 30 m/s. Using the concepts of thermal softening and velocity hardening of soil, Veveakis et al. (2007) proposed that a balancing of these two mechanisms was responsible for the creeping phase of the slide.

The proposed expression for the frictional coefficient at critical state combined thermal softening and velocity hardening as follows.

$$\mu_{cs} = \mu_{ref}\left(\frac{\dot{\gamma}}{\dot{\gamma}_{ref}}\right)^{N} e^{-M(\theta-\theta_1)} \qquad 2.72$$

where N, M are the frictional rate sensitivity and the thermal sensitivity parameters respectively. Catastrophic acceleration is triggered, when a critical pressurization temperature is reached inside the shear zone, at which temperature thermal pressurization controls the acceleration of the rigid sliding mass. Even before the pressurization temperature is reached, however, the slide becomes critical because dissipation of heat progressively localizes inside an ever shrinking shear zone with time. This model was applied to the Vaiont slide and compared with the real values obtained from the case studies.

2.5.4 Goren and Aharonov‘s Thermo-poro-elastic model

Goren and Aharonov (2007, 2009) developed a model for large scale landslides using a thermo-poro-elastic approach. Frictional heating and thermal pressurization, were taken as possible mechanisms explaining catastrophic failure as well as slow movement. In this model also, governing equations were proposed based on the mass, energy and momentum balances. The results from this model show that the permeability of sliding mass is the dominant factor on the behaviour of landslides. Low permeability leads to catastrophic failure, while high permeability leads to slow movement (creep like movement) due to rapid dissipation of pore water pressure.

2.5.5 Puzrin’s model (shear band propagation)

Puzrin and co-workers presented a model for the growth of a shear band leading to catastrophic failure (Puzrin et al., 2010, Puzrin and Germanovich, 2005, Puzrin and Schmid, 2011, Puzrin and Sterba, 2006). Initially, the Palmer-Rice (PR) fracture mechanics was used to explain the propagation of the shear band. The original PR fracture mechanics was proposed for over consolidated soil only. Puzrin and Schmid (2011) attempted to develop a general approach based on the fracture mechanics, which is applicable to a wider range of soils such as saturated and unsaturated-normally and over consolidated soils. Finally, shear band propagation was studied with different approaches such as limiting equilibrium, linear elastic fracture mechanics, energy balance and the process zone technique. Among these approaches, energy balance was identified as the most conservative method.

Puzrin and Germanovich (2005) explained the different types of failure (progressive, catastrophic and delayed failure) using fracture mechanics. Puzrin et al. (2010) explained the shear band propagation of submarine landslides using the energy balance approach. Finally, this model was applied to back analyse the Storegga slides, the Western Goleta slide, and the Lake Lucerne slide submarine landslides. Velocity and acceleration were calculated and compared. Findings show that, stiffness of the soil, the viscosity of water and any yearly precipitation (pore water pressure) play main role on velocity and acceleration of landslides.

2.5.6 Alonso’s thermo-hydro-mechanics of rapid landslide

Another model was developed by Alonso et al. (2010) and Pinyol and Alonso (2010) using the thermo-hydro-mechanics approach to explain the final stage of the failure of Vaiont landslide. The same thermal pressurization concept was used here as well, to explain the heat induced pore pressure build-up. Alonso et al. (2010) also derived a set of governing equations using the energy, mass and momentum balances with some assumptions as listed below;

1. Pore water pressure changes due to thermal pressurization only.
2. The heat produced cannot escape through the band boundaries. The final failure of Vaiont is considered so quick, that conductive heat transfer is assumed negligible within the shear band.

Finally, pore water pressure isochrones, velocity and displacement profiles were plotted and compared with real geological results of Vaiont slide. The parameters selection was made based on Hendron and Patton (1985). Permeability was identified as one of the key parameters controlling failure.

2.5.7 Discussion on presented models of large scale landslides

Even though the Vardoulakis model is comprehensive some drawbacks were identified as listed below.

- The constitutive model adopted for the soil (simple Mohr-Coulomb failure line) does not capture the full range of temperature dependent behaviour of soils, such as thermal hardening and decrease in friction angle with temperature.
- The model cannot be easily generalized to two and three dimensions.
- The model covers catastrophic failure phase only. However slow creep-like movement of slopes for long periods of time is also known to often precede that.

Although Cecinato (2009) made improvements over Vardoulakis's model, still creep-like movement of the landslides is not included in that model either. Furthermore, Cecinato's model assumes a shear band of infinite length. In reality, the shear band initiates at a given location and propagates with time till global failure occurs. Growth of the shear band is not included in this model.

Creep-like movement was on the other hand included in Veveakis et al. (2007) thermo-poro-mechanical model. This model considered that the balancing of velocity hardening and thermal softening mechanisms keeps the slide in the creep stage. However, there is experimental evidence of velocity softening in clays (Tika and Hutchinson, 1999). Therefore one can conclude that, this model does not cover the full range of the behaviour of soil during the entire life time of a landslide either. Also, creep-like movement is observed in soils even in isothermal conditions, where thermal softening is irrelevant.

Absence of some possible mechanism can also be seen in Goren and Aharonov’s model. In particular;

- Inelastic soil behaviour such as hardening, strain softening, and strain rate softening mechanisms are not included.
- Although energy balance is used, the heat advection term is neglected.
- Thermal dependence of parameters such as the friction angle is not included.

Similar drawbacks are also presented in the model developed by Alonso et al. (2010).

- This model also does not cover the creeping phase of a landslide.
- Thermal conductivity was assumed as zero. In reality, it is possible to conduct the heat through the boundary.

Although a number of models are available in the literature, a comprehensive model covering all aspects of material behaviour at all stages of a landslide is still lacking. Due to the above reasons, more improvements are still needed to cover the wide range of possible mechanism of landslides

2.6 Further developments

In this Chapter, a comprehensive review of existing constitutive models on soils and landslide model was presented.

In the next chapter, a refined dynamic thermo-poro-mechanical landslide model is developed based on that developed by Cecinato (Cecinato, 2009, Cecinato and Zervos, 2012, Cecinato et al., 2011). Here a more realistic formulation for the dynamics of the moving slide is included.

In chapters 4, 5 & 6, Different thermo-poro-mechanical models are developed to simulate the transition between the creep and the catastrophic stages of a landslide. Three different types of model have been selected out of all reviewed creep models to represent the soil behaviour.

The first model is rate process theory which is based on activation of flow units (Section 2.4.5). Moreover, flow units can be activated by thermal energy as well as externally applied stress. Therefore, it should be possible to use it to model the creep like movement of landslides, as it incorporates the time dependent behaviour of soils and also the concept of thermal activation is inherently included.

The second one is the model proposed by Borja and co-workers (Section 2.4.3). This model explains the time dependent behaviour of soils in the context of Modified Cam-Clay. Moreover, Cecinato's thermo-plasticity explains the thermo-mechanical behaviour of soils with MCC. Therefore, it possible to combine the models developed by Borja's and Cecinato's to describe the both temperature and time-dependent behaviour of soil.

The third one is viscoplasticity of soil proposed by Perzyna and co-workers which explains the time dependent behaviour of soils (Section 2.4.9). It also can be combined with the Laloui's thermal softening law (applied to static yield locus) to include the thermal dependency on the soil behaviour in it.

Chapter 3: A refined thermo-poro-mechanical model for landslides

As described in section 2.5.2, Cecinato developed a two dimensional landslide model that is based on an advanced constitutive model describing the thermo-plasticity of soils (Cecinato, 2009, Cecinato and Zervos, 2008, Cecinato and Zervos, 2012, Cecinato et al., 2011, Cecinato et al., 2008). A limitation of this model, however, is that when formulated for a circular slip surface, the dynamic equation assumes a constant driving moment throughout the entire movement history of the landslide. In other words, the fact that the distance of the centre of gravity of the sliding mass from the centre of the slip circle, and therefore the driving moment, changes during sliding, has been ignored . In reality, the change of lever arm reduces the driving moment as displacement progresses. In this chapter, this landslide model is further refined by considering the change in the driving moment. First, the dynamic equation is modified, and then it is coupled with the same heat and pore pressure equations proposed by Cecinato (2009). Numerical results are subsequently presented and discussed.

3.1 Modified dynamic equation

The dynamic equation describes the velocity of the sliding mass over time. Cecinato (2009) and Vardoulakis (2002) assumed that the landslide mass rotates as a rigid body with respect to the centre of the predefined failure circle. Furthermore, the net driving moment was assumed constant. This assumption is a gross one as the net driving moment changes significantly during rotation of the mass. A more refined formulation is derived below.

A schematic diagram for the friction circle method is shown in Figure 44. With reference to Figure 44, the driving moment M_{drv} can be written as

$$M_{drv} = DR_D \tag{3.1}$$

The term D in Equation 3.1 is the resultant driving force, and R_D is the lever-arm from the centre of the failure circle. Angular displacement is measured from the initial position of limiting equilibrium. From Taylor's friction circle theorem, R_D (at the initial position) is written as; (Taylor, 1948)

$$R_D = R_f \sin \varphi_F \qquad 3.2$$

where, φ_F is the friction angle of the material inside the shear band at incipient failure and R_f is the radius of failure circle. R_D depends on displacement, therefore a general expression for R_D can be written as;

$$\begin{gathered} R_D = K_c R_f \sin(\varphi_F - \theta_d) \\ K_c = \frac{\alpha}{\sqrt{2(1-\cos\alpha)}} \end{gathered} \qquad 3.3$$

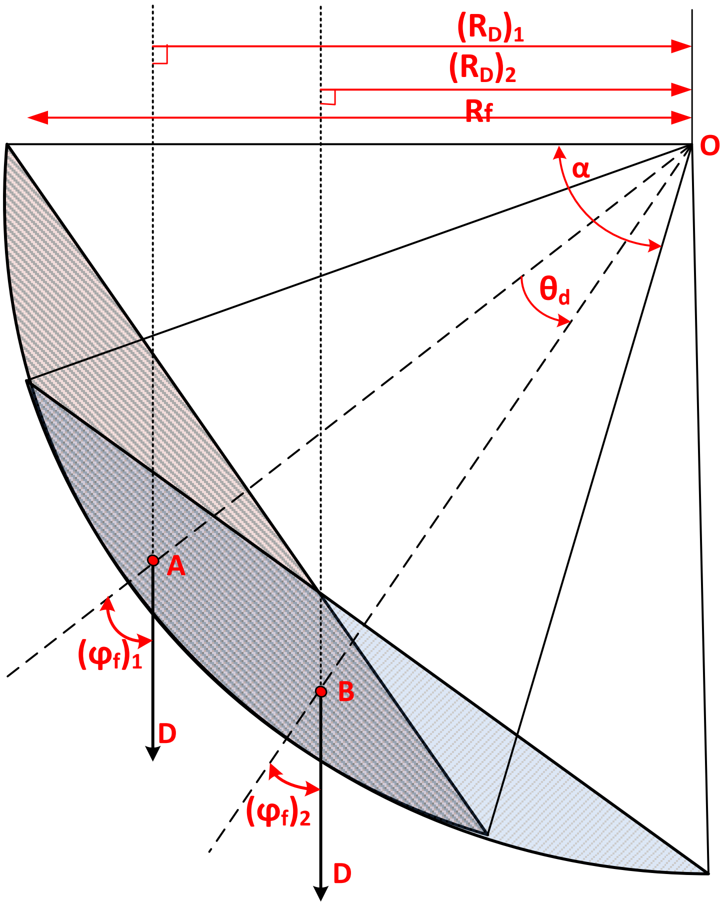

Figure 44: Schematic diagram schematic diagram representing friction circle method

where, θ_d is the angular displacement of the sliding mass, α is the opening angle of the failure arc, and K_c is a correction factor proposed by Taylor (1948). The resultant of normal reaction (σ'_{n0}) and tangential stress (due to friction) acting along the failure arc is at an obliquity of $R_f \sin(\varphi_F - \theta_d)$ to the centre of the failure arc. The circle drawn with this obliquity , $R_f \sin(\varphi_F - \theta_d)$, is called the friction circle. However, depending on the type of normal reaction (σ'_{n0}) distribution (uniformly, sinusoidal etc.), there is a deviation of tangency to the friction circle. In order correct this tangency, a factor K_c is used which depends on the opening angle of the failure arc. Factor K_c shown in Equation 3.3 is proposed for uniformly distributed load. Therefore the final expression for driving moment can be written as;

$$M_{drv} = D \frac{\alpha}{\sqrt{2(1-\cos\alpha)}} R_f \sin(\varphi_F - \theta_d) \tag{3.4}$$

The above result is valid only if the direction and magnitude of the resultant driving force are unchanged with time. This is plausible in cases where the magnitude of the seepage force is very small compared to the weight of the sliding mass, and it is the assumption made here.

Motion is resisted by the total friction force that develops along the failure circle. This depends on the friction angle and the normal effective stress. Assuming that the normal effective stress is constant along the failure circle, at any time it is given by

$$\sigma'_{n0} = \frac{D}{R_f\sqrt{2(1-\cos\alpha)}} \cos(\varphi_F - \theta_d) \tag{3.5}$$

Therefore the resisting moment can be written as;

$$M_{res} = \left[\sigma'_{n0} R_f \alpha - p_d R_f (\alpha - \alpha_1)\right] \mu R_f \tag{3.6}$$

where $\mu = \tan\varphi_m$ (φ_m is the mobilized friction angle of the shear band material) and $\alpha_2 = (\alpha - \alpha_1)$ is the opening angle of the part of the failure circle that is below the phreatic surface. p_d is the excess pore water pressure generated by thermal pressurization at the interface between the shear band and the moving rigid mass.

Balance of angular momentum gives

$$\rho I_p \frac{d\omega}{dt} = M_{drv} - M_{res} \tag{3.7}$$

where ρI_p is the polar moment of inertia of the sliding mass (ρ is the density of the mass and I_p the second moment of area) and ω is its angular velocity. Substituting the corresponding expressions for M_{drv} and M_{res} yields

$$\rho I_p \frac{d\omega}{dt} = \omega_0^2 \left(A + \frac{p_d(t)}{p_c}\right) \tag{3.8}$$

$$A = \frac{D R_f R_d}{\gamma_s I_p}\left(1 - \frac{\tan\varphi_m}{\tan(\varphi_F - \theta_d)}\right) \tag{3.9}$$

$$p_c = \frac{\gamma_s I_p}{R_f^3} \frac{1}{(\alpha - \alpha_1)\tan\varphi_m} \tag{3.10}$$

According to Equation 3.9, if $\tan \varphi_m \geq \tan(\varphi_F - \theta_d)$ the slide will be stable, whereas if $\tan \varphi_m < \tan(\varphi_F - \theta_d)$ the slide will be unstable. The sliding velocity is calculated from the angular velocity as follows.

$$v_d = R_f \omega(t) \tag{3.11}$$

To make this consistent with the constitutive relationship used by Cecinato (2009), the mobilized and incipient friction angles should be expressed in terms of a critical state parameter *(M)*. Since $\varphi' = \arctan(\mu)$ and $M = \sqrt{3} \sin \varphi'$ in plane strain, M is written as;

$$M = \sqrt{3} \sin(\arctan(\mu)) \tag{3.12}$$

From Equation 3.12

$$\mu = \tan\left\{\arcsin\left(\frac{M}{\sqrt{3}}\right)\right\} \tag{3.13}$$

Using the trigonometric identity

$$\arcsin(y) = \arctan\left(\frac{y}{\sqrt{1 - y^2}}\right) \tag{3.14}$$

and substituting $y = M/\sqrt{3}$ gives

$$\mu = \frac{M}{\sqrt{3 - M^2}} = \tan \varphi_m \tag{3.15}$$

The term $\tan \varphi_m$ in Equation 3.9 can be replaced with Equation 3.15 to obtain the dynamic equation in terms of the critical state parameter.

3.1.1 Computational results for the dynamic equation

To gain insights on the behaviour of the system, the dynamic equation was solved on its own by assuming that excess pore water pressure is zero. Strain and strain rate friction softening were taken into account. Friction strain and strain rate softening was reported by Tika and Hutchinson (1999) in ring shear experiments, and Vardoulakis (2002a) proposed simple hyperbolic expressions to describe the friction angle as a function of displacement and velocity.

In the analysis, the parameters given in Table 1 were chosen; they correspond to the dynamic analysis of Section 5 of Vaiont slide (Hendron and Patton, 1985) carried out by Vardoulakis (2002a) and Cecinato (2009). Peak mobilized friction angle was taken equal to the incipient failure angle(φ_F). However, setting the two values equal will result to no movement, because the initial acceleration will be zero. In order to trigger the landslide, φ_m was taken 1% lower than the incipient failure angle φ_F.

Results with the assumption of constant driving moment are also reported here for comparison. For constant driving moment, the acceleration of the slide reaches 2.25 m/s^2 and remains constant (Figure 46a). But for varying driving moment, the acceleration of the slide reaches 2.15 m/s^2, then decreases and becomes negative (deceleration), from which time onwards the resultant driving moment acts in the opposite direction of movement (Figure 46b).

Velocity and displacement of the slide are given in Figure 47 and Figure 48 respectively. For constant driving moment, the velocity of the slide increases linearly, reaches 100 m/sec after 45 sec and is predicted to increase even further (Figure 47a). For varying driving moment, the velocity increases initially and reaches a peak value of $32.5\,ms^{-1}$ then gradually decreases (Figure 47b). The sliding mass eventually becomes stable at about 45 sec at which stage $\tan\varphi_m$ is equal to $\tan(\varphi_F - \theta_d)$.

For varying driving moment, the displacement increased rapidly up to 20 sec then started to level off due to deceleration, reaching a total predicted run-out of 900 m at 45 sec (Figure 48b). But for constant varying moment, the displacement increases continuously and reaches 2250 m after 45 sec.

The plots of velocity and displacement within 1sec are found to be identical for constant and varying driving moment (Figure 47 and Figure 48). Therefore, the respective plots of friction angle against time coincide and are given in Figure 45. The mobilized friction angle starts at 22.3^o then decreases over time due to strain and strain rate friction softening, and reaches a residual value of 4.6^o within 1sec from triggering.

Although the results allow the effect of varying driving moment to be assessed, these predictions are not realistic. Before the total run out reaches 900m for varying driving moment or 2250m for constant driving moment, the sliding mass will have ceased to behave as rigid block. The total length of the analysed section 5 of Vaiont slide is 1500 m. When the slide reaches a displacement of 900 m (60 % of the total length of the slip arc), the sliding mass should have broken in to pieces (Figure 47b). Also, the actual run out for the Vaiont slide was observed nearly 200m (Hendron and Patton, 1985).

Table 1: Material parameters chosen for dynamic analysis

Soil density	ρ	2.44×10^3	kg/m^3
Unit weight of the soil	γ_s	23.89×10^3	N/m^3
Polar moment of inertia of the slide	I_p	0.511	km^4
Resultant driving force	D	3.94	GN/m
Opening angle of failure circle	α	62	$degrees$
Incipient failure angle	φ_F	22.3	$degrees$
Static residual friction angle	φ_{rs}	10.15	$degrees$
Dynamic residual friction angle	φ_{rd}	4.4	$degrees$
Peak failure angle	φ_p	22.277	$degrees$

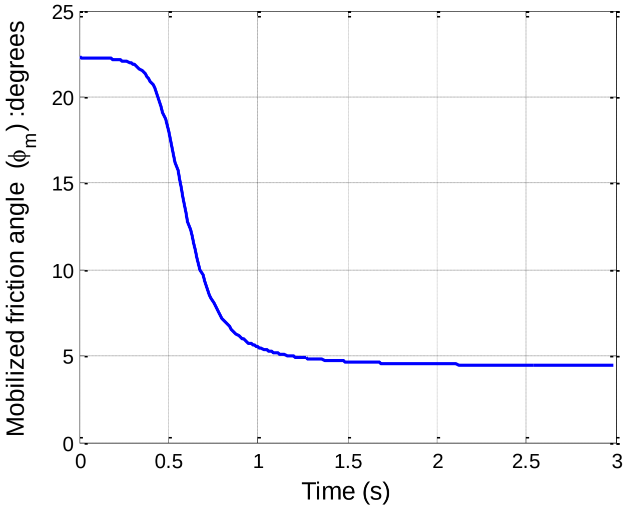

Figure 45: Mobilized friction angle against time for constant and varying driving moments

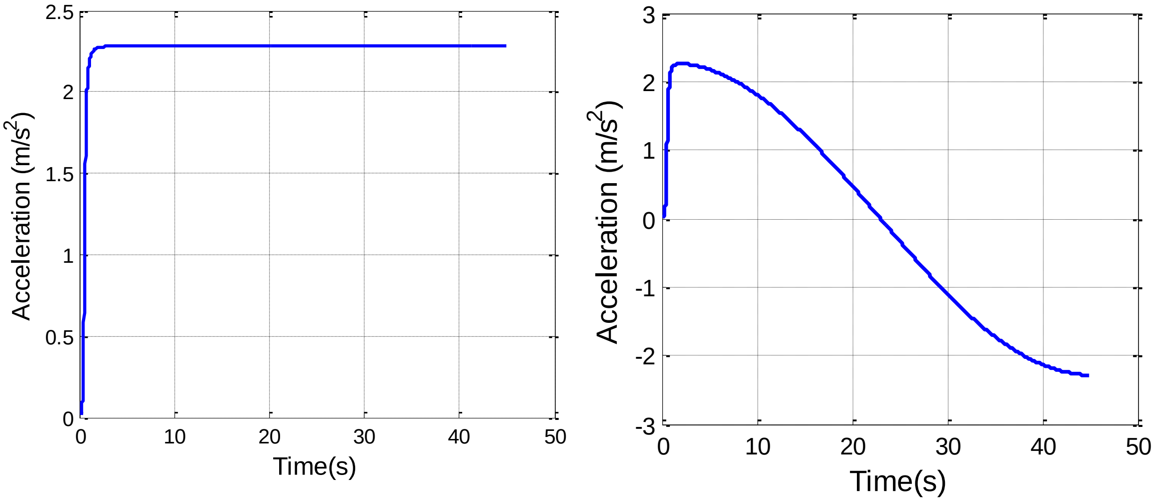

Figure 46: Acceleration of the slide a) with constant b) with varying driving moment

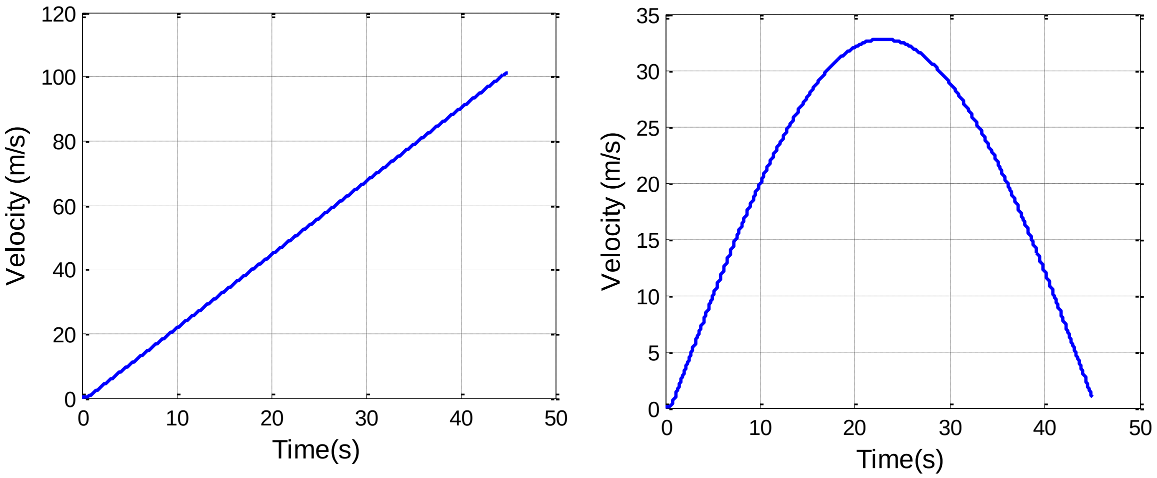

Figure 47: Velocity plot of the slide a) with constant b) with varying driving moment

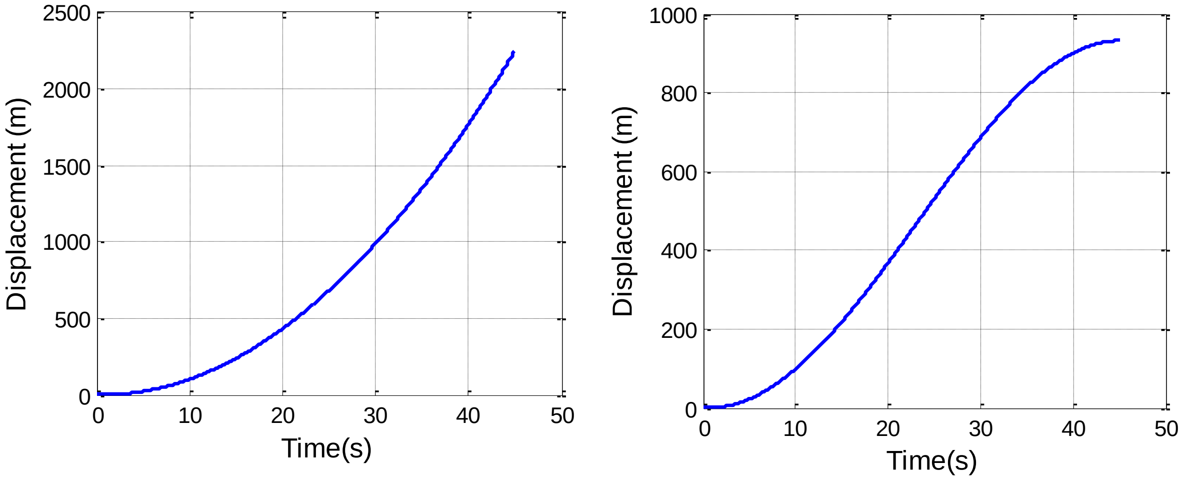

Figure 48: Displacement plot of sliding mass a) with constant b) varying driving moment

3.2 Heat equation

The heat equation provides the temperature variation and evolution inside the shear band with time and consists of a heat diffusion equation with a dissipation term. It is written as; (Cecinato, 2009).

$$\frac{\partial\theta}{\partial t} = D_i \frac{\partial^2\theta}{\partial z^2} + F_i \frac{v_d(t)}{Z_b} \qquad 3.16$$

where

$$D_i = \frac{k_m}{1 - \frac{(M\sigma_c')^2 F_1}{2C_f}} \qquad 3.17$$

$$F_i = \frac{(Mp_c')^2 F_2}{2C_f - (Mp_c')^2 F_1} \qquad 3.18$$

$$F_1 = f_\theta - \frac{2K\beta_s f_p}{\widetilde{H}} \qquad 3.19$$

$$\widetilde{H} = Kf_p^2 + 3Gf_q^2 - f_{\varepsilon_v^p} \qquad 3.20$$

$$F_2 = \frac{G}{\sqrt{3}} \frac{f_q}{\widetilde{H}} \qquad 3.21$$

Equation 3.16 is derived using the thermo-plastic constitutive model developed by Cecinato (2009) (Section 2.3.4). Factor D_i is a nonlinear diffusivity term that depends on temperature and pore pressure. F_i, F_1, F_2 are coefficients that depend on the temperature and pore pressure. The second term of the non-linear heat diffusion equation (3.16) describes the dissipation of heat inside the shear band. Other parameters are given as follows;

$v_d(t)$ – Velocity at the interface between the shearing zone and the landslide mass.

M – Critical state parameter

C_f – Thermal constant of soil

p_c' – Preconsolidation pressure

f_θ , f_q f_p and $f_{\varepsilon_v^p}$ – Derivative of yield locus with respect to temperature, q and p and volumetric plastic strain

K, G – Bulk and shear modulus of soils

k_m – Thermal diffusivity of soils

β_s – Plastic contraction coefficient

3.2.1 Critical State parameter (*M*)

In critical state soil mechanics the friction angle at critical state is always constant. However, Vardoulakis (2002a) proposed a relationship to incorporate the reduction as well as strain and strain rate dependence of friction angle from its critical state to a residual value (Section 2.2.5).

The critical state parameter M for plane strain is written in terms of the friction coefficient $\hat{\mu}$ as;

$$\widehat{M} = \sqrt{3} \frac{\hat{\mu}}{\sqrt{1 - \hat{\mu}^2}} \qquad 3.22$$

Laloui’s thermal friction softening law (2.29) can also be modified to include the effects of displacement and velocity as;

$$M(\dot{\gamma}, \ddot{\gamma}, \theta) = \widehat{M}(\dot{\gamma}, \ddot{\gamma}) - \tilde{g}(\theta - \theta_{ref}) \qquad 3.23$$

where θ_{ref} is the reference temperature, and $\tilde{g}$ is the rate of decrease of the critical state parameter M with temperature. This simple linear law allows the possibility that the value of M may become unrealistically small or even negative. Therefore, the value of M was not allowed to become lower than M_{rd}, which corresponds to the dynamic friction coefficient μ_{rd}.

3.3 Pore pressure equation

The pore pressure equation gives the variation and the evolution of excess pore water pressure inside the shear zone and its surroundings with time and it is given by

$$\frac{\partial u}{\partial t} = \frac{\partial}{\partial z}\left(c_v \frac{\partial u}{\partial z}\right) + \lambda_m \frac{\partial \theta}{\partial t} \tag{3.24}$$

where c_v is the consolidation coefficient and $\lambda_m$is the pressurization coefficient. Different authors have proposed different expressions for the consolidation and pressurization coefficients (Sections 2.2.5 and 2.3.7). In the following subsection the formulations proposed by different authors for pressurization coefficients are discussed in detail.

3.3.1 Consolidation coefficient

The consolidation coefficient of soil is a function of soil permeability and compressibility, and it can be written as;

$$c_v = \frac{k_w}{g \rho_w c} \tag{3.25}$$

where c is the soil compressibility, g is the acceleration of gravity, ρ_w is density of the pore-fluid and k_w is the Darcy permeability coefficient. k_w is an increasing function of porosity and pore-fluid density and decreasing function of dynamic viscosity. Vardoulakis (2002a) proposed that pore-fluid density and dynamic viscosity are functions of temperature. In particular, viscosity is a decreasing function of temperature. Therefore, the consolidation coefficient is temperature dependent. Delage et al. (2000) suggested that the consolidation coefficient can be written as a function of temperature based on experimental results (Figure 49) as;

$$c_v = c_{v0} \exp\left(\frac{\theta}{\theta_c}\right) \tag{3.26}$$

where $c_{v0}$is the value of consolidation coefficient at the temperature of 0℃ . θ_c is a reference temperature. Nevertheless, Equation 3.26 shows that the consolidation coefficient is a weakly increasing function with temperature. Therefore, based on experimental evidence Vardoulakis (2002) suggested using a mean value for the consolidation coefficient of Vaiont clay.

$$\bar{c_v} = 7.3 \times 10^{-8} \frac{m^2}{s} \tag{3.27}$$

This mean value is used in throughout the thesis.

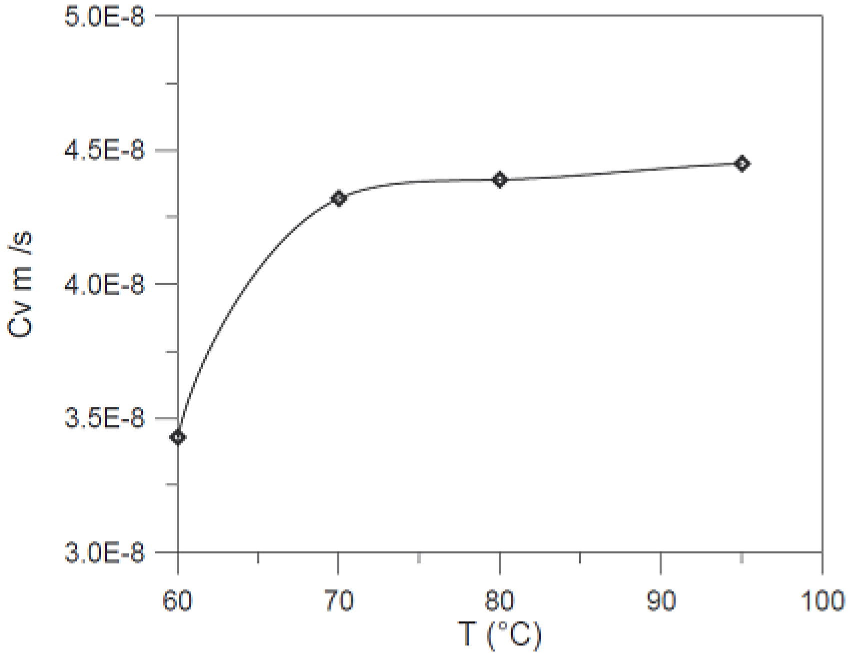

Figure 49: Variations of consolidation coefficient with temperature (after Delage et al. (2000))

3.3.2 Pressurization coefficient (λ_m)

Based on this experimental evidence (Section 2.3.7) Vardoulakis (2002a) proposed that the thermal expansion coefficient can be approximated by a bi-linear law incorporating a critical temperature. Above this critical temperature plastic contraction starts.

$$\alpha_c = \begin{cases} \alpha_c^e & if\ \theta \leq \theta_{crit} \\ \alpha_c^{ep} & if \theta \geq \theta_{crit} \end{cases} \tag{3.28}$$

where α_c^e and α_c^{ep} denotes the elastic and elasto-plastic thermal expansion coefficients of the soil skeleton respectively. The elastic thermal expansion coefficient was considered constant (slope of A-B in Figure 50) and equal to the thermal expansion coefficient of the soil-water mixture i.e. $\alpha_c^e = \alpha_m$, calculated as;

$$\alpha_m = (1-n)\alpha_s + n\alpha_w \tag{3.29}$$

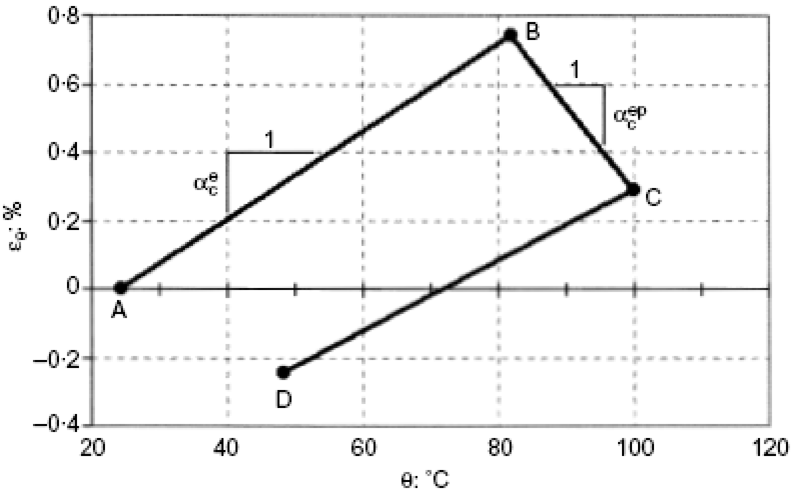

Figure 50: Isotropic thermal volumetric deformation of an over-consolidated Boom clay specimen for OCR=12. Line A-B: Thermo elastic expansion, Line B-C: Thermo plastic collapse and Line C-D: cooling phase representing thermoelastic contraction. (Vardoulakis, 2002a)

In the above, n is the porosity and α_s and α_w are the thermal expansion coefficient of soil and water respectively. Due to the above assumption, the thermal expansion coefficient becomes zero below the critical temperature θ_{crit} $(\alpha = \alpha_m - \alpha_c = 0)$. Therefore the final form of the pressurization coefficient was written as (Vardoulakis, 2002a);

$$\lambda_m = \begin{cases} 0 & if\ \theta \leq \theta_{crit} \\ \dfrac{-\alpha_c^p}{c} & if \theta \geq \theta_{crit} \end{cases} \qquad 3.30$$

where $\alpha_c^p = -(\alpha_c^{ep} - \alpha_c^e)$

Subsequently, Cecinato (2009) determined the pressurization coefficient consistently with the thermo plastic constitutive relation he used. In this model, the thermal contribution of thermal-mechanical strain rate is defined as;

$$\dot{\varepsilon}^{tep} = \frac{\partial \varepsilon}{\partial \theta}\frac{\partial \theta}{\partial t} = \alpha_c^{tp}\frac{\partial \theta}{\partial t} \qquad 3.31$$

From, the new constitutive law used, volumetric plastic strain rate is given as

$$\dot{\varepsilon}_v^p = F_\theta \dot{\theta} + F_m \dot{\varepsilon}_v^m \qquad 3.32$$

$$F_\theta = M^2 p_c' \left\{ \frac{f_{p_c'}(p_c')_\theta - 2K\beta_s f_p}{\chi} \right\} \qquad 3.33$$

$$F_m = M^2 p_c' \left\{ \frac{K f_p}{\chi} \right\} \qquad 3.34$$

In Equation 3.32, $F_\theta \dot{\theta}$ is the thermal contribution of the volumetric plastic strain and $F_m \dot{\varepsilon}_v^m$ is the mechanical contribution of that. Therefore, by comparing Equation 3.31 and 3.32 gives

$$\alpha_c^{tp} = F_\theta \qquad 3.35$$

Substituting the respective definitions on Equation 3.33, α_c^{tp} is given as,

$$\alpha_c^{tp} = \frac{\lambda - \kappa}{\lambda}\left\{\frac{\gamma\kappa}{(1+e)\theta(1-\gamma\, log(\theta/\theta_0))} - 2\beta_s\right\} \qquad 3.36$$

The above formulation eliminates the critical temperature introduced by Vardoulakis (2002), allowing for gradual soil skeleton collapse. Finally, the pressurization coefficient can be written as;

$$\lambda_m = \frac{-\alpha_c^{tp}(\theta)}{c} \qquad 3.37$$

which is now a function of temperature.

3.4 Numerical implementation

The governing equations 3.8 3.16 and 3.24 can be summarised as;

$$\rho I_p \frac{d\omega}{dt} = \omega_0^2 \left(A + \frac{p_d(t)}{p_c}\right) \qquad 3.38$$

$$\frac{\partial\theta}{\partial t} = D_i \frac{\partial^2\theta}{\partial\theta^2} + F_i \frac{v_d(t)}{Z_b} \qquad 3.39$$

$$\frac{\partial u}{\partial t} = \frac{\partial}{\partial z}\left(c_v \frac{\partial u}{\partial z}\right) + \lambda_m \frac{\partial\theta}{\partial t} \qquad 3.40$$

These are non-linear parabolic partial differential equations that need to be solved using appropriate initial and boundary conditions (Section 3.4.3). The finite difference method was chosen to solve the above equations. The techniques used as well as stability conditions of each method are described in detail in the following subsections.

3.4.1 Overview of finite difference scheme

In a finite difference scheme, the solution of a one dimensional time dependent problem is sought on a number of space and time grid points. The grid points are created by dividing the space and time domains into a finite number of discrete increments.

A finite difference scheme can be explicit or implicit. Examples are given below in the context of a simple first order differential equation $y' = f\big(t, y(t)\big)$. A typical explicit scheme is the first-order forward Euler method. The derivative of $y(t)$ is discretised as

$$y' = \frac{y(t+\Delta t) - y(t)}{\Delta t} = f\big(t, y(t)\big) \qquad 3.41$$

which yields, after re arrangement;

$$y(t+\Delta t) = y(t) + f\big(t, y(t)\big)\Delta t \tag{3.42}$$

If t is considered as time, the solution at each time step point can be computed by using the following recursive formula

$$y_{t+\Delta t} = y_t + \Delta t f(t, y_t) \tag{3.43}$$

Although this explicit method is simple to implement, it has some drawbacks. The solution $(y_{t+\Delta t})$ calculated for the end of the interval Δt, is based on the derivative and the solution at the beginning of the interval. Any numerical errors will thus propagate and accumulate, progressively reducing the accuracy of the solution. In order to reduce the accumulated error, the size of the interval Δt should be very small which may not be practical for modelling large domains or long time intervals.

A simple implicit scheme is the first-order backward Euler method. Contrary to Equation 3.41, the derivative $y(t)$ is discretised as

$$y' = \frac{y(t) - y(t-\Delta t)}{\Delta t} = f\big(t, y(t)\big) \tag{3.44}$$

which yields that the solution at each time step should satisfy;

$$y_{t+\Delta t} = y_t + \Delta t f(t+\Delta t, y_{t+\Delta t}) \tag{3.45}$$

In an implicit method each recursive formula contains more than one unknown; therefore a system of discretised equations for the entire domain should be solved simultaneously. This implicit method is unconditionally stable, i.e. errors do not accumulate indefinitely, although it needs more computation effort.

The dynamic equation given in Equation 3.38 is a first order differential equation with respect to time. Backward Euler method is chosen to solve this equation to avoid accumulation of errors and ensure stability.

The heat and pore pressure equations presented here (Equations 3.38 and 3.39) are nonlinear parabolic partial differential equations (PDE) containing second order derivatives in space and first order derivatives in time. Both are discretised as shown in Figure 51, where, i and j represent the discretisation points in the space and time domains respectively. Among several numerical methods available to solve PDE, three well known methods are discussed here; The Forward-time centred space (FTCS) scheme, which is an explicit one and the Backward-time centred space (BTCS) and Crank-Nicholson (CN), schemes, which are both implicit.

The FTCS method employs a forward Euler approximation in time and a centred second order approximation in space. Let us assume a general diffusion equation given by;

$$\frac{\partial A(z,t)}{\partial t} = B\frac{\partial^2 A(z,t)}{\partial z^2} \text{for } 0 \leq z \leq D, 0 \leq t \leq T_f \qquad 3.46$$

With reference to Figure 51, the discretised form to calculate the solution at point Q using the FTCS method can be written as

$$\frac{\left(A_i^{j+1} - A_i^j\right)}{\Delta t} = B\frac{\left(A_{i+1}^j - 2A_i^j + A_{i-1}^j\right)}{\Delta z^2} \qquad 3.47$$

Solving Equation 3.47 is straightforward as it has one unknown A_i^{j+1} i.e. the solution at point Q. Essentially A_i^{j+1}, i.e. the solution at the 'next' time step, can be calculated using the values of A_i^j only, i.e. the solution at the 'current' time step only. However, a von-Newman stability analysis shows that for the FTCS to be stable, the following stability condition must hold (Yang et al., 2005)

$$B\frac{\Delta t}{\Delta z^2} \leq \frac{1}{2} \qquad 3.48$$

where Δz and $\Delta \mathrm{t}$ are the spatial discretisation step and the time step respectively.

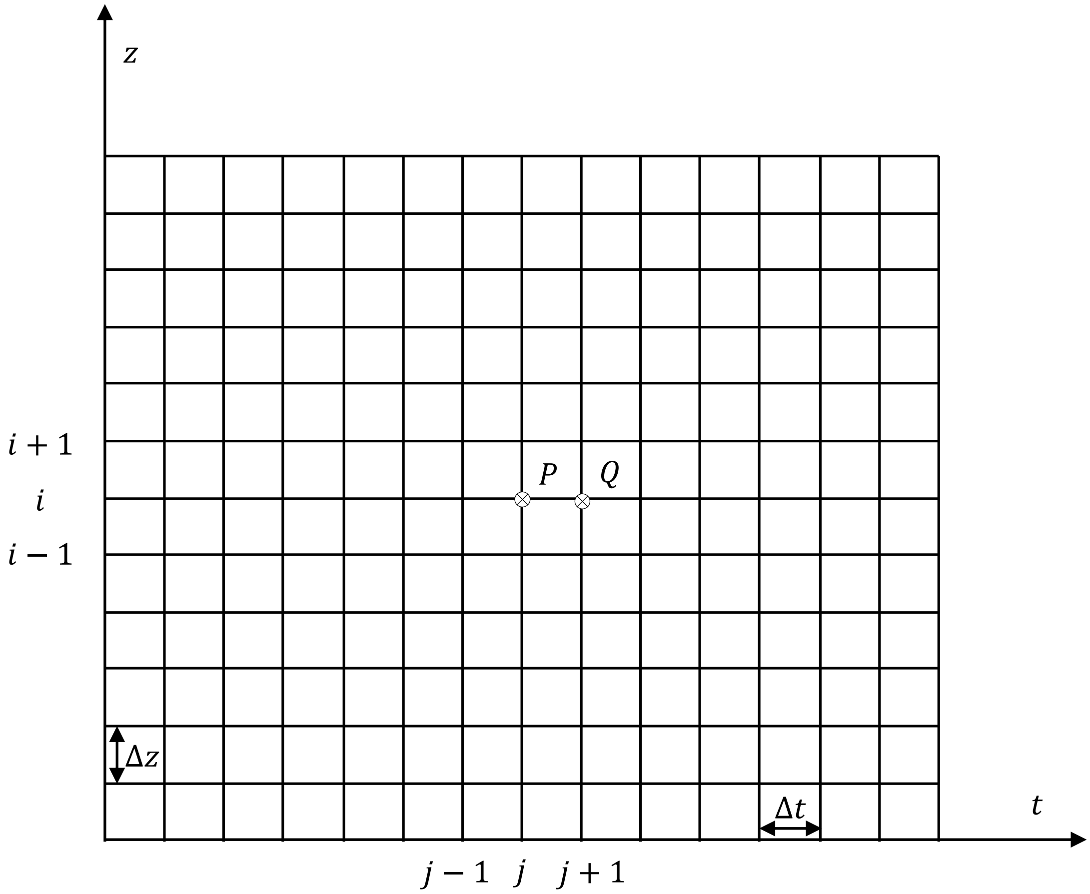

Figure 51: Finite difference grid for a parabolic PDE

The BTCS method, on the other hand, provides the solution employing a backward Euler approximation in time and a centred second order Euler approximation in space. In BTCS the discretised form to compute the solution can be written as

$$\frac{\left(A_i^{j+1} - A_i^j\right)}{\Delta t} = B\,\frac{\left(A_{i+1}^{j+1} - 2A_i^{j+1} + A_{i-1}^{j+1}\right)}{\Delta z^2} \qquad 3.49$$

Solving this equation requires more computational effort as it contains more than one unknown in each equation. Therefore, a system of equations corresponding to all spatial points must be formed and solved at each time step. Compared to FTCS this represents significant additional computational effort. Nevertheless, the BTCS is unconditionally stable and therefore it can be used with relatively large time steps unlike FTCS.

Finally, the Crank-Nicholson method represents an improvement over FTCS. Here, the average of centred Euler approximations, at time points j and $j+1$ is considered. The discretised form can be written as;

$$\frac{\left(A_i^{j+1} - A_i^j\right)}{\Delta t} = \frac{B}{2}\left\{\frac{\left(A_{i+1}^{j+1} - 2A_i^{j+1} + A_{i-1}^{j+1}\right)}{\Delta z^2} + \frac{\left(A_{i+1}^{j} - 2A_i^{j} + A_{i-1}^{j}\right)}{\Delta z^2}\right\} \qquad 3.50$$

Again, the CN method needs more computational effort than FTCS and still needs to satisfy the stability condition of 3.48.

Out of the three described methods the BTCS method was selected because it is unconditionally stable. Therefore, the simulation can be performed with relatively large time steps.

3.4.2 Parameter selection

For the simulation presented in the following, material parameters relevant to section 5 of the Vaiont landslide, which are summarized in Table 2, are used. Some of the other necessary parameters are calculated in the following.

The initial mean effective stress p'_0 can be calculated by using the normal effective stress σ'_n acting on the slip plane. In order calculate p'_0 three main assumptions are made as follows (Vardoulakis, 2002a);

1. Plane strain conditions are assumed
2. Further, odeometric conditions were assumed, so that $\varepsilon_{xx} = \varepsilon_{yy} = 0$ (Figure 52)
3. For simplicity, $\sigma'_{xx} = \sigma'_n$ is assumed (Vardoulakis, 2000)

By using the above assumptions, the initial effective mean pressure p'_0 was found as

$$p'_0 = \frac{2}{3}(1+\nu)\sigma'_n \qquad 3.51$$

The compressibility of the soil c was calculated by Cecinato (2009) as follows;

$$c = \left(\frac{e}{1+e}\right)c_w + \frac{2\kappa(1+\nu)}{3p'_0(1+e)} \qquad 3.52$$

where; e – void ratio at CSL

c_w – Compressibility of water

ν –Poisson ratio of the soils

p'_0 – Initial mean effective stress

κ – Slope of URL line of odeometric test.

Table 2: Parameters chosen to back analyse the Vaiont slide section 5 (Cecinato, 2009)

Soil density	ρ	2.44×10^3	Kg/m^3
Unit weight of the soil	γ_s	23.89×10^3	N/m^3
Unit weight of water	γ_w	9.81×10^3	N/m^3
Thermal constant	C_f	2.84	*MPa/°C*
Radius of the failure circle	R	1493	*m*
Radius of the "friction circle"	R_D	594.8	*m*
Polar moment of inertia of slide	I_p	0.511	km^4
Resultant driving force	D	3.94	*GN/m*
Slide geometry parameter	ω_o	8.1×10^{-2}	s^{-1}
Shearband thickness	Z_b	1.4×10^{-3}	*m*
Reference temperature	θ_{ref}	12	*°C*
Soil thermal diffusivity coefficient	K_m	1.45×10^{-7}	m^2/s
Slope of URL of clay	κ	1.85×10^{-2}	-----
Slope of NCL of clay	λ	0.16	-----
Specific volume intercept of clay	Γ	1.42	-----
Initial (mean) normal effective stress	σ'_n	2.38	*MPa*
Soil (drained) Poisson's ratio	v	0.2	-----
Compressibility of water	c_w	4.93×10^{-4}	MPa^{-1}
Incipient failure (peak) friction coefficient	μ_p	0.410	-----
Static residual friction coefficient	μ_{rs}	0.179	-----
Dynamic residual friction coefficient	μ_{rd}	0.077	-----

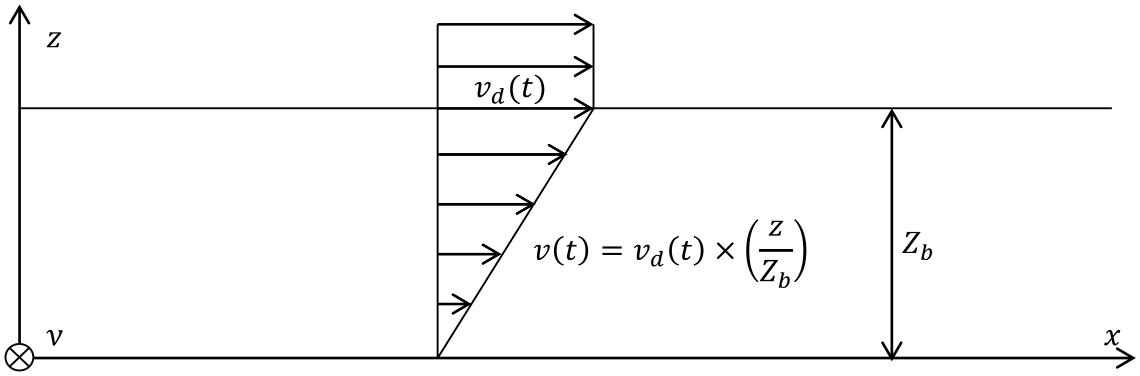

Figure 52: Scheme of the shearband with axis reference system

In the above, it was assumed that the soil in the shear band has reached a critical state. The void ratio at critical state e is calculated by using the parameter Γ, which is the soil's specific volume intercept on $v - \ln p'$ plane at unit mean effective stress. Therefore the void ratio is given by

$$e = \Gamma - \lambda\, ln(p_0') \qquad 3.53$$

where, p_o' initial effective mean pressure.

The thermo-elastic expansion coefficient β_s depends on the temperature and the mean effective stress. Experimental data show that the temperature dependence on the thermo elastic expansion coefficient is weak (Laloui and Cekerevac, 2003, Sultan et al., 2002). Therefore a constant value of $7.41 \times 10^{-5}\,°C$ is used for β_s in this analysis, in line with Cecinato (2009), Cui et al. (2000), Delage et al. (2000), Sultan et al. (2002) and Vardoulakis (2002a).

The critical state parameter M varies with temperature as shown in Equation 2.29. The thermal friction sensitivity parameter $\tilde{g}$, which gives the rate of friction softening due to temperature, is calculated using available experimental data (Laloui, 2001). By examining the behaviour of different soils shown in Figure 18, it can be concluded that the value of $\tilde{g}$ falls in the range of $10^{-3} \leq \tilde{g} \leq 10^{-2}$.

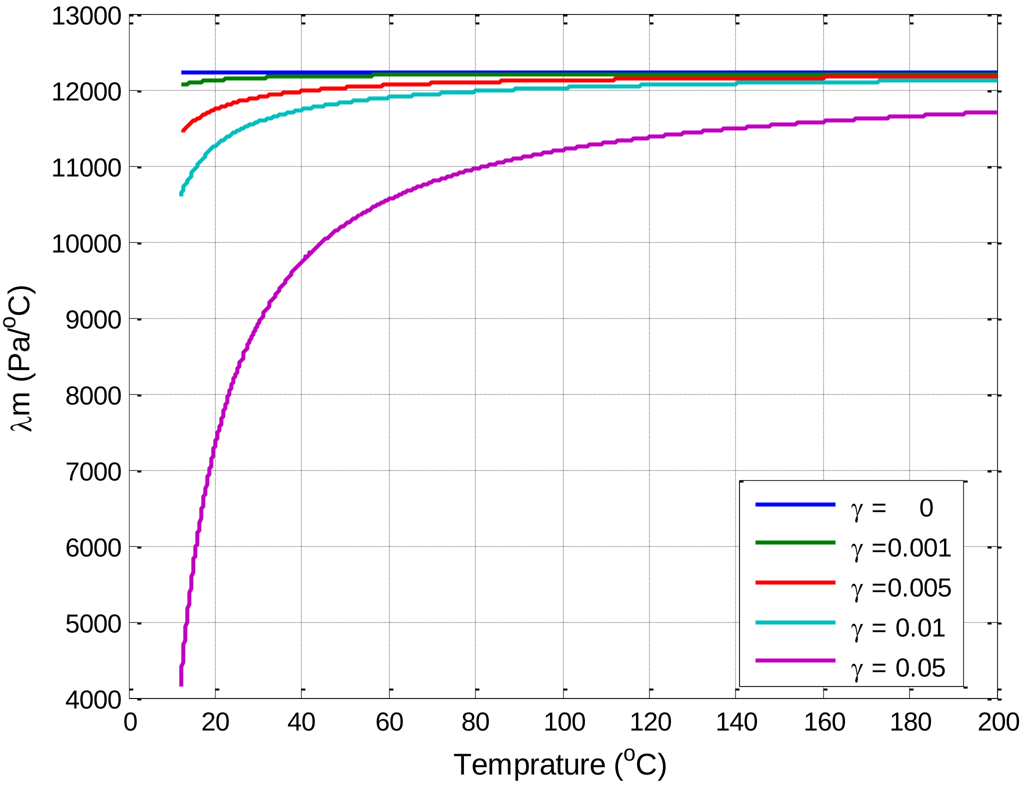

Figure 53: Pressurization coefficient λ_m with temperature for different values of γ

The thermal softening parameter γ plays a critical role in this model as it controls the rate of change of preconsolidation pressure with temperature. This parameter also affects the value of the pressurization coefficient λ_m . Therefore, a systematic analysis was carried out to obtain a value of γ which is consistent with plausible values of λ_m. From Equation 3.37 it can be seen that λ_m is a function of temperature. Therefore for different values of γ, λ_m was calculated for values of temperature ranging between $12°C$ and $300°C$ (Figure 53). For lower temperature values, λ_m is more sensitive to the value of γ than for higher temperature. From this study, an average value of $\bar{\lambda}_m = 0.0122\ MPa/℃$ was established which is in line with the value of $0.012\ MPa/℃$, proposed by Vardoulakis (2002a)

3.4.3 Initial and boundary conditions

The final governing equations given in Equations 3.38, 3.39 and 3.40 are solved using the BTCS scheme. The heat and pore pressure equations are parabolic partial differential equation describing changes of temperature and pore pressure across the shear band over time. To solve them, it is necessary to define appropriate initial and boundary conditions. As boundary conditions, ambient temperature and zero excess pore pressure are assumed far away from the shear band boundaries. To implement that, the domain was assumed 11 times bigger than the shear band (5 times on each side). Moreover, ambient temperature and zero excess pore pressure were taken as initial conditions in line with Vardoulakis (2002a). In summary, initial and boundary conditions can be written as;

$$\begin{aligned} u(z,0) &= 0; \qquad \theta(z,0) = \theta_{ref}; \\ u(\pm\infty,t) &= 0; \qquad \theta(\pm\infty,t) = \theta_{ref} \end{aligned} \qquad 3.54$$

The velocity profile through the spatial domain can be written as (Figure 52);

$$\begin{cases} v = 0 & z \epsilon [-\infty, 0] \\ v = v_d(t) \times \left(\dfrac{z}{Z_b}\right) & z \epsilon [0, Z_b] \\ v = v_d(t) & z \epsilon [Z_b, \infty] \end{cases} \qquad 3.55$$

It was assumed that the slide is at rest at $t = 0$, so that the initial condition for the dynamic equation is

$$v(z,0) = 0; \qquad 3.56$$

The equations were integrated for a time window of 10 seconds after initiation of movement which corresponds to a landslide movement less than 110 m. This upper limit of run out was imposed so that movement of the sliding mass as rigid body without significant disintegration may be assumed throughout. The numerical results obtained are presented hereafter.

3.4.4 Numerical results for the Vaiont slide

First, the results assuming constant driving moment are presented for comparison. Such analyses were also carried out by Cecinato (2009) using an FTCS numerical integration scheme. Subsequently, the results for varying driving moment are presented as described in section 3.1.

The solution of the system of finite difference equations is not straight forward; it is a non-linear system and hence an iterative procedure with an appropriate initial guess needs to be employed. MATLAB numerical software was used to solve the non-linear equations using an in-built algorithm fsolve. The initial guess used is the solution of the previous time step, or the initial conditions for the first time step.

It is worth noting that the model is no longer valid as soon as the maximum temperature within the shearband θ_{max} reaches the vaporization limit θ_{vap} for the current pore water pressure. The vaporization threshold can be calculated as follows (Vardoulakis, 2000).

$$p = 62\left(\theta_{vap} + 273.15\right)_k \exp\left(-\frac{4650}{\theta_{vap} + 273.15}\right) \qquad 3.57$$

where, p is the maximum pore water that can be reached, which is equal to the initial effective normal pressure (2.38 Mpa). By solving the above equation, θ_{vap} is found as 210 ^{o}C. In all of our simulation, the condition $\theta_{max} < \theta_{vap}$ was always found to hold.

Analyses were run with different combinations of friction law as described below.

1. Analysis with displacement and velocity softening only (hereafter referred to as “dynamic friction softening only”) i.e. no thermal friction softening was taken in to account.
2. Analysis with displacement, velocity and thermal frictions softening (will be referred as “full friction softening”.)
3. Analysis with thermal friction softening only, i.e. no velocity or displacement softening.

The results are presented in the following subsections.

3.4.4.1 Results for dynamic softening only - constant driving moment

As a first step, It is assumed the displacement and velocity softening only by neglecting thermal friction softening. This analysis allows us to compare the results with no pressurization effect as presented in Section 3.1.1. Therefore, in this context the thermal friction sensitivity parameter $\tilde{g}$ is set to zero. 1% reduction in peak friction angle was assumed in order to trigger the landslide event.

Temperature and excess pore pressure isochrones are shown in Figure 54 and Figure 55 respectively. Temperature starts to kick in from 1 sec after landslide initiation and reaches 141.4℃ at the end of 10 seconds. During this period, excess pore pressure of 1.82 MPa is generated due to pressurization. This pore pressure is below the initial normal effective stress of 2.38 MPa but is significant in proportion.

Velocity and displacement plots are shown in Figure 56 and Figure 57. In this particular case, the activation point of the catastrophic phase, i.e. the point at which the acceleration of the sliding mass starts to increase rapidly is observed as 0.5 sec. The mass reaches a maximum velocity of 22.9 m/sec in 10 sec. This final velocity is about 5% greater than the velocity obtained without the pressurization effect (Section 3.1.1). Accordingly, the displacement reaches 106 m, after 10 sec.

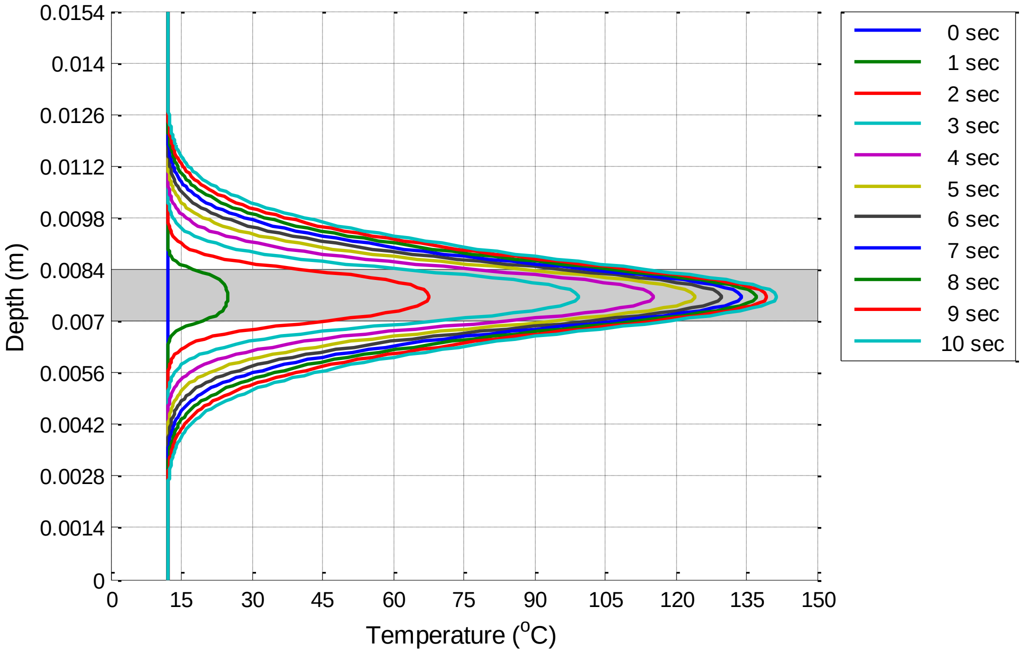

Figure 54: Temperature isochrones within the shearband and its surroundings shear band area is shaded (case of constant driving moment, dynamic softening only)

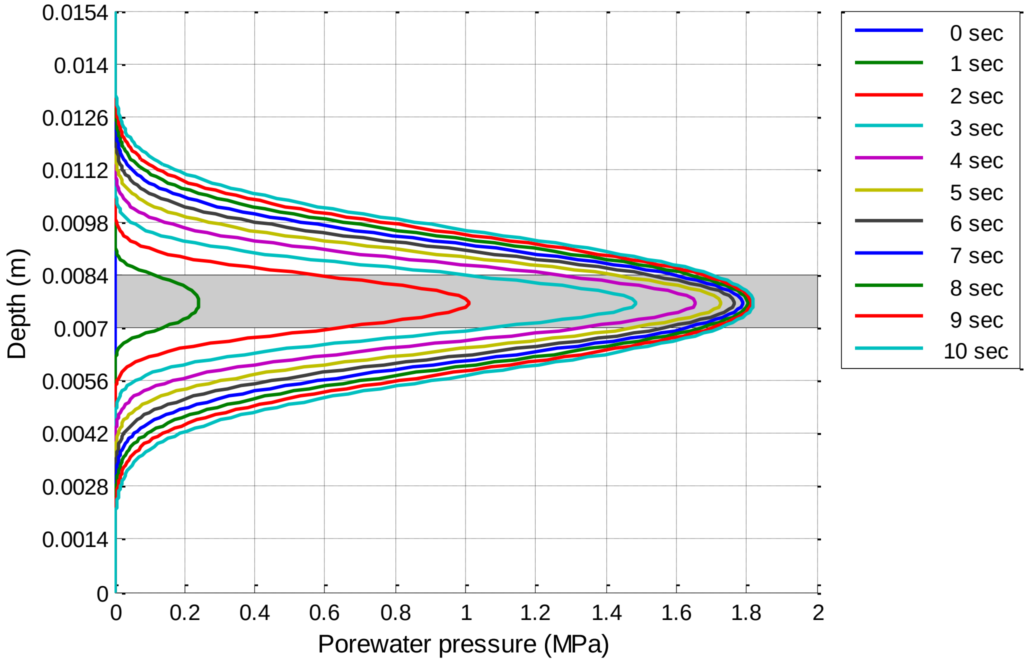

Figure 55: Pore water pressure isochrones within the shearband and its surroundings shear band area is shaded (case of constant driving moment, dynamic softening only)

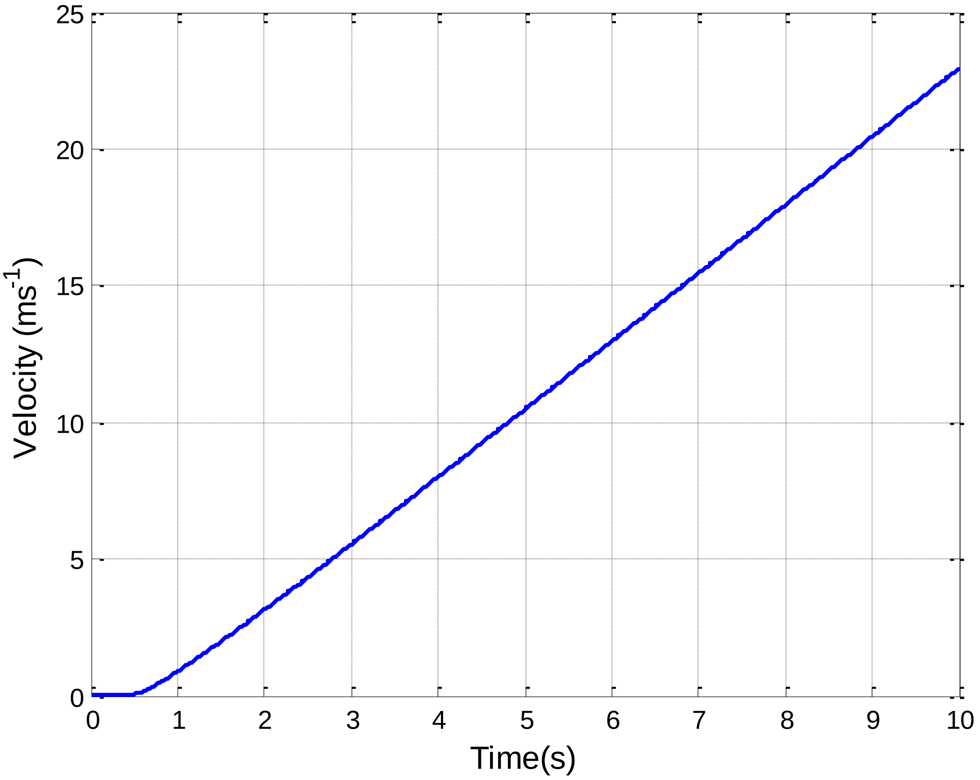

Figure 56: Velocity plot for the case of constant driving moment and dynamic softening only

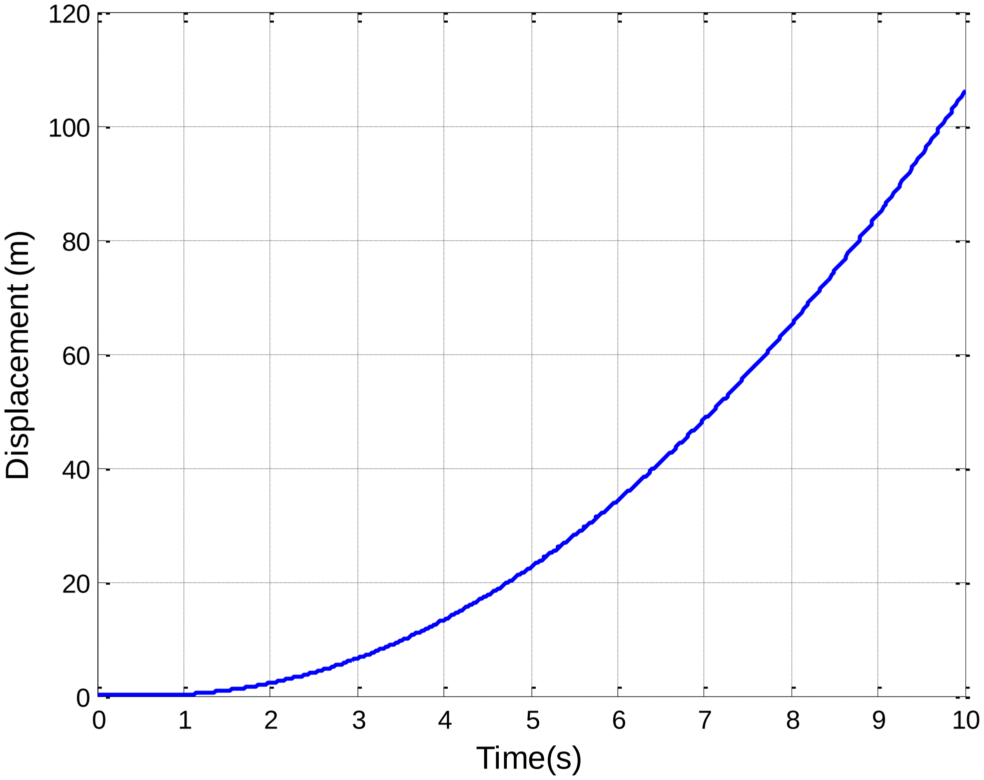

Figure 57: Displacement plot for the case of constant driving moment and dynamic softening only

3.4.4.2 Results for dynamic softening – variable driving moment

Here, again the results for dynamic friction softening are presented but with the modified dynamic equation that assumes variable driving moment. Temperature and pore pressure isochrones across the shearband and its surroundings are given in Figure 58 & Figure 59. In this case, the temperature reaches a value of 141.2℃ which is practically equal to the temperature obtained with constant driving moment. Moreover, the generated pore pressure is also practically the same (1.81MPa), as well as the “activation point” (0.5 sec).

The velocity and displacement plots are given in Figure 60 and Figure 61 respectively. The velocity reaches a maximum value of 21.4 m/sec while displacement reaches to 102.65 m. Here, a more noticeable although still small difference in the velocity and the displacement is seen and it will be discussed later in this chapter in more detail.

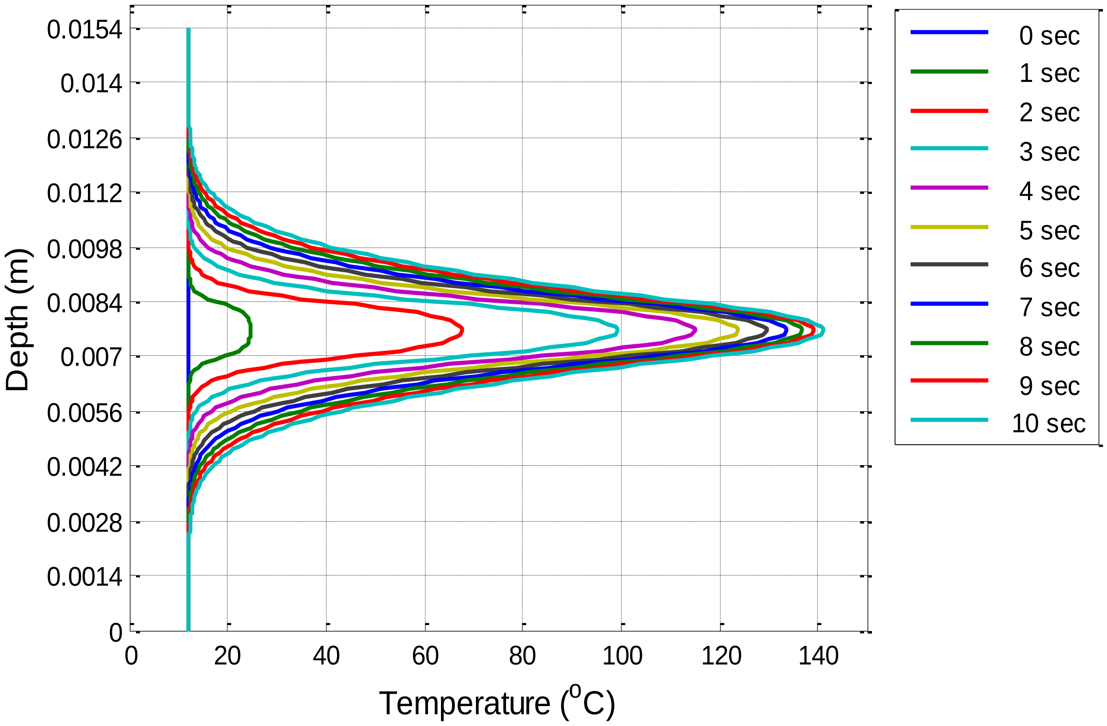

Figure 58: Temperature isochrones within the shearband and its surroundings shear band area is given between 0.007m and 0.0084m (case of variable driving moment, dynamic softening only)

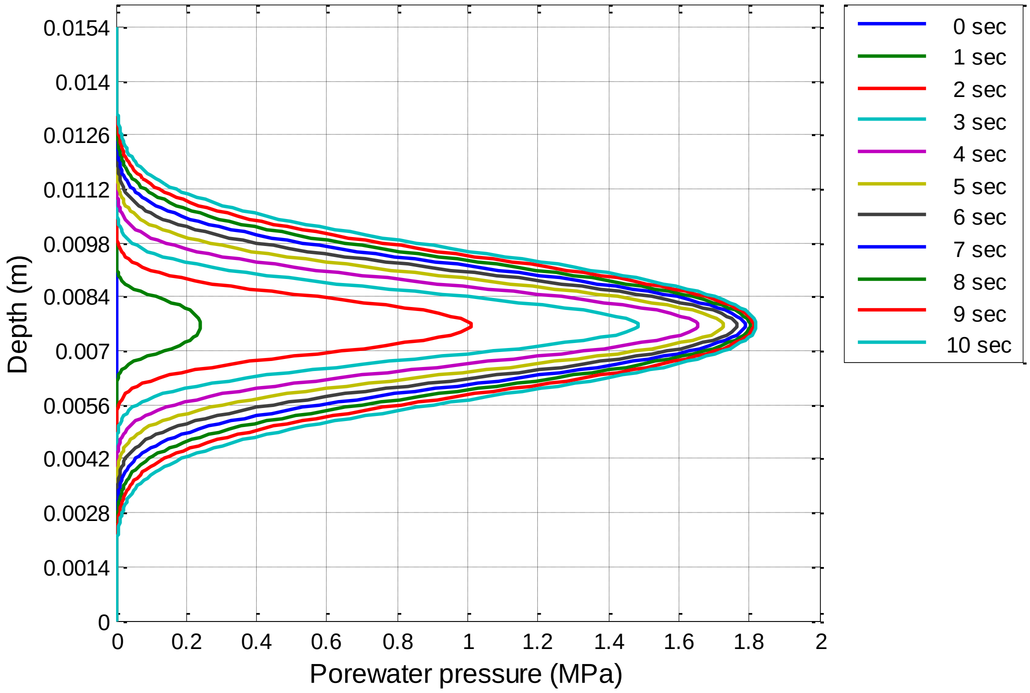

Figure 59: Pore water pressure isochrones within the shearband and its surroundings shear band area is given between 0.007m and 0.0084m (case of variable driving moment, dynamic softening only)

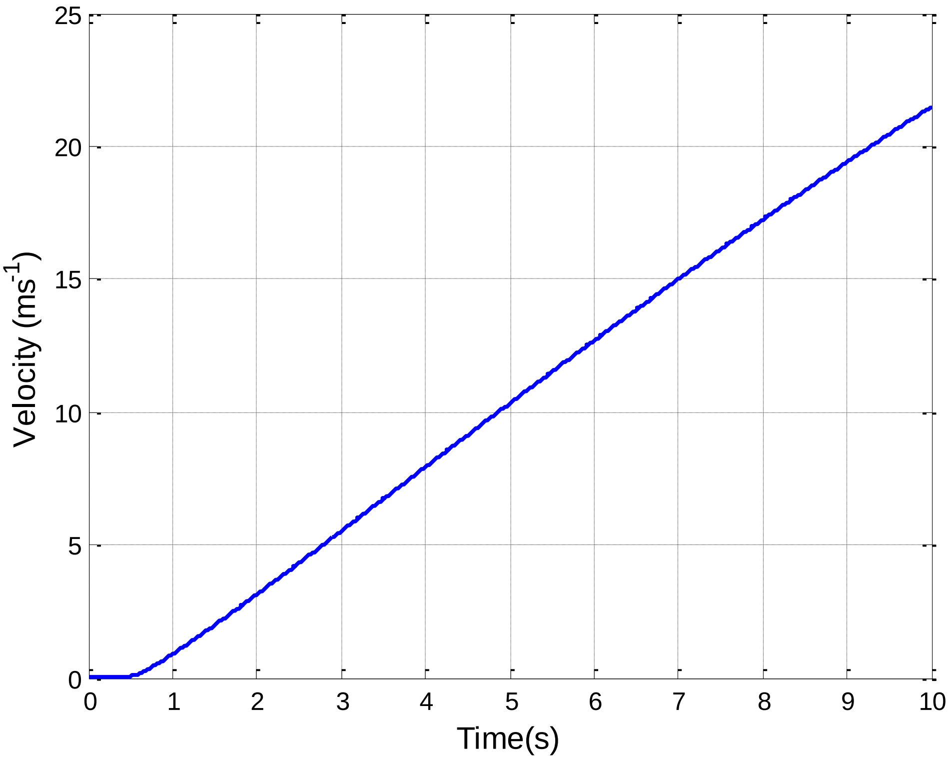

Figure 60: Velocity plot for the case of variable driving moment and dynamic softening only

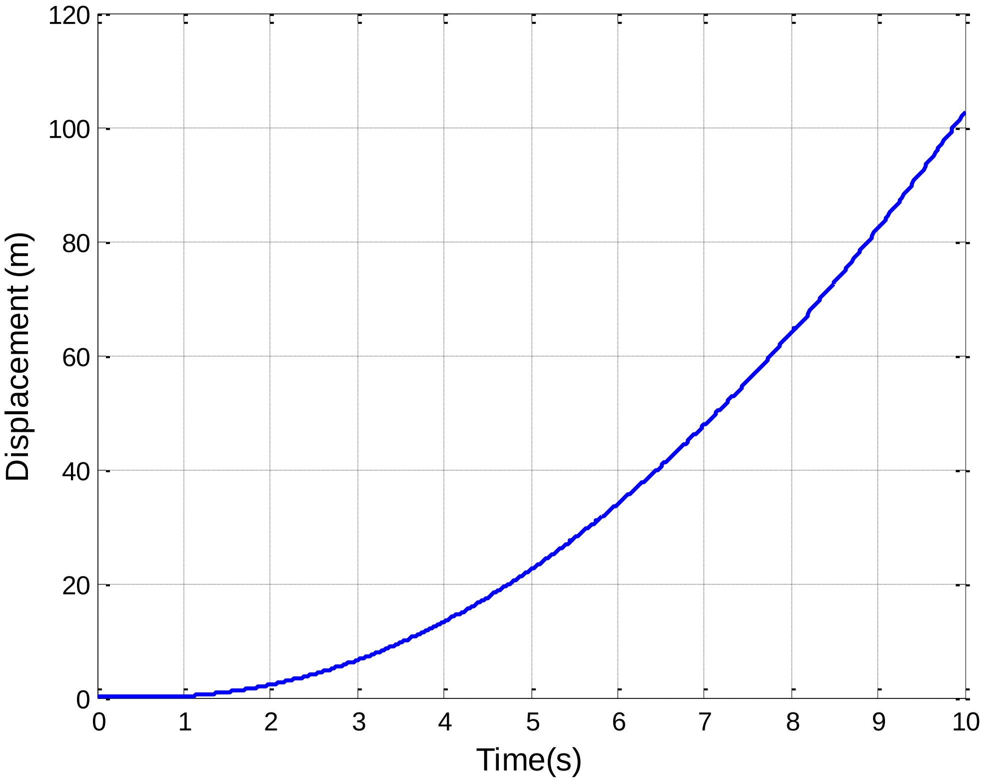

Figure 61: Displacement plot for the case of variable driving moment and dynamic softening only

3.4.4.3 Results for full friction softening – constant driving moment

In this subsection, constant driving moment analysis is presented, the most general case, where all possible types of friction softening are taken in to account i.e. velocity, displacement and thermal friction softening as given in Equation 3.23.

In Figure 62 and Figure 63, temperature and excess pore pressure isochrones inside the shear band and its surroundings are presented. At the middle of the shear band, temperature rises to a maximum value of 141.38°C after 10 sec. Excess pore pressure reaches to 1.82 MPa due to pressurization. Moreover, the "activation point" is at 0.5 sec as in the case of dynamic softening only (Section 3.4.4.1).

The velocity and the displacement plots are given in Figure 64 & Figure 65 respectively. Velocity reaches 23.1m/sec at 10 sec and the landslide moved to a total distance of 107.46m during that time. These values are not far off those corresponding to the case of dynamic friction softening only, and this will be discussed in more detail later in this chapter.

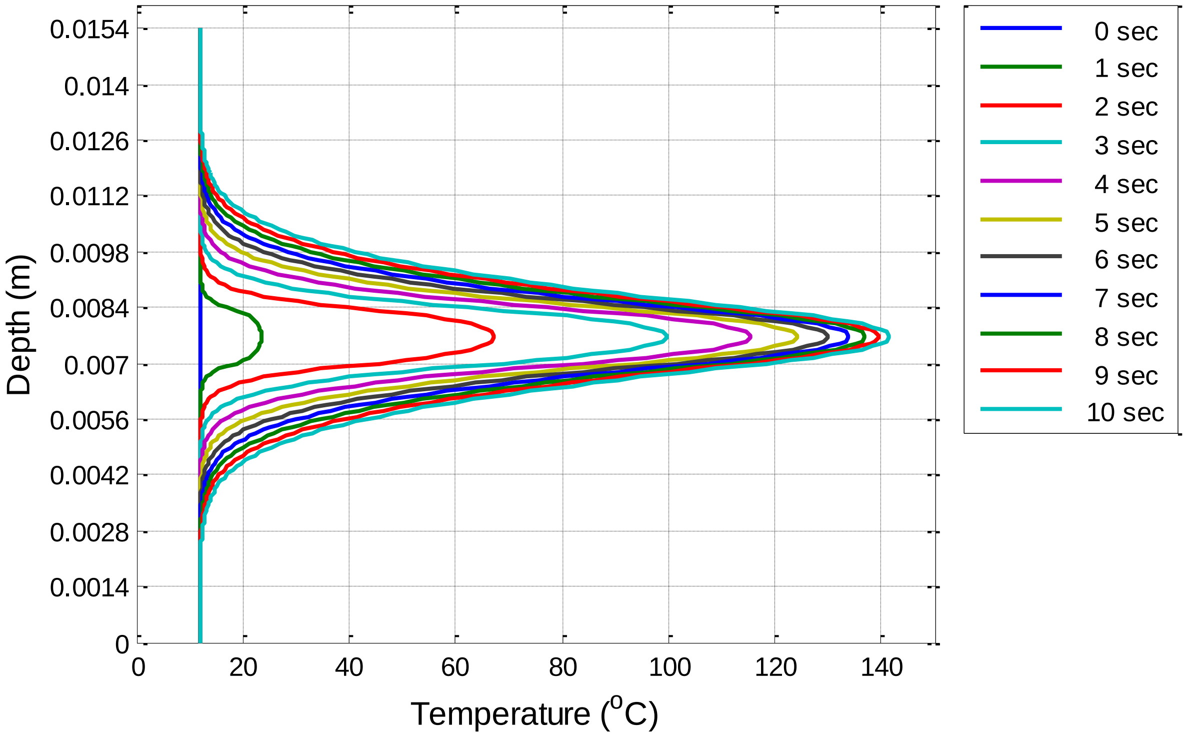

Figure 62: Temperature isochrones within the shearband and its surroundings shear band area is given between 0.007m and 0.0084m (case of constant driving moment, full softening)

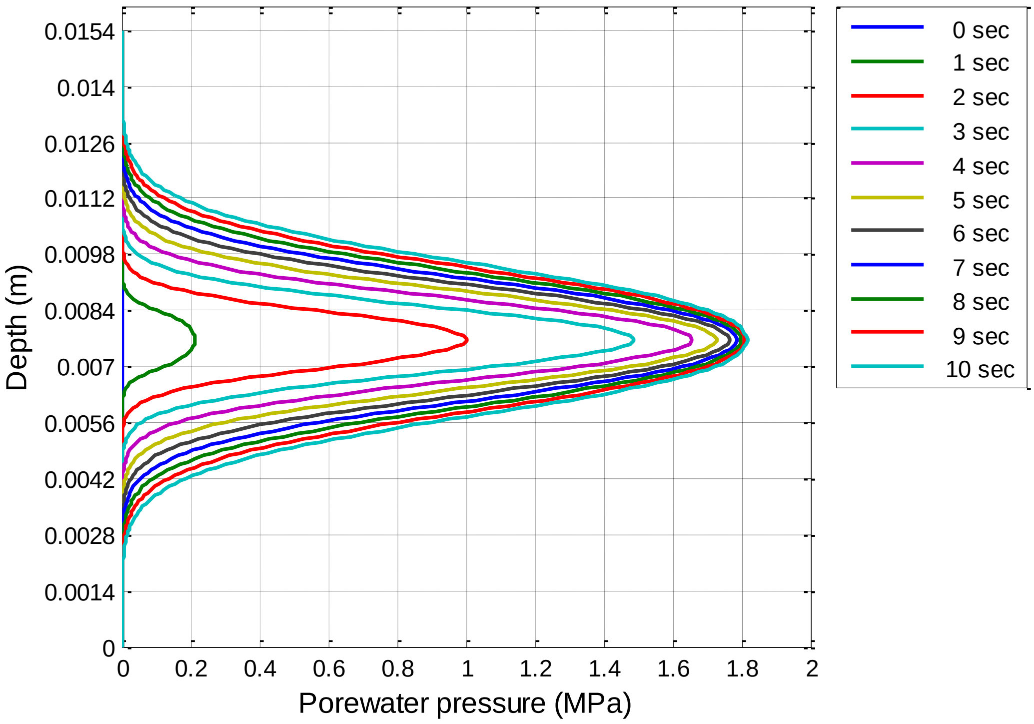

Figure 63: Pore water pressure isochrones within the shearband and its surroundings shear band area is given between 0.007m and 0.0084m (case of constant driving moment and full softening)

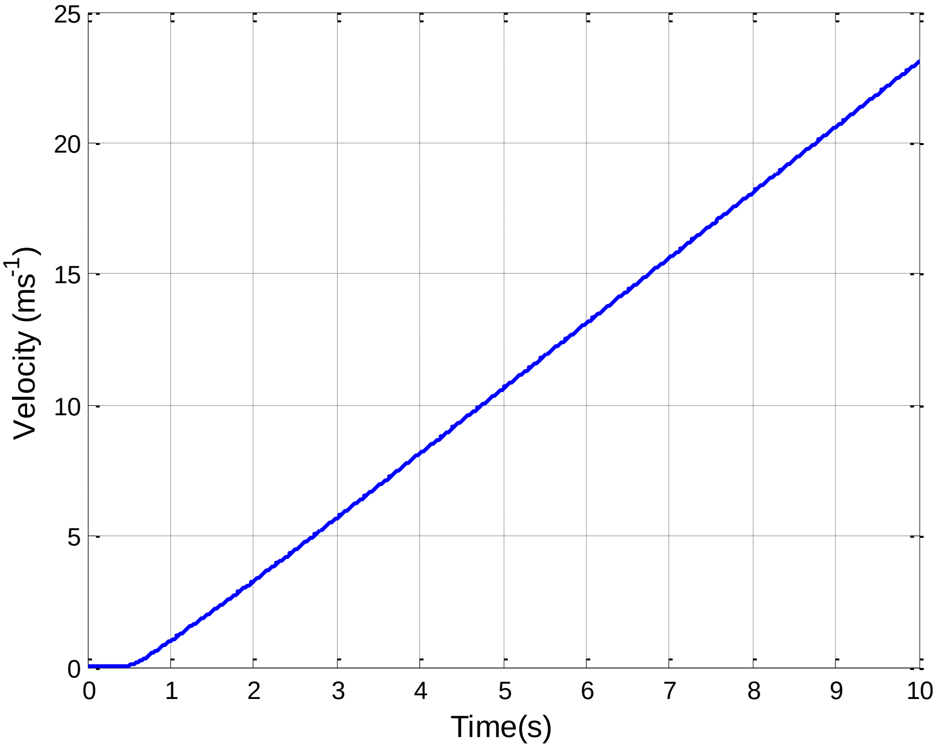

Figure 64: Velocity plot for the case of constant driving moment and full softening

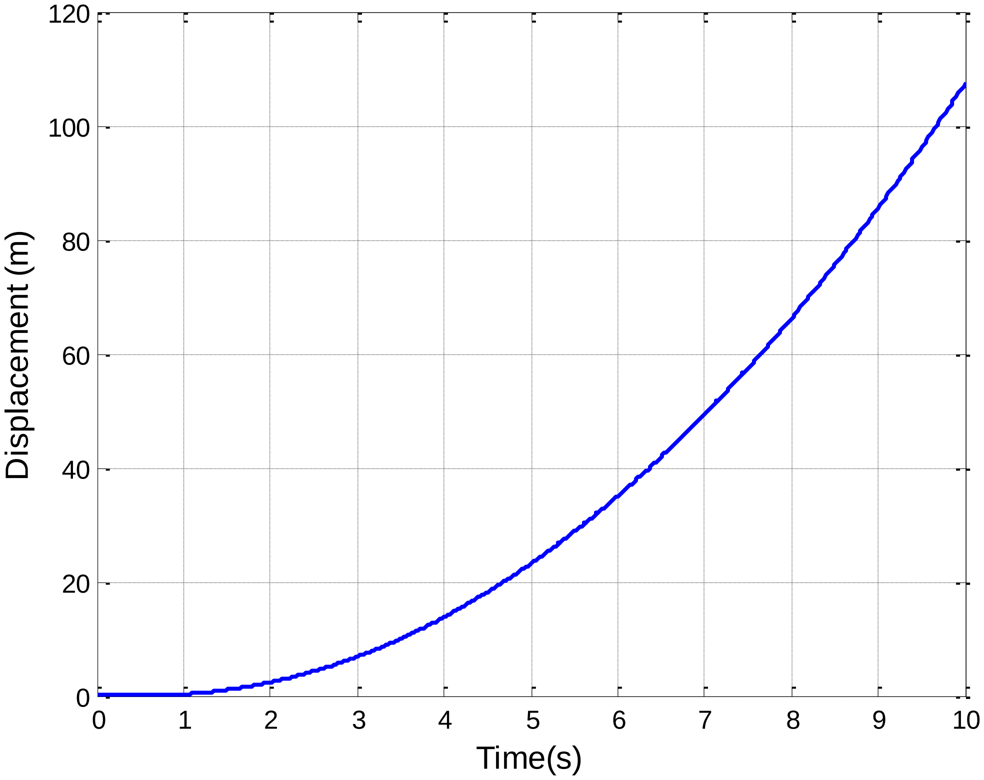

Figure 65: Displacement plot for the case of constant driving moment and full softening

3.4.4.4 Results for full friction softening – variable driving moment

In this subsection, the results for full friction softening are again presented but use the modified dynamic equation. Temperature and pore pressure isochrones across the shear band and its surroundings are given in Figure 66 and Figure 67. In this case, temperature and pore pressure rise to the values of 141.22^{o}C and 1.82 MPa respectively after 10sec, which are practically equal to the results obtained with the constant driving moment dynamic equation.

The velocity and displacement plots are given Figure 68 and Figure 69 respectively. The velocity reaches a value of 21.60 m/sec which is about 4.5 % less than the velocity reached in the case of constant driving moment and displacement reaches a value of 103.93 m at 10 sec. Here again a more noticeable although still small difference in the velocity and displacement is seen. Again, the activation point is found here as 0.5sec.

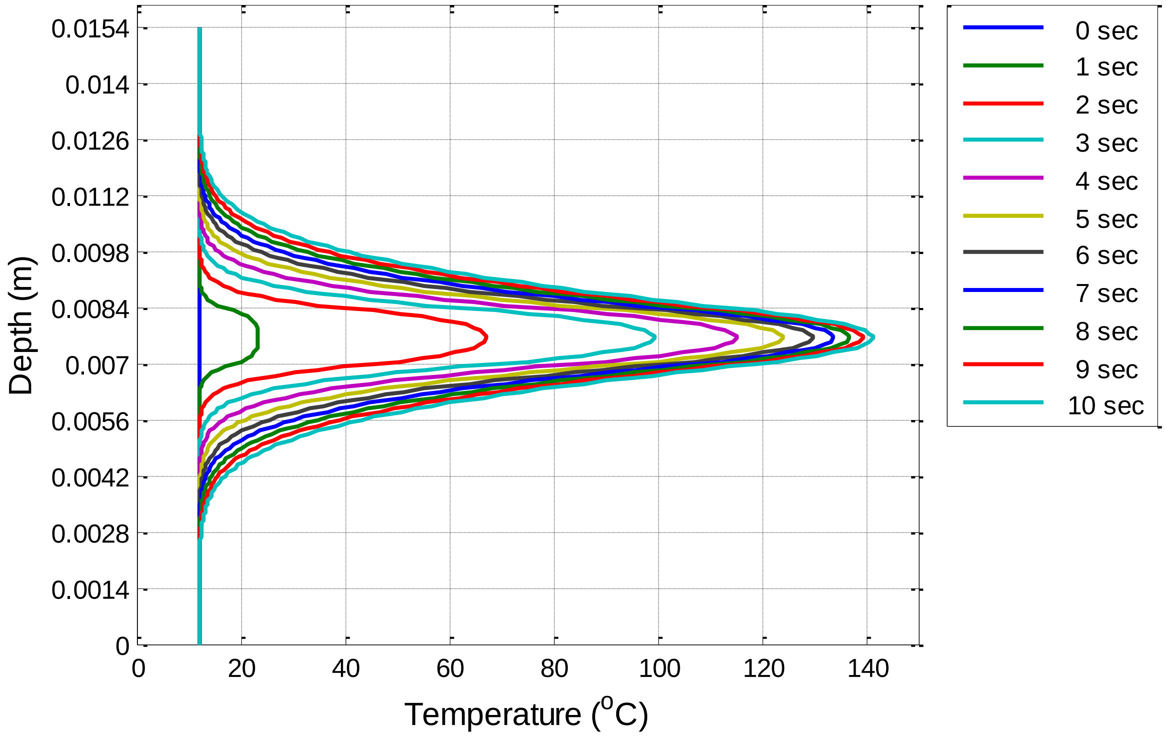

Figure 66: Temperature isochrones within the shearband and its surroundings shear band area is given between 0.007m and 0.0084m (case of variable driving moment and full softening)

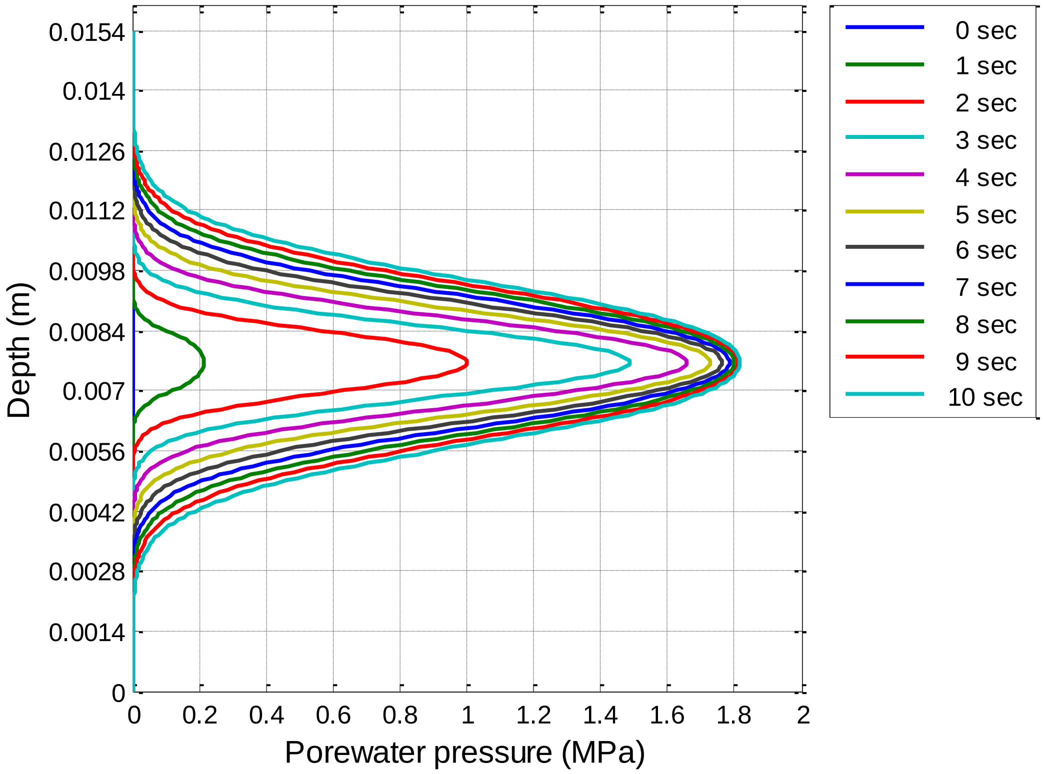

Figure 67: Temperature isochrones within the shearband and its surroundings shear band area is given between 0.007m and 0.0084m (case of variable driving moment and full softening)

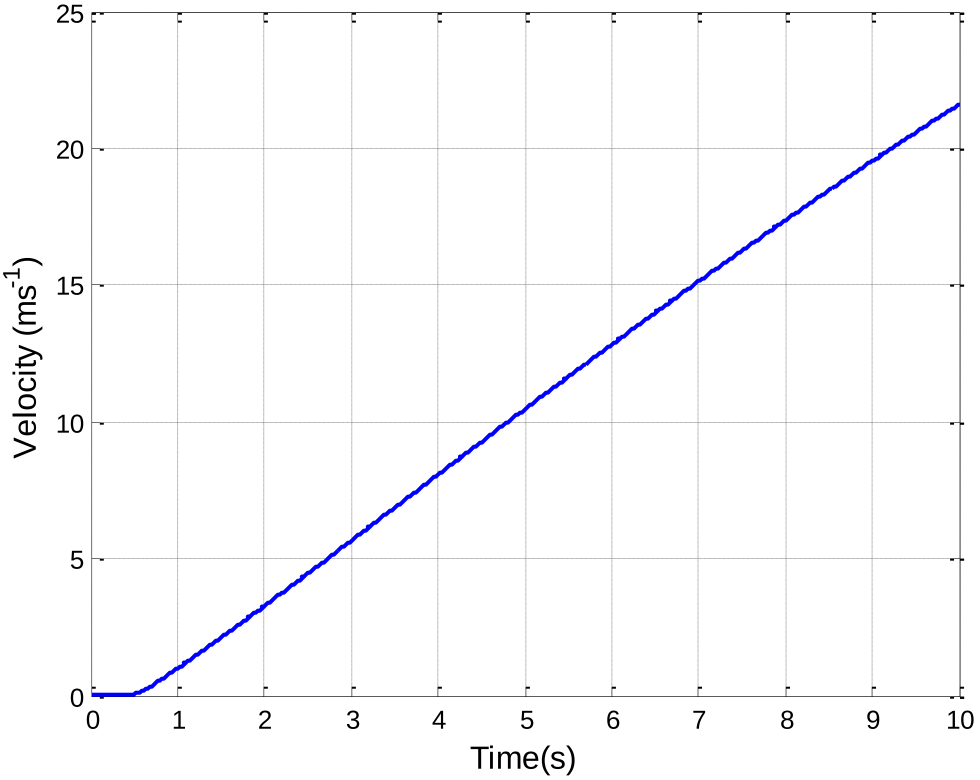

Figure 68: Velocity plot for the case of variable driving moment and full softening

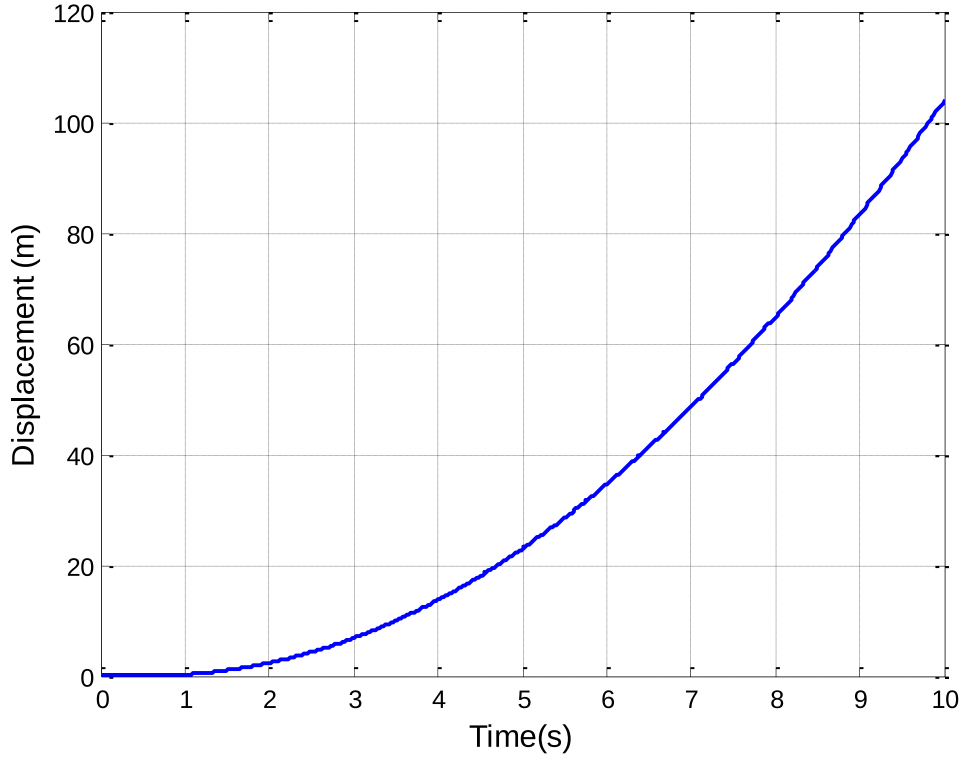

Figure 69: Displacement plot for the case of variable driving moment and full softening

3.4.4.5 Results for thermal friction softening only – constant driving moment

As a final case, it is only assumed the thermal friction softening, neglecting velocity and displacement softening. Therefore, in this context, the expression for the critical state parameter becomes (Equation 3.23);

$$M(\theta) = M_{ref} - \tilde{g}(\theta - \theta_{ref}) \tag{3.58}$$

where, $M_{ref} = 0.657$ is the reference critical state parameter corresponding to the peak friction angle given in Table 2. The thermal sensitivity parameter $\tilde{g}$ is set to 10^{-2} as explained in line with Cecinato (2009). This linear law may give a very small or even negative value of critical state parameter at high temperatures, which is not realistic. Therefore, a lower limit value of the critical state parameter is considered in this analysis corresponding to dynamic residual friction coefficient given in section 2.2.5.

In contrast to previous analyses, the “activation point” is seen here to be at nearly 1.8 sec, while in all previous cases it was 0.5sec. From the temperature isochrones given in Figure 70, it can be seen that the temperature rises to a maximum value of 139.09°C, and Figure 71 shows that excess pore pressure increases to 1.81 MPa. Velocity and displacement plots are given in Figure 72 and Figure 73 respectively. A significant difference in the final velocity and displacement is observed compared to previous cases. The velocity reaches to nearly 19.5 m/sec after 10 sec whereas displacement reaches to 76.822m.

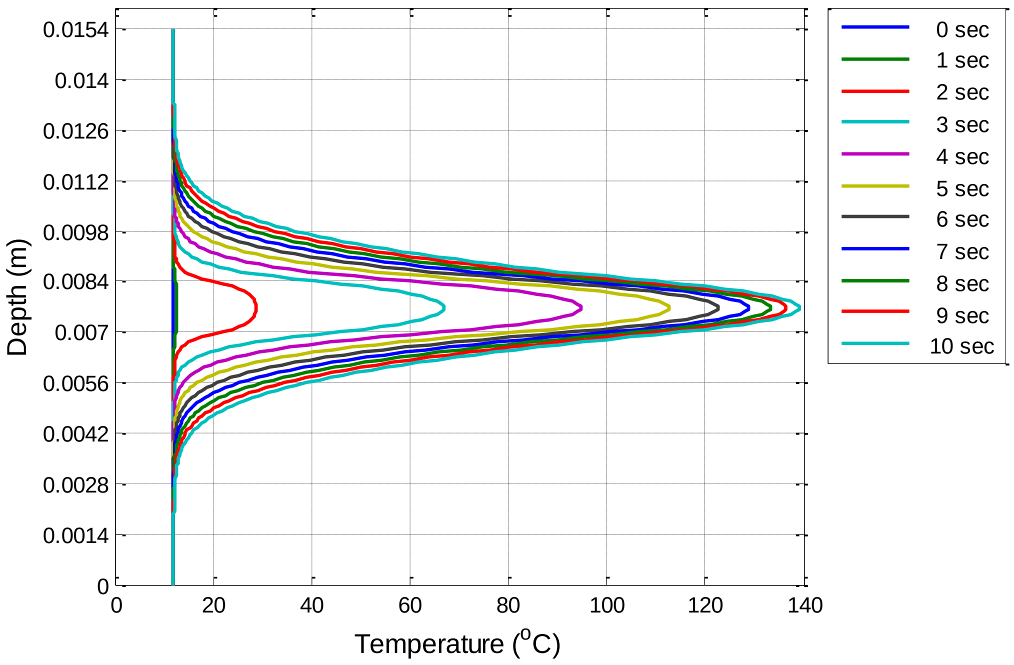

Figure 70: Temperature isochrones within the shearband and its surroundings shear band area is given between 0.007m and 0.0084m (case of constant driving moment and thermal softening)

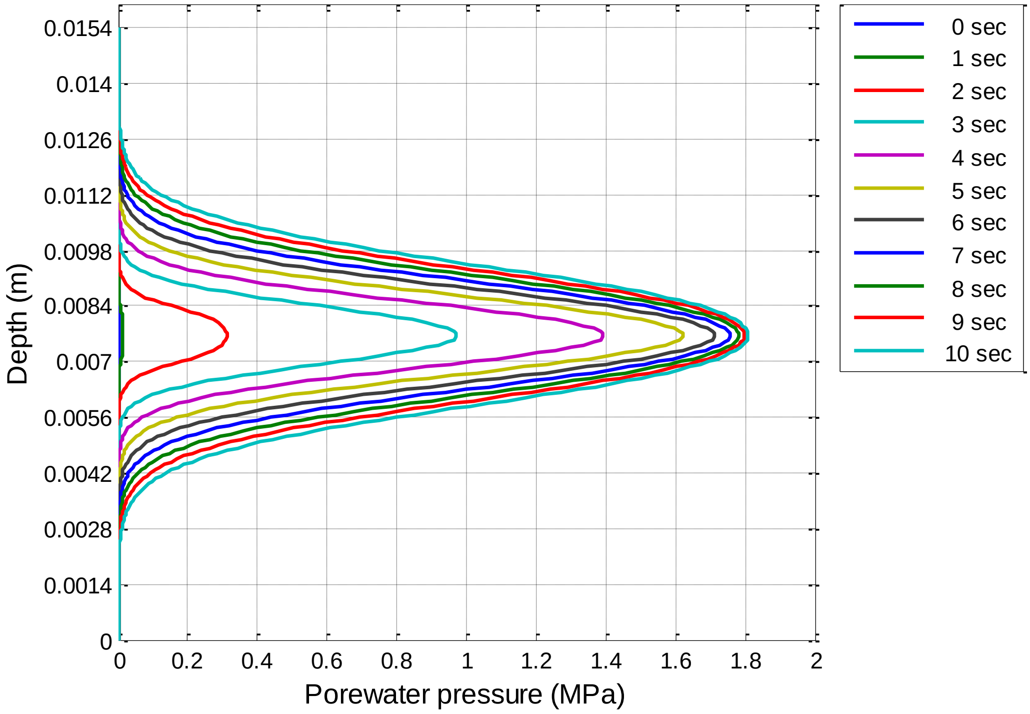

Figure 71: Pore water pressure isochrones within the shearband and its surroundings shear band area is given between 0.007m and 0.0084m (case of constant driving moment and thermal softening)

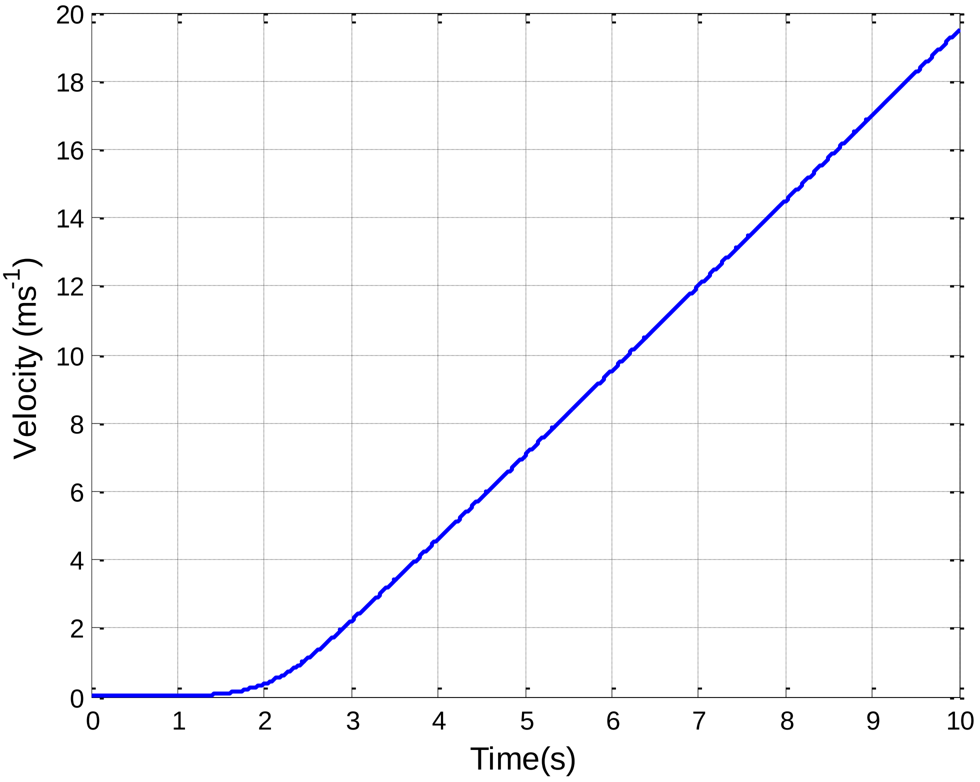

Figure 72: Velocity plot for the case of constant driving moment and thermal softening

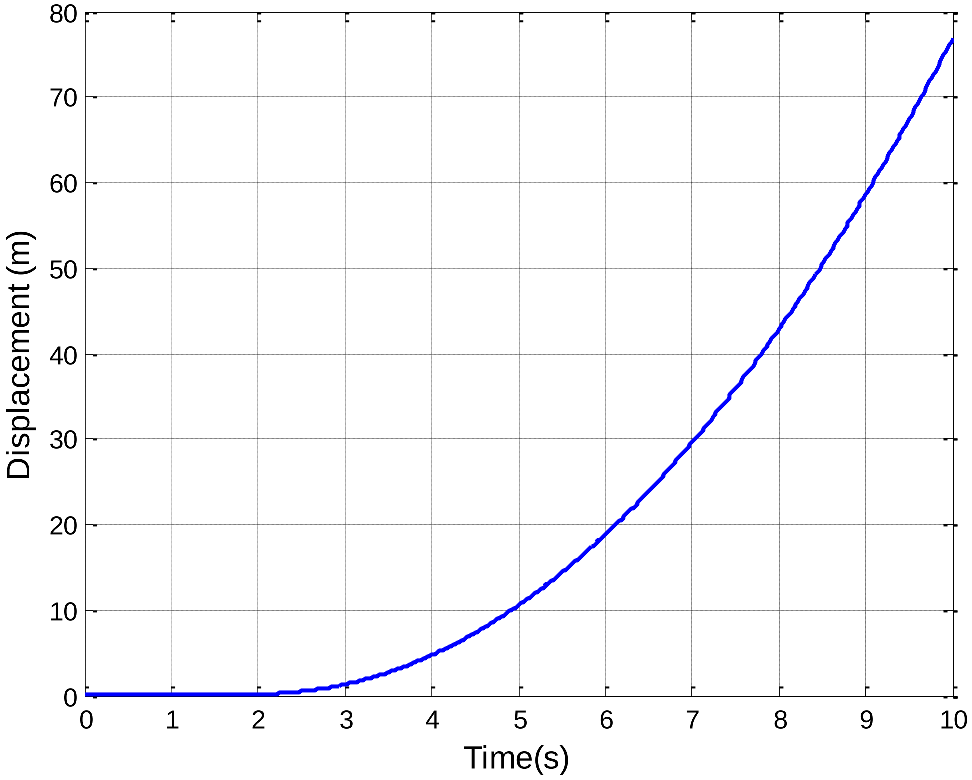

Figure 73: Displacement plots plot for the case of constant driving moment and thermal softening

3.4.4.6 Results for thermal friction softening only – variable driving moment

In this subsection the results for thermal friction softening only are presented but use the modified dynamic equation. The same M_{ref} value was used as described in section 3.4.4.5. The temperature and pore water pressure isochrones are given in Figure 74 and Figure 75 respectively. The temperature and pore pressure rise were observed same as the previous case (thermal friction softening - constant driving moment)

The velocity and the displacement plots are given Figure 76 and Figure 77 respectively. Velocity reaches a value of 18.5m/s at 10 seconds while displacement reaches 75 m. Difference of 1m/sec in velocity and 1.8m in displacement are observed compared to the case of thermal friction softening with constant driving moment. However, this difference is negligible compared to the total run-out reached at 10 sec.

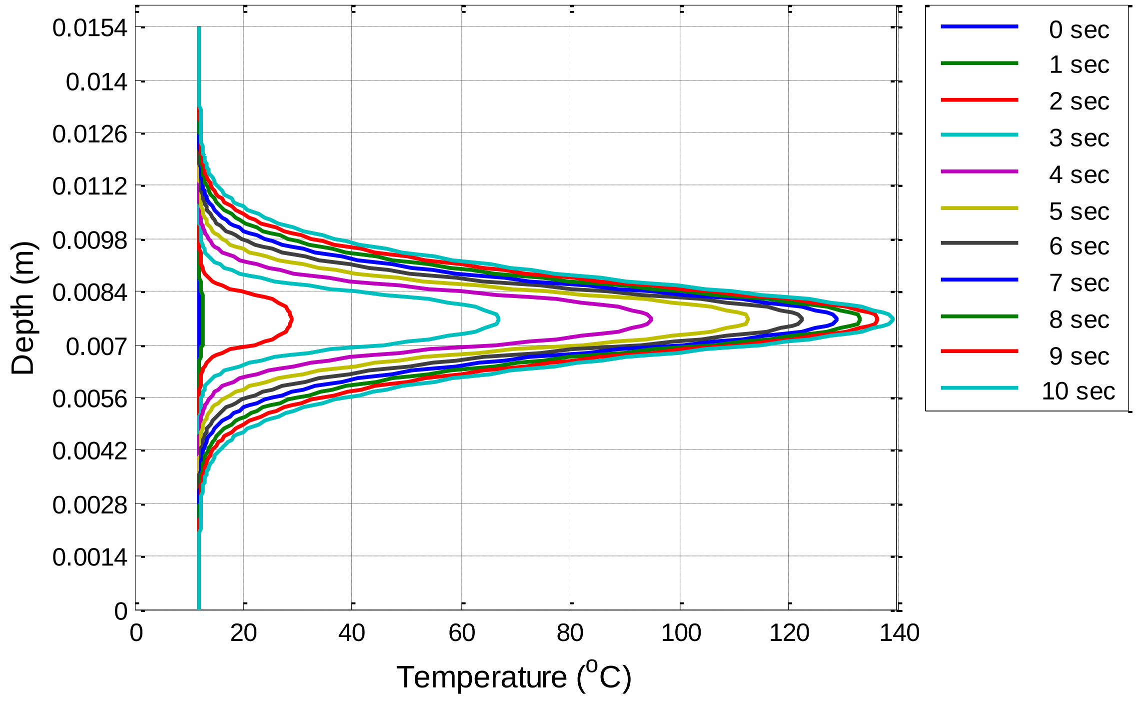

Figure 74: Temperature isochrones within the shearband and its surroundings shear band area is given between 0.007m and 0.0084m (case of variable driving moment and thermal softening)

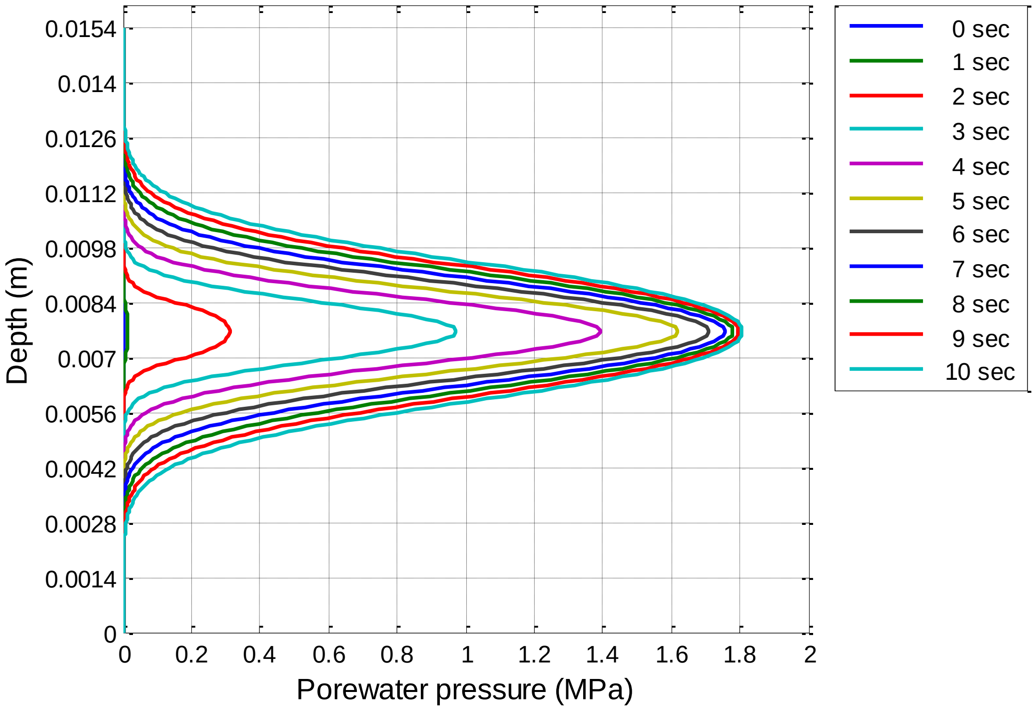

Figure 75: Pore water isochrones within the shearband and its surroundings shear band area is given between 0.007m and 0.0084m (case of variable driving moment and thermal softening)

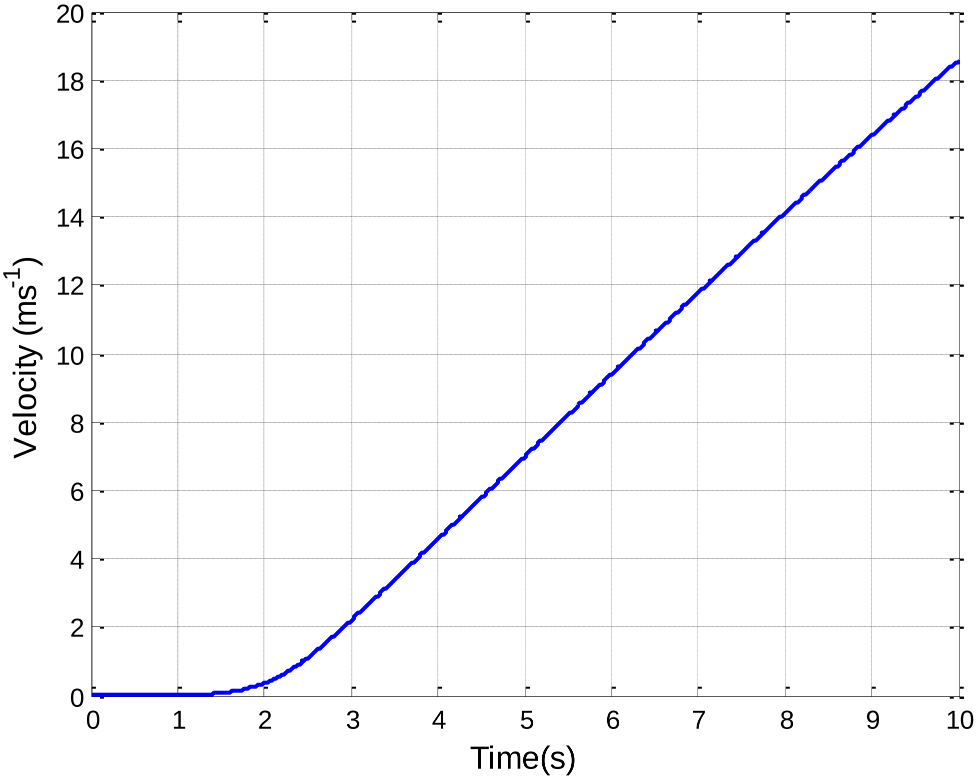

Figure 76: Velocity plot for the case of variable driving moment and thermal softening

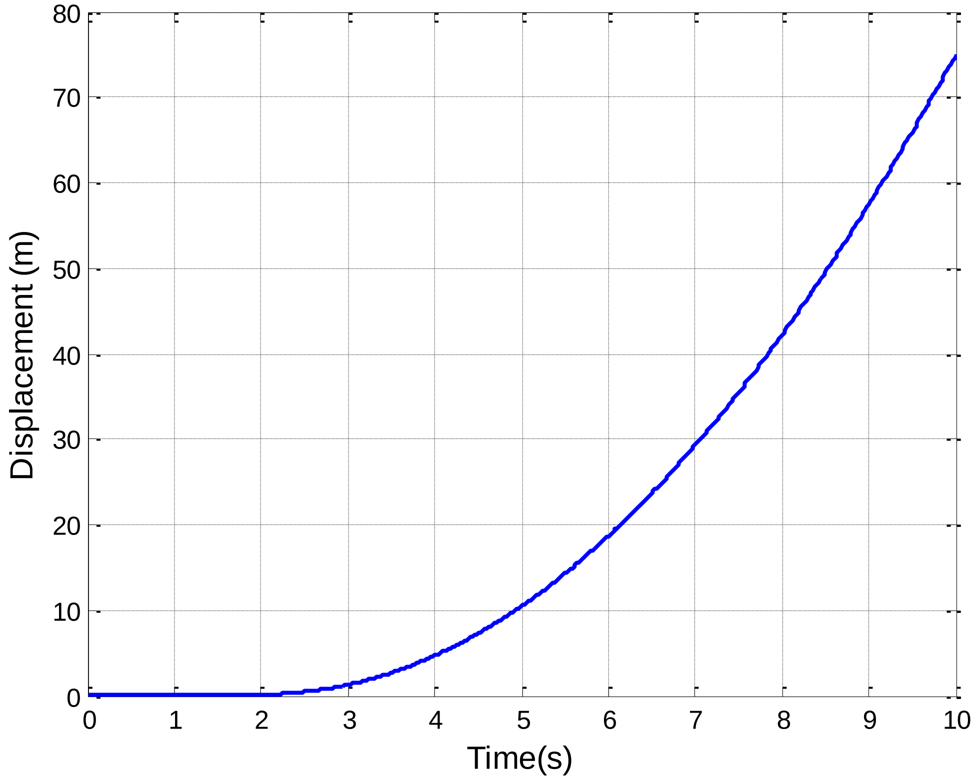

Figure 77: Displacement plot for the case of variable driving moment and thermal softening

3.4.5 Discussion of the numerical results

The results presented in the last six subsections (3.4.4.1 to 3.4.4.6) correspond to the predicted behaviour of section 5 of the Vaiont slide given different assumption. The magnitude of all results is consistent with the observations reported in Hendron and Patton (1985).

The results are very similar to those reported by Vardoulakis (2002a) & Cecinato (2009), despite the fact that they both considered constant driving moment. Using variable driving moment leads to reduction in the predicted velocity of 5~10%, which however is not significant given the other uncertainties involved in the model.

More appreciable differences can be seen if the analyses are run for longer; 25 sec after initiation, the variable driving moment assumption leads to deceleration of the slide, as the extensive movement of the sliding mass causes the driving moment to change sign.

In contrast, assuming constant driving moment leads to continuing acceleration. However, by the time the difference becomes appreciable the mass has already displaced by a large amount (500m), to the point that it can no longer be assumed to move as a rigid body, thus violating a basic assumption of the model. Hence the maximum time modelled is limited here to 10 sec.

Moreover, the cases of “full friction softening” and “dynamic softening only” give practically the same results. Thermal friction softening on the other hand only gives 16.5% lower velocity than full friction softening. According to the modified dynamic equation, the velocity of the rotational failure mass depends on the mobilized friction angle. The lower the friction angle, the higher the velocity of the slide, therefore the rate of change of friction angle dominates the velocity of the slide. The displacement and velocity softening law decreases the friction angle more rapidly than the linear thermal friction softening law. Ultimately, all softening laws reach the same dynamic residual value. So that, in the case of full friction softening, the effect of dynamic friction softening overtakes the effect of thermal friction, explaining the similarity of the results for “full friction softening” and “dynamic friction softening only”.

3.5 The effect of slip circle geometry

In the previous subsections, Section 5 of the Vaiont slide is used to validate the landslide model. Cecinato (2009) carried out a parametric study on a planar slide to investigate the effect of the overburden thickness on the slide velocity. It was found that, if thermal pressurization is ignored, overburden thickness does not affect slide velocity, but it becomes important when thermal pressurization is present. In the latter case, a thicker sliding mass accelerates faster than a thinner slide as shown in Figure 78 (Cecinato, 2009). Generally, the shape of the failure mass can take different forms other than planar, and one possibility is a circular slip. In this section, a parametric study is carried out to investigate the effect of the size of the circular failure mass on the velocity of the slide as well as to establish the effect of thermal pressurization for slides of different size. For simplicity, different circular slips on an infinite slope are assumed.

It is acknowledged that circular slip is not generally a relevant failure mode for an infinite slope, unless particular geological conditions make it possible. On the other hand, consideration of a general slope would complicate the analysis significantly. The approach chosen represents a compromise that still allows us to investigate the effects of frictional heating.

The size of the failure arc is varied in the following two ways, also shown in Figure 79.

- The radius of the circular slip is varied while keeping centre at the same position.
- For constant radius, the distance of the centre from the slope surface is varied.

First, analyses were carried out neglecting the thermal pressurization effect and the results are compared for each case stated above. Subsequently, analyses taking thermal pressurization in to account are also performed.

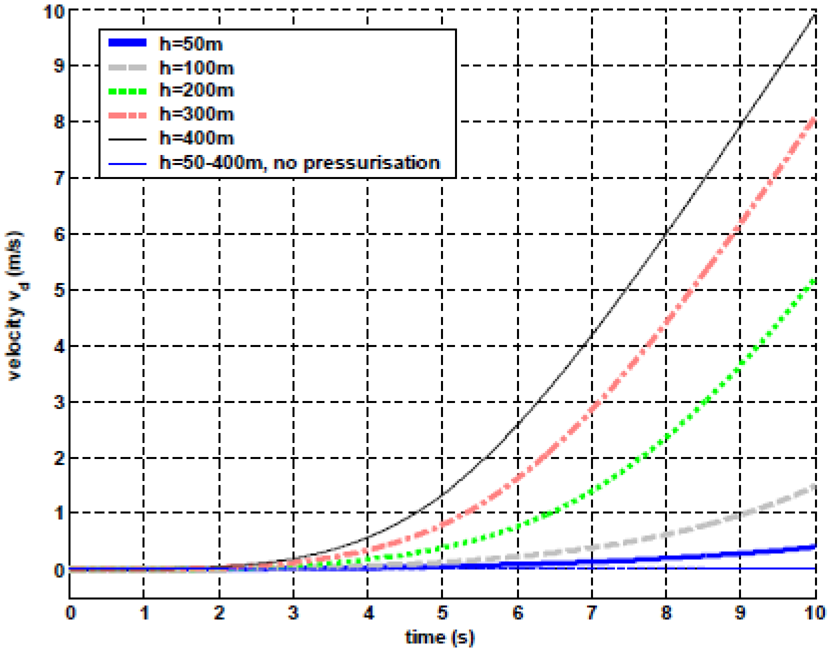

Figure 78: Effect of overburden thickness of the plannar slide (Cecinato, 2009)

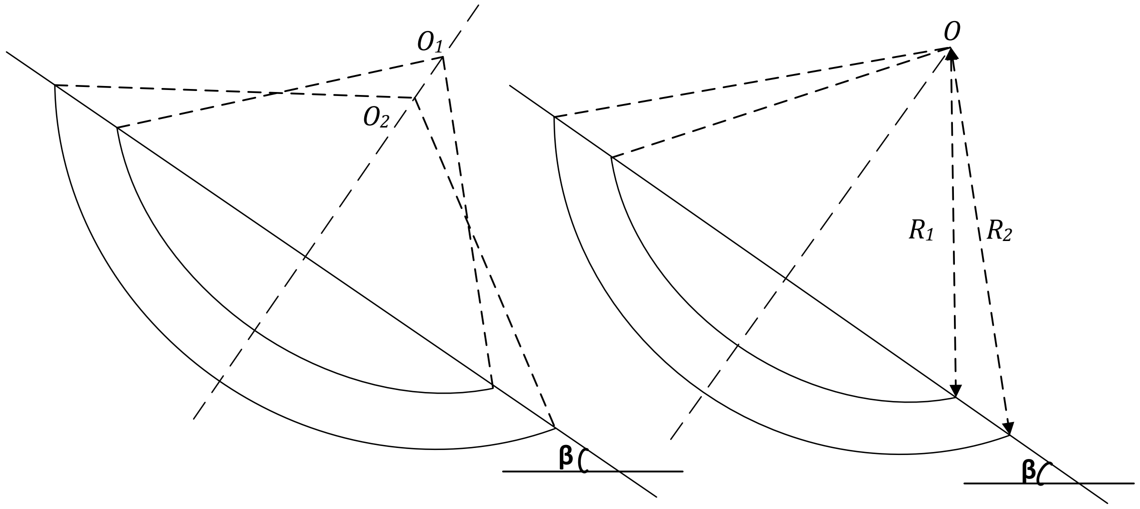

Figure 79: Slip circle with a) different centre and same radius, b) different radii

3.5.1 Dynamic equation

In this section a general dynamic equation is derived for a circular slip surface on infinite slope. It is further assumed that ground water flow is parallel to the slope, as in Cecinato (2009). The material properties of the soil such as mobilized friction angle and density are assumed uniform.

For the geometry shown in Figure 80, the driving moment can be written as (Vardoulakis, 2002a);

$$(M_{drv})_i = D_i \frac{\alpha_i}{\sqrt{2(1-\cos\alpha_i)}} R_{fi} \sin(\varphi_F - (\theta_d)_i) \tag{3.59}$$

D_i is the effective weight, α_i & R_{fi} are the reference opening angle and the radius of the failure circle respectively, φ_F is the incipient failure angle which equals the slope angle β and $(\theta_d)_i$ is the angular displacement.

The initial normal effective stress acting on the slip plane can be written as;

$$(\sigma'_{n0})_i = \frac{D_i}{R_i\sqrt{2(1-\cos\alpha_i)}} R_{fi} \cos(\varphi_F - (\theta_d)_i) \tag{3.60}$$

Therefore, the resisting moment can be written as;

$$(M_{res})_i = R_{fi}^2 \alpha_i \mu((\sigma'_{n0}) - p_d) \tag{3.61}$$

where $\mu = \tan\varphi_m$,φ_m is the mobilized friction angle of the shear band material and p_d is the excess pore water pressure generated by thermal pressurization at the interface between the shear band and the moving rigid mass.

Angular momentum balance gives;

$$\rho\left(I_p\right)_i\left(\frac{d\omega}{dt}\right)_i = (M_{drv})_i - (M_{res})_i \qquad 3.62$$

where $\rho\left(I_p\right)_i$ is the polar moment of inertia of the sliding mass, ρ density of the mass, $\left(I_p\right)_i$ the second moment of area, and ω is the angular velocity. Substituting the corresponding expressions for $(M_{drv})_i$ and $(M_{res})_i$ gives

$$\rho\left(I_p\right)_i\left(\frac{d\omega}{dt}\right)_i = (\omega_0^2)_i\left\{\frac{D_i R_{fi}(R_d)_i}{\gamma_s\left(I_p\right)_i}\left(1-\frac{\tan\varphi_m}{\tan(\varphi_F-(\theta_d)_i)}\right)+\frac{p_d(t)}{(p_c)_i}\right\} \qquad 3.63$$

where;

$$p_c = \frac{(\gamma_s)_i\left(I_p\right)_i}{R_{fi}^3}\frac{1}{\alpha_i\tan\varphi_m}$$

$$(R_d)_i = \frac{\alpha_i}{\sqrt{2(1-\cos\alpha_i)}}R_{fi}\sin(\varphi_F-(\theta_d)_i) \qquad 3.64$$

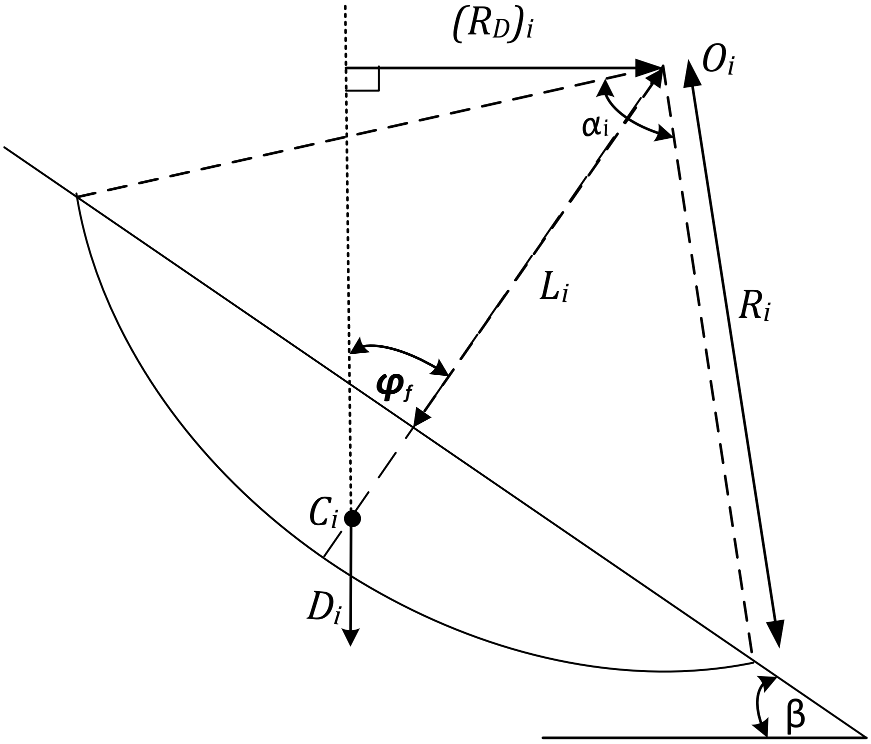

Figure 80: Reference circular slip surface on an infinite slope

γ_s is the density of the soil and $(\omega_0)_i = \sqrt{g/R_{fi}}$. The sliding velocity is calculated from the angular velocity as follows.

$$(v_d)_i = R_{fi}\omega_i(t) \qquad 3.65$$

The polar moment of inertia of the sliding mass, shown in Figure 80, can be written as (Zwillinger, 2002);

$$\left(I_p\right)_i = \frac{R_{fi}^4}{4}\left(\alpha_i - \sin\alpha_i + \frac{2}{3}\sin\alpha_i \sin^2\alpha_i\right) \tag{3.66}$$

As flow lines are parallel to the slope, the resultant effective weight is;

$$D_i = (\gamma_s - \gamma_w)\cos(\beta)\, A_i \tag{3.67}$$

where γ_w is the density of water and A_i is the area, given by;

$$A_i = \frac{R_{fi}^2}{2}(\alpha_i - \sin\alpha_i) \tag{3.68}$$

The opening angle α_{new} of circle with the same centre but different radius R_{fnew} can be written as;

$$\alpha_{new} = 2 \times \arccos\left(\frac{R_i}{R_{fnew}}\cos\left(\frac{\alpha_i}{2}\right)\right) \tag{3.69}$$

For a circle with the same radius whose centre is at different distance L_{new} from the slope, it is proceeded as follows: The relationship between the opening angle and L_i can be written as (Figure 80);

$$L_i = R_{fi}\cos\left(\frac{\alpha_i}{2}\right) \tag{3.70}$$

The new opening angle α_{new} can be written as;

$$\alpha_{new} = 2 \times \arccos\left(\frac{L_{new}}{L_i}\cos\left(\frac{\alpha_i}{2}\right)\right) \tag{3.71}$$

In the following, the change in perpendicular distance is referred as follows;

$$(\Delta L)_{new} = L_{new} - L_i \tag{3.72}$$

3.5.2 Numerical results

It is now presented the numerical results for each one of the cases stated above with and without thermal pressurization effects. For the case of “without thermal pressurization” only velocity and displacement friction softening is included. Full friction softening is included when thermal pressurization is considered. To trigger the landslide, φ_m is set to 22.277^0 which is 1% less than the incipient failure angle φ_F.

The governing equations were discretised and solved using the BTCS scheme. The equations were integrated for a time window of 10 seconds after initiation of movement. As reference geometry, section 5 of the Vaiont slide with radius of 1500 m and opening angle of 62° is used.

3.5.2.1 Case of different radii

First, the dynamic equation without thermal pressurization was solved numerically for slip circles of fixed centre (at $L_i = 1285m$) and radius varying between 1300 and 1900 m. Velocity and displacement plots are given Figure 81 and Figure 82 respectively. The velocity obtained ranges from 15.5 m/sec to 23 m/sec at 10 sec after initiation for the selected range of radii and the displacement varies from 75 m to 110 m. No significant change in the activation point is noticed; all analyses give an activation point of 0.5sec.

Subsequently, analyses were carried out coupling the dynamic equation with the heat and pore pressure equations. The corresponding velocity and displacement plots are given in Figure 83 and Figure 84 respectively. The velocity obtained here ranges from 16.5 m/sec to 26.2 m/sec at 10 sec after initiation for the selected range of radii and the displacement varies from 75.5 m to 125 m.

The plot of velocity at 10 sec versus the radius of the respective circular surface is given in Figure 85. It can be seen from Figure 85 that, although the predicted velocity in both cases increases with the radius of the slip circle, the larger the radius is the bigger the influence of thermal pressurization on the results, as can be seen by the increasing distance between the two lines.

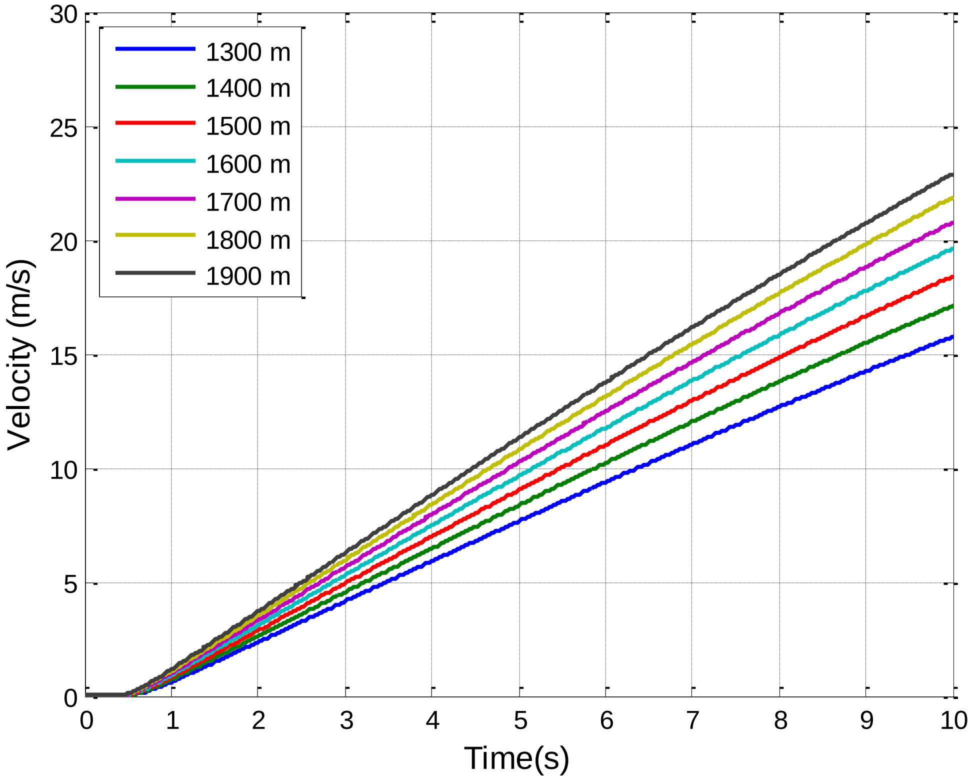

Figure 81: Velocity plot for different radius of failure mass- absence of pressurization effect

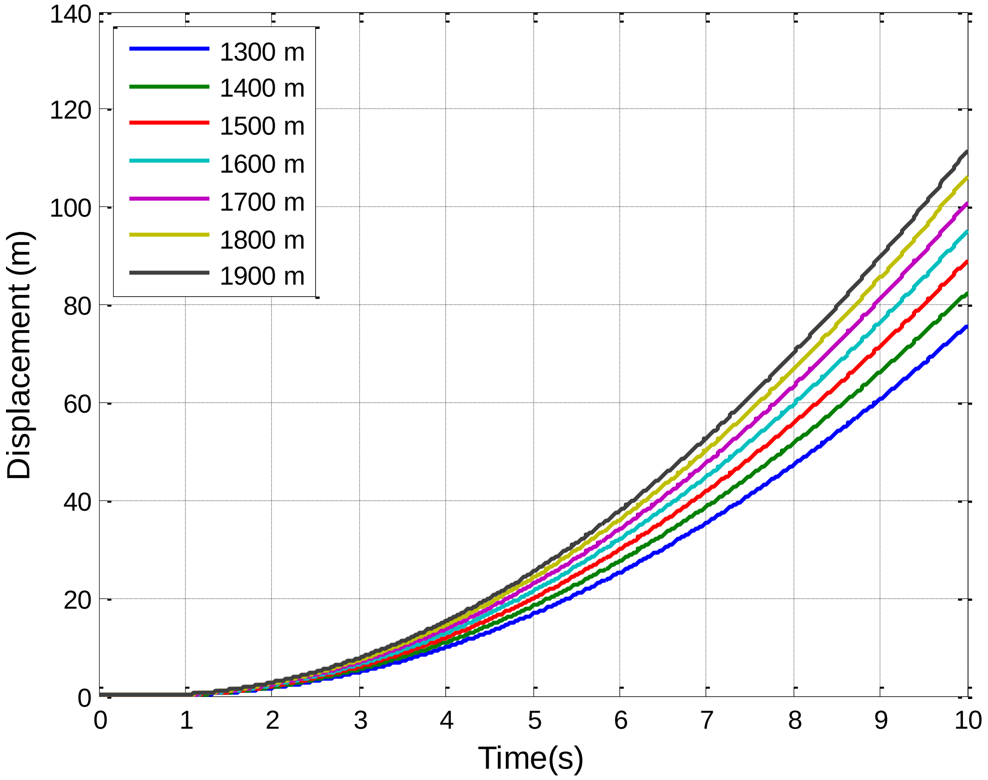

Figure 82: Displacement plot for different radius of failure mass- absence of pressurization effect

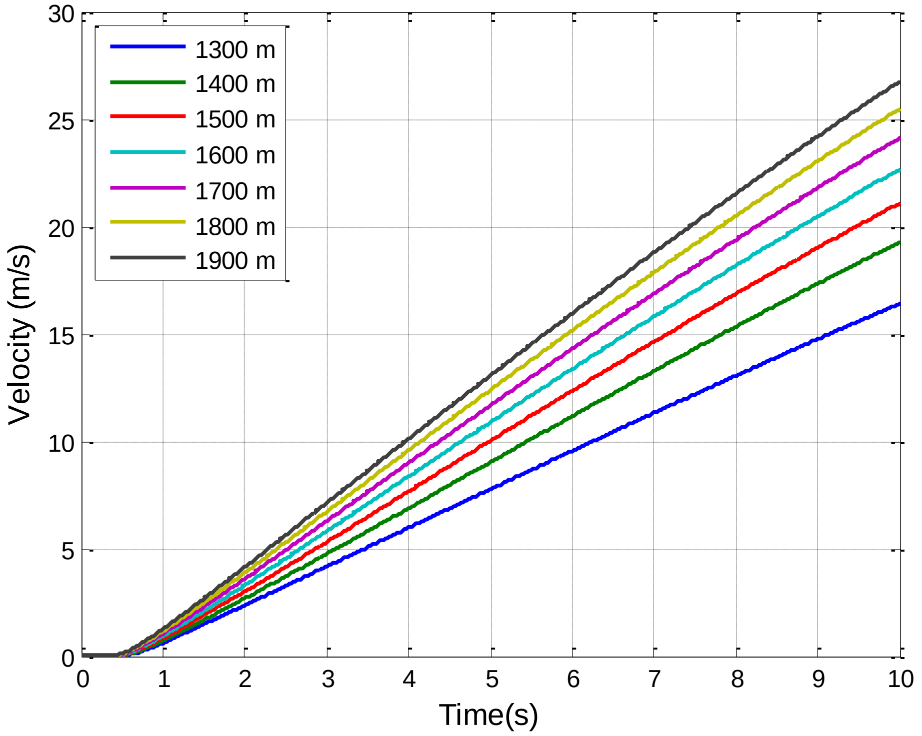

Figure 83: Velocity plot for different radius of failure mass coupled with pressurization effect

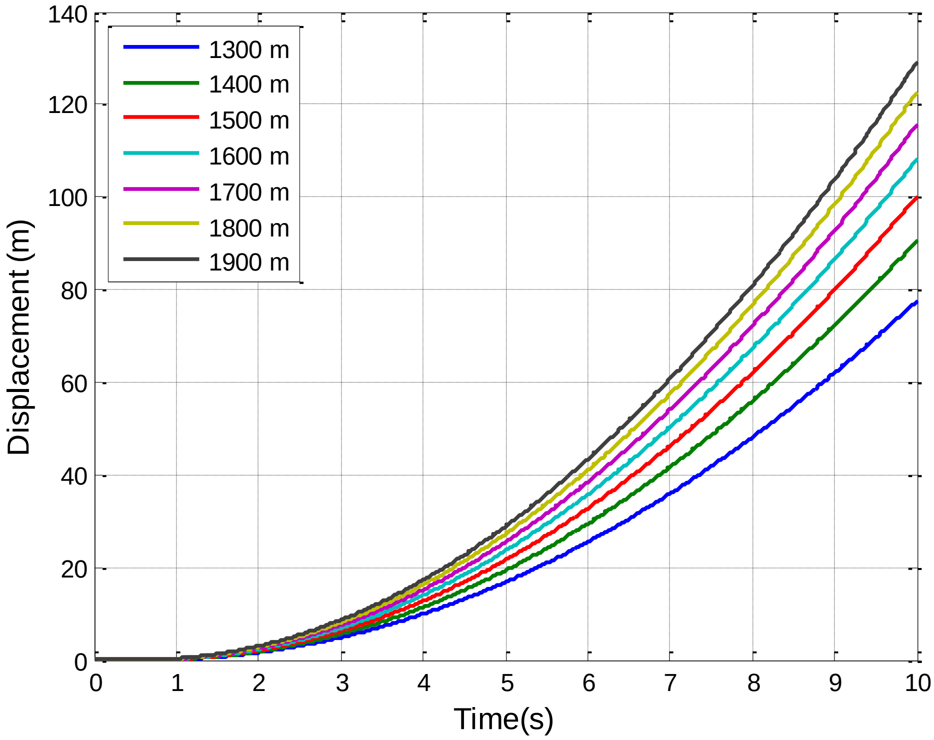

Figure 84: Displacement plot for different radius of failure mass coupled with pressurization effect

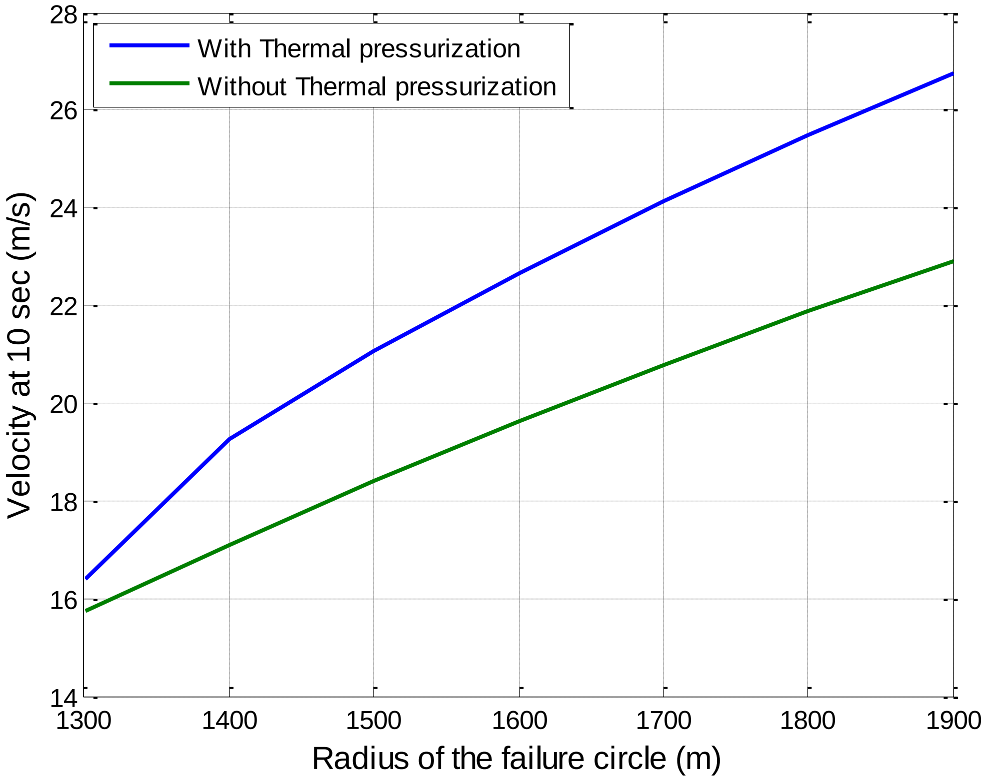

Figure 85: Plot of slide velocity at 10 sec versus radius of failure plane

3.5.2.2 Case of moving centre

The numerical results for slip circles of the same radius but different centres are presented in this section. The analyses were carried out by varying the values of ΔL given in Equation 3.72. ΔL is negative when the centre moves away from the reference position and positive if it moves towards the slope. $\Delta L = 0$ represents the reference geometry which corresponds to section 5 of the Vaiont slide.

The velocity and displacement plots when the pressurization effects are ignored given in Figure 86 and Figure 87. The final velocity at 10 sec varies from 15.5m/sec to 25m/sec for the range of ΔL between -200 m and 400 m, whereas the displacement varies from 75m to 123m.

The results when the effects of thermal pressurization are included are given in Figure 88 and Figure 89. In that case the velocity varies from 16.3 m/sec to 28.8 m/sec and displacement varies from 78m to 140m.

The plot of velocity at 10 sec versus the values of ΔL is given in Figure 90. It can be seen from Figure 90, although the predicted velocity in both cases increases with ΔL, the larger the ΔL is, the bigger the influence of thermal pressurization on the results, as can be seen by the increasing distance between the two lines.

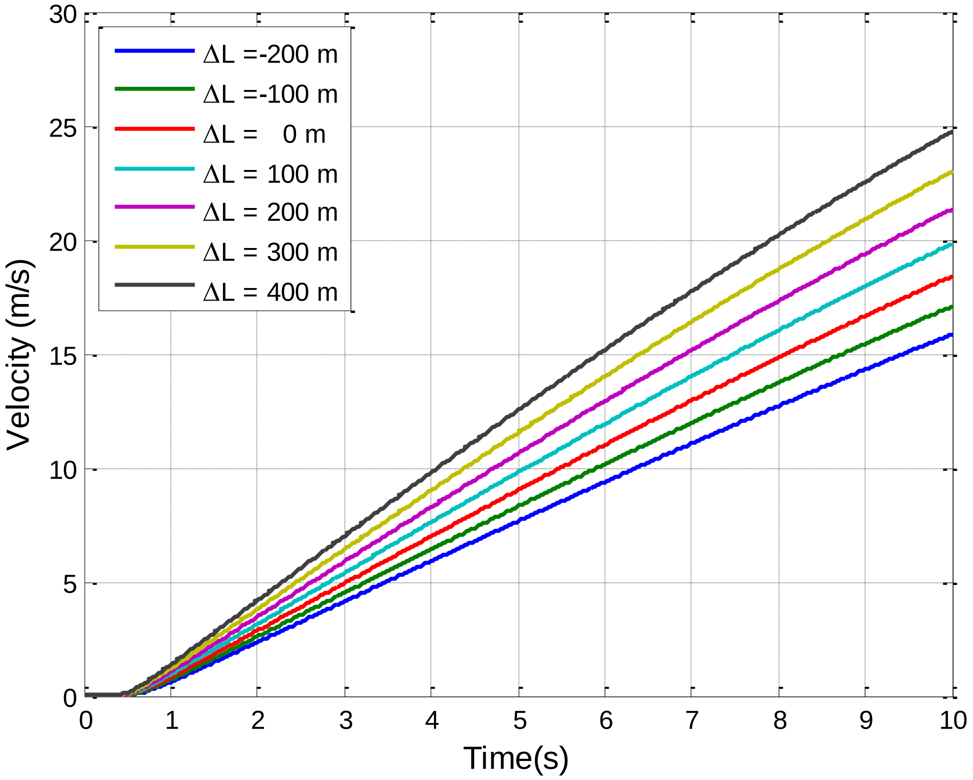

Figure 86: Velocity plot for moving centre - absence of pressurization effect

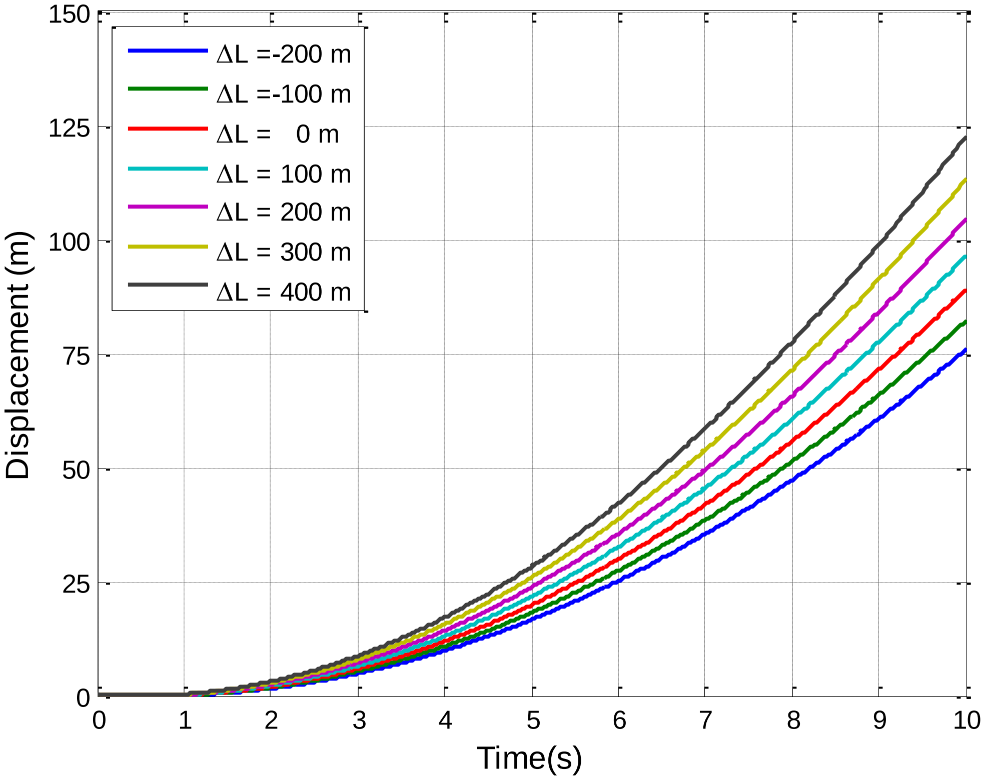

Figure 87: Displacement plot for moving centre-absence of pressurization effect

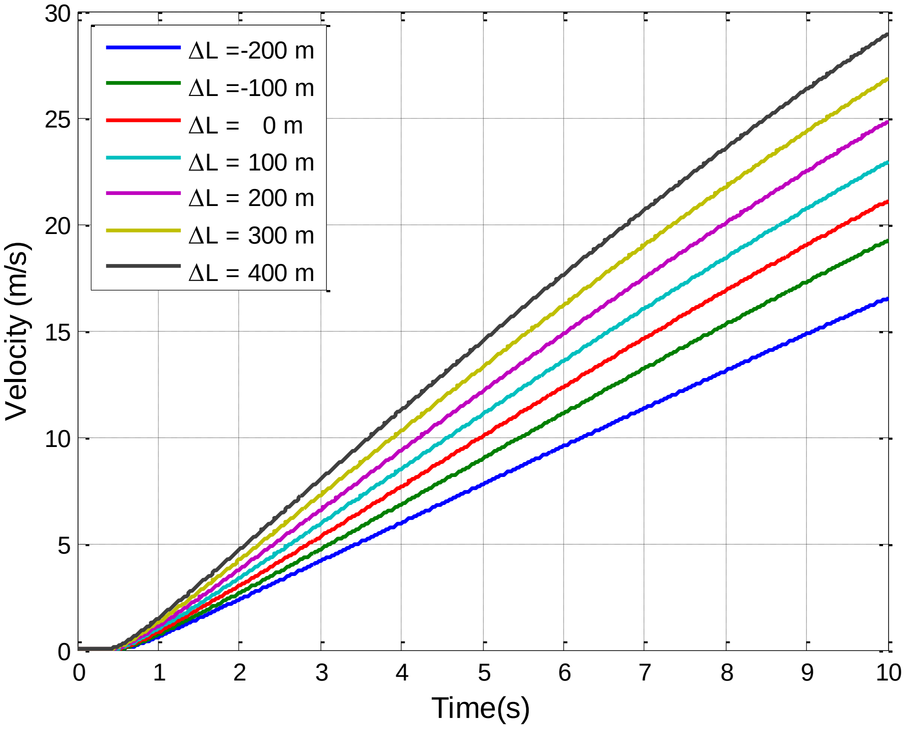

Figure 88: Velocity plot for moving centre of failure circle coupled with pressurization effect

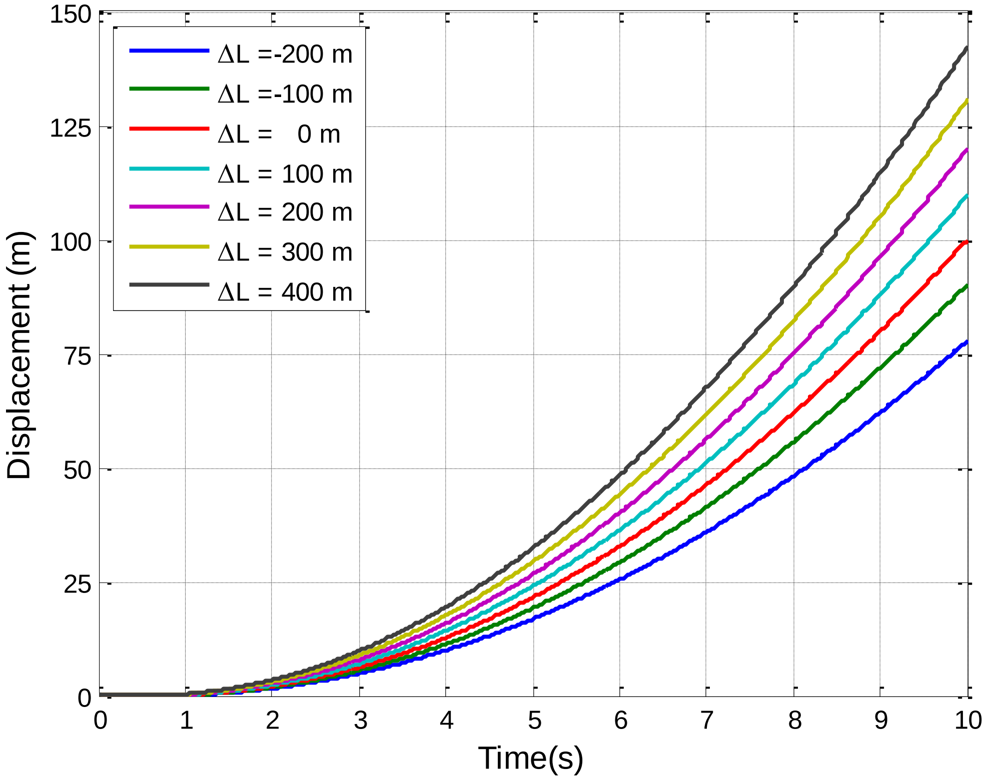

Figure 89: Displacement plot for moving centre of failure circle coupled with pressurization effect

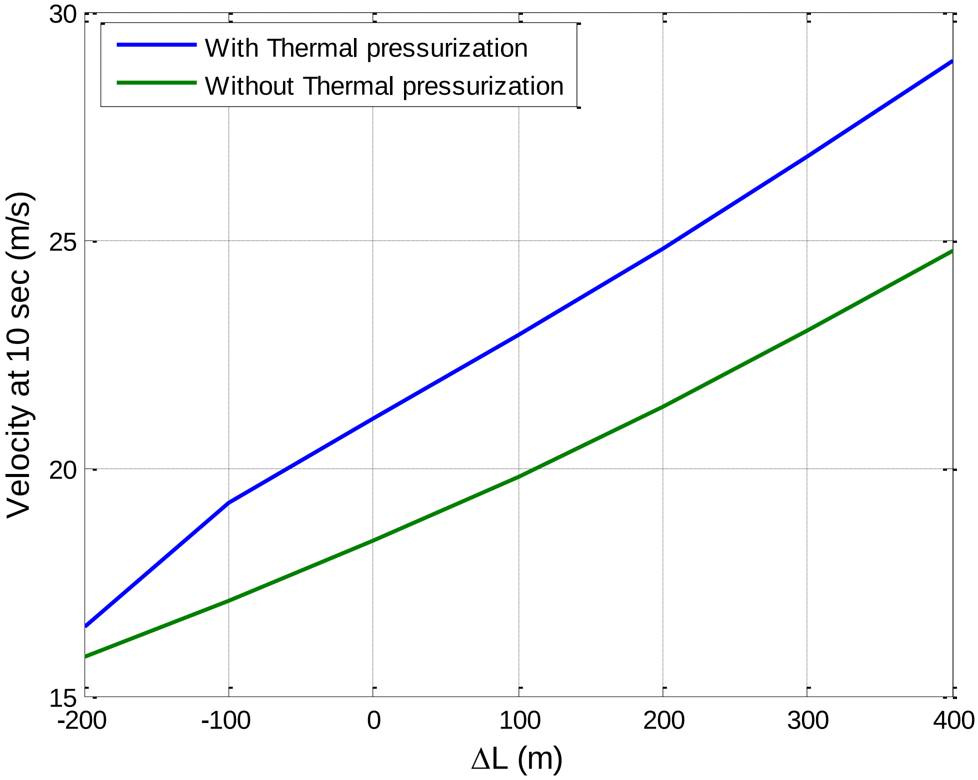

Figure 90: Plot of slide velocity at 10 sec versus ΔL.

3.5.3 Discussion on numerical results

Cecinato (2009) showed that, in planar slides, the overburden thickness plays an important role when thermal pressurization effects are considered. A thicker sliding mass accelerates faster than a thinner slide as shown in Figure 78 (Cecinato, 2009).

Similar analyses were carried out but with circular slip surface rather than a planar one, to investigate the influence of the size of the circular slip surface on slide acceleration. Both the radius and the location of the centre of the slip surface were varied. Overall, the results show that, even without pressurization, size influences significantly the dynamics of the slide as a slide with larger radius accelerates faster than a slide with smaller one.

The results also show that, for a given radius, slides whose centre is close to slope, accelerates faster.

Chapter 4: A thermo-poro-mechanical landslide model based on rate process theory

The model described in Chapter 3 is applicable to the final phase of catastrophic failure of a landslide. However, in many landslides, slow creep-like movement is observed before the slide reaches a catastrophic phase.

Rate process theory is based on activation of flow units (Section 2.4.5). Moreover, flow units can be activated by thermal energy as well as externally applied stress. Therefore, it should be possible to use it to model the creep like movement of landslides, as it incorporates the time dependent behaviour of soils and also the concept of thermal activation is inherently included.

In this chapter, a new thermo-poro mechanical landslide model is developed on this basis. First, a preliminary validation of rate process theory was done in isothermal conditions. Subsequently, a thermo-mechanical formulation for a shear band was developed. Finally, a complete landslide model, which includes heat production, thermal pressurization and the dynamics of the slide was developed.

4.1 Soil creep as a rate process

Several authors applied rate process theory to explain the creep behaviour of soils (Andersland and Douglas, 1970, Christensen and Wu, 1964, Kuhn and Mitchell, 1993, Mitchell, 1964). Rate process theory, developed by Eyring (1936), considers the movement of flow units such as atoms or molecules. The movement of flow units is opposed by an energy barrier called activation energy, U_0 (as shown in Figure 91) which keeps a flow unit in an equilibrium position. If enough energy to exceed the activation energy is applied to the flow unit by an external source, it will move and deformation will occur. This energy source can have different forms, e.g. a heat source or an applied stress.

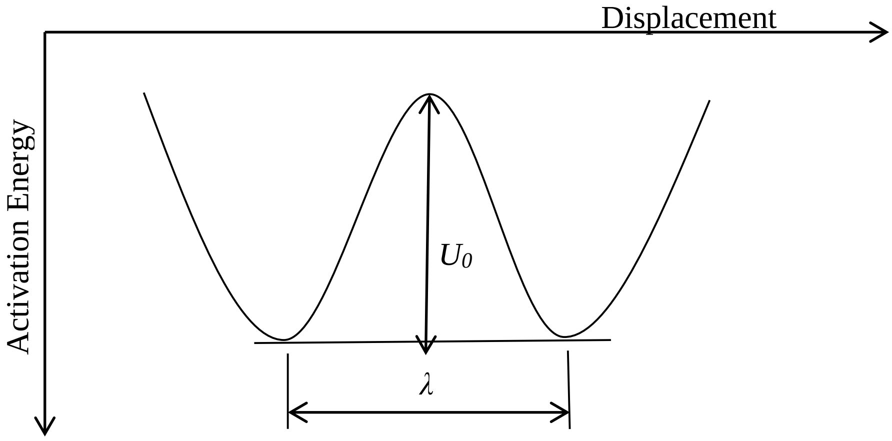

Figure 91: Schematic representation of activation energy between two flow units

4.2 Activation frequency

Curve A in Figure 92 represents the potential energy-displacement relationship for a material at rest. From statistical mechanics, the average thermal energy per flow unit is given as *kT,* where k is Boltzmann's constant ($1.38 \times 10^{-23} JK^{-1}$) and T is the absolute temperature *(*K*)*. Even though a material is at rest, each flow unit is vibrating with a frequency of *kT/h,* (where h is Planck's constant, $6.624 \times 10^{-34} Js^{-1}$). In addition, it is assumed that the thermal energy of a material is divided among flow units following a Boltzmann distribution. Therefore, at rest, the probability of a given flow unit becoming activated is given by

$$p(U_0) = \exp\left(-\frac{U_0}{NkT}\right) \tag{4.1}$$

where N is the Avogadro's number and $Nk = R$ the universal gas constant ($8.3144\, JK^{-1}mol^{-1}$). In other words, the above expression can be interpreted as the proportion of flow units activated at a single oscillation. Therefore, the frequency of activation a_f is given by

$$a_f = \frac{kT}{h}\exp\left(-\frac{U_0}{NkT}\right) \tag{4.2}$$

If an additional amount of energy is supplied, e.g. through the application of a shear force $\bar{f}$, the energy barrier becomes distorted (curve B in Figure 92). The barrier height will be reduced by $(\bar{f}\lambda_l/2)$ in the direction of the applied force and increased by the same amount in the opposite direction; λ_l is the distance between two successive equilibrium points of a flow unit. Due to reduced barrier height, the activation frequency in the direction of the applied force becomes

$$\overrightarrow{a_f} = \frac{kT}{h}\exp\left(-\frac{\frac{U_0}{N}-\frac{\bar{f}\lambda_l}{2}}{kT}\right) \qquad 4.3$$

and in the opposite direction, due to increased barrier height, it becomes,

$$\overleftarrow{a_f} = \frac{kT}{h}\exp\left(-\frac{\frac{\mathrm{U}_0}{\mathrm{N}}-\frac{\bar{f}\lambda_l}{2}}{kT}\right) \qquad 4.4$$

Finally, the net activation frequency can be written as;

$$\overrightarrow{a_f} - \overleftarrow{a_f} = \frac{2kT}{h}\exp\left(-\frac{U_0}{RT}\right)\sinh\left(\frac{\bar{f}\lambda_l}{2kT}\right) \qquad 4.5$$

From the net activation frequency, the shear strain rate can be written in the following form; (Feda, 1989)

$$\dot{\gamma} = \frac{2kT}{h}\exp\left(-\frac{U_0}{RT}\right) \times \sinh\left(\frac{\tau\lambda}{2SkT}\right) \qquad 4.6$$

where

k = Boltzmann’s constant, 1.38×10^{-23}J/K
h = Plank’s Constant 6.62×10^{-34}J s
R = Universal gas constant, 8.31 J/ (mol K)
T = Absolute temperature, K
λ_l = Distance between successive equilibrium points of a flow unit
U_0= Free activation Energy, a measure of bonding strength kJ/mol
τ = Applied shear stress
S = Number of bonds/m^2

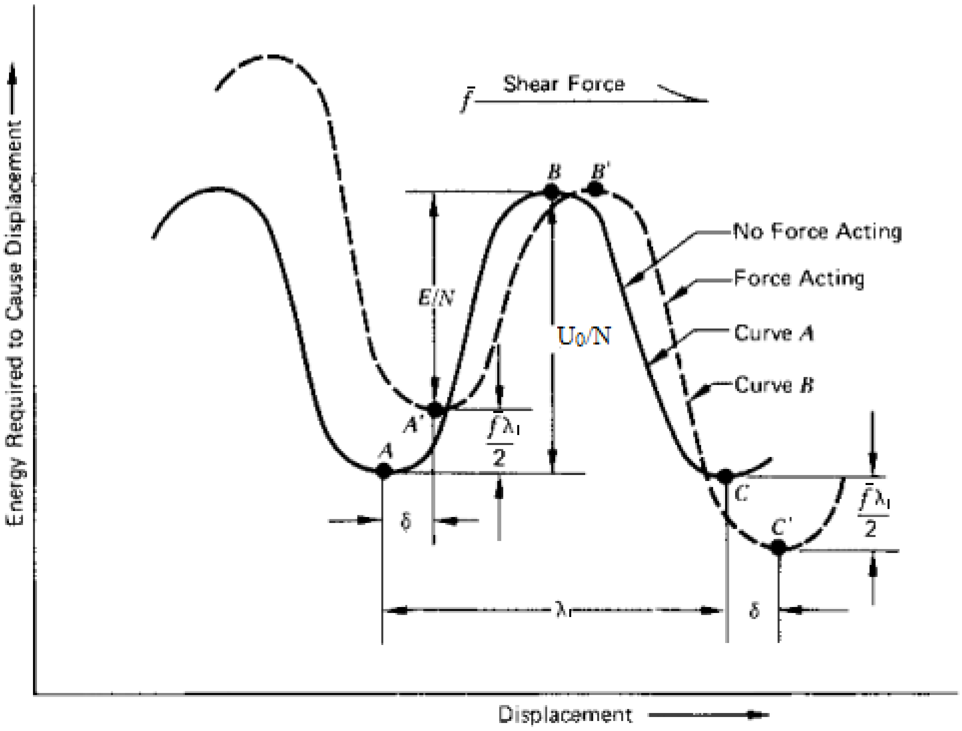

Figure 92: The distorting effect of a shear force on energy barrier (Mitchell and Soga, 2005)

4.3 Parameter estimation

4.3.1 Activation energy

The activation energy is a measure of bonding strength between two atoms or two molecules and depends on the type of flow unit considered and the applied shear stress.

It was measured experimentally by several authors for different types of soils using triaxial tests with temperature control (Campanella and Mitchell, 1968, Mitchell and Campanella, 1964, Mitchell et al., 1969, Mitchell and Soga, 2005) on the basis of the following equation.

$$\frac{\partial\left(\ln\frac{\dot{\gamma}}{T}\right)}{\partial\left(\frac{1}{T}\right)} = -\frac{E}{R} \tag{4.7}$$

Equation 4.7 follows from Equation 4.6, if $\sinh(.) = \frac{1}{2}\exp(.)$ is considered and standard algebraic manipulation is carried out.

$$E = U_0 - \frac{\tau\lambda_l k}{2SR} \tag{4.8}$$

Different values of E were measured for different applied shear stress. The free activation energy U_0 is defined as, the activation energy of a material under zero applied shear stress and can be obtained by extrapolating the line of $E\ vs\ 1/T$ to zero shear stress. Hence, free activation energy is a constant for a particular type of soil (Feda, 1989); its value ranges between 84-190 *kJ/mol* (Christensen and Wu, 1964, Kuhn and Mitchell, 1993, Kwok and Bolton, 2010, Mitchell and Soga, 2005, Ter-Stepanian, 1975).

From the studies done by Mitchell and co-workers, four main features of the activation energy of soil were identified, (Mitchell et al., 1969)

1. Activation energies are relatively large, much higher than for viscous flow of water.
2. Variations in water content (including completely dry soil), consolidation pressure, void ratio, and pore fluid have no significant effect on the required activation energy.
3. The values for sand and clay are very similar.
4. Clays in suspension with insufficient solids to form a continuous structure deform with activation energy equal to that of water.

4.3.2 Distance between successive equilibrium points of two flow units (λ_l)

Different values of λ_l have been proposed by different authors depending on the type of flow unit considered. If the flow unit is a single oxygen atom, then creep is considered to occur due to the displacement of oxygen atoms surrounding silicate mineral, and λ_l is taken as the diameter of the oxygen atom (2.8×10^{-10} m) (Campanella and Mitchell, 1968, Mitchell et al., 1968). If a hexagonal SiO_2 molecule is taken as a flow unit, then λ_l is assumed as the distance between holes of two SiO_2 molecules along the cleavage plane of a mica particle (5.2×10^{-10}m) (Erlandsson et al., 1988). These two ways of measuring distance between successive equilibrium points of two flow units is illustrated in Figure 93.

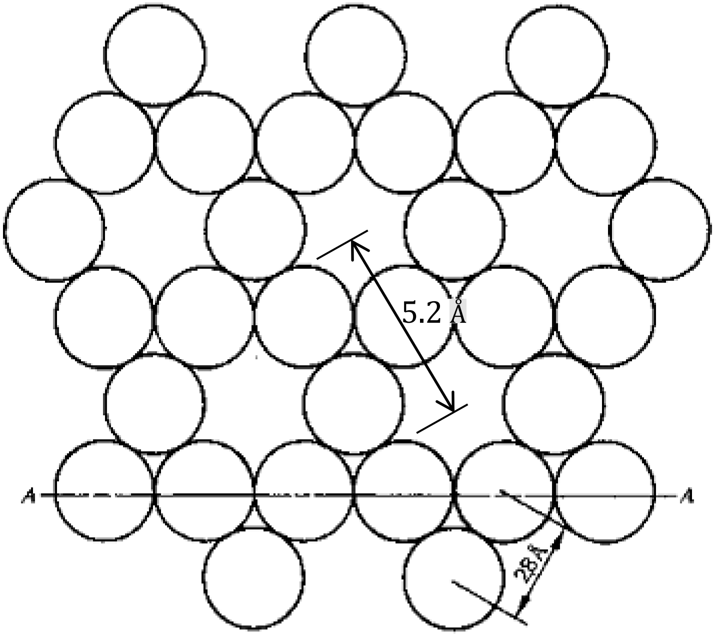

Figure 93: Interpretation of λ in terms of silicate mineral surface structure (circles represents configuration oxygen atoms in silicate mineral surface) (modified after Mitchell et al. (1969)

4.3.3 Number of bonds per unit area (S)

Inter-particle bonds are formed due to the normal force applied between two soil particles, and the number of bonds is proportional to this applied force. Therefore, macroscopically, the number of bonds can be related to the effective stress applied on the specimen.

Furthermore, the number of bonds per unit area for a particular confining pressure, can be shown to be constant and independent of particle size. This is because soils with larger particle size may contain fewer inter-particle contacts per unit volume. However, each contact forms a greater contact area between particles. In contrast, soils with smaller particle size contain more inter particle contacts per unit volume, but the corresponding contact area is smaller. The above can be shown by using Hertz's contact zone theory (Johnson, 1987); this is done below.

It is considered, for simplicity, soil particles to be represented by identical spheres arranged in a regular array (Figure 94a). For contact between two spheres with equal radius, the area of contact is a circle of radius a (Figure 94b);

$$a^3 = \frac{3F_f\phi}{16E^*} \tag{4.9}$$

where F_f is the applied force between two particles, ϕ is the particle size and

$$\frac{1}{E^*} = \frac{1-\upsilon_1^2}{E_1} + \frac{1-\upsilon_2^2}{E_2} \tag{4.10}$$

where E_1 & E_2 are the elastic moduli and υ_1 & υ_2 are the Poisson's ratios associated with each sphere. From the definition given in Equation 4.9, the contact area between two particles can be written as;

$$A_1 = \pi \left(\frac{3F_f \phi}{16E^*}\right)^{\left(\frac{2}{3}\right)} \tag{4.11}$$

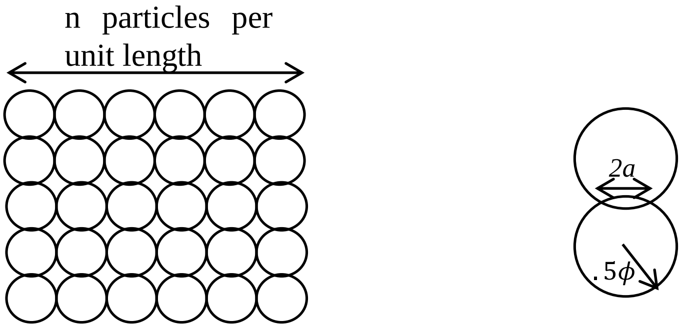

(a) (b)

Figure 94: (a) Regular assembly of spherical soil particles (b) contact zone between two particles

Let us assume the total normal stress applied on the surface is P, and the number of particles per unit length is n. Therefore, the applied force between two particles can be written as;

$$F_f = \frac{PA}{n^2} \tag{4.12}$$

where A is the total area of the particle assembly and n the number of particles in each direction. If a unit area is considered, then $A = 1$ and F_f becomes as;

$$F_f = \frac{P}{n^2} \tag{4.13}$$

If a unit length is assumed, due to the array being regular

$$n\phi = 1 \tag{4.14}$$

Substituting Equations 4.13 and 4.14 into Equation 4.11 gives

$$A_1 = \pi \left(\frac{3P}{16n^3 E^*}\right)^{\left(\frac{2}{3}\right)} \tag{4.15}$$

The total number of contacts per unit area is n^2. Therefore the total contact area per unit area of sample is given as;

$$A = \pi \left(\frac{3P}{16E^*}\right)^{\left(\frac{2}{3}\right)} \tag{4.16}$$

which is independent of the particle size ϕ. Moreover, it is predicted to vary with $P^{\left(\frac{2}{3}\right)}$ using Hertz theory.

Mitchell et al. (1969) proposed a linear relationship between the effective confining pressure and the number of inter-particle bonds based on experimental results. For a large value of applied stress, the hyperbolic sine in Equation 4.6 can be approximated by a simple exponential form. Therefore, the rate process equation becomes

$$\dot{\gamma} = K(t)\exp(\alpha D') \tag{4.17}$$

$$K(t) = \frac{2kT}{h}\exp\left(-\frac{U_0}{RT}\right)$$
$$\alpha = \frac{\lambda_l}{4SkT} \tag{4.18}$$

where D' is the applied deviator stress in triaxial conditions. Creep tests were carried out by applying step increments to the deviator stress. Parameter α is a constant for a given value of effective consolidation pressure and can be calculated from the slope of the stress vs log strain rate plot. With α known, the ratio λ_l/S can be calculated as a measure of the number of interparticle bonds (Mitchell et al., 1969). Three types of soil were tested under different values of effective consolidation pressure, water content, saturation (between saturated and completely dry) and OCR. Results show that normally consolidated San Francisco Bay mud gives 2.3×10^{13} bonds/N (bonds/unit area for a unit of applied consolidation pressure) (Figure 95). Furthermore, it was observed that the number of inter-particle bonds is a decreasing function of water content. The explanation of this was that effective stress decreases with water content leading to the reduction in number of bonds (nearly 100 times greater for dry than for wet clay). Finally, the number of bonds was found to be an increasing function of OCR values.

It was predicted from Hertz theory that S varies with $P^{\left(\frac{2}{3}\right)}$. Mitchell et al. (1969) found that S varies linearly with P. Possible reasons for this difference are listed below.

1. It was assumed that soil particles are spherical. In reality, soil particles may have different shapes depending on their mineralogy.
2. It was assumed that particles are arranged in a regular array form. In reality, particle arrangement will be more complex.

3. Hertz contact theory assumes elastic contact only. There is the possibility of plastic contacts existing between soil particles, which would change the force-area relationship.

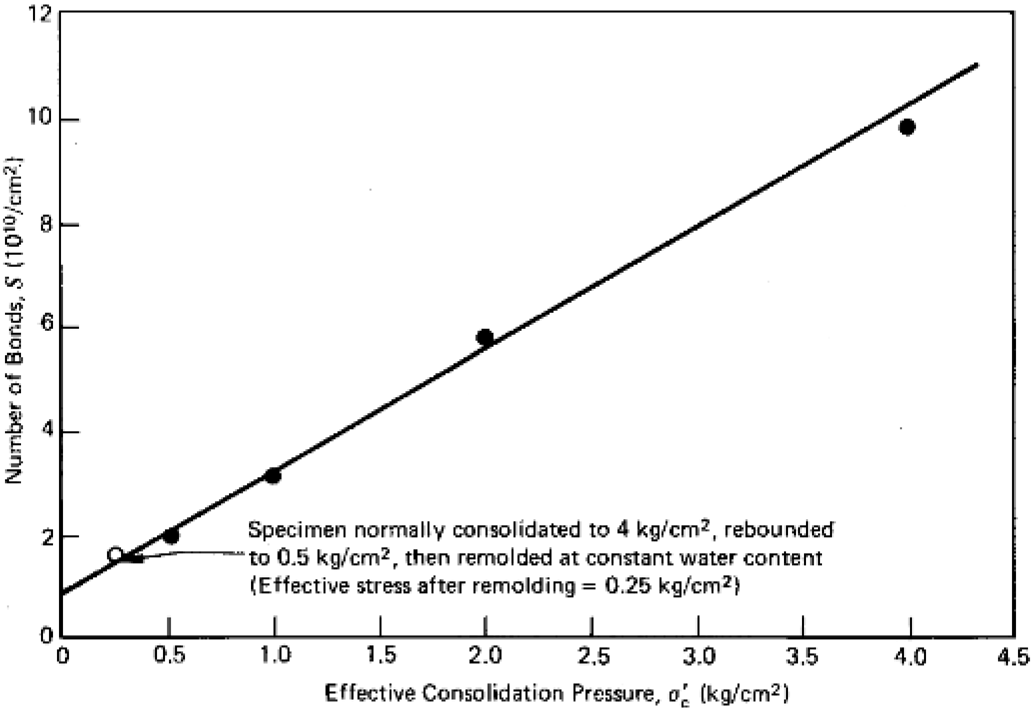

Figure 95: Number of interparticle bonds as function of consolidation pressure for normally consolidated San Francisco Bay mud (Mitchell et al., 1969)

4.4 Modelling a ring shear test using rate process theory

As a validation step of the above approach in isothermal conditions, the velocity of ring shear test was calculated using the rate process equation for different values of the applied shear stress. The results were compared with ring shear laboratory tests carried out by Tika and co-workers.

Tika et al. (1996) carried out ring shear tests on various types of soils. The tests were carried out with constant shear velocity and constant confining pressure. Shear stress (applied to maintain the constant velocity), and change in pore water pressure were measured as outputs. The experiments were carried out at two stages of speed, i.e. slow shearing (0.01-2.0 mm/min) and fast shearing (100-6000 mm/min). Additionally, the change in temperature of the specimen was also measured during fast shearing.

It is recognised that, in ring shear experiments, strain rate is controlled and shear stress is measured, whereas the rate process expression gives strain rate as a function of stress, so that it corresponds a process where the stress is controlled and the strain rate is taken as an output. Also, the rate process theory is meant to give predictions for steady state strain rates that correspond to constant values of temperature and shear stress. In the ring shear, although the strain rate is constant, shear stress varies during stages of the test before reaching a steady state. Despite these limitations, comparing rate process theory with ring shear experiments is a worthwhile exercise because these are the only data available where particular type of clay sheared and, at the same time, temperature is measured.

The displacement rate v (velocity) at the top of the shearing zone can be written as;

$$v = \dot{\gamma} Z_b \tag{4.19}$$

where Z_b is the thickness of the specimen and $\dot{\gamma}$ the strain rate (Equation 4.6) It was assumed that strain rate and applied shear stress are uniform throughout the deforming shear zone.

As mentioned earlier, the number of bonds per unit area is proportional to the applied confining pressure. Kuhn and Mitchell (1993) proposed the following expression for the number of bonds in terms of confining pressure.

$$S = S_1 \sigma'_c \tag{4.20}$$

Where, S_1 is the proportionality factor given by the number of bonds per unit area per unit of effective confining pressure. Mitchell et al. (1969) estimated the value of S_1 from different creep tests and it is constant for a given soil ranging from 1×10^8 to 1×10^{10} bonds/N. 3.6×10^8 was selected for the claystone material tested by Tika et al. (1996).

The absolute temperature was assumed as 300 K (i.e.26.85°C), $\lambda_l = 2.8 \times 10^{-10}$ m and $U_0 = 105$ kJ/mol in line with the values used by several other authors (Kuhn and Mitchell, 1993, Kwok and Bolton, 2010). The thickness of the shearing zone was selected as 11.2 mm. i.e. equal to the sample thickness. The vertical effective stress (σ'_c) was 495 kPa and the shear stress required to maintain constant shear strain rate at large strains (τ_{res}) was 50 kPa.

Using the above values in Equations 4.6 & 4.19, the displacement rate was obtained as 28.35 mm/min. This value is much lower than the displacement rate of 160mm/min maintained in this ring shear test. However, this is a preliminary validation in isothermal conditions, but the temperature is expected to play a role on shearing. This temperature rise would change the velocity in rate process equation 4.6. Therefore, a thermo-mechanical formulation for a shear zone using rate process theory is developed in the next section.

4.5 A thermo-mechanical formulation for a shear band

4.5.1 Heat Equation

As some heat can be expected to be produced during shearing, conditions will not be strictly isothermal and this may affect the behaviour of soil. To include this effect, energy balance was applied to the deforming shear zone in order to arrive at the heat equation. (Vardoulakis, 2002a);

$$\frac{\partial \theta}{\partial t} = \kappa_m \frac{\partial^2 \theta}{\partial z^2} + \frac{\tau \dot{\gamma}}{j(\rho C)_m} \qquad 4.21$$

In the above, the first term on the right hand side of the equation is a heat diffusion term, where κ_m is Kelvin's thermal diffusivity coefficient. Vardoulakis (2002a) recommended a constant value of κ_m equal to $1.47 \times 10^{-7} m^2/s$ for a soil water mixture. The second term is the heat generation term; it is assumed that all plastic work done inside the shear zone is converted to heat. $j(\rho C)_m = C_f$ is the thermal constant of the soil water mixture, taken equal to 2.85MPa/^{o}C (Vardoulakis, 2002a). τ is the applied shear stress and $\dot{\gamma}$ is the shear strain rate.

Although the expression for shear strain rate based on rate process theory depends on temperature, it was derived assuming isothermal conditions, i.e. that there is no heat flux through the material. Also, it explains soil deformation as movement of flow units between two successive, discrete equilibrium points. However, the heat diffusion equation can be applied to a material assuming that the heat diffuses through it in a continuous manner. In order to combine rate process theory with heat diffusion, the former should be derived for non-isothermal conditions; this will result to a highly non-linear and complex problem. Therefore, here the isothermal rate process shear stain rate equation is used as a first approximation. Provided the rate of change of temperature is not high, successive time steps can be treated as successive isothermal states with different values of temperature. This assumption will no more be valid, when the temperature rate becomes rapid as is expected immediately before failure.

On the basis of above description, the isothermal strain rate equation (4.6) is substituted in Equation 4.21. Thus, the final heat equation can be written as,

$$\frac{\partial T}{\partial t} = \kappa_m \frac{\partial^2 \theta}{\partial z^2} + \frac{\tau}{j(\rho C)_m} \times \frac{2k\theta}{h} \exp\left(-\frac{U_0}{R(\theta + 273)}\right) \times \sinh\left(\frac{\tau \lambda_l}{2Sk(\theta + 273)}\right) \qquad 4.22$$

The above equation can be solved numerically using a finite difference scheme with appropriate initial and boundary conditions.

4.5.2 Initial and boundary conditions

In ring shear experiments, all soils exhibit a residual stage at the end of the test, at which the applied shear stress remains almost constant (Tika et al., 1996, Tika and Hutchinson, 1999). However, before attaining the residual stage, the soil exhibits a peak and then a softening phase where the applied shear stress decreases (Figure 96). The temperature at the beginning of the residual stage was assumed as the initial condition for the above governing heat equation (Equation 4.22).

To find this temperature, heat balance was considered during the softening phase, assuming a linear reduction of the applied stress over time.

$$\frac{\partial \theta}{\partial t} = \kappa_m \frac{\partial^2 \theta}{\partial z^2} + \frac{(\tau_{ult} - mt)}{j(\rho C)_m} \times \frac{v}{Z_b} \qquad 4.23$$

300 K (i.e.26.85℃) which is the initial temperature of the ring shear system was assumed as the initial condition(θ_{ref1}) for equation 4.23. The temperature increase obtained during the softening phase was 0.42°C (Figure 97). This temperature value is used as the initial condition (θ_{ref}) for Equation 4.22 to model the residual phase. $(\theta_{ref} = \theta_{ref1} + \Delta\theta)$.

As boundary conditions, the temperature far from the shear band boundaries was taken constant, in-line with Vardoulakis (2002a). In summary, the initial and boundary conditions are;

$$\begin{aligned} \theta(\pm\alpha, t) &= \theta_{ref} \\ \theta(z, 0) &= \theta_{ref} \end{aligned} \qquad 4.24$$

The total spatial domain for the heat equation was set to 21 times the specimen thickness. This represents 10 times the specimen thickness above and below the sample. In practice, in a ring shear apparatus, the soil specimen is covered by ceramic or metal plates. However, for simplicity, same specimen soil properties are chosen to model the metal or ceramic plates.

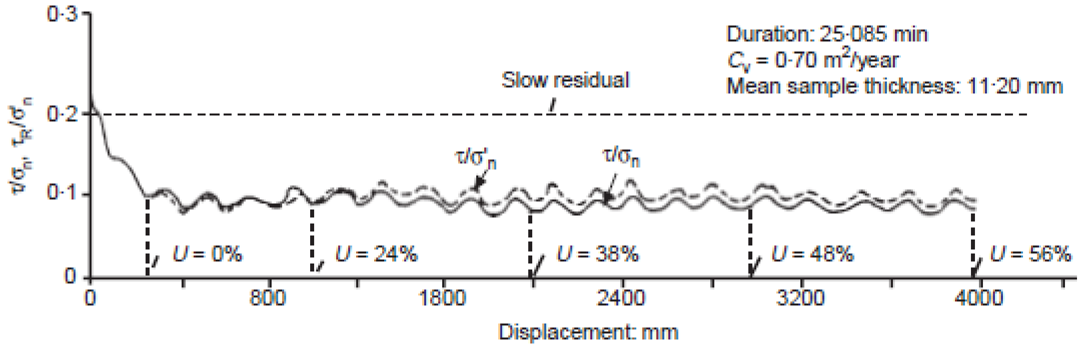

Figure 96: Results of fast ring shear test with 160 mm/min displacement rate (Tika et al., 1996)

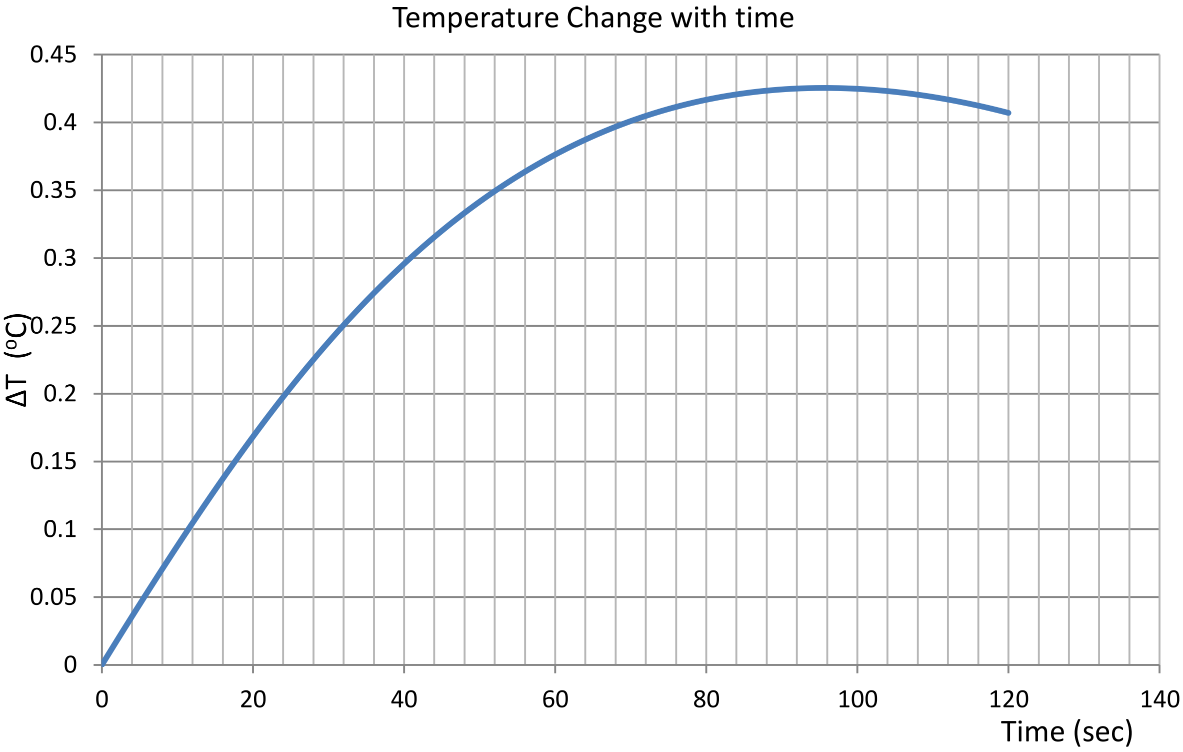

Figure 97: Temperature vs time at the mid of the shear zone during softening phase

4.5.3 Numerical results

Equations 4.22 & 4.23 are non-linear parabolic partial differential equations. To solve them a backward-time centred-space (BTCS) finite difference method was used.

The same parameters were used as in the isothermal formulation (Section 4.4). Temperature changes were calculated across the domain of the shear zone. Temperature profiles with depth for different times are given in Figure 98. Furthermore, temperature at the middle of the shear zone is plotted against time in Figure 99. The total temperature increment was calculated as 7^{o}C (Figure 99). The shear strain obtained from rate process theory depends on temperature. In Equation 4.6 all parameters are constant except temperature; therefore strain rate would increase throughout the shear zone due to temperature rise.

The temperature changes obtained from a fast ring shear test are in the range of 0.59 - 2.5 °C (Tika et al., 1996) which is less than the temperature predicted using this model (7°C). The model presented here considers 1-D heat diffusion, assuming adiabatic conditions in other two directions. However, in the ring shear apparatus there is a possibility that any heat produced would diffuse in all directions. Therefore the temperature rise would be lower than the predicted temperature rise using this model.

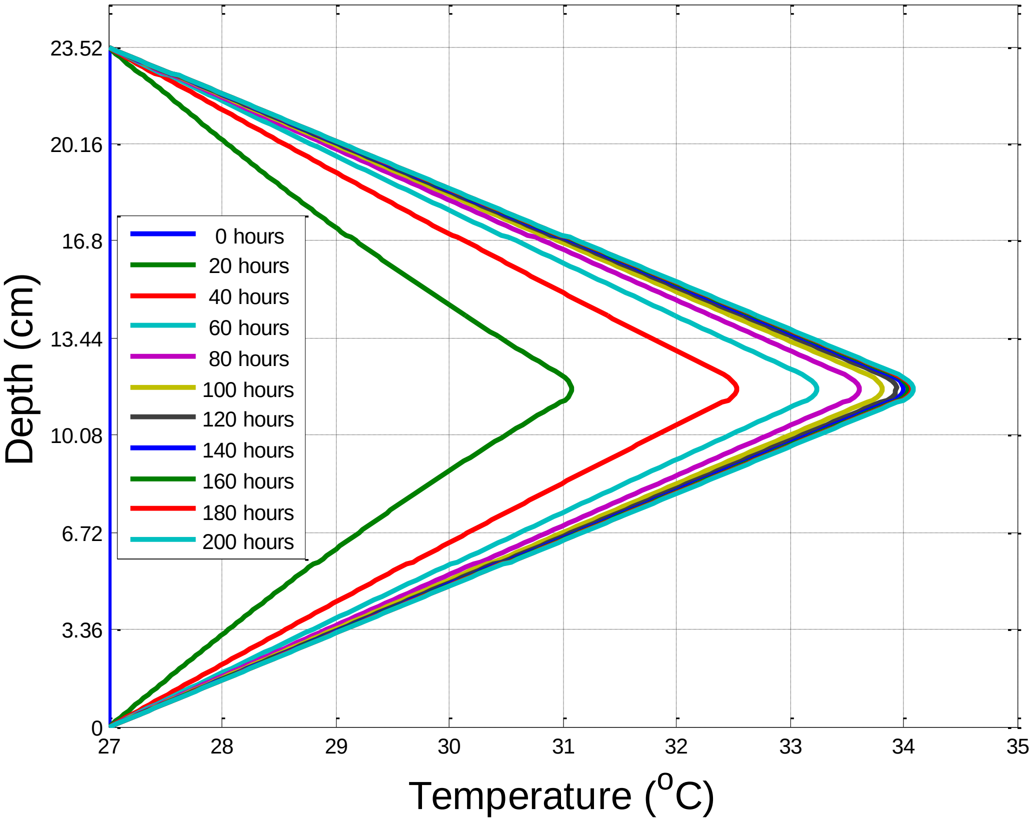

Figure 98: Temperature isochrones for applied shear stress of 50 kPa

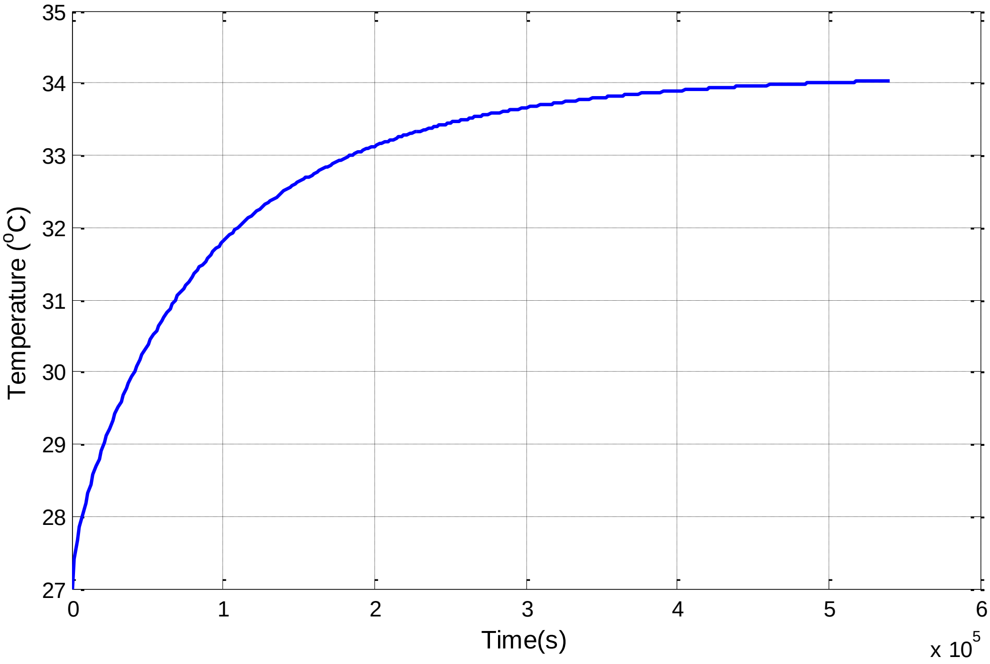

Figure 99: Temperature changes at the mid of the shear zone (50 kPa applied shear stress)

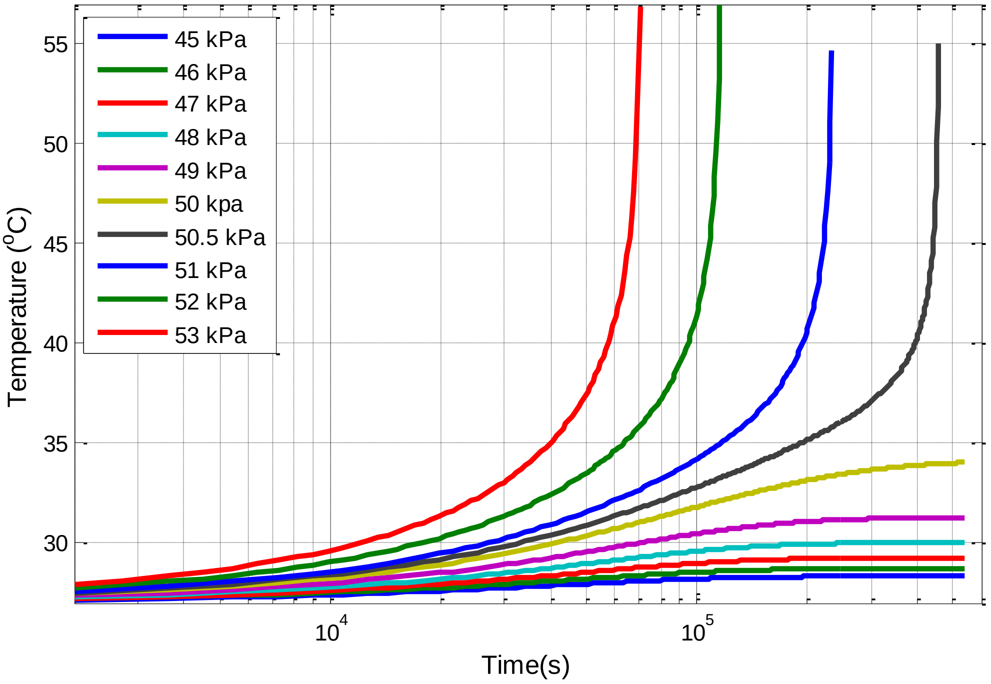

Figure 100: Temperature changes for different applied shear stresses

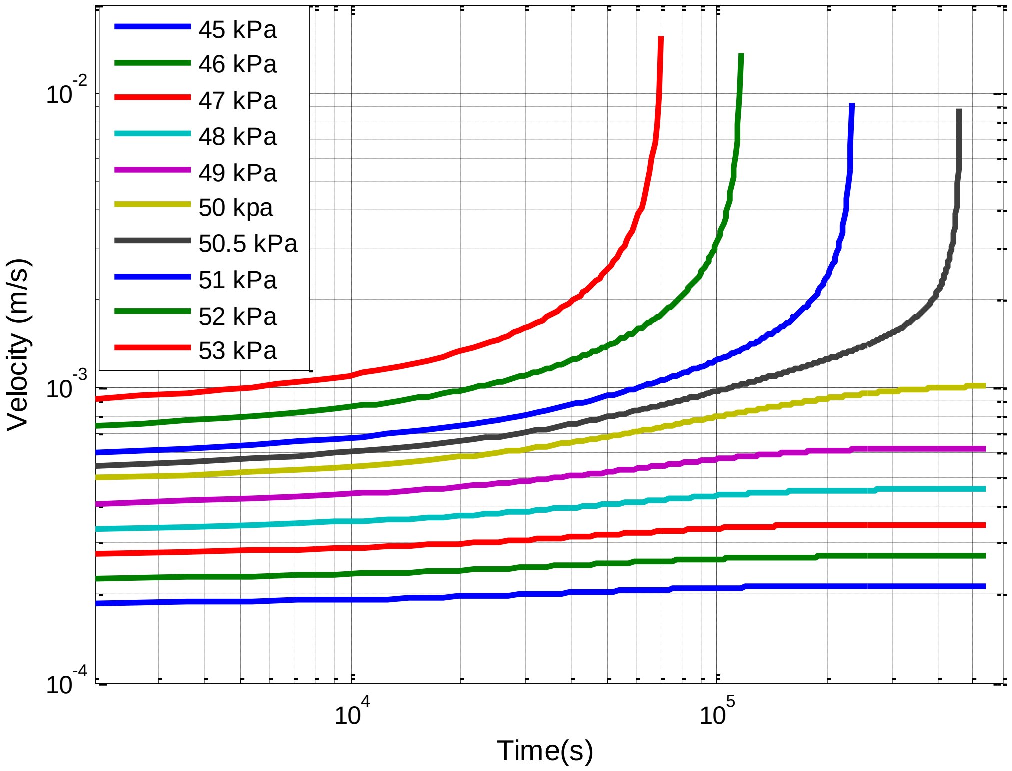

Figure 101: Velocity changes for different applied shear stresses

From the strain rate profile, the velocity at the top of the shear zone was calculated. For 50 kPa of applied shear stress, our model velocity reaches a maximum value of 61.06 mm/min then remains constant, which is still lower than the fast shearing ring shear displacement rate of 160 mm/min. However, it increased significantly compared to the value obtained for isothermal conditions.

This velocity cannot be directly compared to the ring shear test because, in the ring shear test, velocity was kept constant as it is a strain controlled process. In the model on the other hand, velocity increases with time as it is a stress controlled process.

Subsequently, the model was used to analyse a soil layer under different levels of applied shear stresses. The temperature at the mid-point and the velocity at the top of the shear zone are plotted against time in Figure 100 and Figure 101 respectively.

4.5.4 Discussion

The results show that applying a shear stress above 50 kPa gives blow-up in temperature and also unconstrained acceleration within a time frame of 50,000 seconds. Shear stresses lower than 50 kpa seem to lead to a steady state, where temperature and velocity stabilise.

Typically soil creep has three stages: primary, secondary and tertiary. The model presented here, can simulate secondary and tertiary creep as during these two phases the strain rate either increases or remains constant. Primary creep cannot be simulated, as during that stage the strain rate should decrease with time. Therefore, there should be an additional mechanism to be imposed to include primary creep. For this purpose, Mitchell and co-workers proposed two assumptions (Mitchell, 1964, Mitchell and Campanella, 1964). The first one is that the free activation energy is time dependent and increases with time. The second one is that a time dependent factor *(X)* must be included before the strain rate equation to describe the structural changes taking place during primary creep. However, these two assumptions are not supported by direct observations from experiments. Feda (1989) on the other hand proposed that primary creep occurs due to changes in the number of inter-particle bonds with time; this can be explained as an increase in the number of contacts with time due to particle rearrangement.

As mentioned earlier, ring shear tests were carried out with different speeds at different stages (Tika, 1989, Tika et al., 1996, Tika and Hutchinson, 1999). The results show that when the speed of shearing increases, the change of residual strength can be of any of the three following types (Tika et al., 1996).

1. Constant residual strength irrespective of rate of displacement: neutral effect.
2. Significant drop in residual strength with increasing displacement rate: negative rate effect/ rate softening effect
3. Increase in residual strength with increasing displacement rate: positive rate effect/ rate hardening effect

These types of behaviour are attributed to viscous effects and structural changes during shearing of soil. However, a particular soil type can exhibit more than one of the above effects depending on the level of normal effective stress. If the normal effective stress σ_c' is reduced, the behaviour changes from neutral to softening. A summary of observed rate dependent behaviour is given in Figure 102. Negative rate dependent phenomena cannot be captured by the model presented because temperature either increases or remains constant over time. Therefore the strain rate and the velocity follow the same trends. Additional assumptions or mechanisms would be needed to cover the entire range of creep behaviour observed in soils.

A different issue is the shear band thickness, which plays an important role. Many authors proposed different values for the shear band thickness. While soil is in creep, initially the specimen deforms uniformly across its thickness, however progressively strains localise in a narrow zone (strain localization). Vardoulakis (2002a) proposed a shear band thickness of 1.4 mm based on the experimental evidences on kaolin specimen (Morgenstern and Tchalenko, 1967) and on Vaiont clay (Tika and Hutchinson, 1999).

In the simulations presented here the thickness was assumed as 11.2 mm which is the whole thickness of a ring shear specimen. The stain rate profile, at the later stage of deformation (17.5-19.5 hours), is given in Figure 103. Observing the strain rate profile, initially the strain rate is constant across the shear band, but subsequently increases at the middle of the shear zone much more rapidly than at the boundaries. This shows that a level of strain localization develops as shearing progresses, as due to frictional heating the temperature at the middle of the shear band is higher than at the boundaries. Therefore heat dissipation progressively localises into a shrinking zone inside the shear band, and so does the deformation. If the shear zone thickness increases, the time to reach stain localization into a particular thinner zone will also increases. Therefore the assumption of “thick” shear zone is inconsistent with the eventual strain localization in to a thinner band.

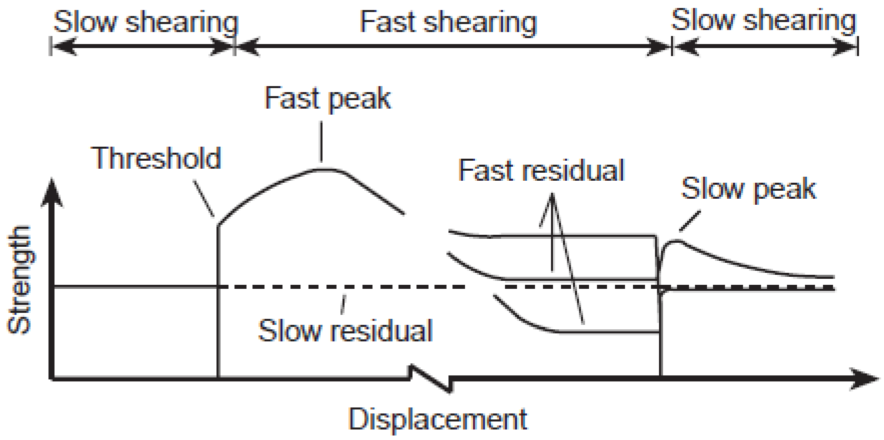

Figure 102: Summary of the observed rate-dependent phenomena for residual strength (After Tika et al., 1996)

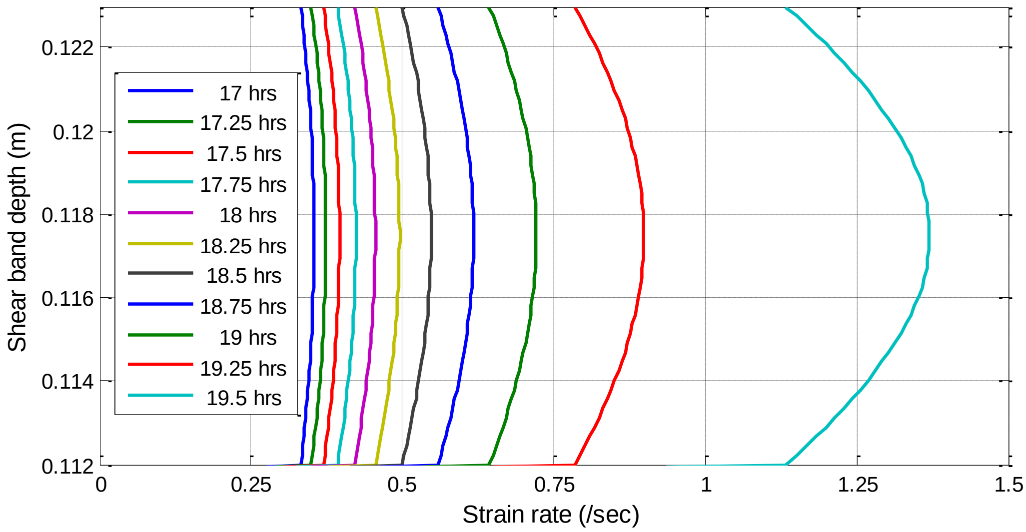

Figure 103: Shear strain rate profile for applied shear stress 53 kPa

4.6 Landslide model

In the previous sections a thermo mechanical formulation for a shear band was developed. In this section, a landslide model is developed that includes thermal pressurization and the dynamics of the slide. The model is then used to attempt a back analysis of the Vaiont slide.

4.6.1 Modified heat equation

When thermo mechanical formulation is used, progressive strain localization is observed, which gives a non-linear strain rate and velocity profile inside the shear zone. However, it was observed that the velocity profile is very close to linear and deviates slightly from a straight line as seen in Figure 104 . For simplicity, in this landslide formulation, an average linear velocity profile is assumed as shown in Figure 105.

With the assumption of a linear velocity profile inside the shear band, the heat equation with modified dissipation term can be written as;

$$\frac{\partial \theta}{\partial t} = \kappa_m \frac{\partial^2 \theta}{\partial z^2} + \frac{\tau}{j(\rho C)_m}\left(\frac{v_d}{Z_b}\right) \qquad 4.25$$

In the above, in addition to all other parameters given in section 4.5.1, Z_b is the thickness of the shear band and v_d is the velocity of the slide. An expression that describes v_d will be derived in Section 4.6.3.

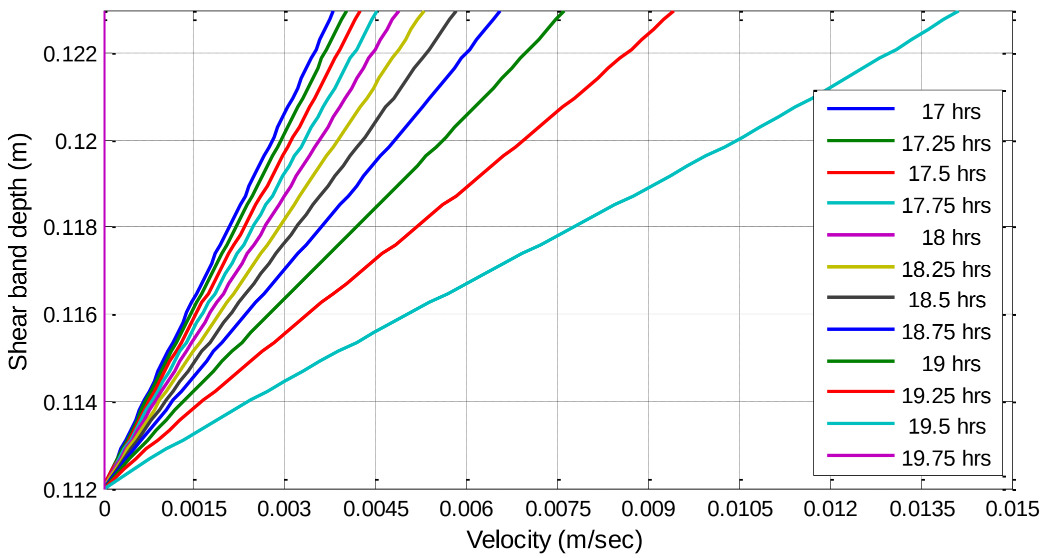

Figure 104: Velocity profile inside for thermo mechanical formulation (applied shear stress of 53 kPa)

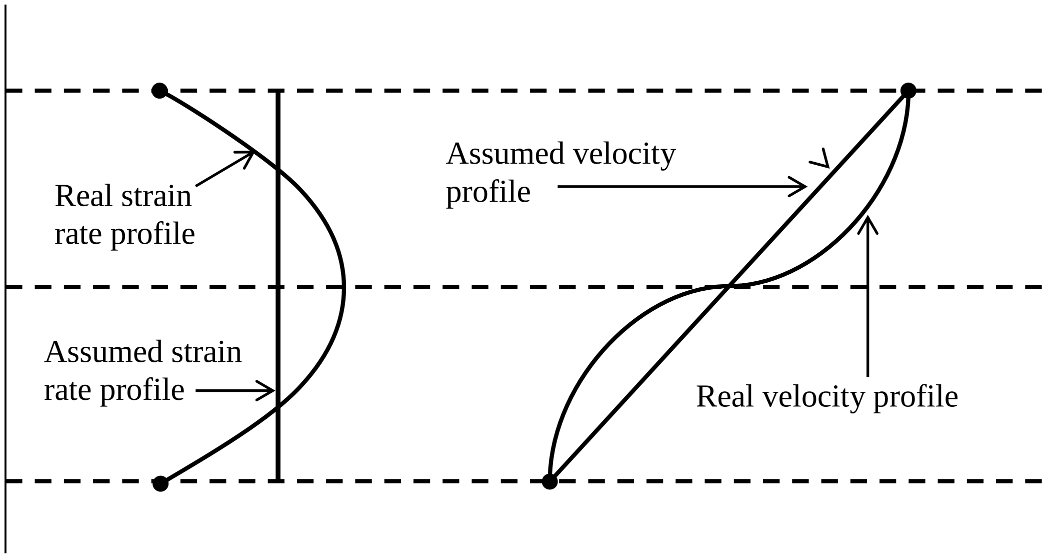

Figure 105: Stain rate and velocity profile (real and linear) inside the shear band

4.6.2 Pore pressure equation

The pore pressure equation gives the excess pore pressure inside the shear band and its surroundings. The same equation given in section 3.3 is used here, i.e.

$$\frac{\partial u}{\partial t} = \frac{\partial}{\partial z}\left(c_v \frac{\partial u}{\partial z}\right) + \lambda_m \frac{\partial \theta}{\partial t} \qquad 4.26$$

In the above, c_v and λ_m are the consolidation pressurization coefficients as discussed in sections 3.3.1 and 3.3.2 respectively.

4.6.3 Dynamic equation

The dynamic equation describes the velocity of landslide. For simplicity, a block on an infinite slope is assumed here in order to derive the dynamic equation.

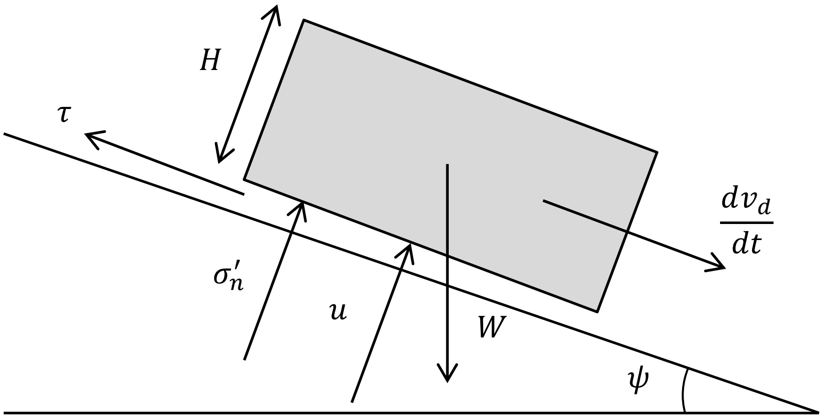

Figure 106: Schematic diagram for block on infinite slope (rate process theory)

With reference to Figure 106, the dynamics of the block sliding on a slope can be written as;

$$\frac{dv_d}{dt} = g\left(\sin\psi - \frac{\tau}{\gamma_e H}\right) \qquad 4.27$$

where, v_d is the velocity of the block, ψ is the slope angle, H is the block thickness, γ_e is the effective density of the soils $(\gamma_s - \gamma_w)$ and τ is the shear stress acting on the block. Recalling the rate process equation (4.6)

$$\dot{\gamma} = \frac{2kT}{h}\exp\left(-\frac{U_0}{RT}\right) \times \sinh\left(\frac{\tau\lambda_l}{2SkT}\right) \qquad 4.28$$

For values of $x \geq 2$, $\sinh(x)$ can be approximated as $(1/2)\exp(x)$. In the above rate process formulation, the value of $\frac{\tau\lambda_l}{2SkT}$ lies in the range between 8 and 20, so Equation 4.28 can be written as;

$$\dot{\gamma} = \frac{kT}{h}\exp\left(-\frac{U_0}{RT}\right)\exp\left(\frac{\tau\lambda_l}{2SkT}\right) \qquad 4.29$$

By assuming a linear velocity profile inside the shear band, the shear strain rate can be written as;

$$\dot{\gamma} = \frac{v_d}{Z_b} \qquad 4.30$$

where Z_b is the thickness of the shear band. Solving 4.29 for shear stress τ gives;

$$\tau = \frac{S}{F_a}\ln\left(\frac{\dot{\gamma}}{F_b}\right) \qquad 4.31$$

In the above, S is number of bonds per unit area, which is a function of effective normal stress as in Equation 4.20, and F_a and F_b temperature dependent coefficients given as

$$F_a = \frac{\lambda_l}{2kT} \quad 4.32$$

$$F_b = \frac{kT}{h}\exp\left(-\frac{U_0}{RT}\right) \quad 4.33$$

Substituting Equation 4.31 into Equation 4.27 gives

$$\frac{dv_d}{dt} = g\sin\psi - \frac{g}{\gamma_e H F_b} S\ln\left(\frac{v_d}{Z_b}\frac{1}{F_a}\right) \quad 4.34$$

Therefore the dynamic equation becomes

$$\frac{dv_d}{dt} + \frac{g}{\gamma_e H F_b} S(\sigma_n')\ln(v_d) = g\sin(\psi) + \frac{g}{\gamma_e H F_b} S(\sigma_n')\ln(F_a Z_b) \quad 4.35$$

In the above, $\gamma_e H$ is the effective weight per unit area, and this can be written as

$$\gamma_e H = \frac{\sigma_{n0}'}{\cos\psi} \quad 4.36$$

where σ_{n0}' is the initial effective normal stress acting on the slide. Substituting 4.36 onto 4.35 gives,

$$\frac{dv_d}{dt} + \frac{g(\cos\psi)}{\sigma_{n0}' F_b} S(\sigma_n')\ln(v_d) = g\sin(\psi) + \frac{g(\cos\psi)}{\sigma_{n0}' F_b} S(\sigma_n')\ln(F_a Z_b) \quad 4.37$$

4.6.4 Numerical results for the Vaiont slide

In summary, the landslide model contains heat, pore pressure and dynamic equation as follows;

$$\frac{\partial\theta}{\partial t} = \kappa_m\frac{\partial^2\theta}{\partial z^2} + \frac{\tau}{j(\rho C)_m}\left(\frac{v_d}{Z_b}\right) \quad 4.38$$

$$\frac{\partial u}{\partial t} = \frac{\partial}{\partial z}\left(c_v\frac{\partial u}{\partial z}\right) + \lambda_m\frac{\partial\theta}{\partial t} \quad 4.39$$

$$\frac{dv_d}{dt} + \frac{g\cos\psi}{\sigma_{n0}' F_b} S(\sigma_n')\ln(v_d) = g\sin(\psi) + \frac{g\cos\psi}{\sigma_{n0}' F_b} S(\sigma_n')\ln(F_a Z_b) \quad 4.40$$

The above system of equations (4.38, 4.39 and 4.40) will be solved numerically to determine the evolution of excess pore pressure, temperature and the slide velocity. The discretisation of Equations 4.38 and 4.39 is carried out same as in Chapter 3. Equation 4.40 is a first order differential equation and is discretised using the backward Euler method.

The initial and boundary conditions were taken as follows;

$$\begin{aligned} &\theta(\pm\alpha, t) = \theta_{ref} = 12.5℃ \\ &\theta(z, 0) = \theta_{ref} = 12.5℃ \\ &u(\pm\alpha, t) = 0 \end{aligned} \quad 4.41$$

$u(z, 0) = 0$

The initial condition for the velocity was calculated using the initial shear stress τ_0 at the onset of sliding as:

$$v_d(t = 0) = F_a \exp\left(F_b \frac{\tau_0}{S}\right) Z_b \qquad 4.42$$

The solution of the system of finite difference equations is not straight forward; it is a non-linear system and hence an iterative procedure with an appropriate initial guess needs to be employed. MATLAB numerical software was used to solve the non-linear equations using an in-built algorithm, fsolve. The initial guess used is the solution of the previous time step, or the initial conditions for the first time step.

The system of equations was solved with the stress state obtained from the Vaiont slide (Hendron and Patton, 1985). The spatial domain for the diffusion equations was set to 20 times the shear band thickness. As mentioned earlier, the BTCS is an unconditionally stable finite difference scheme allowing for large time steps to be used. The time step between 10 and 10000 sec were used depending on the total time duration of the landslide process. Subsequently, the value of the rate process parameters was varied within reasonable ranges (Mitchell and Soga, 2005) to investigate the behaviour of the model.

First, an analysis was carried out using average parameter values given in Mitchell et al. (1968). This will be hereafter referred to as the Base line case. Nearly 3 years before the catastrophic collapse of the Vaiont slide, creep velocity was recorded as approximately 1-2.5 mm/day (Müller, 1964). Creep parameters were chosen to match this velocity, which are in the reasonable range of parameters reported in Mitchell et al. (1968) as follows;

$U_0 = 128.5 \frac{kJ}{mol}$

$S_0 = 1.1 \times 10^9 \frac{bonds}{m^2 pa}$

$\lambda_l = 2.8 \times 10^{-10} m$

Furthermore, heat and pore pressure parameters, shear band thickness and average slope angle are chosen in line with Vardoulakis (2002a) as follows;

$Z_b = 1.4 mm$

$\kappa_m = 1.45 \times 10^{-7} m^2 s^{-1}$

$\psi = 22°$

$c_v = 7.5 \times 10^{-8} m^2 s^{-1}$

$\lambda_m = 0.012 Mpa/°\mathrm{C}$

The initial stress state was obtained from Hendron and Patton (1985) as:

$\tau_0 = 0.976 MPa$

$\sigma'_{n0} = 2.380 MPa$

The entire spatial domain was divided in to 200 grid points and temperature and pore pressure were computed at the each grid point.

4.6.4.1 Results for base line case

Figure 107 presents temperature isochrones across the shear band and its surroundings. The time evolution of temperature at the middle of the shear band is given in Figure 108. The pore pressure isochrones and the time evolution of pore pressure at the middle of the shear band are illustrated in Figure 109 and Figure 110 respectively. The maximum temperature rise is practically zero (2×10^{-4}°C) and so is the maximum excess pore pressure that develops (1Pa, dropping to zero after 8000 sec). The velocity plot Figure 111 shows that, after a very short transient period, the block is predicted to maintain a steady state of creep at 1mm/day. The displacement plot Figure 112 shows that the displacement increases linearly with time as expected for a constant velocity.

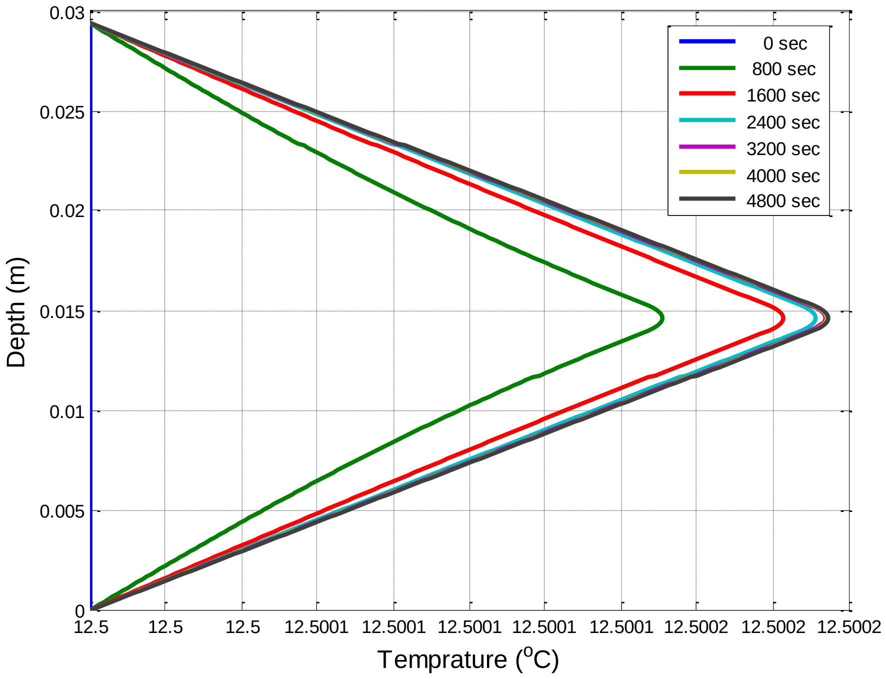

Figure 107: Temperature isochrones within the shearband and its surroundings (Base line case)

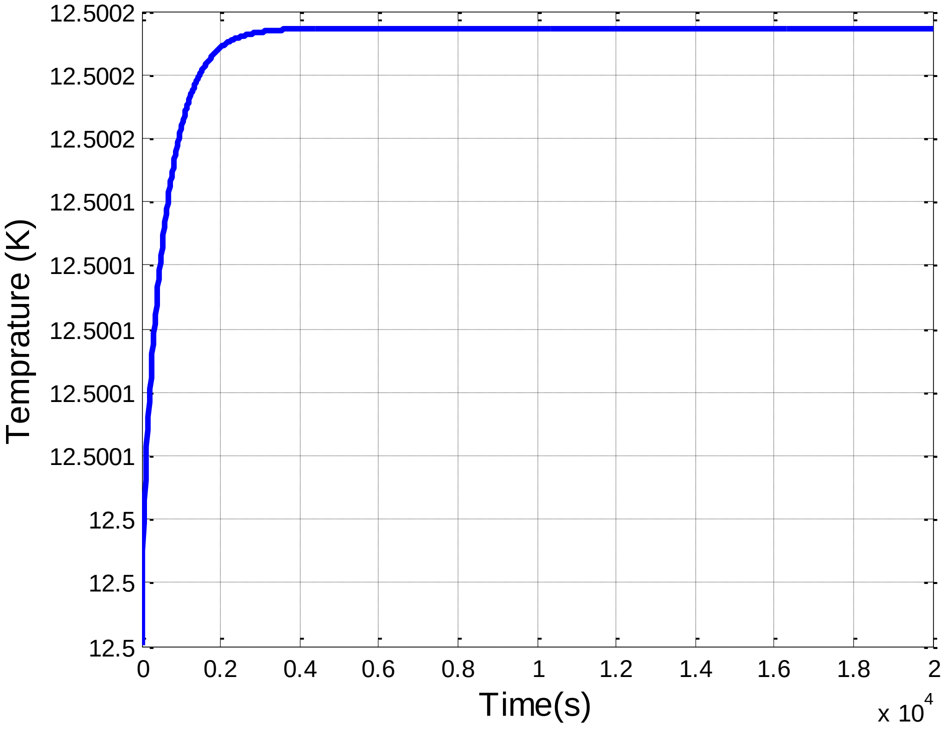

Figure 108: **The time evolution of temperature at the middle of the shear band (Base line case)**

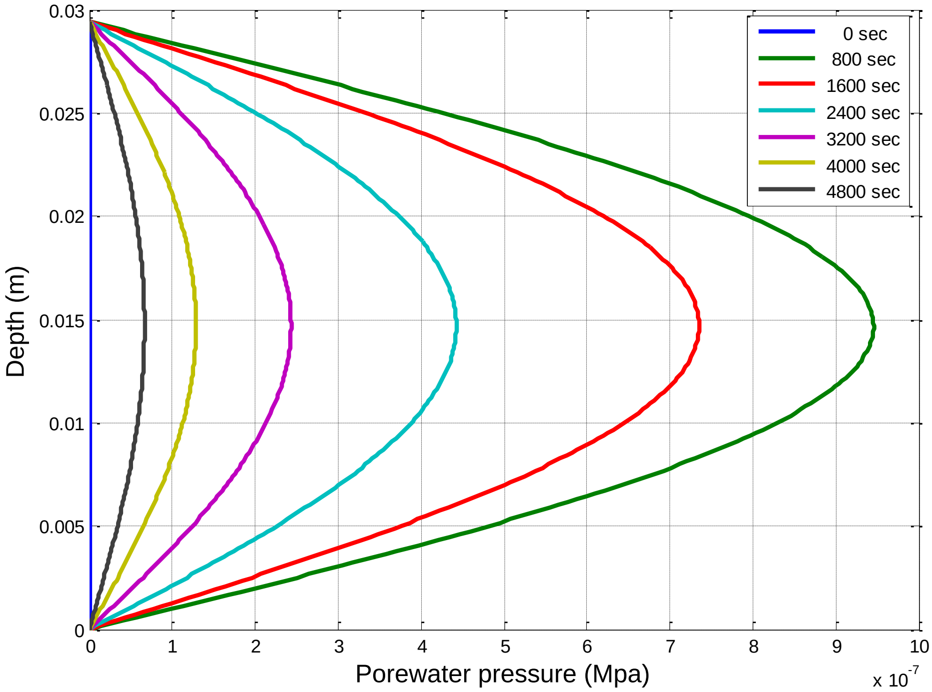

Figure 109: **Excess pore water pressure isochrones within the shearband and its surroundings (baseline case)**

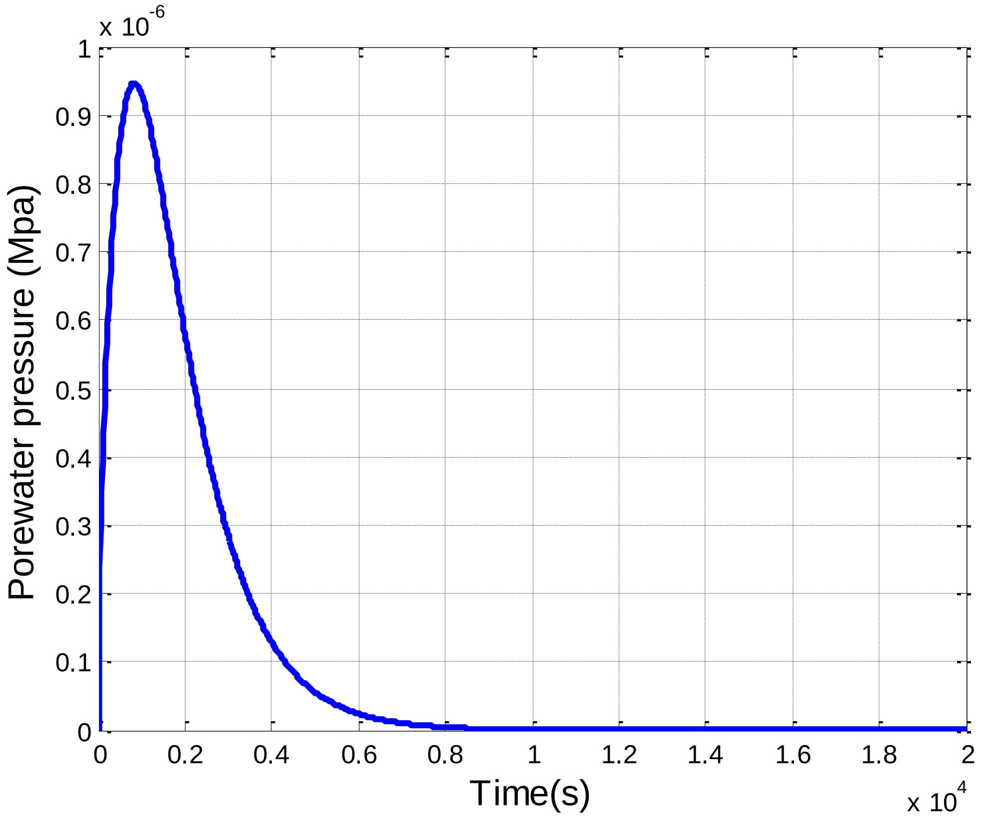

Figure 110: The time evolution of excess pore pressure at the middle of the shear band (Base line case)

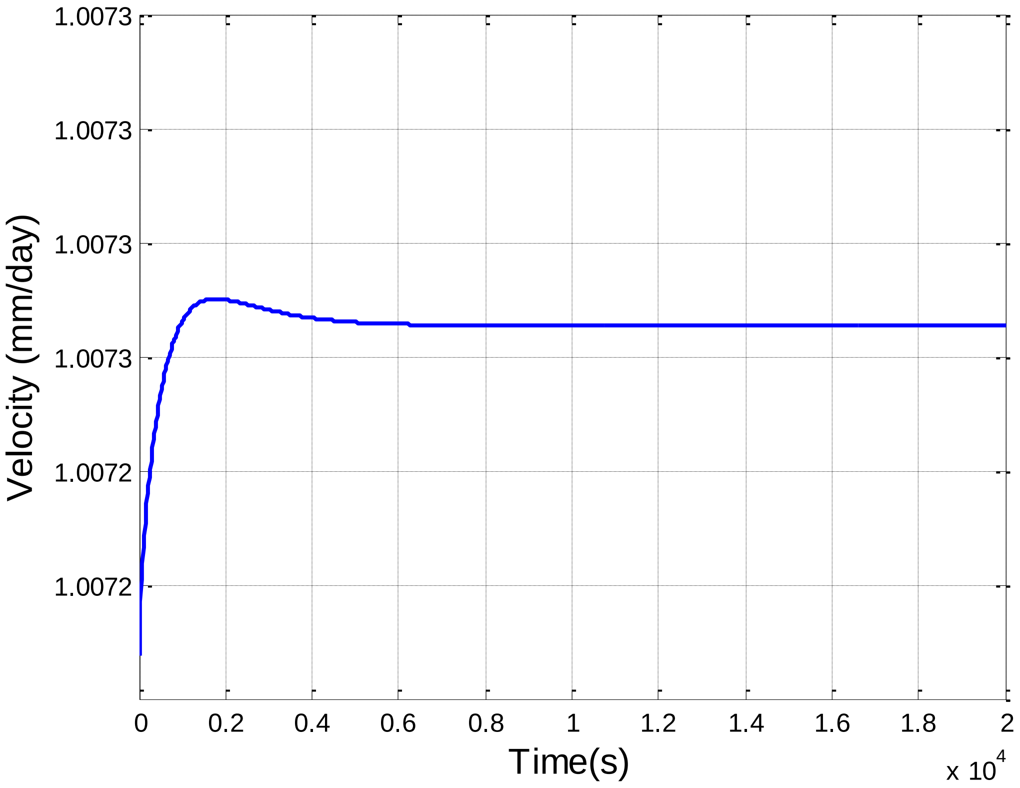

Figure 111: Plot of slide velocity (Base line case)

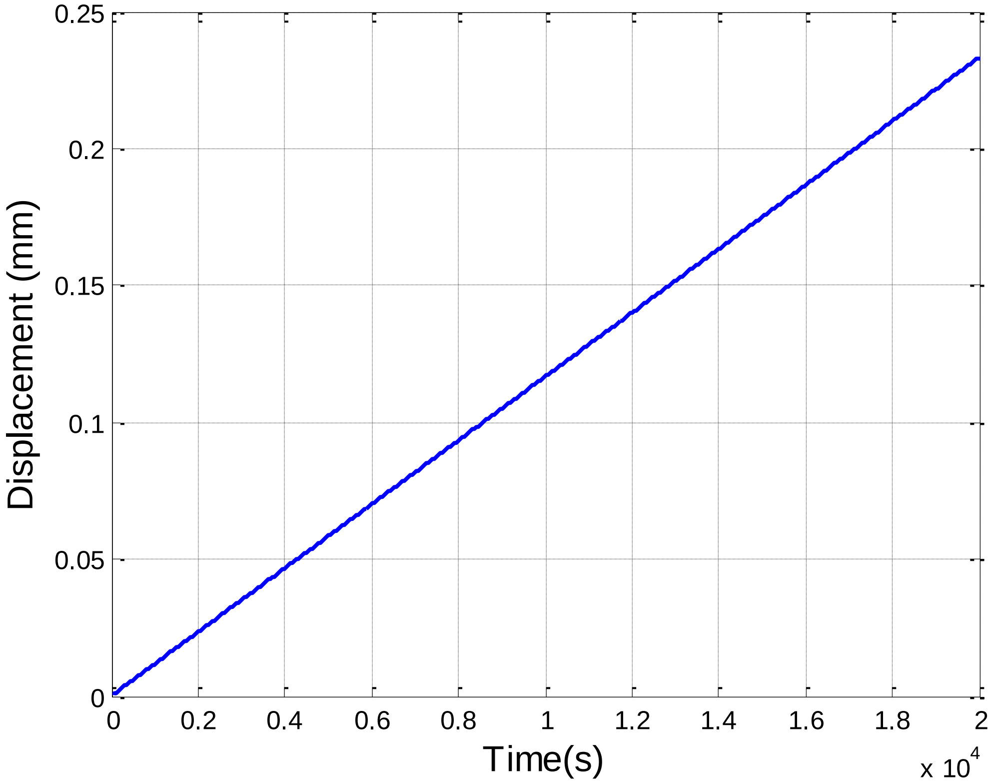

Figure 112: Plot of slide displacement (baseline case)

4.6.4.2 Results for different initial velocities

In the above subsection, results for the base line case were presented. To investigate the possible transition from creep to a catastrophic phase the activation energy was varied; this meant a different initial velocity, consistent with Equation 4.42. The activation energies are varied between 107 kJ/mol and 102 kJ/mol which are within the range of values reported in Mitchell et al. (1969). The temperature at the middle of the shear band for the initial velocities investigated is presented in Figure 113. The pore pressure at the middle of the shear band is presented in Figure 116 and the corresponding velocity plots in Figure 120. It can be clearly seen that, for the parameters used here, an initial velocity above about 0.2 mm/sec leads to a catastrophic phase whereas an initial velocity lower than 0.2mm/sec leads to steady state. Temperature isochrones for the lowest and highest chosen initial velocities are presented in Figure 114 and Figure 115 respectively and corresponding pore water pressure isochrones are shown in Figure 117 (0-800sec for 0.1 mm/sec), Figure 118 and Figure 119. Temperature and pore water pressure localization inside the shear band is clearly visible during the catastrophic phase.

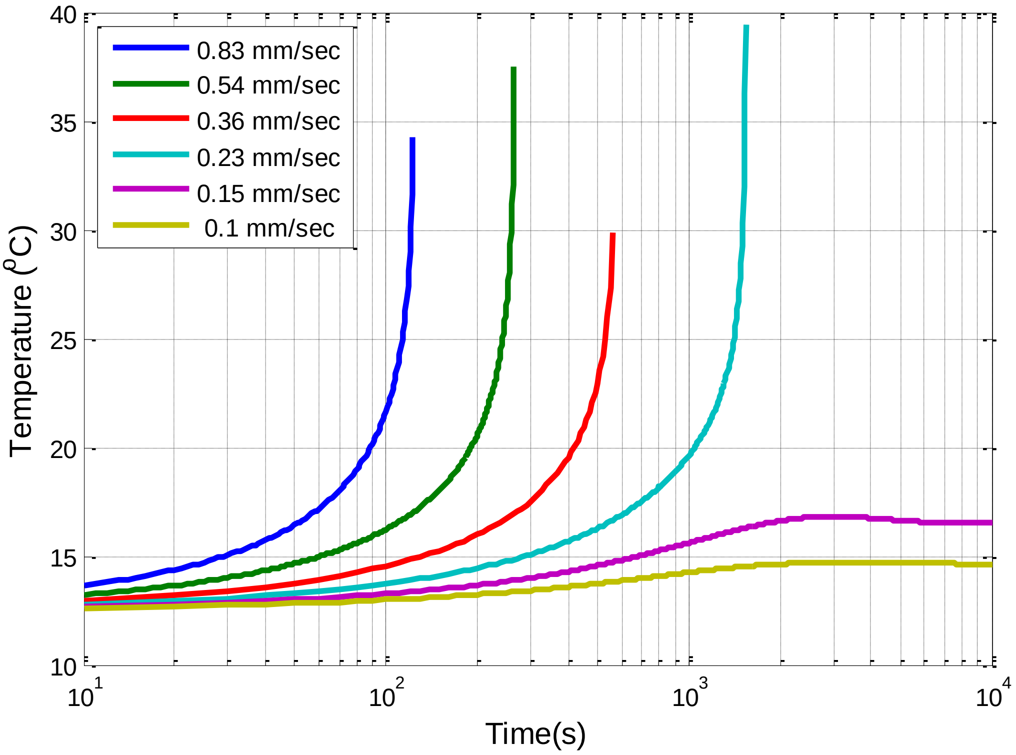

Figure 113: Temperature at middle of the shear band for different initial velocities

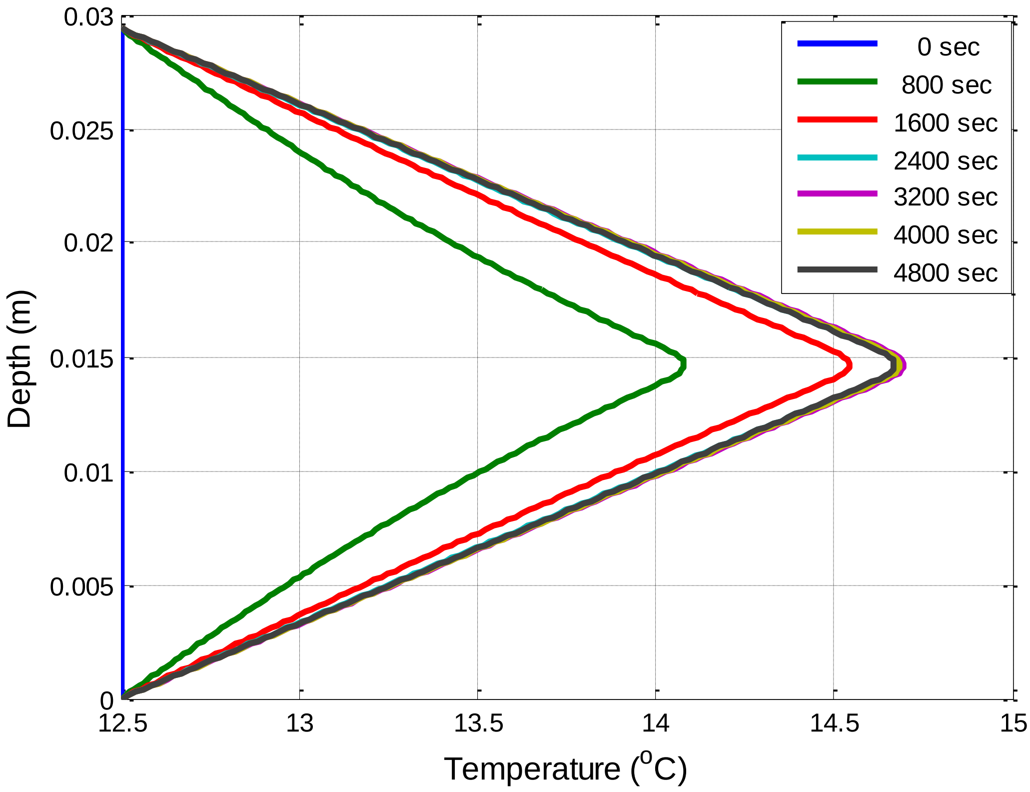

Figure 114: Temperature isochrones for the initial velocity of 0.10 mm/sec

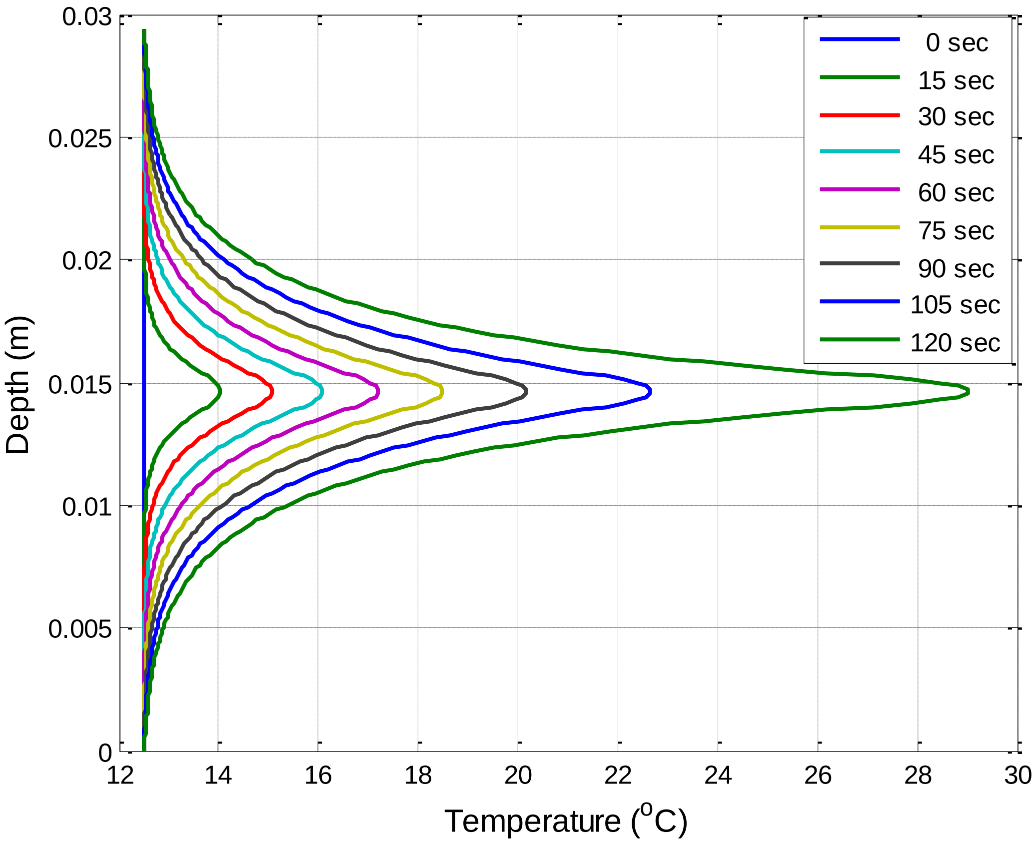

Figure 115: Temperature isochrones for the initial velocity of 0.83 mm/sec

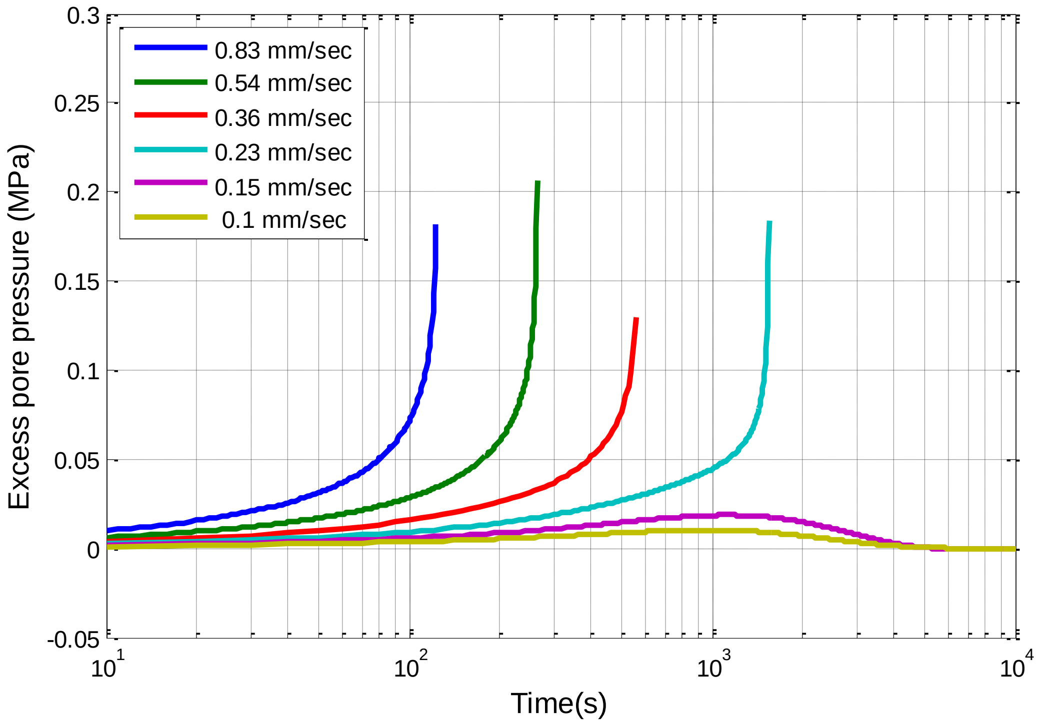

Figure 116: Excess pore pressure at middle of the shear band for different initial velocities

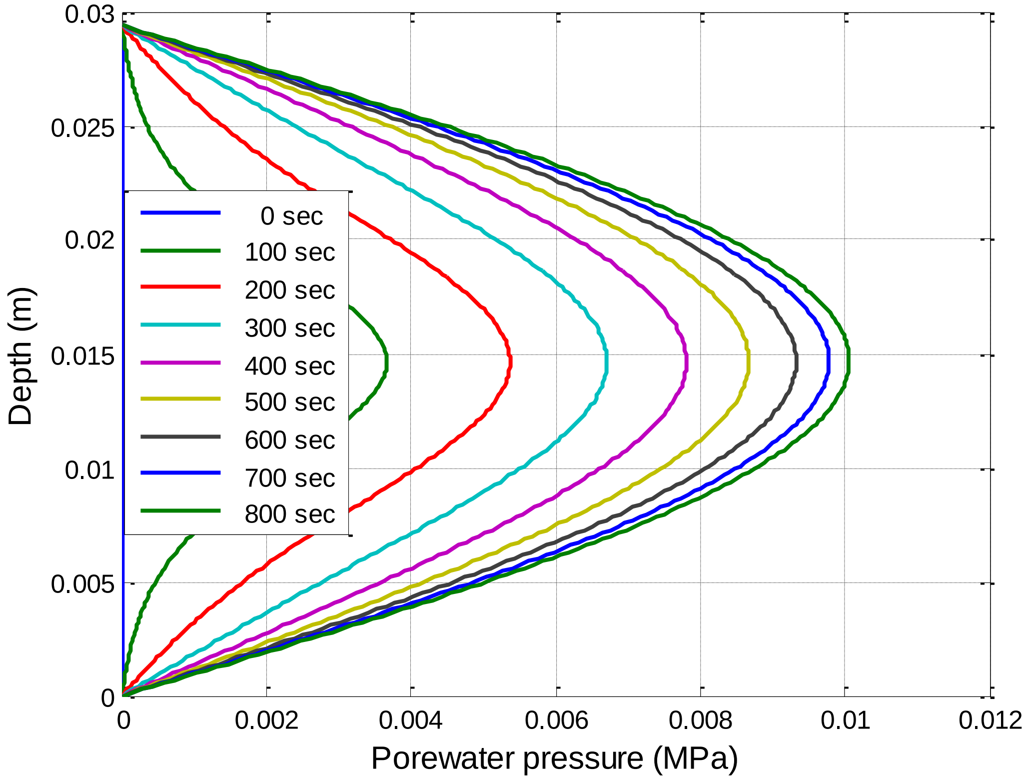

Figure 117: **Excess pore pressure isochrones for the initial velocity of 0.100 mm/sec (first 800sec)**

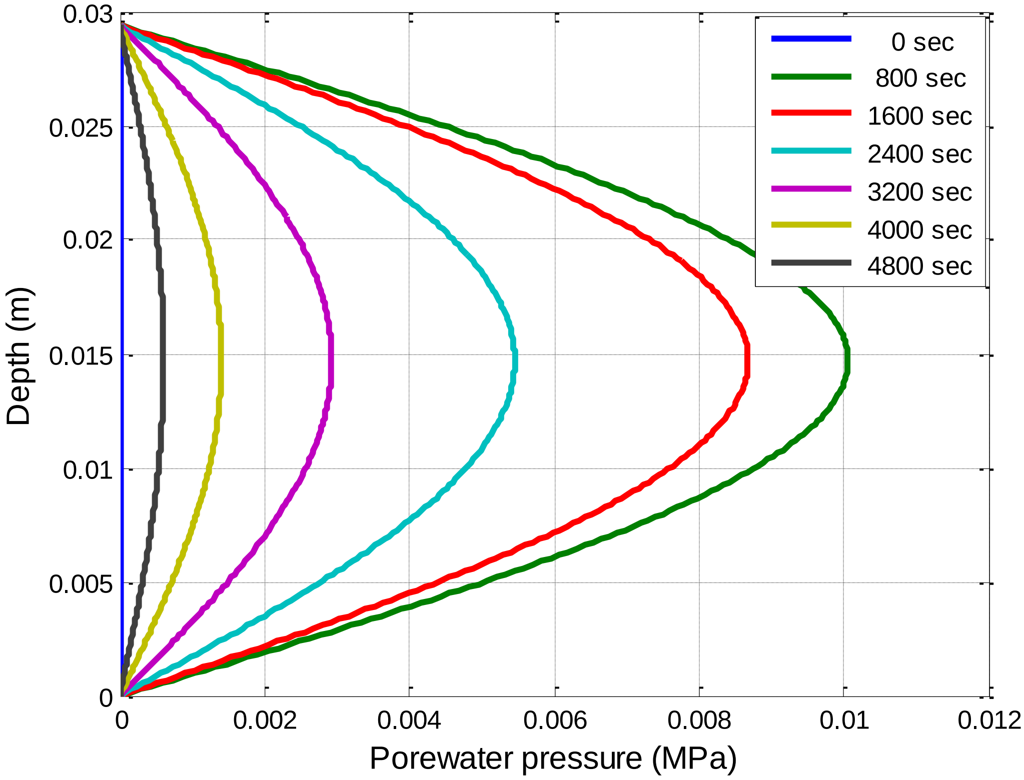

Figure 118: **Excess pore pressure isochrones for the initial velocity of 0.100 mm/sec**

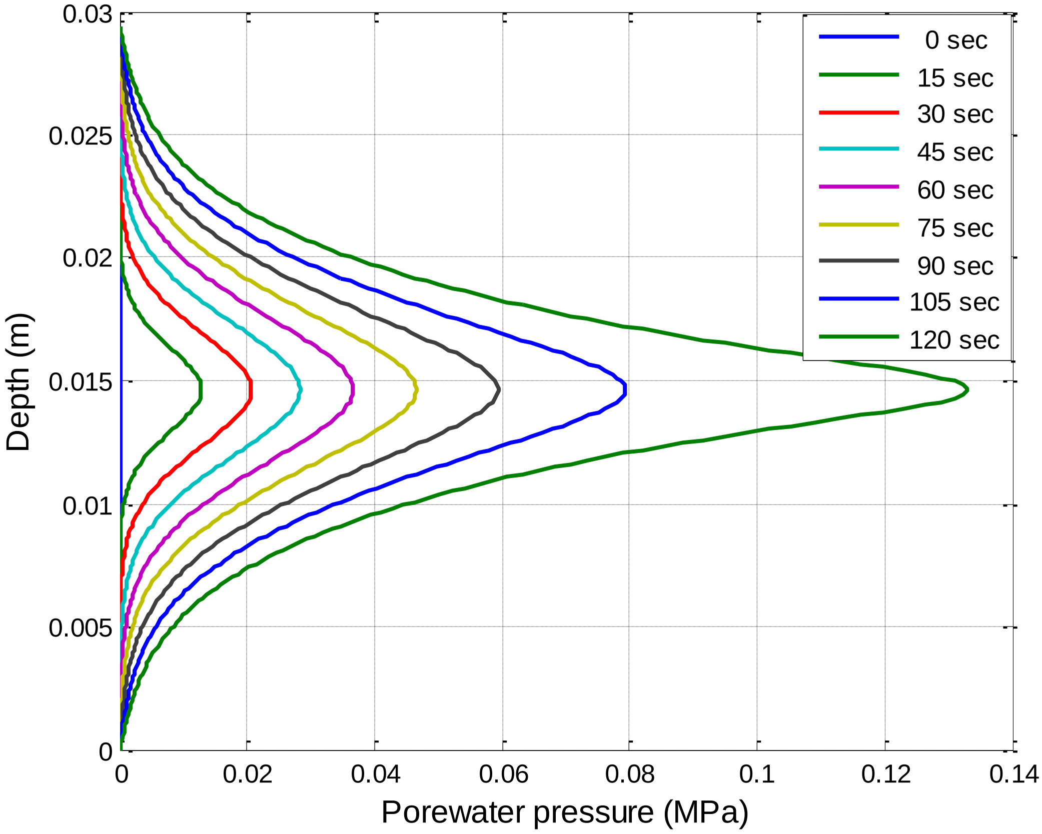

Figure 119: Excess pore pressure isochrones for the initial velocity of 0.83 mm/sec

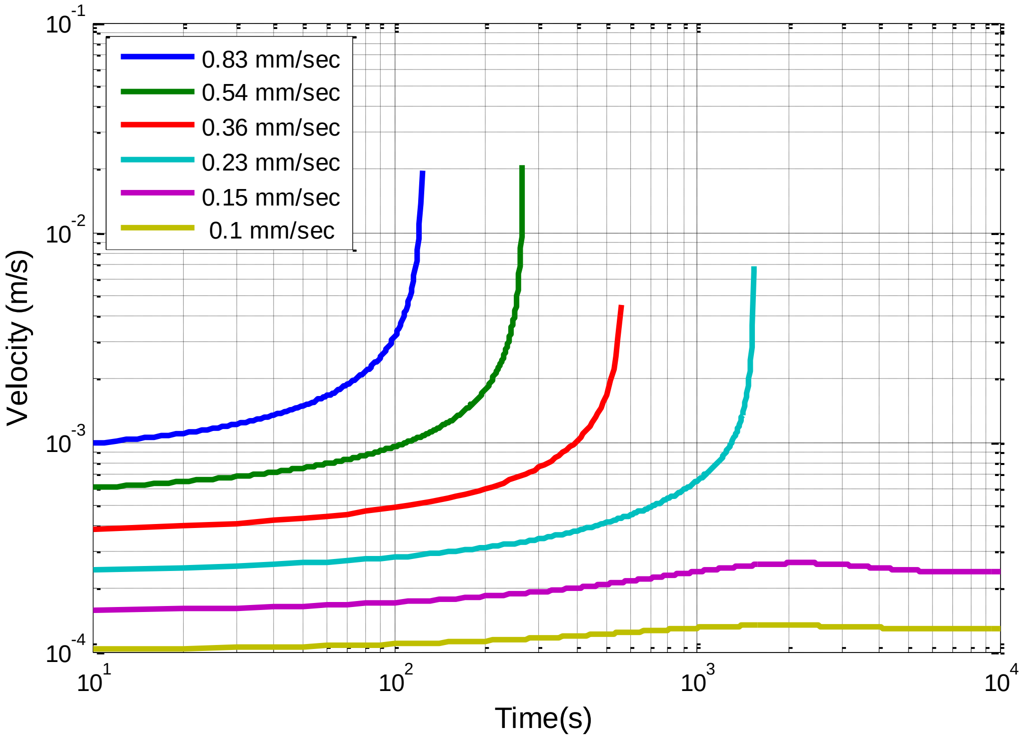

Figure 120: Velocity plot for different initial velocities

4.6.5 Influence of the size of the modelled spatial domain

In the above section, the results for initial velocities of 0.15mm/sec and 0.1mm/sec and baseline (1mm/day) predict a steady state of creep with constant velocity after a short transient period (Figure 111 and Figure 120). For these particular cases, temperature rise is much lower than for the cases with higher initial velocity (Figure 108 and Figure 113). Furthermore, excess pore water pressure inside the shear band initially increases then drops as shown in Figure 109 and Figure 116 i.e. diffusion of excess pore water pressure eventually becomes more significant than thermal pressurization. The balance between the diffusion and generation of excess pore water pressure may be influenced by the total spatial domain in the finite difference scheme. Therefore, in this section a parametric study is carried out to investigate the influence of the size of the modelled spatial domain.

Recalling the boundary conditions used;

$$\theta(\pm\alpha, t) = \theta_{ref} = 12.5\text{°C} \qquad 4.43$$

In reality, it is not possible to maintain these boundary conditions at an infinite distance from the shear band. In the previous analyses, the total domain was chosen as 21 times the shear band thickness assuming that this choice places the boundaries “far enough”. To investigate the influence of boundaries, further analyses are performed for the selected cases, with different model thickness i.e. 11, 21, 51 and 101 times bigger than the shear band thickness as described in Figure 121. The results are presented in the following subsections.

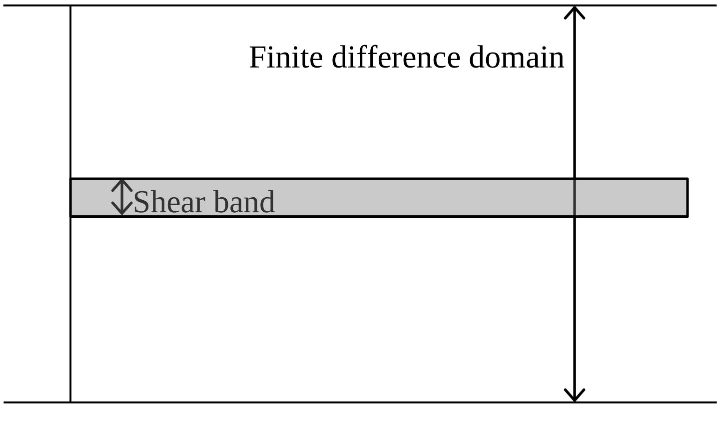

Figure 121: Schematic diagram of shear band and finite difference domain

4.6.5.1 Results for the baseline case

Figure 122 presents the temperature at the middle of the shear band for different model thicknesses, and the corresponding temperature isochrones are given in Figure 123 to

Figure 126. It can be clearly seen that the total temperature rise predicted increases with model thickness. However, the difference in temperature rises between the cases of $11 \times Z_b$ and $101 \times Z_b$, where Z_b is the shearband thickness, is found nearly 8.5×10^{-4}℃ which is still practically negligible. Similarly, the pore water pressure isochrones for different domains are given in Figure 128 to Figure 131. The peak value of pore pressure increases with the thickness of the model as seen in Figure 127. The difference in peak values of pore pressure between the cases of $11 \times Z_b$ and $101 \times Z_b$ is found to be practically zero (i.e. 4Pa). The velocity plot of Figure 132 shows that analyses for all domain thicknesses reach a steady state, although the respective final velocities are different but the differences are not significant.

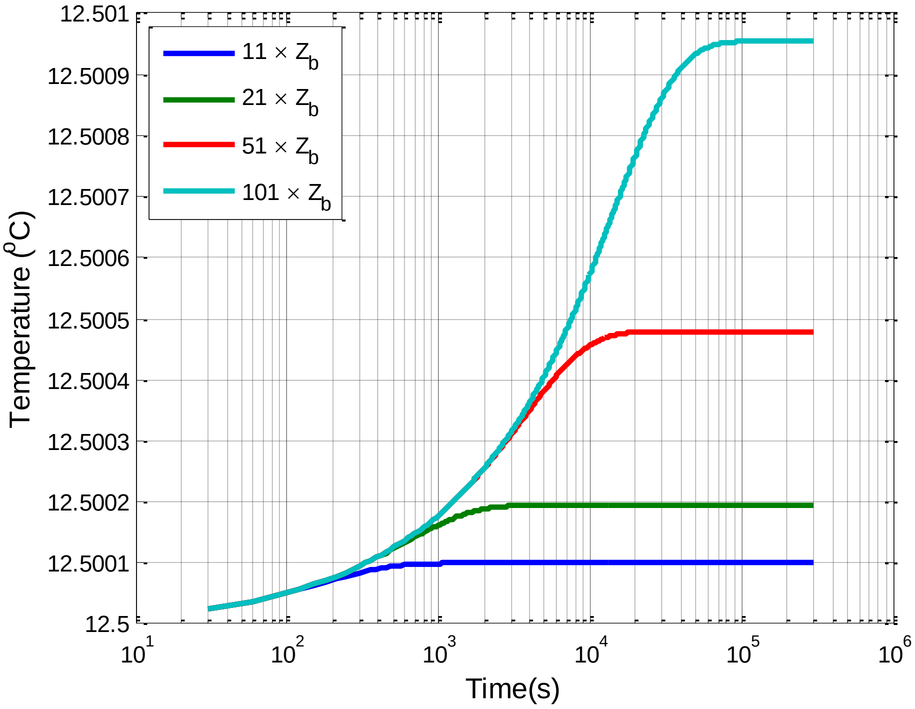

Figure 122: Temperature at the mid-point of the shear band (different boundaries, base line case)

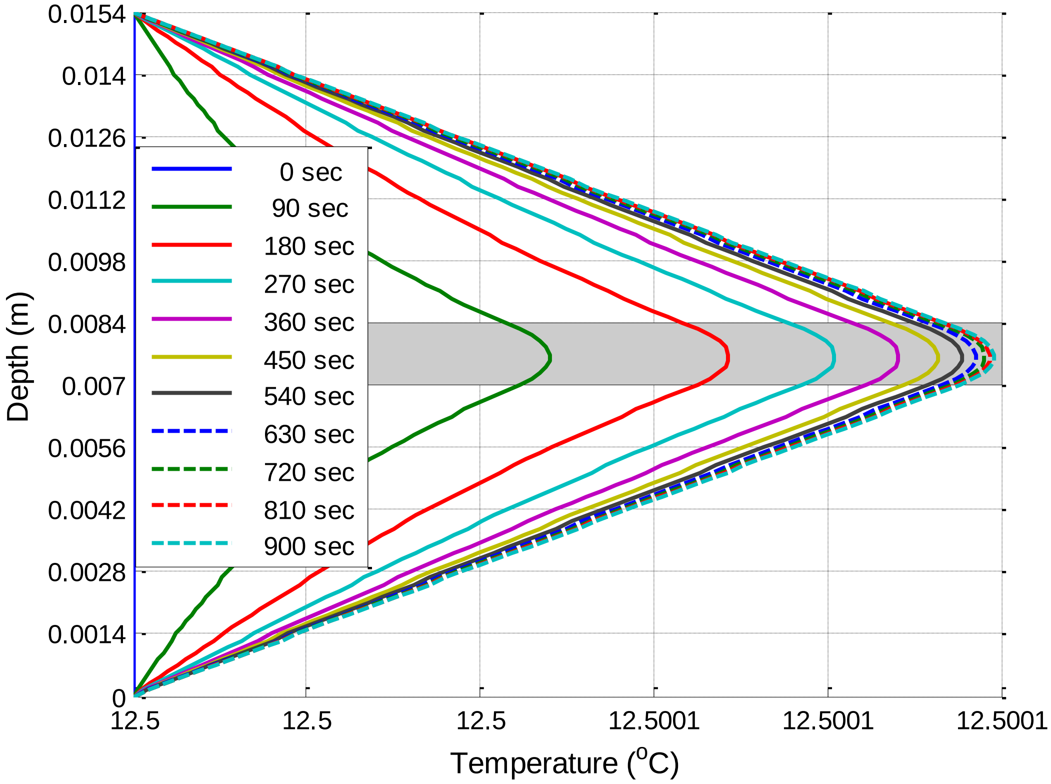

Figure 123: Temperature isochrones for domain thickness $11 \times Z_b$, baseline case (shearband area is shaded)

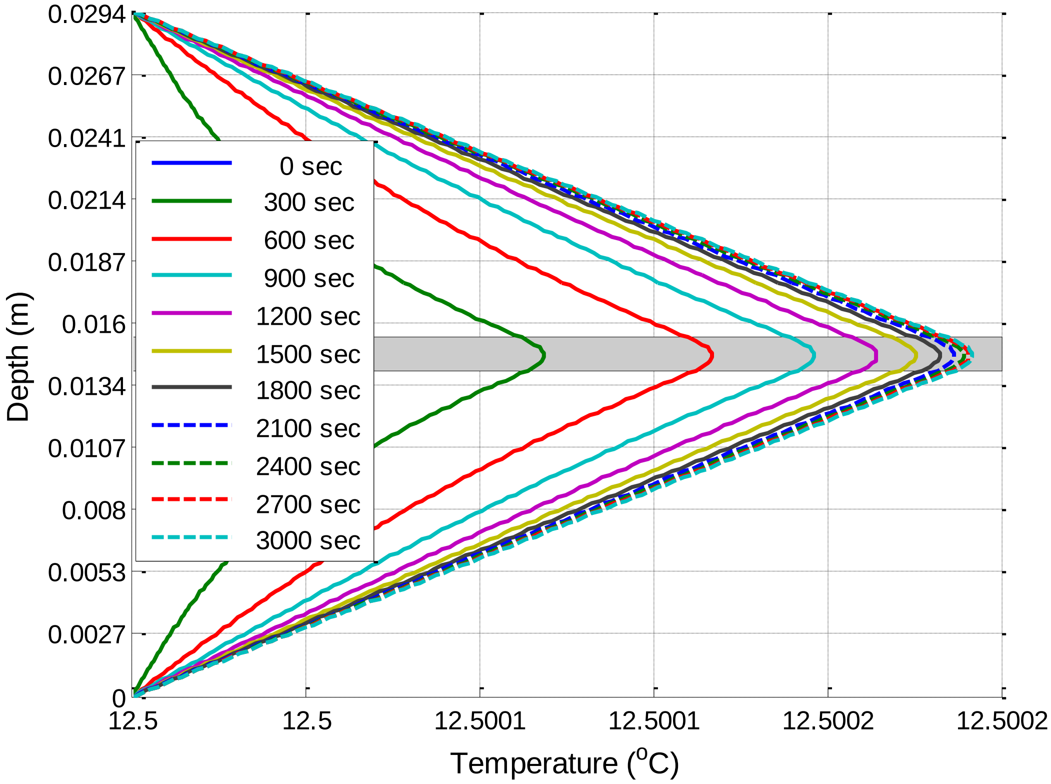

Figure 124: Temperature isochrones for domain thickness $21 \times Z_b$, baseline case (shearband area is shaded)

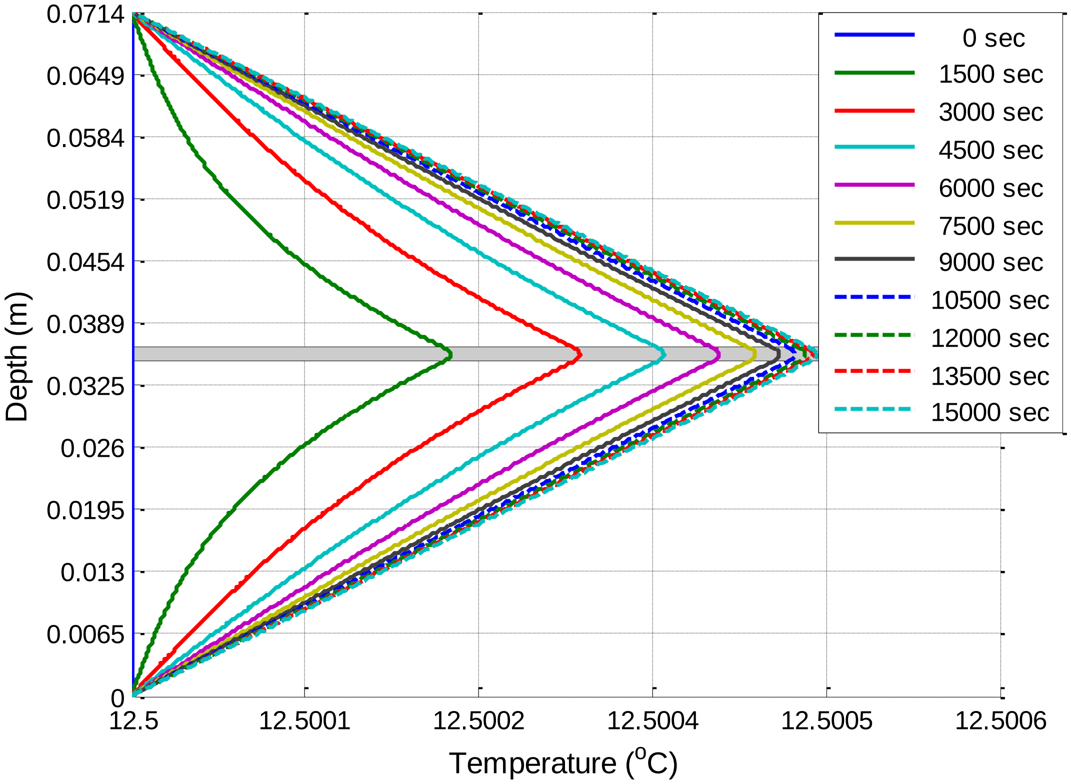

Figure 125: Temperature isochrones for domain thickness 51 × Z_b , baseline case (shearband area is shaded)

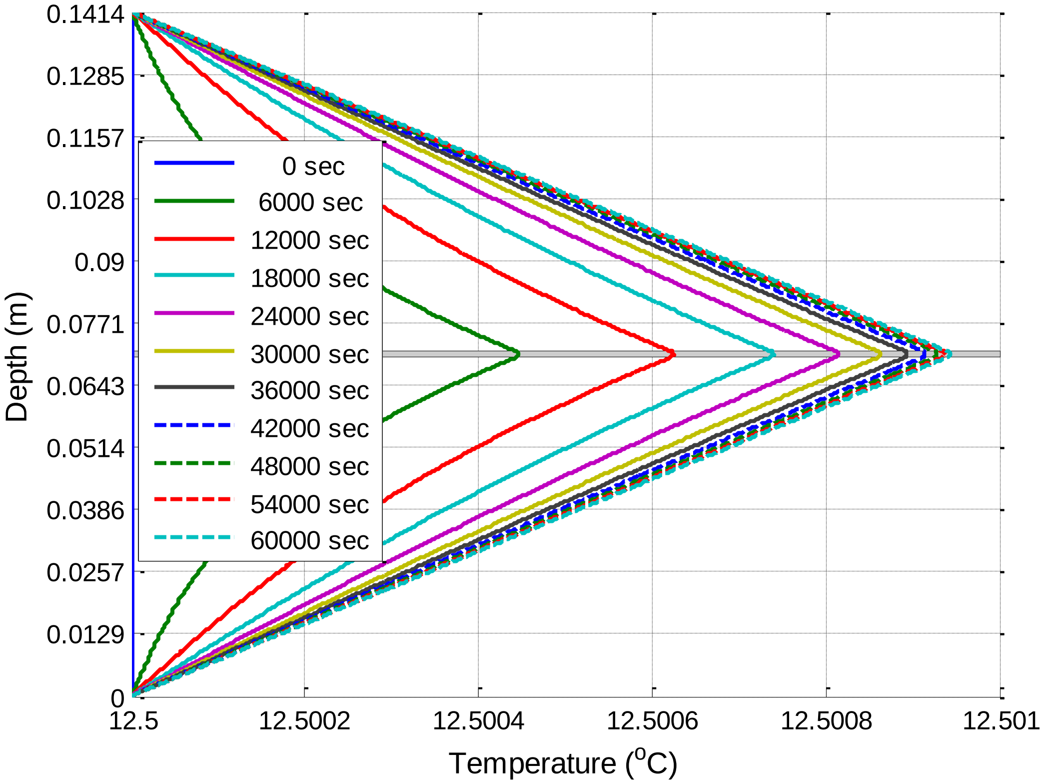

Figure 126: Temperature isochrones for domain thickness 101 × Z_b , baseline case (shearband area is shaded)

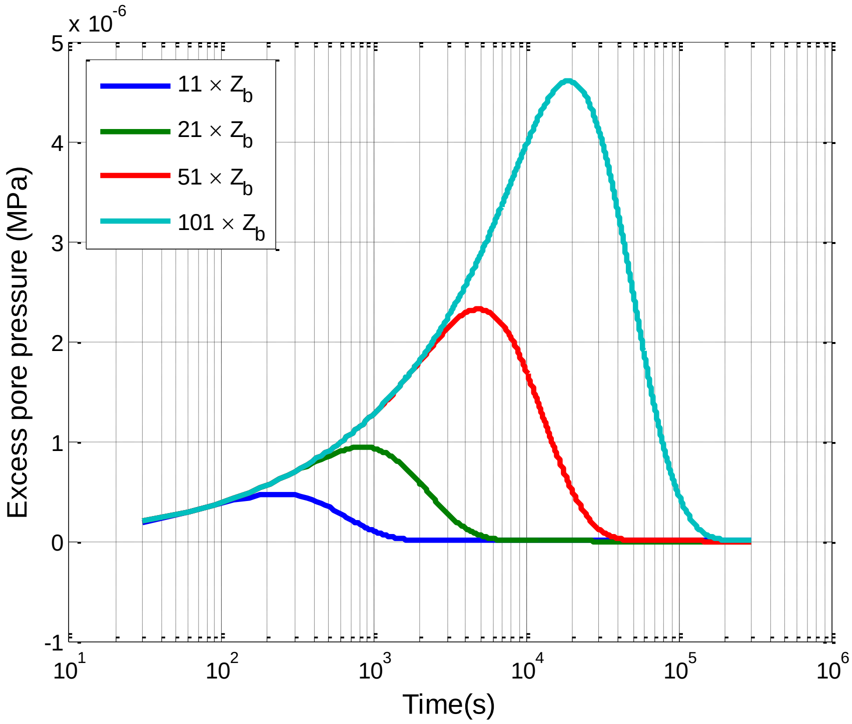

Figure 127: Excess pore water pressure at the mid-point of the shear band (different boundaries, base line case)

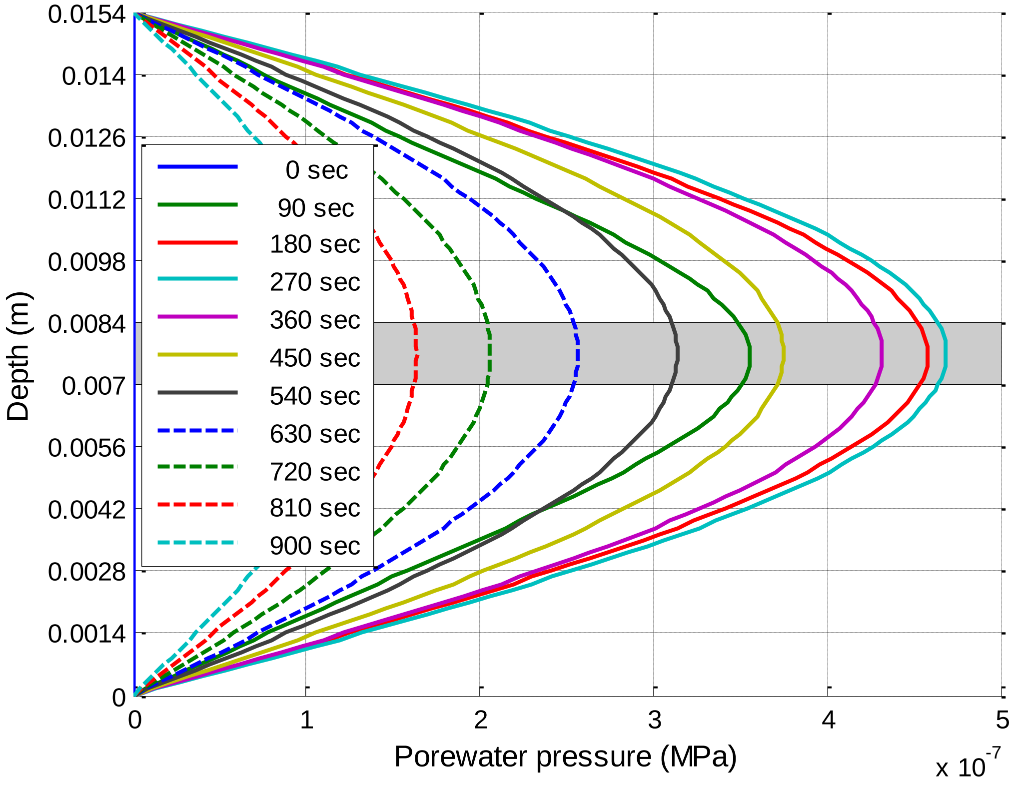

Figure 128: Pore water pressure isochrones for domain thickness $1 \times Z_b$, baseline case (shearband area is shaded)

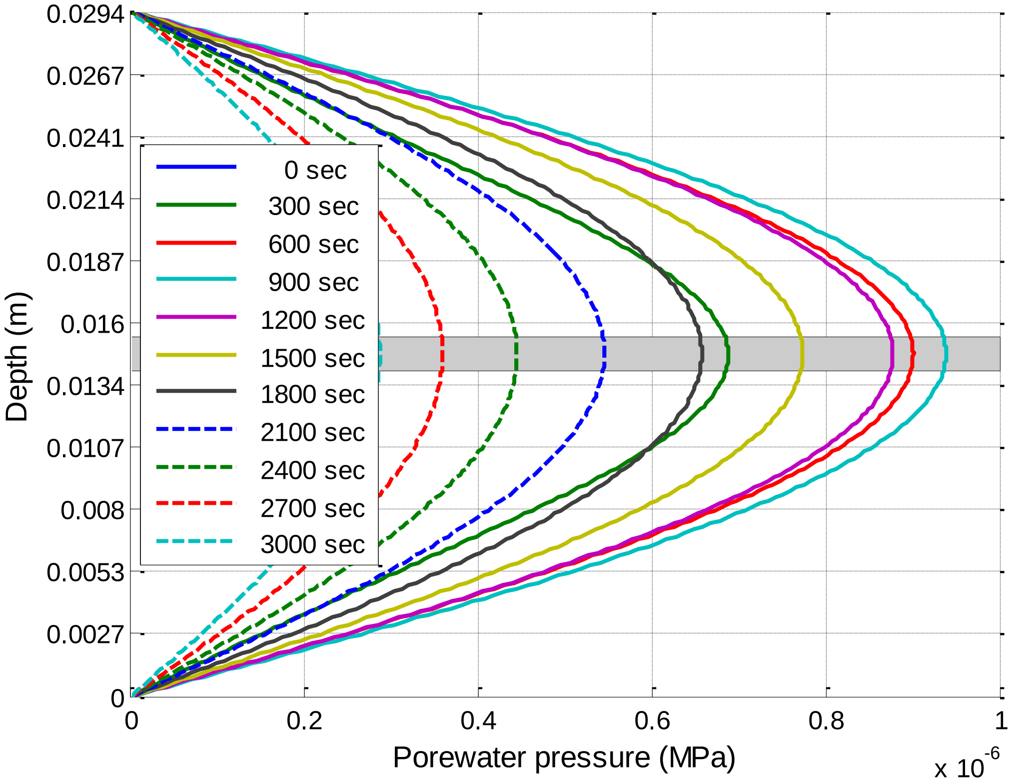

Figure 129: Pore water pressure isochrones for domain thickness 1 × Z_b , baseline case (shearband area is shaded)

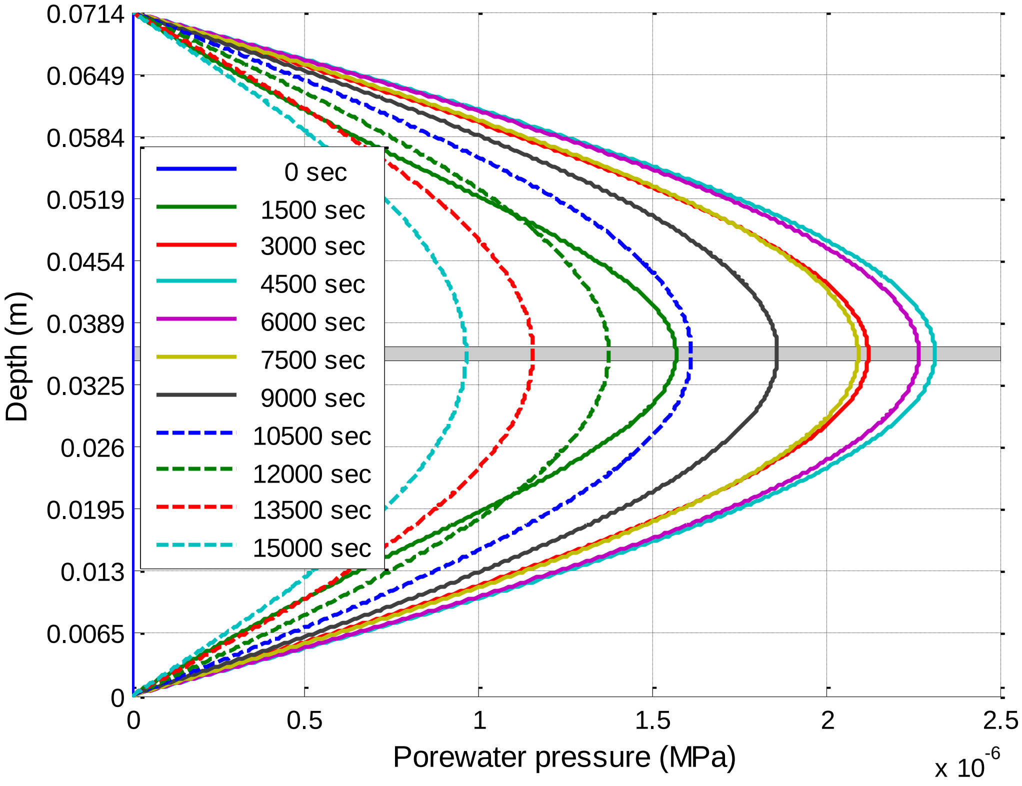

Figure 130: Pore water pressure isochrones for domain thickness 1 × Z_b , baseline case (shearband area is shaded)

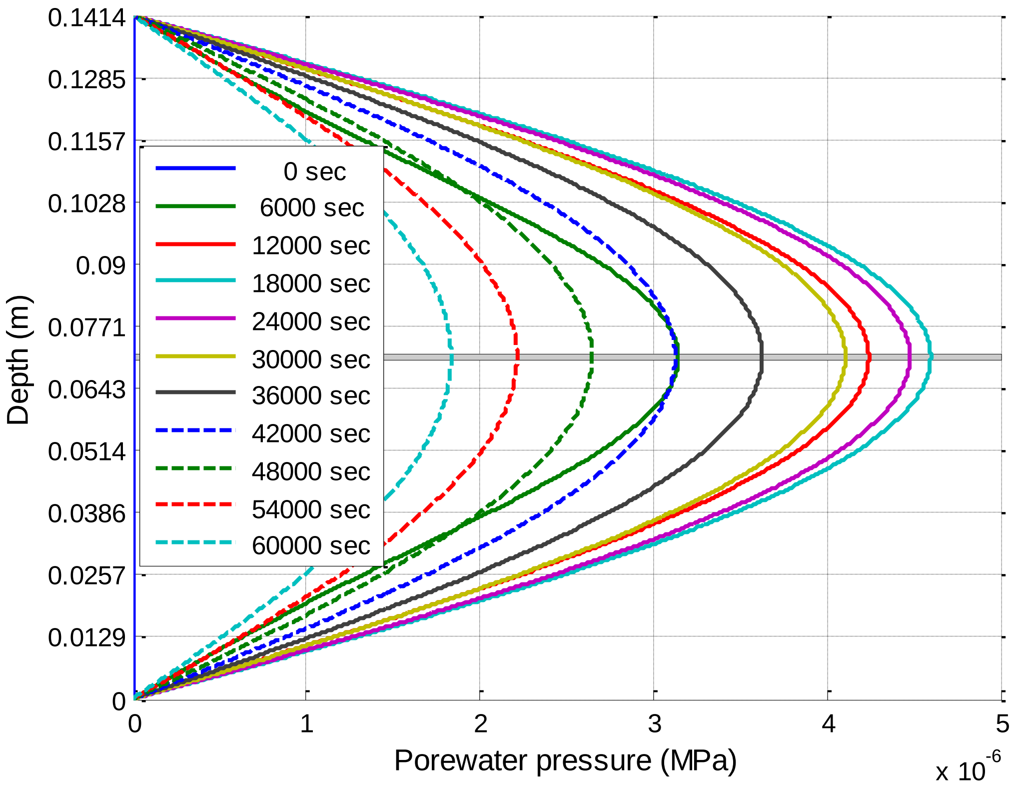

Figure 131: Pore water pressure isochrones for domain thickness $101 \times Z_b$, baseline case (shearband area is shaded)

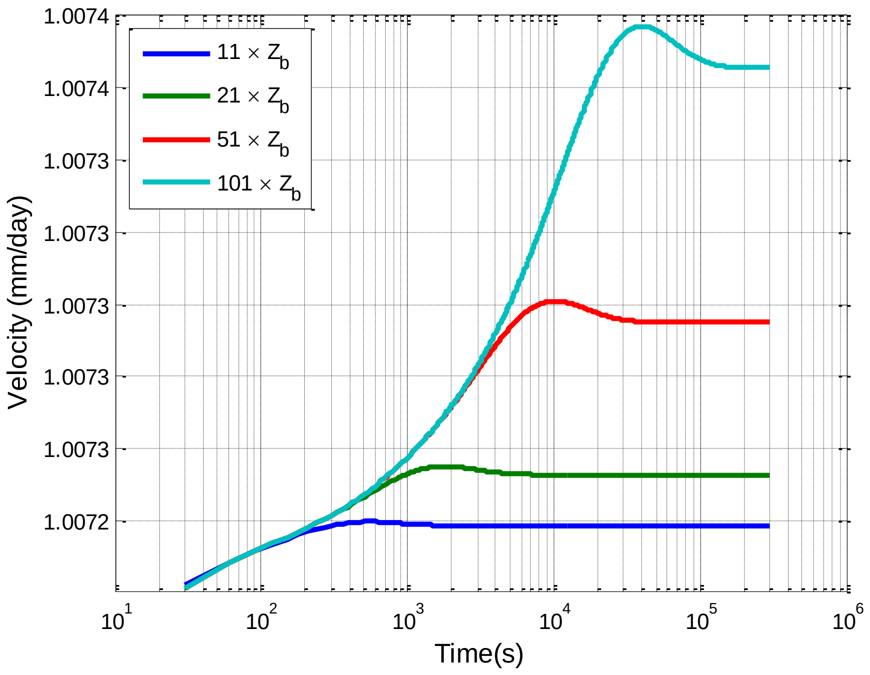

Figure 132: Velocity of the slide (different boundaries, base line case)

4.6.5.2 Results with 0.15mm/sec initial velocity

For the baseline case, the maximum rise in temperature, the peak value of pore water pressure and the final velocity at steady state increases with increasing model thickness. In this section, a similar analysis is carried out with a higher initial velocity.

The results presented in subsection 4.6.4.2 showed that, an initial velocity above 0.2 mm/sec leads to a catastrophic phase whereas an initial velocity lower than 0.2mm/sec leads to steady state. In this subsection, an initial velocity of 0.15 mm/sec is chosen to investigate the influence of the model thickness. This particular initial velocity predicted a steady state in the previous analysis presented in Subsection 4.6.4.2, where $21 \times Z_b$ was used as the model thickness (Figure 120).

The temperature and pore water pressure isochrones for different model thicknesses are given from Figure 133 to Figure 136 and from Figure 138 to Figure 141 respectively. The plots for the temperature and pore water pressure at the middle of the shear band are given in Figure 137 and Figure 142 respectively and the corresponding velocity plot in Figure 143.

It can be clearly seen that, using a model thickness of $51 \times Z_b$ or $101 \times Z_b$ leads to a catastrophic phase, whereas a model thickness of $11 \times Z_b$ or $21 \times Z_b$ leads to a steady state. Moreover, the predictions given by domains $51 \times Z_b$ and $101 \times Z_b$ are practically the same as seen in Figure 137, Figure 142 and Figure 143.

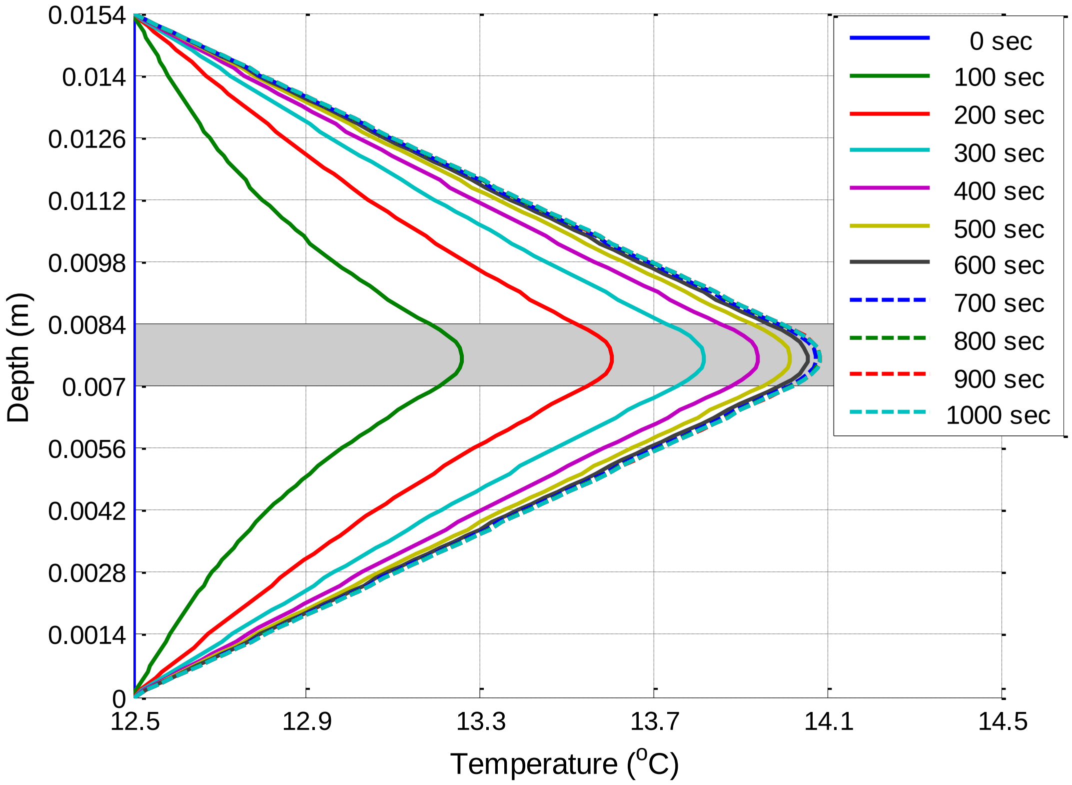

Figure 133: Temperature isochrones for domain thickness $11 \times Z_b$, initial velocity = 0.15mm/sec (shearband area is shaded)

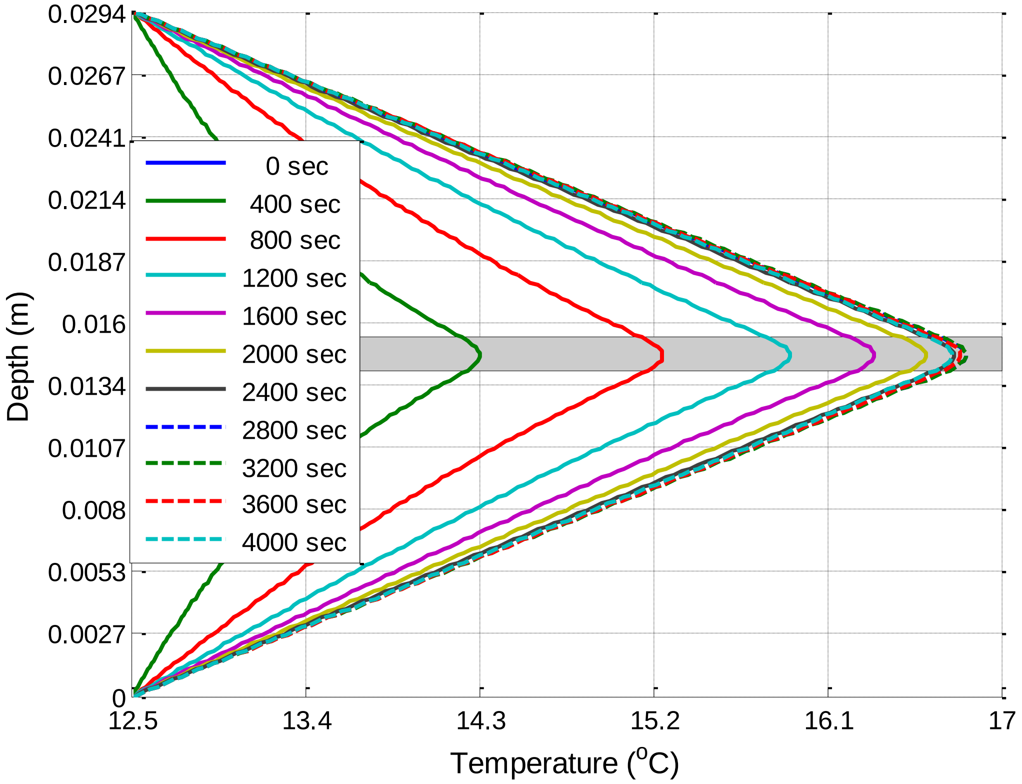

Figure 134: Temperature isochrones for domain thickness $1 \times Z_b$, initial velocity = 0.15mm/sec (shearband area is shaded)

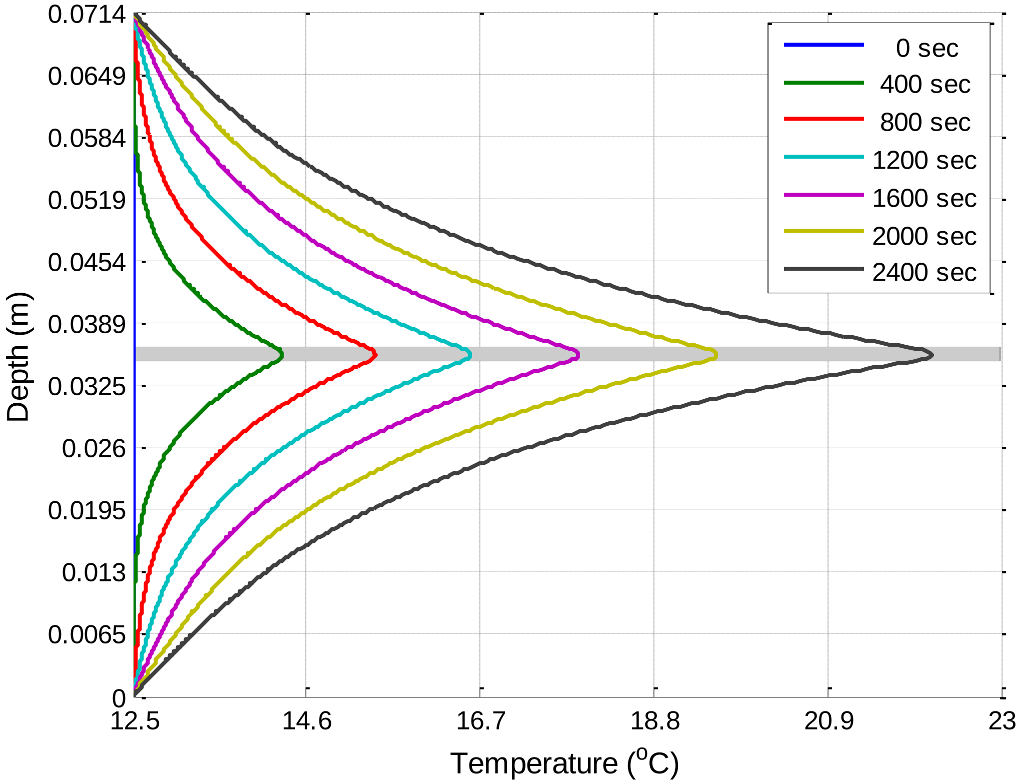

Figure 135: Temperature isochrones for domain thickness $51 \times Z_b$, initial velocity = 0.15mm/sec (shearband area is shaded)

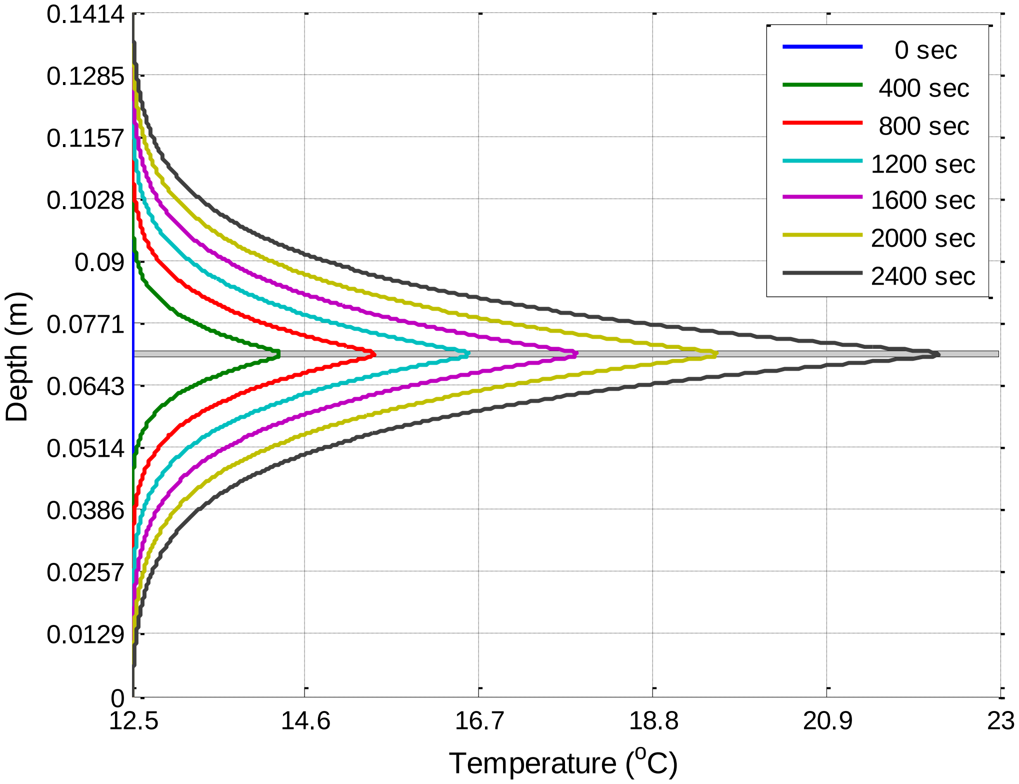

Figure 136: Temperature isochrones for domain thickness $101 \times Z_b$, initial velocity = 0.15mm/sec (shearband area is shaded)

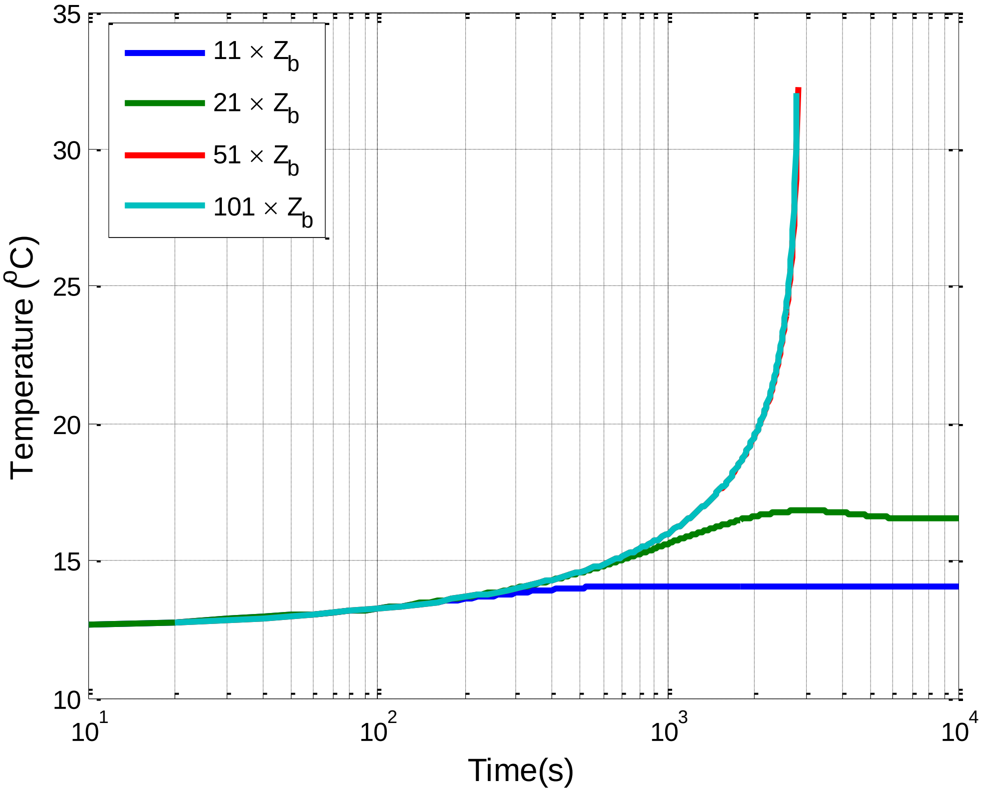

Figure 137: Temperature at the mid-point of the shear band (different boundaries, initial velocity = 0.15mm/sec)

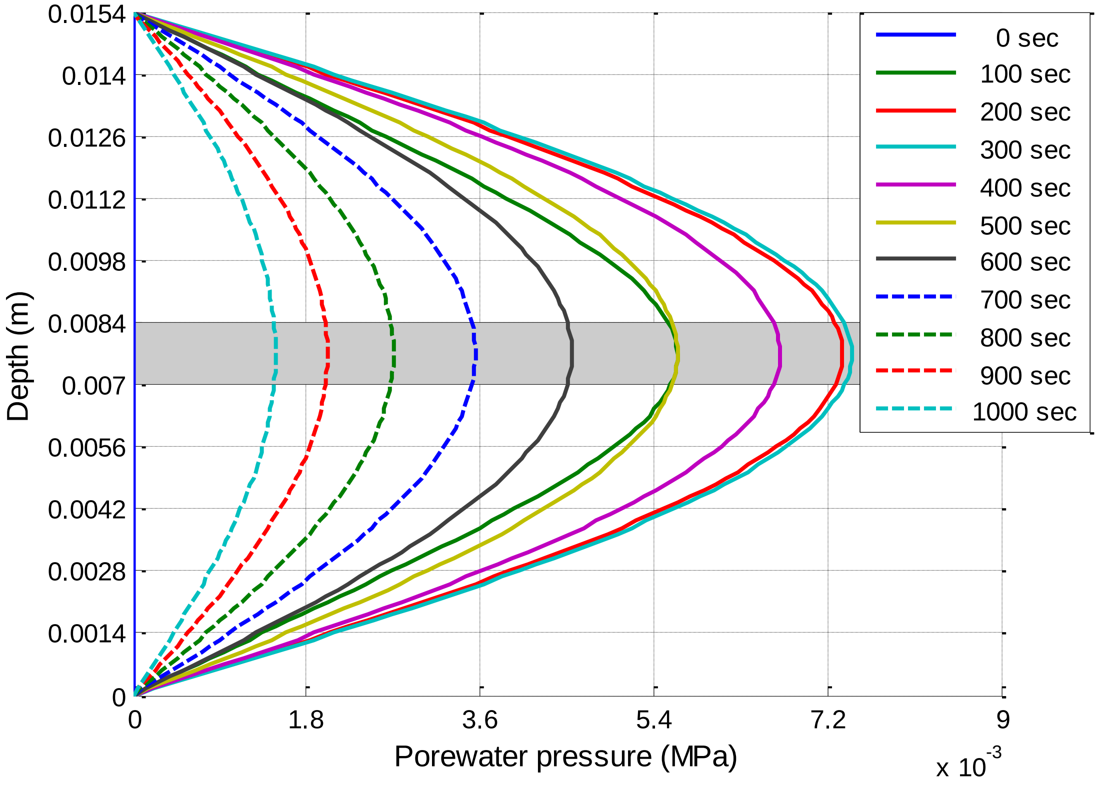

Figure 138: Pore water pressure isochrones for domain thickness $11 \times Z_b$, initial velocity = 0.15mm/sec (shearband area is shaded)

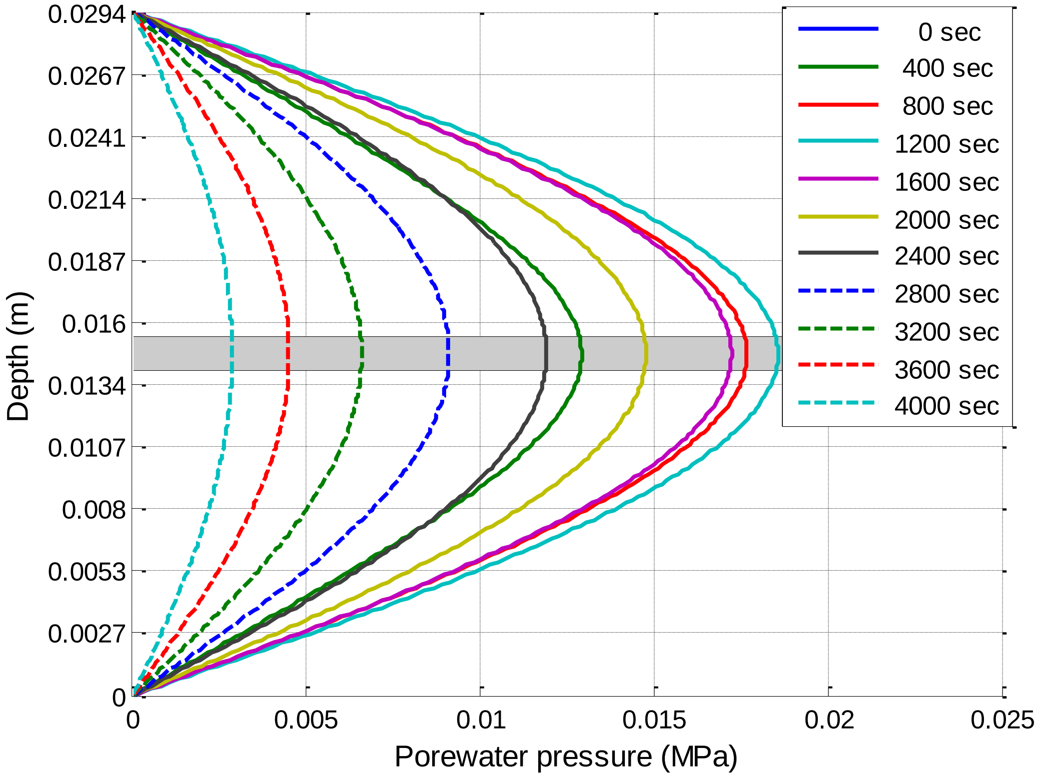

Figure 139: Pore water pressure isochrones for domain thickness $21 \times Z_b$, initial velocity = 0.15mm/sec (shearband area is shaded)

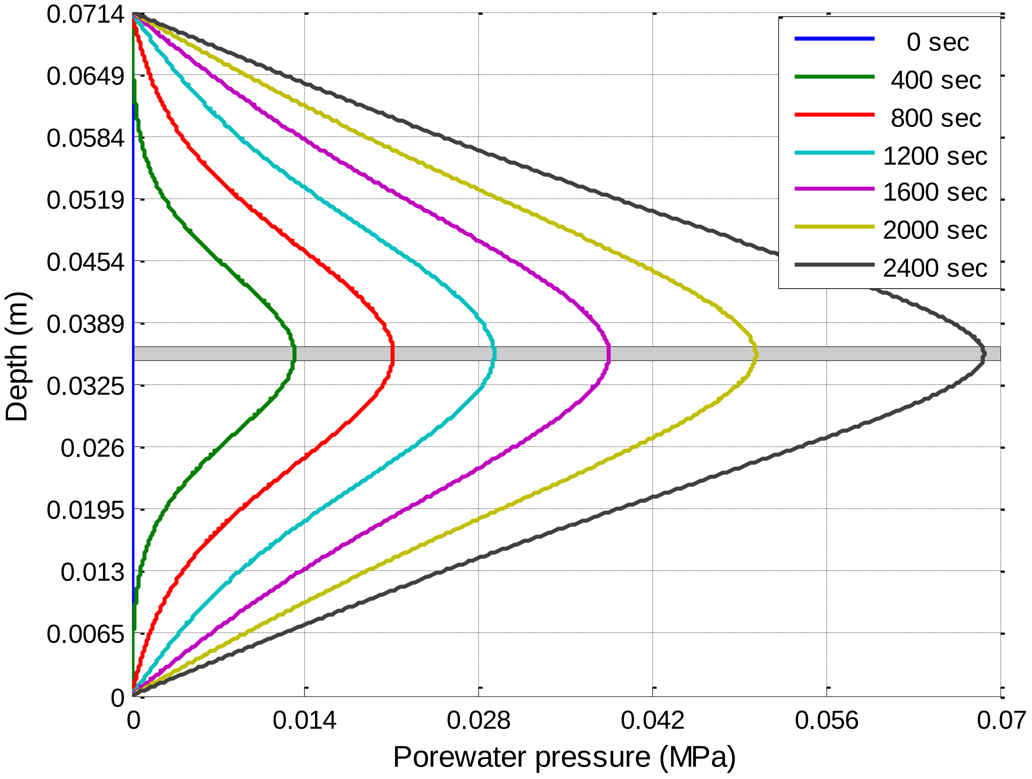

Figure 140: Pore water pressure isochrones for domain thickness $51 \times Z_b$, initial velocity = 0.15mm/sec (shearband area is shaded)

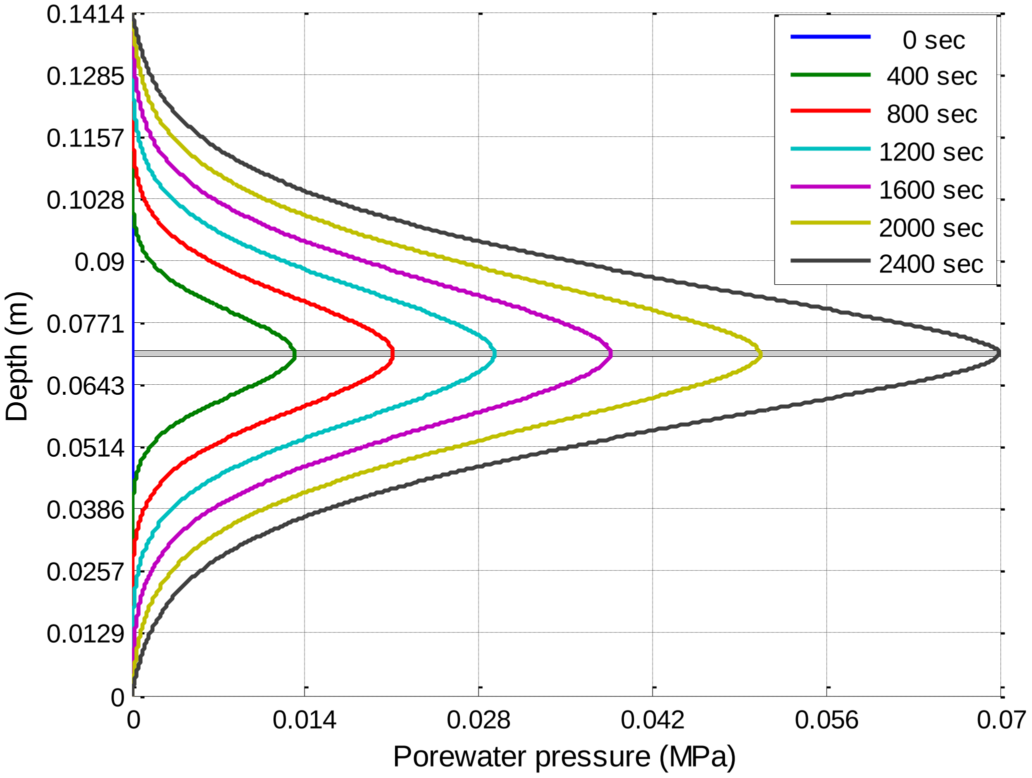

Figure 141: Pore water pressure isochrones for domain thickness $101 \times Z_b$, initial velocity = 0.15mm/sec (shearband area is shaded)

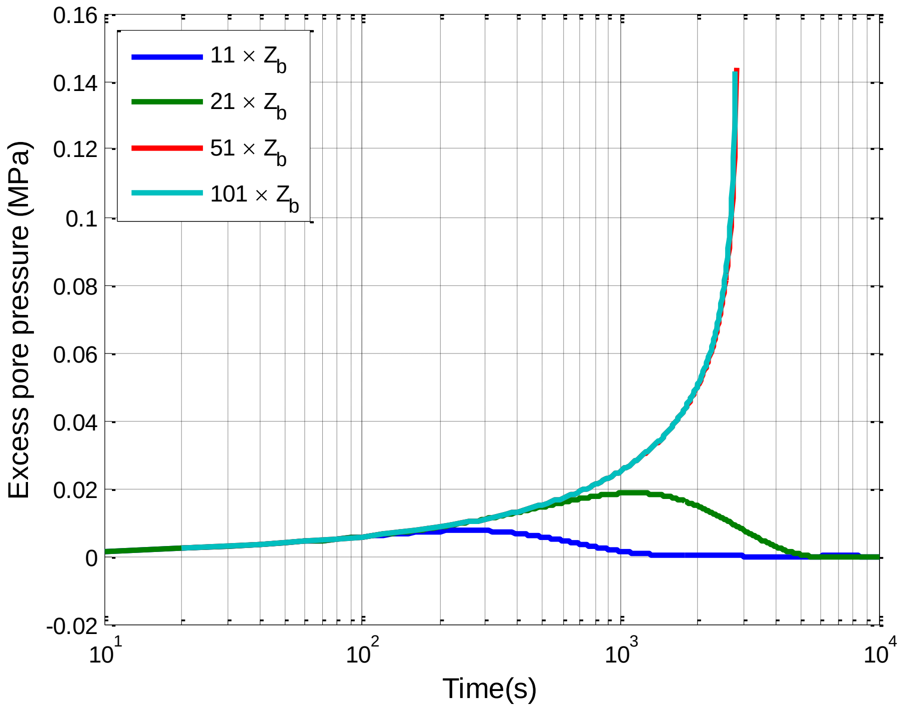

Figure 142: Excess pore water pressure at the mid-point of the shear band (different boundaries, initial velocity = 0.15mm/sec)

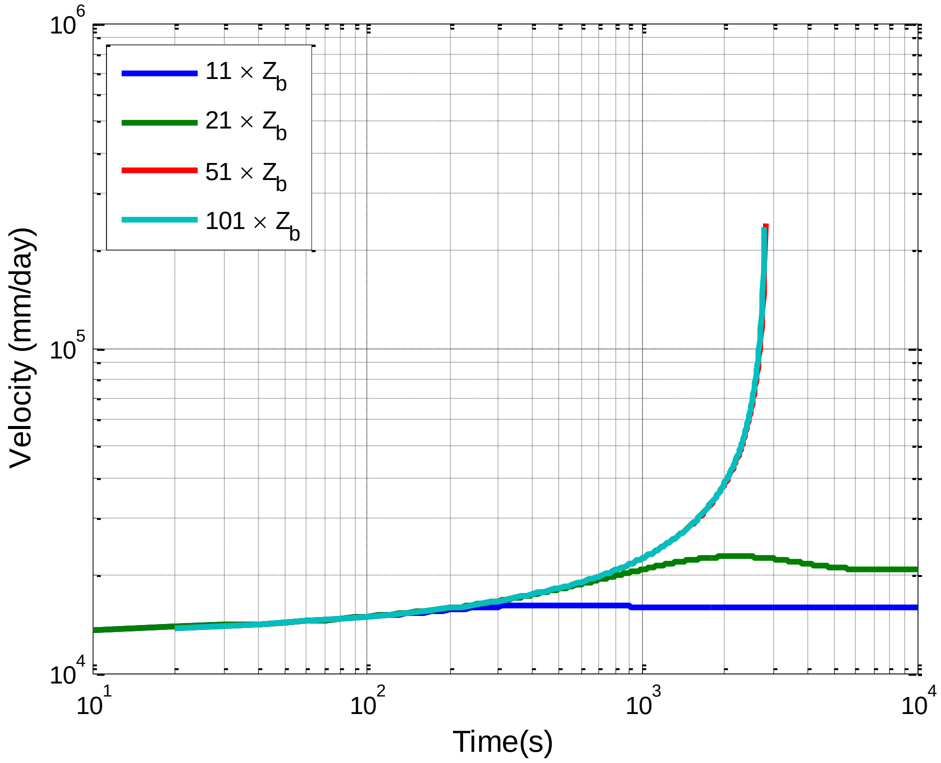

Figure 143: Velocity of the slide (different boundaries, initial velocity = 0.15mm/sec)

It can therefore be concluded that, although the low initial velocities predicted a steady state in the previous analyses (Sections 4.6.4.1 and 4.6.4.2), this was due to the effect of the thickness of the model. On the other hand, results that predicted catastrophic failure are not influenced by the thickness of the model.

Base on the above analysis, modelling the exact thickness is important as it affects the significantly the predicted outcome. To predict the failure time of the Vaiont case, the domain thickness should kept extremely large, which is practically not possible to model. However, a way is needed to assess whether, if full thickness is modelled, the model would predict Vaiont's collapse in reasonable timescales. Therefore, the following approach is proposed here in order to predict the failure time of the Vaiont case.

First, initial velocities and the corresponding failure times of the slide are obtained from Figure 120 and Figure 143. The logarithmic plot of failure time (sec) vs initial velocity (mm/day) and the best linear fit is given in Figure 144. Furthermore, the best linear fit takes the following form;

$$\ln\left(\frac{t_f}{t_{f0}}\right) = \bar{C}_1 \ln\left(\frac{v_i}{v_{i0}}\right) + \bar{C}_2 \qquad 4.44$$

where t_f is the failure time, t_{f0} is the reference failure time (taken here as 1 sec) v_i is the initial velocity of the slide, v_{i0} is areference initial velocity (taken here as 1mm/day) and $\bar{C}_1$ and the $\bar{C}_2$ are the dimensionless coefficients obtained from linear fit ($\bar{C}_1 = -1.9$ and $\bar{C}_2 = 26.04$). Substituting Vaiont initial velocity (base line case, 1mm/day) into Equation 4.44 give failure time of 6460 years which is still very long period compared to the actual creep duration observed in the Vaiont (3 years).

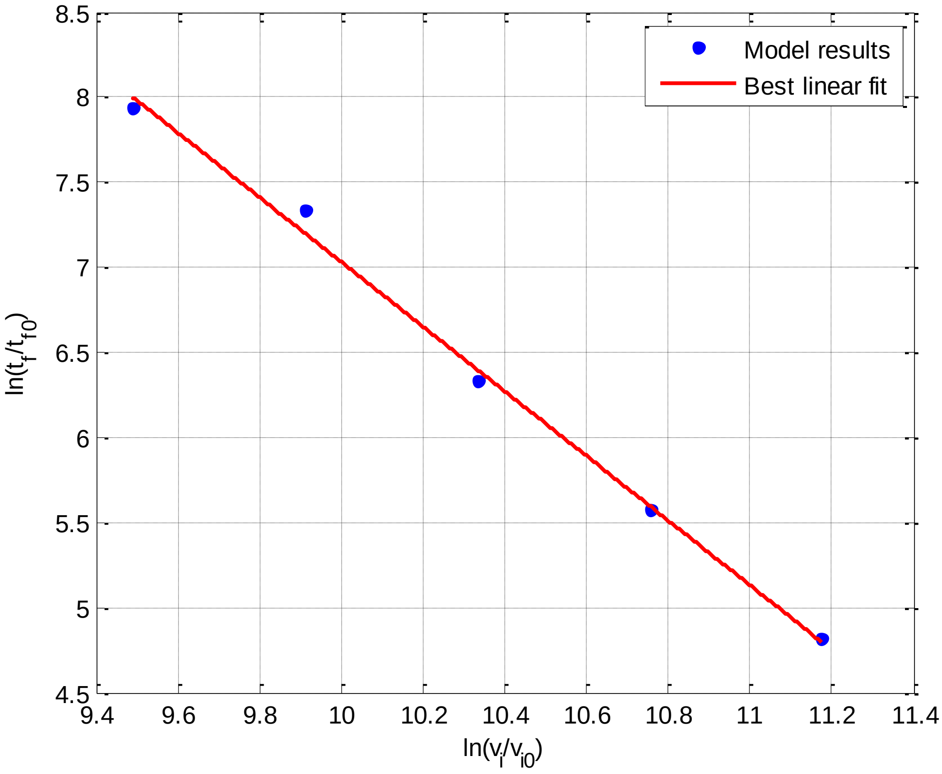

Figure 144: Logarithmic plot of failure time (sec) vs initial velocity (mm/day)

4.7 Discussion and conclusions

In this Chapter, first a thermo-mechanical model for a shear band and then a thermo-poro-mechanical landslide model were developed. Rate process theory was used to describe the constitutive behaviour of the soil.

From the thermo-mechanical model of a shear band that was developed in Section 4.5, the following conclusions can be made.

- In non-isothermal conditions, for a given model thickness, beyond a particular threshold value of applied stresses, the model predicts blow-up in temperature and also unconstrained acceleration. Shear stress lower than that threshold seems to lead to a steady state, where temperature and velocity stabilise.
- Strain localization is predicted by this model and this is promoted by localization of heat dissipation inside the shear band.
- In non-isothermal conditions, the development of secondary and tertiary creep is possible to simulate. Primary creep cannot however be simulated as it would imply a decrease in temperature and temperature either increases or remains constant over time in this model.
- Negative rate effects cannot be simulated by this model because it assumes strain rate to be an increasing function of the applied shear stress.
- Parameters such as activation energy (U_0), number of bonds (S) and distance between two equilibrium points of two flow units (λ_l) have uncertainty associated with them. They have a wide range of values and not all of them are possible to measure directly. Moreover, the model is relatively sensitive to their values.

It was considered that rate process theory may provide a possible framework for describing the transition between creep and catastrophic failure of a landslide. Subsequently, a landslide model was developed by incorporating thermal pressurization and the dynamics of the sliding mass.

First, this model was used in an attempt to back analyse the Vaiont case history. The rate process parameters were chosen within the reasonable range of values available in the literature (Mitchell and Soga, 2005). The other Vaiont parameters were chosen from Vardoulakis (2002a). However, the model did not predict the complete history (creep and the catastrophic phase) of the landslide. The total time to catastrophic failure was predicted to be much longer than the observed duration in the Vaiont case history. The possible reasons are listed below.

- The chosen rate process parameters are the best guess values chosen from the literature; however parameter values specific to the Vaiont material are not available. Moreover, the results presented here were found to be sensitive to the values of the rate process parameters used
- Some activities such as reservoir level changes were carried out during the creep phase of the Vaiont slide. These particular activities were not included in the model presented in this chapter.
- Significant rainfall was observed over the entire period of the landslide event. The precipitation effects are not included in this model.

Subsequently, using the model, results were obtained for initial velocities which are higher than the creep velocity observed in the Vaiont case history. It was found that the initial velocity, which depends on activation energy and number of bonds, and also the thickness of the spatial domain modelled, have significant impact on the predicted results. For low enough initial velocity, corresponding to higher activation energy and number of bonds, the model predicts that, for a given model thickness, a steady state is reached as any heat generated dissipates without a significant temperature increase. Higher initial velocity, however, leads to temperature build-up and causes the slope to eventually accelerate.

Furthermore, the extent of the modelled spatial domain plays a dominant role on the failure of a landslide. The larger the domain, more likely to predict the catastrophic failure. Therefore, for infinite upper and lower boundary, the model is expected to predict catastrophic failure irrespective of the value of initial velocity. However, the time it will take for failure to be reached (t_f) depends on the initial velocity of the slide, i.e. the higher the initial velocity the sooner failure.

In the creep phase temperature effects are not significant, as energy dissipation and heat production are low. Therefore frictional heating on its own is not predicted to cause the collapse of a slope; other external actions, such as dynamic loading or pore pressure increase, need to be invoked to push the velocity over the threshold. Once the threshold is exceeded, however, frictional heating is predicted to facilitate catastrophic collapse.

Although the model presented is able to predict a transition between the creep and the catastrophic phases of a landslide, due to the drawbacks stated above, a more reliable constitutive theory is needed in order to capture the entire creep behaviour of the soil. Therefore, a different constitutive relation, not based on rate process theory will be investigated in the next chapter.

Chapter 5: A Thermo-poro-mechanical landslide model: using a refined thermo mechanical constitutive model including creep

5.1 Introduction

In Chapter 4, a thermo-poro-mechanical landslide model was developed based on rate process theory. Although rate process theory could describe the transition between creep and the catastrophic phase, due to the sensitivity of the rate process parameters the duration of the creep phase is too short compared to a real landslide case.

This chapter presents a new framework for modelling the evolution of landslides from creep to final collapse, using an advanced constitutive model. First, a new constitutive model is developed in Section 5.2 to 5.8, combining the constitutive models developed by Borja and Kavazanjian (1985) and Laloui and Francois (2009). Subsequently, this constitutive assumption is inserted in a landslide model. The model equations are numerically solved and the results are presented and discussed.

5.2 General formulation

As discussed in section 2.4.3, Borja and Kavazanjian (1985) proposed a time dependent constitutive model that includes the creep effects of soils. This model was developed assuming two different empirical relations for volumetric and deviatoric creep: Taylor's secondary creep law was considered for the volumetric part and the Singh-Mitchell expression was used to determine the deviatoric part. The Modified Cam-Clay yield locus was used in this model to incorporate elasto-plasticity. Finally, time dependent evolution of the yield locus was also introduced.

Laloui and Francois (2009) proposed a thermo-plastic constitutive model for soils as explained in Section 2.3.3. It should be noted that Laloui and Francois (2009) used the original Cam-Clay yield surface (OCC) for the deviatoric mechanism (Section 2.3.3.2).

Cecinato modified Laloui's model replacing the OCC with the Modified Cam-Clay (MCC) yield locus as described in Section 2.3.4 (Cecinato, 2009, Cecinato et al., 2011).

It is possible to develop a material model that includes both the effect of creep and temperature by combining Borja's creep model and Cecinato's thermo-plastic model. The development of this material model is given in the following subsections.

According to classical elasto-plasticity theory, the total strain rate can be decomposed in to two parts, i.e. elastic and plastic, as shown in Equation 5.1;

$$\dot{\boldsymbol{\varepsilon}} = \dot{\boldsymbol{\varepsilon}}^{\boldsymbol{e}} + \dot{\boldsymbol{\varepsilon}}^{\boldsymbol{p}} \tag{5.1}$$

When creep is included, the total strain rate can be decomposed into three parts i.e. elastic, plastic and time-dependent (Borja and Kavazanjian, 1985) as follows;

$$\dot{\boldsymbol{\varepsilon}} = \dot{\boldsymbol{\varepsilon}}^{\boldsymbol{e}} + \dot{\boldsymbol{\varepsilon}}^{\boldsymbol{p}} + \dot{\boldsymbol{\varepsilon}}^{\boldsymbol{t}} \tag{5.2}$$

If thermal loads exist, the elastic part is further decomposed into two contributions, i.e. the mechanical elastic and the thermo elastic parts (Laloui and Francois, 2009). Therefore, the final strain rate can be written as;

$$\dot{\boldsymbol{\varepsilon}} = \dot{\boldsymbol{\varepsilon}}^{\boldsymbol{me}} + \dot{\boldsymbol{\varepsilon}}^{\boldsymbol{te}} + \dot{\boldsymbol{\varepsilon}}^{\boldsymbol{p}} + \dot{\boldsymbol{\varepsilon}}^{\boldsymbol{t}} \tag{5.3}$$

5.3 Thermo-elasticity

According to standard continuum mechanics, for a body subjected to thermal and mechanical loadings, the stress-strain-temperature rate equation is given by (Mase, 1970);

$$\dot{\boldsymbol{\sigma}} = \lambda \boldsymbol{\delta} \dot{\varepsilon}_v^{me} + 2\mu \dot{\boldsymbol{\varepsilon}}^{\boldsymbol{me}} - (3\lambda + 2\mu)\alpha \boldsymbol{\delta} \dot{\theta} \tag{5.4}$$

where λ and μ are the *Lame* constants (Mase, 1970), and α is the thermal elastic expansion coefficient. The stress and strain rates vectors $\dot{\boldsymbol{\sigma}}$ and $\dot{\boldsymbol{\varepsilon}}$ are written as;

$$\dot{\boldsymbol{\sigma}} = \begin{pmatrix} \dot{\sigma}'_{11} \\ \dot{\sigma}'_{22} \\ \dot{\sigma}'_{33} \\ \dot{\tau}_{12} \\ \dot{\tau}_{23} \\ \dot{\tau}_{31} \end{pmatrix} \quad \dot{\boldsymbol{\varepsilon}} = \begin{pmatrix} \dot{\varepsilon}_{11} \\ \dot{\varepsilon}_{22} \\ \dot{\varepsilon}_{33} \\ \dot{\gamma}_{12} \\ \dot{\gamma}_{23} \\ \dot{\gamma}_{31} \end{pmatrix} \text{ and } \boldsymbol{\delta} = \begin{pmatrix} 1 \\ 1 \\ 1 \\ 0 \\ 0 \\ 0 \end{pmatrix} \tag{5.5}$$

Laloui proposed the thermo elastic equation as (Laloui and Francois, 2009)

$$\dot{\varepsilon}_v^{te} = \beta_s \dot{\theta} \tag{5.6}$$

Equivalently, Equation 5.6 can be written in vector form as follows,

$$\dot{\boldsymbol{\varepsilon}}^{\boldsymbol{te}} = \boldsymbol{C}^{\boldsymbol{Te}} \dot{\theta} \tag{5.7}$$

where $\boldsymbol{C^{Te}} = \frac{1}{3}\beta_s\boldsymbol{\delta}$

Substituting definitions of Lame constant and the Laloui's relationship (Equation 5.6) into 5.4 gives

$$\dot{\boldsymbol{\sigma}} = \left(K - \frac{2}{3}G\right)\boldsymbol{\delta}\dot{\varepsilon}_v^{me} + 2G\dot{\boldsymbol{\varepsilon}}^{\boldsymbol{me}} - \beta_s K\boldsymbol{\delta}\dot{\theta} \qquad 5.8$$

where *K* and *G* are the stress dependent elastic bulk and shear moduli of the soil and can be written as;

$$K = \lambda + \frac{2}{3}\mu$$
$$G = \mu \qquad 5.9$$

Therefore, Equation 5.8 can be written in the following general form

$$\dot{\boldsymbol{\sigma}} = \boldsymbol{D^{me}}\dot{\boldsymbol{\varepsilon}}^{\boldsymbol{me}} + \boldsymbol{D^{te}}\dot{\theta} \qquad 5.10$$

where $\boldsymbol{D^{me}}$ is the standard elasticity matrix given by

$$\boldsymbol{D^{me}} = \begin{bmatrix} \left(K + \frac{4}{3}G\right) & \left(K - \frac{2}{3}G\right) & \left(K - \frac{2}{3}G\right) & 0 & 0 & 0 \\ \left(K - \frac{2}{3}G\right) & \left(K + \frac{4}{3}G\right) & \left(K - \frac{2}{3}G\right) & 0 & 0 & 0 \\ \left(K - \frac{2}{3}G\right) & \left(K - \frac{2}{3}G\right) & \left(K + \frac{4}{3}G\right) & 0 & 0 & 0 \\ 0 & 0 & 0 & G & 0 & 0 \\ 0 & 0 & 0 & 0 & G & 0 \\ 0 & 0 & 0 & 0 & 0 & G \end{bmatrix} \qquad 5.11$$

and $\boldsymbol{D^{te}}$ is the thermo-elasticity vector given by

$$\boldsymbol{D^{te}} = -\beta_s K\boldsymbol{\delta} \qquad 5.12$$

5.4 Proposed relationship for hardening law

Laloui and Cekerevac (2003) proposed that the apparent preconsolidation pressure is a decreasing function of temperature as follows;

$$p'_c = p'_{c0T0}\exp(\tilde{\beta}\varepsilon_v^p)\left\{1 - \gamma\log\left(\frac{\theta}{\theta_0}\right)\right\} \qquad 5.13$$

where p'_{c0T0} is the reference preconsolidation pressure i.e. at temperature θ_0 and before plastic deformation commences.

In the time-dependent model of Borja and Kavazanjian (1985), the presconsoildation pressure depends on time and its rate is given as:

$$\dot{p}_c' = \tilde{\beta} p_c' \dot{\varepsilon}_v^p + \tilde{\omega}\frac{p_c'}{t_v} \qquad 5.14$$

where $$\tilde{\beta} = \frac{1+e}{\lambda-\kappa} \qquad 5.15$$

$$\tilde{\omega} = \frac{\psi_\alpha}{\lambda-\kappa} \qquad 5.16$$

ψ_α is the coefficient of secondary compression plotted against natural logarithmic time and t_v is the volumetric age of the soil relative to an initial reference time t_{vi}. If there is no primary loading or unloading, then t_v is equal to natural time ($\Delta t_v = \Delta t$) (Section 5.8.4).

Equation 5.13 & 5.14 can now be combined to form a new hardening/softening relationship as follows: Integrating Equation 5.14 over $t_{vi} \rightarrow t_v$, $p_c' \rightarrow p_{c0}'$ and $0 \rightarrow \dot{\varepsilon}_v^p$ yields

$$p_c' = p_{c0}' \exp(\tilde{\beta}\varepsilon_v^p)\left(\frac{t_v}{t_{vi}}\right)^{\tilde{\omega}} \qquad 5.17$$

where p_{c0}' is the preconsolidation pressure at $t_v = t_{vi}$ and $\varepsilon_v^p = 0$. Equation 5.17 can now be modified to include the temperature dependence of Equation 5.13. Therefore, the final expression for the preconsolidation pressure becomes;

$$p_c' = p_{c0T0}' \exp(\tilde{\beta}\varepsilon_v^p)\left(\frac{t_v}{t_{vi}}\right)^{\tilde{\omega}} \left\{1 - \gamma \log\left(\frac{\theta}{\theta_0}\right)\right\} \qquad 5.18$$

Here, p_{c0T0}' is the preconsolidation pressure at $t_v = t_{vi}$ and $\theta = \theta_0$, called the reference preconsolidation pressure.

5.5 Yield function and consistency condition

As a result of the new hardening law (Equation 5.18), the yield locus now depends on temperature (θ) and time (t_v) in addition to the state of stress ($\boldsymbol{\sigma}$) and the hardening parameter(ε_v^p). This can be written as;

$$f\big(\boldsymbol{\sigma}, p_c'(\varepsilon_v^p, \theta, t_v)\big) = 0 \qquad 5.19$$

The consistency condition ($\dot{f} = 0$) ensures that, at yielding, the stress state lies on the evolving yield function and this can be expressed as;

$$\dot{f} = f_{\boldsymbol{\sigma}}\dot{\boldsymbol{\sigma}} + f_{p_c'}\dot{p}_c' = 0 \qquad 5.20$$

Subscripts in Equations 5.20 and 5.23 describe the partial derivatives of the yield function or effective preconsolidation pressure with respect to other model variables. As the yield function is a function of time, it will expand with time even under constant stress. Therefore $\dot{f} < 0$ is possible when $\dot{\boldsymbol{\sigma}} = 0$.

Plastic loading requires

$$f = 0 \text{ and } \dot{\boldsymbol{\sigma}}.(\nabla f) > 0 \tag{5.21}$$

where ∇f is the gradient of the yield function and $\dot{\boldsymbol{\sigma}}.(\nabla f)$ denotes the dot product of $\dot{\boldsymbol{\sigma}}$ and ∇f. Neutral loading requires

$$f = 0 \text{ and } \dot{\boldsymbol{\sigma}}.(\nabla f) = 0 \tag{5.22}$$

Borja and Kavazanjian (1985) further assumed that plastic loading and creep are two decoupled processes i.e. that creep can be ignored while plastic loading occurs. This assumption is valid only if the duration of loading is comparatively small (i.e. rapid loading rate). During this short time period, any expansion of the yield the locus due to creep can be ignored. Therefore, the consistency condition (5.20) is valid only during plastic loading.

The rate of change of preconsolidation pressure $\dot{p_c'}$ can be written as;

$$\dot{p_c'} = (p_c')_{\varepsilon_v^p}(\dot{\varepsilon}_v^p) + (p_c')_\theta(\dot{\theta}) + (p_c')_{t_v}(\dot{t_v}) \tag{5.23}$$

Each partial derivative can be defined as follows;

$$f_{\boldsymbol{\sigma}} = \left(\frac{\partial f}{\partial \boldsymbol{\sigma}}\right) = \frac{\partial f}{\partial p'}\frac{\partial p'}{\partial \boldsymbol{\sigma}} + \frac{\partial f}{\partial q}\frac{\partial q}{\partial \boldsymbol{\sigma}}$$

$$f_{p_c'} = \left(\frac{\partial f}{\partial p_c'}\right), \qquad (p_c')_{\varepsilon_v^p} = \left(\frac{\partial p_c'}{\partial \varepsilon_v^p}\right), \qquad (p_c')_\theta = \left(\frac{\partial p_c'}{\partial \theta}\right), \qquad (p_c')_{t_v} = \left(\frac{\partial p_c'}{\partial t_v}\right)$$

Recalling the Modified Cam-Clay (MCC) yield locus expression

$$f = q^2 - M^2 p'(p_c' - p') \tag{5.24}$$

and substituting the final hardening relationship (Equation 5.18) into the MCC yield function (Equation 5.24) yields;

$$f = q^2 - M^2 p' \left[p_{c0}' \exp(\tilde{\beta}\varepsilon_v^p)\left(\frac{t_v}{t_{vi}}\right)^{\tilde{\omega}} \left\{1 - \gamma \log\left(\frac{\theta}{\theta_0}\right)\right\} - p'\right] \tag{5.25}$$

5.6 Thermo-plasticity

The plastic strain rate can be obtained using the flow rule as follows;

$$\dot{\boldsymbol{\varepsilon}}^{\boldsymbol{p}} = \dot{\lambda}\frac{\partial g}{\partial \boldsymbol{\sigma}} \tag{5.26}$$

where g is the plastic potential (a curve to which the directions of plastic strain increments are normal) and $\dot{\lambda}$ is the plastic multiplier. In the MCC framework, the plastic potential g coincides with the yield locus f, (i.e. $g = f$). The volumetric plastic strain rate can be written as;

$$\dot{\varepsilon}_v^p = \dot{\lambda}\frac{\partial f}{\partial p} \tag{5.27}$$

Substituting Equation 5.4 into Equation 5.10 gives

$$\dot{\boldsymbol{\sigma}} = \boldsymbol{D}^{\boldsymbol{me}}(\dot{\boldsymbol{\varepsilon}} - \dot{\boldsymbol{\varepsilon}}^{\boldsymbol{te}} - \dot{\boldsymbol{\varepsilon}}^{\boldsymbol{p}} - \dot{\boldsymbol{\varepsilon}}^{\boldsymbol{t}}) + \boldsymbol{D}^{\boldsymbol{te}}\dot{\theta} \tag{5.28}$$

Applying thermo-elasticity and the associative plastic flow rule to Equation 5.28 yields,

$$\dot{\boldsymbol{\sigma}} = \boldsymbol{D}^{\boldsymbol{me}}(\dot{\boldsymbol{\varepsilon}}) - (\boldsymbol{D}^{\boldsymbol{me}}\boldsymbol{C}^{\boldsymbol{Te}} - \boldsymbol{D}^{\boldsymbol{te}})\dot{\theta} - \boldsymbol{D}^{\boldsymbol{me}}\dot{\lambda} f_{\boldsymbol{\sigma}} - \boldsymbol{D}^{\boldsymbol{me}}\dot{\boldsymbol{\varepsilon}}^{\boldsymbol{t}} \tag{5.29}$$

Equation 5.29 can be substituted in to the consistency condition (5.20), yielding

$$\begin{aligned} f_{\sigma}\{\boldsymbol{D}^{\boldsymbol{me}}(\dot{\varepsilon}) - (\boldsymbol{D}^{\boldsymbol{me}}\boldsymbol{C}^{\boldsymbol{Te}} - \boldsymbol{D}^{\boldsymbol{te}})\dot{\theta} - \boldsymbol{D}^{\boldsymbol{me}}\dot{\lambda} f_{\boldsymbol{\sigma}} - \boldsymbol{D}^{\boldsymbol{me}}\dot{\boldsymbol{\varepsilon}}^{\boldsymbol{t}}\} \\ + f_{p'_c}\left\{(p'_c)_{\varepsilon_v^p}(\dot{\lambda} f_p) + (p'_c)_{\theta}(\dot{\theta}) + (p'_c)_{t_v}(\dot{t_v})\right\} = 0 \end{aligned} \tag{5.30}$$

From equation 5.30 the plastic multiplier is given as

$$\begin{aligned} \dot{\lambda} = \chi\big[f_{\boldsymbol{\sigma}}\boldsymbol{D}^{\boldsymbol{me}}(\dot{\boldsymbol{\varepsilon}} - \dot{\boldsymbol{\varepsilon}}^{\boldsymbol{t}}) + \big(f_{p'_c}(p'_c)_{\theta} - f_{\boldsymbol{\sigma}}\boldsymbol{D}^{\boldsymbol{me}}\boldsymbol{C}^{\boldsymbol{Te}} + f_{\boldsymbol{\sigma}}\boldsymbol{D}^{\boldsymbol{te}}\big)\dot{\theta} \\ + f_{p'_c}(p'_c)_{t_v}(\dot{t_v})\big] \end{aligned} \tag{5.31}$$

where $(1/\chi) = f_{\boldsymbol{\sigma}}\boldsymbol{D}^{\boldsymbol{me}} f_{\boldsymbol{\sigma}} - f_{p'_c}(p'_c)_{\varepsilon_v^p} f_{\boldsymbol{\sigma}}$

The term $-f_{\boldsymbol{\sigma}}\boldsymbol{D}^{\boldsymbol{me}}\boldsymbol{C}^{\boldsymbol{Te}} + f_{\boldsymbol{\sigma}}\boldsymbol{D}^{\boldsymbol{te}}$ can be algebraically manipulated as:

$$\begin{aligned} & f_{\boldsymbol{\sigma}}(\boldsymbol{D}^{\boldsymbol{te}} - \boldsymbol{D}^{\boldsymbol{me}}\boldsymbol{C}^{\boldsymbol{Te}}) \\ & = f_{\boldsymbol{\sigma}}\left(\boldsymbol{D}^{\boldsymbol{te}} - \boldsymbol{D}^{\boldsymbol{me}}\frac{1}{3}\beta_s\boldsymbol{\delta}\right) \\ & = f_{\boldsymbol{\sigma}}\left\{-\beta_s K\boldsymbol{\delta} - \frac{1}{3}\beta_s(3K)\boldsymbol{\delta}\right\} \\ & = -2K\beta_s f_{\boldsymbol{\sigma}}\boldsymbol{\delta}_{\boldsymbol{ij}} \\ & = 2f_{\boldsymbol{\sigma}}\boldsymbol{D}^{\boldsymbol{te}} \end{aligned} \tag{5.32}$$

Therefore the final form for the plastic multiplier is given as;

$$\dot{\lambda} = \frac{1}{\chi}\big[f_{\boldsymbol{\sigma}}\boldsymbol{D}^{\boldsymbol{me}}(\dot{\boldsymbol{\varepsilon}} - \dot{\boldsymbol{\varepsilon}}^{\boldsymbol{t}}) + \big(f_{p'_c}(p'_c)_{\theta} + 2f_{\boldsymbol{\sigma}}\boldsymbol{D}^{\boldsymbol{te}}\big)\dot{\theta} + f_{p'_c}(p'_c)_{t_v}(\dot{t_v})\big] \tag{5.33}$$

The partial derivatives of f are given by

$$\begin{gathered} f_{p'} = M^2(2p' - p'_c) \\ f_q = 2q \\ f_{p'_c} = -M^2 p \end{gathered} \qquad 5.34$$

and the partial derivatives of p'_c are given by

$$(p'_c)_{\varepsilon_v^p} = \tilde{\beta} p'_{c0} \exp(\tilde{\beta}\varepsilon_v^p)\left(\frac{t_v}{t_{vi}}\right)^{\widetilde{\omega}}\left\{1 - \gamma \log\left(\frac{\theta}{\theta_0}\right)\right\} \qquad 5.35$$

$$(p'_c)_\theta = -\gamma p'_{c0} \exp(\tilde{\beta}\varepsilon_v^p)\left(\frac{t_v}{t_{vi}}\right)^{\widetilde{\omega}}\left(\frac{1}{\theta}\right) \qquad 5.36$$

$$(p'_c)_{t_v} = \left(\frac{\widetilde{\omega}}{t_{vi}}\right) p'_{c0} \exp(\tilde{\beta}\varepsilon_v^p)\left(\frac{t_v}{t_{vi}}\right)^{\widetilde{\omega}-1}\left\{1 - \gamma \log\left(\frac{\theta}{\theta_0}\right)\right\} \qquad 5.37$$

5.7 General stress-strain rate equations

Substituting the expression for thermo elastic strain (Equation 5.7) into Equation 5.28 gives

$$\dot{\boldsymbol{\sigma}} = \boldsymbol{D^{me}}(\dot{\boldsymbol{\varepsilon}} - \dot{\boldsymbol{\varepsilon}}^{\boldsymbol{p}} - \dot{\boldsymbol{\varepsilon}}^{\boldsymbol{t}}) + (\boldsymbol{D^{te}} - \boldsymbol{D^{me}}\boldsymbol{C^{Te}})\dot{\theta} \qquad 5.38$$

Applying the associative flow rule for the plastic strain rate (5.26) gives

$$\dot{\boldsymbol{\sigma}} = \boldsymbol{D^{me}}\left\{\dot{\boldsymbol{\varepsilon}} - \left(\dot{\lambda}\frac{\partial f}{\partial \boldsymbol{\sigma}}\right) - \dot{\boldsymbol{\varepsilon}}^{\boldsymbol{t}}\right\} + (\boldsymbol{D^{te}} - \boldsymbol{D^{me}}\boldsymbol{C^{Te}})\dot{\theta} \qquad 5.39$$

Applying the expression for the plastic multiplier (Equation 5.33) into Equation 5.39 yields

$$\begin{aligned} \dot{\boldsymbol{\sigma}} = {} & \{(\boldsymbol{D^{me}} - \boldsymbol{D^{me}}\chi \boldsymbol{f_\sigma f_\sigma} \boldsymbol{D^{me}})(\dot{\boldsymbol{\varepsilon}} - \dot{\boldsymbol{\varepsilon}}^{\boldsymbol{t}})\} - \boldsymbol{D^{me}}\chi\big(B\dot{\theta} + f_{p'_c}(p'_c)_{t_v}(\dot{t_v})\big)\boldsymbol{f_\sigma} \\ & + (\boldsymbol{D^{te}} - \boldsymbol{D^{me}}\boldsymbol{C^{Te}})\dot{\theta} \end{aligned} \qquad 5.40$$

where $B = f_{p'_c}(p'_c)_\theta - \boldsymbol{f_\sigma}\boldsymbol{D^{me}}\boldsymbol{C^{Te}} + \boldsymbol{f_\sigma}\boldsymbol{D^{te}}$

From Equation 5.40 the general form of the stress-strain rate relationship can be written as

$$\dot{\boldsymbol{\sigma}} = \boldsymbol{D^{mep}}\dot{\boldsymbol{\varepsilon}} - \dot{\boldsymbol{\sigma}}^t \qquad 5.41$$

where $\boldsymbol{D^{mep}}$ is the fourth order thermo-elasto-plastic stress strain tensor

$$\boldsymbol{D^{mep}} = \big(\boldsymbol{D^{me}} - \chi(\boldsymbol{D^{me}}\boldsymbol{f_\sigma f_\sigma}\boldsymbol{D^{me}})\big) \qquad 5.42$$

and $\dot{\boldsymbol{\sigma}}^t$ is the stress relaxation rate given by

$$\dot{\boldsymbol{\sigma}}^t = \boldsymbol{D^{mep}}\dot{\boldsymbol{\varepsilon}}^{\boldsymbol{t}} + \chi f_{p'_c}(p'_c)_{t_v}(\dot{t_v})\boldsymbol{D^{me}}\boldsymbol{f_\sigma} + (\boldsymbol{D^{me}}\chi B\boldsymbol{f_\sigma} + \boldsymbol{D^{te}} - \boldsymbol{D^{me}}\boldsymbol{C^{Te}})\dot{\theta} \qquad 5.43$$

If creep and temperature effects are ignored (i.e. $\dot{\boldsymbol{\varepsilon}}^{\boldsymbol{t}} = 0$, $f_{p'_c}(p'_c)_{t_v}(\dot{t_v}) = 0$ and $\dot{\theta} = 0$,) then $\dot{\boldsymbol{\sigma}}^t = 0$, and the formulation revert the classical elasto-plasticity expression. If only creep is ignored, the resulting expression is similar to Laloui's thermo-plasticity model. In the general case, however, where both creep and temperature effects are considered the stress-strain relationship is given by Equation 5.41;

5.8 Creep strain rate

As suggested by Borja and Kavazanjian (1985) the direction of the creep strain rate $\dot{\varepsilon}^t$ is obtained from the normality rule applied on the equivalent yield locus as follows;

$$\dot{\boldsymbol{\varepsilon}}^{\boldsymbol{t}} = \varphi \frac{\partial f}{\partial \boldsymbol{\sigma}} \qquad 5.44$$

where φ is a proportionality factor that determines the magnitude of the strain rate and f is the yield surface before creep deformation takes place referred to here as the equivalent yield locus with the size of equivalent preconsolidation pressure p_0'. The latter is given by

$$p_0' = p' + \frac{q^2}{M^2 p} \leq p_c' \qquad 5.45$$

where p_0' is the preconsolidation pressure, before creep deformation takes place. For normally consolidated clays, before the onset of creep, $p_0' = p_c'$

Accordingly, the equivalent preconsolidation pressure also depends on temperature from Laloui's thermal hardening law (Equation 2.25). Therefore, the size of the initial yield locus also depends on temperature and can be written as

$$p_0' \left\{1 - \gamma \log\left(\frac{\theta}{\theta_0}\right)\right\} = p' + \frac{q^2}{M^2 p} \leq p_c' \qquad 5.46$$

The proportionality factor φ can be determined using two empirical models of volumetric and deviatoric creep respectively. The first model used is Taylor's secondary compression line from which the volumetric creep is determined while the second one is the Singh-Mitchel creep law that describes the deviatoric creep.

5.8.1 Temperature dependence on volumetric creep strain rate

Few researchers investigated the dependence of volumetric creep on temperature (Campanella and Mitchell, 1968, Towhata et al., 1993). Findings show that, during the secondary compression stage, when temperature is increased over a comparatively small time period, an instant compression is observed (Towhata et al., 1993). This instant compression due to temperature increase is taken in to account in Laloui's thermo-plasticity model (Laloui and Cekerevac, 2003, 2008, Laloui and Francois, 2009) and referred to as "thermal loading" (Section 2.3.3). Also the secondary compression index (ψ_α) is independent of temperature as seen in Figure 145. Nevertheless, researchers found that for organic soils such as peats, the secondary compression index, (ψ_α) increases with temperature (Fox and Edil, 1996).

In this context it is assumed that the secondary compression index is constant i.e. inorganic soils are assumed.

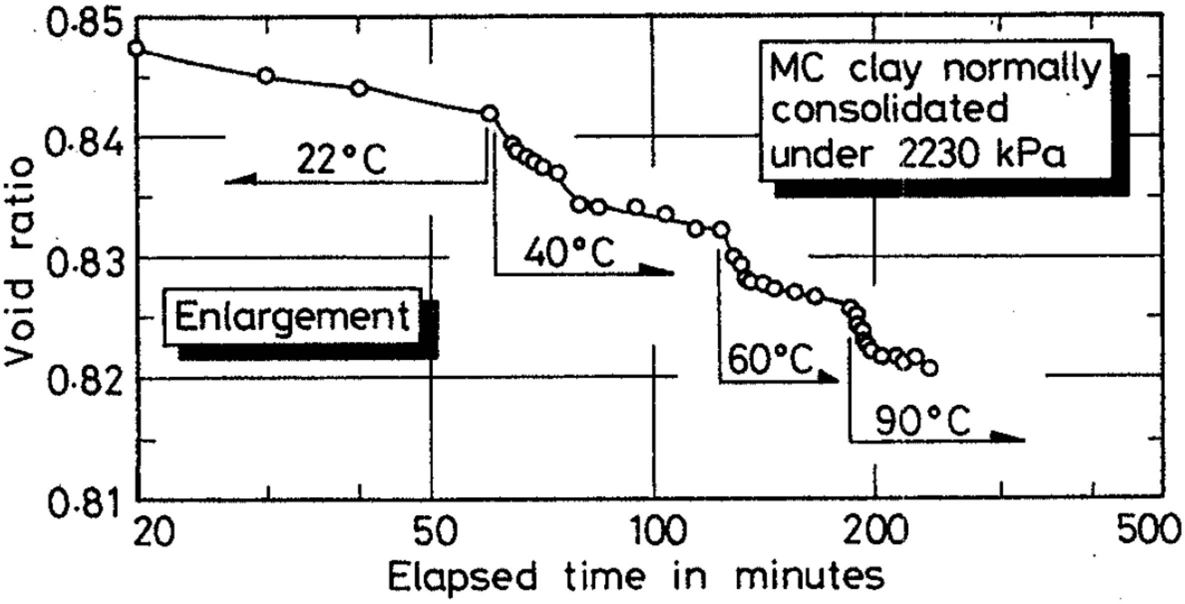

Figure 145: Secondary compression with different temperature (Towhata et al., 1993)

5.8.2 Dependence of deviatoric strain rate on temperature

Deviatoric creep was also investigated to determine the relationship between the strain rate and temperature.

The Singh-Mitchell creep equation for axial strain rate is given as;

$$\dot{\varepsilon}_a^t = A \exp \bar{\alpha}\bar{D} \left(\frac{t_0}{t}\right)^m \qquad 5.47$$

where $A, \bar{\alpha}$ and m are parameters and $\bar{D}$ is a measure of the applied deviatoric stress.

The influence of parameter m was explained in Section 2.4.2. Eriksson (1989) carried out an experimental study to investigate the effects of temperature on deviatoric creep of soils. His findings show that the parameter m depends on temperature and varies as in Figure 146. As a result, the following linear relationship between the parameter m and temperature was proposed by Eriksson (1989).

$$m = 1.03 - 0.0072\theta \qquad 5.48$$

where θ is the temperature in ℃.

Equation 5.48 is based on creep tests up to a temperature of 50℃. This simple linear law makes it possible that the value of m may become unrealistically small or even negative at higher temperatures. To prevent this, here m is not allowed to become lower than the value of 0.73 which is the minimum value obtained in the test at 50℃ carried out by Eriksson (1989). Therefore, a twofold expression for parameter m is proposed as;

$$\begin{aligned} m &= 1.03 - 0.0072\theta \qquad && \theta \leq 50^oC \\ m &= 0.73 && \theta > 50^oC \end{aligned} \tag{5.49}$$

Accordingly, the Singh-Mitchell creep equation can now be written as

$$\begin{aligned} \dot{\varepsilon}_a^t &= A \exp \bar{\alpha}\bar{D} \left(\frac{t_0}{t}\right)^{(1.03-0.0072\theta)} \qquad && \theta \leq 50^oC \\ \dot{\varepsilon}_a^t &= A \exp \bar{\alpha}\bar{D} \left(\frac{t_0}{t}\right)^{0.73} && \theta > 50^oC \end{aligned} \tag{5.50}$$

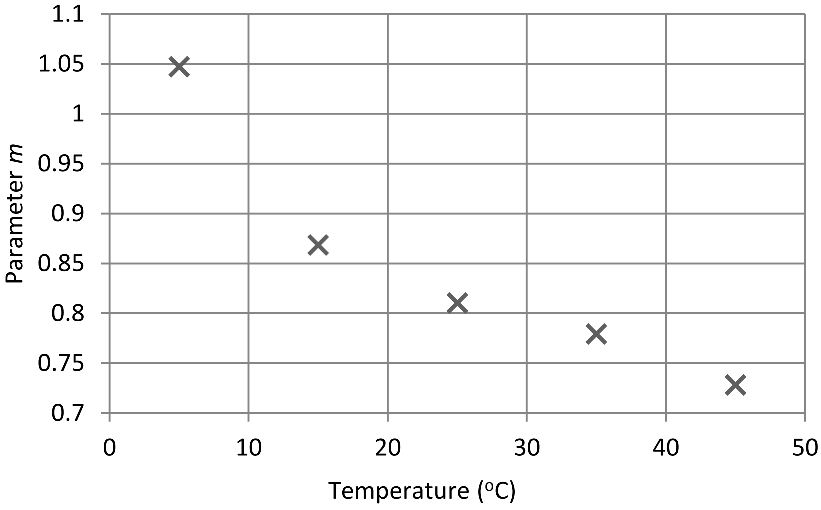

Figure 146: Variation of creep parameter, *m*, with temperature (Eriksson, 1989)

5.8.3 Determination of φ using volumetric scaling

From Taylor's secondary compression equation, the volumetric strain rate is given by

$$\dot{\varepsilon}_v^t = \frac{\psi}{(1+e)t_v} \tag{5.51}$$

Also, the volumetric strain rate can be calculated using an associative flow rule from the equivalent yield function.

$$\dot{\varepsilon}_v^t = \frac{\psi}{(1+e)t_v} = \varphi \frac{\partial f}{\partial p'} \tag{5.52}$$

Finally combining Equation 5.51 and 5.52 , φ is found as

$$\varphi = \frac{\psi}{(1+e)t_v}\left(\frac{\partial f}{\partial p'}\right)^{-1} = \frac{\psi}{(1+e)t_v\left[2p' - p'_0\left\{1-\gamma\log\left(\frac{\theta}{\theta_0}\right)\right\}\right]} \tag{5.53}$$

Therefore, the creep strain rate can be written as

$$\dot{\boldsymbol{\varepsilon}}^{\boldsymbol{t}} = \frac{\psi}{(1+e)t_v\left[2p' - p'_0\left\{1-\gamma\log\left(\frac{\theta}{\theta_0}\right)\right\}\right]}\left(\frac{\partial f}{\partial \boldsymbol{\sigma}}\right) \tag{5.54}$$

In isothermal conditions, the expression 5.54 is singular when $p' = p'_0/2$ (i.e. when the stress point is at critical state) and at higher deviatoric stress levels, (i.e. $p' \to p'_0/2$) it overpredicts $\dot{\boldsymbol{\varepsilon}}^{\boldsymbol{t}}$. Therefore, volumetric scaling is used for volumetric creep whereas deviatoric scaling for deviatoric creep. The deviatoric scaling will be discussed in Section 5.8.5.

5.8.4 Volumetric age of soils (t_v)

As discussed in Section 5.4 , soil ages volumetrically with time. If there is no externally applied load, its age increases linearly with natural time. If a normally consolidated soil specimen is allowed to creep, the total time period that the specimen remains at constant stress is the volumetric age of the soil ($t_v = t$). If an over consolidated soil specimen is allowed to creep, the total volumetric age of the soil can be written as (Figure 147);

$$t_v = t_0 + t \tag{5.55}$$

where t_0 is the time it would take the soil to creep to its current void ratio, if it were to start from the normal compression line and remains at constant stress. The rate of volumetric aging is given by

$$\dot{t}_v = \dot{t}_0 + \dot{t} \tag{5.56}$$

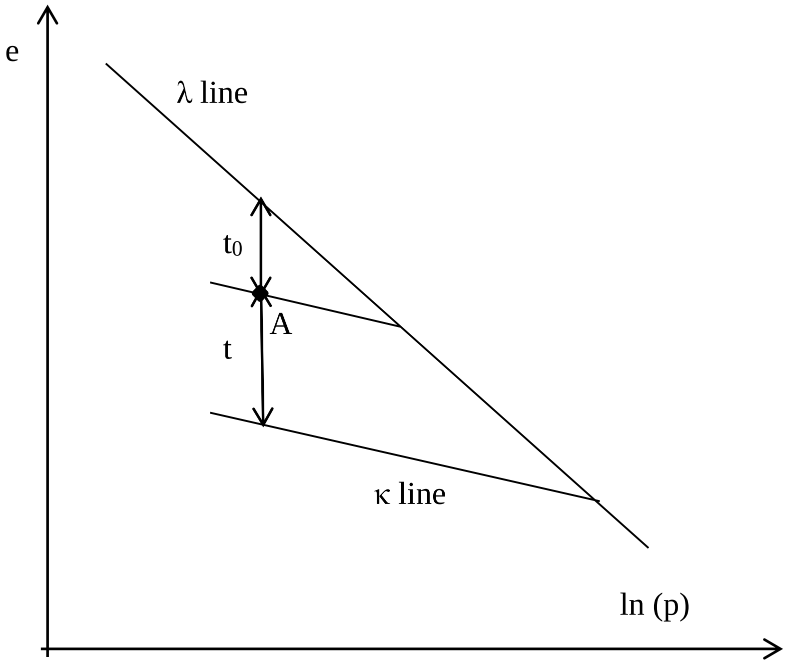

Figure 147: Determination of volumetric age of soil

5.8.5 Determination of φ using deviatoric scaling

For deviatoric creep, the Singh-Mitchell equation can be used to determine φ, (i.e. deviatoric scaling can be applied), by equating the creep strain rate predicted by the Singh-Mitchell equation to that predicted using the associative flow rule. The strain rate tensor can finally be written as follows (Borja and Kavazanjian, 1985);

$$\dot{\boldsymbol{\varepsilon}}^{\boldsymbol{t}} = \sqrt{\frac{3}{2}} A e^{\overline{\alpha q}} \left[\frac{t_i}{t}\right]^{(m)} \left[\frac{\partial f}{\partial \boldsymbol{\sigma}} \times \frac{\partial f}{\partial \boldsymbol{\sigma}} - \frac{1}{3}\left(\frac{\partial f}{\partial p}\right)^2\right]^{-\left(\frac{1}{2}\right)} \frac{\partial f}{\partial \boldsymbol{\sigma}} \qquad 5.57$$

Equation 5.57 is singular when $p' = p_0'$ (isotropic stress conditions) and therefore it overpredicts the strain rate in near isotropic stress conditions. Therefore, for isotropic loading volumetric scaling is more suitable (Section 5.8.3) to determine the strain rate.

Volumetric and deviatoric scalings predict different expressions for φ. As described in Sections 5.8.3 and 5.8.5 volumetric scaling is suitable to obtain volumetric creep whereas deviatoric scaling is to obtain deviatoric creep. This can be summarised as:

$$\dot{\varepsilon}_v^t = \varphi_v \frac{\partial f}{\partial p'} \qquad 5.58$$

$$\dot{\varepsilon}_q^t = \varphi_q \frac{\partial f}{\partial q} \qquad 5.59$$

In the above, φ_v and φ_q are proportionality factors obtained from volumetric and deviatoric scaling respectively.

5.9 Modified landslide model

Cecinato's landslide equations will now be modified to include the constitutive model relations developed in the above sections.

Cecinato (2009) assumed that the shear band is in plane strain conditions and the soil is at critical state. Of these, only the assumption of plane strain is considered for this analysis. It is also assumed that the soil is initially normally consolidated (i.e. $\dot{t}_v = \dot{t}$).

With reference to Figure 52, axis x is considered as the direction of movement, axis y is the direction of zero principal strain and axis z is perpendicular to the direction of movement. Therefore,

$$\begin{aligned} &\varepsilon_{yy} = 0 \\ &\gamma_{zy} = \gamma_{yz} = 0 \\ &\gamma_{xy} = \gamma_{yx} = 0 \end{aligned} \tag{5.60}$$

The strain tensor becomes,

$$\begin{pmatrix} \varepsilon_{xx} & \varepsilon_{xz} & 0 \\ \varepsilon_{xz} & \varepsilon_{zz} & 0 \\ 0 & 0 & 0 \end{pmatrix} = \begin{pmatrix} \varepsilon_{xx} & (1/2)\gamma_{xz} & 0 \\ (1/2)\gamma_{xz} & \varepsilon_{zz} & 0 \\ 0 & 0 & 0 \end{pmatrix} \tag{5.61}$$

5.10 Heat Equation

The heat equation gives the evolution of temperature with time and space. This can be written as;

$$\frac{\partial\theta}{\partial t} = k_m \frac{\partial^2\theta}{\partial z^2} + \frac{D_w}{C_f} \tag{5.62}$$

where D_w is the dissipated work within the shear band. According to the constitutive model presented above, irrecoverable work is due to both plastic and creep deformations. Therefore, the dissipation term could be split in to two parts

$$D_w = D_p + D_t \tag{5.63}$$

where subscripts p and t denotes the plastic and time dependent dissipation respectively. These two terms will be dealt with separately hereafter.

In the following two subsections 5.10.1 and 5.10.2, σ_i is used to denote the vector of the principal stresses, i.e.

$$\sigma_i = \begin{pmatrix} \sigma_1 \\ \sigma_2 \\ \sigma_3 \end{pmatrix} \tag{5.64}$$

and repeated indices means summation over the index, for example:

$$\sigma_i \sigma_i = \sum_{i=1}^{3} \sigma_i \sigma_i = \sigma_1 \sigma_1 + \sigma_2 \sigma_2 + \sigma_3 \sigma_3 \tag{5.65}$$

5.10.1 Dissipation due to creep

Volumetric and deviatoric creep strain rates were obtained from two different empirical relations (Section 5.8). Dissipation due to creep in terms of stress and strain invariants could be written as

$$D_t = p' \dot{\varepsilon}_v^t + q \dot{\varepsilon}_q^t \tag{5.66}$$

where p' and q are the effective mean stress and the deviatoric stress respectively. From the normality rule applied on an equivalent yield surface, the volumetric and the distortional strain rates can be written as,

$$\dot{\varepsilon}_v^t = \varphi_v \frac{\partial f}{\partial p'}, \qquad \dot{\varepsilon}_q^t = \varphi_q \frac{\partial f}{\partial q} \tag{5.67}$$

Substituting the corresponding strain rate equations (Borja and Kavazanjian, 1985) into Equation 5.67 yields,

$$D_t = p' \left\{ \frac{\psi}{(1+e) M^2 (2p' - p_0) t_v} \right\} \frac{\partial f}{\partial p'} + q \left\{ \sqrt{\frac{3}{2}} A \exp \bar{\alpha} \bar{D} \left(\frac{(t_d)_i}{t_d} \right)^m \frac{1}{\sqrt{\bar{Q}}} \right\} \frac{\partial f}{\partial q} \tag{5.68}$$

where, in principal stress space,

$$\bar{Q} = \left[\frac{\partial f}{\partial \sigma_i} \frac{\partial f}{\partial \sigma_i} - \frac{1}{3} \left(\frac{\partial f}{\partial p'} \right)^2 \right] \tag{5.69}$$

In the Equation 5.68, the size of the equivalent yield surface is given by p_0. For normally consolidated soil, p_0 can be considered as the mean effective stress applied to the soil before the onset of creep. Therefore, the equivalent yield surface f is the initial yield surface before creep. In principal stress space,

$$\begin{gathered} \frac{\partial f}{\partial p'} = M^2 (2p' - p_0), \qquad \frac{\partial f}{\partial q} = 2q \\ \frac{\partial p'}{\partial \sigma_i} = \frac{1}{3}, \qquad \frac{\partial q}{\partial \sigma_i} = \frac{3(\sigma_i - p')}{2q} \end{gathered} \tag{5.70}$$

Using the chain rule, the derivative of f with respect to σ_i can be written as;

$$\frac{\partial f}{\partial \sigma_i} = \frac{\partial f}{\partial p'}\frac{\partial p'}{\partial \sigma_i} + \frac{\partial f}{\partial q}\frac{\partial q}{\partial \sigma_i} \qquad 5.71$$

$$= 3(\sigma_i - p') + \frac{M^2}{3}(2p' - p_0)$$

Substituting the definitions of $\frac{\partial f}{\partial \sigma_i}$ and $\frac{\partial f}{\partial p'}$ into Equation 5.69 gives,

$$\begin{aligned}\bar{Q} = \frac{M^4}{3}(2p' - p_0)^2 + 9(\sigma_i - p')^2 \\ - 2M^2(2p' - p_0)(\sigma_i - p') \\ - \frac{M^4}{3}(2p' - p_0)^2\end{aligned} \qquad 5.72$$

$$\bar{Q} = 9(\sigma_i - p')^2 = 9\{(\sigma_1 - p')^2 + (\sigma_2 - p')^2 + (\sigma_3 - p')^2\}$$

Finally, the term $\bar{Q}$ can be written as;

$$\bar{Q} = 6\{(\sigma_1 - \sigma_2)^2 + (\sigma_2 - \sigma_3)^2 + (\sigma_3 - \sigma_1)^2\} = 6q^2 \qquad 5.73$$

Substituting Equation 5.73 into Equation 5.68 the dissipation term becomes

$$D_t = p'\left\{\frac{\psi}{(1+e)t_v}\right\} + q\left\{A \exp \bar{\alpha}\bar{D}\left(\frac{t_0}{t}\right)^m\right\} \qquad 5.74$$

Equation 5.74 is the part of the dissipation term in heat equation 5.62 that is due to creep. In addition to creep, energy will be lost due to plastic work. In the following subsection the derivation of plastic dissipation is presented.

5.10.2 Dissipation due to plastic work

In principal stress space, the dissipation due to plastic work can be written as

$$D_p = \sigma_1\dot{\varepsilon}_1^p + \sigma_2\dot{\varepsilon}_2^p + \sigma_2\dot{\varepsilon}_3^p \qquad 5.75$$

Substituting the relationship for plastic strain rate from the associative flow rule yields:

$$D_p = \dot{\lambda}\left(\sigma_1\frac{\partial f}{\partial \sigma_1} + \sigma_2\frac{\partial f}{\partial \sigma_2} + \sigma_3\frac{\partial f}{\partial \sigma_3}\right) \qquad 5.76$$

where σ_1, σ_2 and σ_3 are the principal stresses, f is the yield locus (the Modified Cam Clay yield locus is used here) and $\dot{\lambda}$ is the plastic multiplier. The derivative of the yield locus with respect to the principal stress components is expressed as;

$$\frac{\partial f}{\partial \sigma_i} = \frac{\partial f}{\partial p'}\frac{\partial p'}{\partial \sigma_i} + \frac{\partial f}{\partial q}\frac{\partial q}{\partial \sigma_i} = 3(\sigma_i - p') + \frac{M^2}{3}(2p' - p'_c) \qquad 5.77$$

Equation 5.77 can be substituted into Equation 5.76 to obtain D_p, yielding

$$\begin{aligned} D_p = \dot{\lambda}\Bigg[&\sigma_1\left\{3(\sigma_1 - p') + \frac{M^2}{3}(2p' - p'_c)\right\} \\ &+ \sigma_2\left\{3(\sigma_2 - p') + \frac{M^2}{3}(2p' - p'_c)\right\} \\ &+ \sigma_3\left\{3(\sigma_3 - p') + \frac{M^2}{3}(2p' - p'_c)\right\}\Bigg] \end{aligned} \qquad 5.78$$

By employing the definition of mean effective stress the above gives

$$\begin{aligned} D_p &= \dot{\lambda}\big(2({\sigma_1}^2 + {\sigma_2}^2 + {\sigma_3}^2 - \sigma_1\sigma_2 - \sigma_2\sigma_3 - \sigma_3\sigma_1) \\ &\quad + p'M^2(2p' - p'_c)\big) \\ &= \dot{\lambda}\big(2q^2 + p'M^2(2p' - p'_c)\big) \end{aligned} \qquad 5.79$$

Recalling Modified Cam Clay yield locus;

$$f = q^2 + p'M^2(p' - p'_c) = 0 \qquad 5.80$$

After substituting 5.80 into 5.79, the final form of D_p becomes

$$D_p = \dot{\lambda}(q^2 + (p'M)^2) \qquad 5.81$$

It should be noted that the above expression (5.81) is derived for any stress state applied. An expression for the plastic multiplier $\dot{\lambda}$ in terms of stress invariants is derived in the following subsection.

5.10.2.1 Plastic multiplier ($\dot{\lambda}$)

In section 5.6, the plastic multiplier was calculated as (Equation 5.33)

$$\dot{\lambda} = \chi\left[f_{\boldsymbol{\sigma}}\boldsymbol{D^{me}}(\dot{\boldsymbol{\varepsilon}} - \dot{\boldsymbol{\varepsilon}}^{\boldsymbol{t}}) + \left(f_{p'_c}(p'_c)_\theta + 2f_{\boldsymbol{\sigma}}\boldsymbol{D^{te}}\right)\dot{\theta} + f_{p'_c}(p'_c)_{t_v}(\dot{t_v})\right] \qquad 5.82$$

where $1/\chi = f_{\boldsymbol{\sigma}}\boldsymbol{D^{me}}f_{\boldsymbol{\sigma}} - f_{p'_c}(p'_c)_{\varepsilon_v^p}f_p$

It was further assumed that the soil was normally consolidated before creep commenced, therefore $\dot{t_v} = 1$ (Section 5.8.4). Without any loss of generality, it is possible to split the terms of Equation 5.82 into spherical and deviatoric parts (Mase, 1970):

$$\begin{aligned} &f_{\boldsymbol{\sigma}}\boldsymbol{D^{me}}(\dot{\boldsymbol{\varepsilon}}-\dot{\boldsymbol{\varepsilon}}^{\boldsymbol{t}}) = Kf_p(\dot{\varepsilon}_v-\dot{\varepsilon}_v^t)+\ 3Gf_q(\dot{\varepsilon}_q-\dot{\varepsilon}_q^t) \\ &2f_{\boldsymbol{\sigma}}\boldsymbol{D^{te}} = -2K\beta_s f_p \\ &f_{\boldsymbol{\sigma}}\boldsymbol{D^{me}}f_{\boldsymbol{\sigma}} = K{f_p}^2+3G{f_q}^2 \end{aligned} \tag{5.83}$$

Partial derivatives of f are given by

$$\begin{aligned} &f_{p'} = M^2(2p'-p_c') \\ &f_q = 2q \\ &f_{p_c'} = -M^2p \end{aligned} \tag{5.84}$$

and partial derivatives of p_c' are given by

$$\begin{aligned} &(p_c')_{\varepsilon_v^p} = \tilde{\beta}p_{c0}'\exp(\tilde{\beta}\varepsilon_v^p)\left(\frac{t_v}{t_{vi}}\right)^{\tilde{\omega}}\left\{1-\gamma\log\left(\frac{\theta}{\theta_0}\right)\right\} \\ &(p_c')_{\theta} = -\gamma p_{c0}'\exp(\tilde{\beta}\varepsilon_v^p)\left(\frac{t_v}{t_{vi}}\right)^{\tilde{\omega}}\left(\frac{1}{\theta}\right) \\ &(p_c')_{t_v} = \left(\frac{\tilde{\omega}}{t_{vi}}\right)p_{c0}'\exp(\tilde{\beta}\varepsilon_v^p)\left(\frac{t_v}{t_{vi}}\right)^{\tilde{\omega}-1}\left\{1-\gamma\log\left(\frac{\theta}{\theta_0}\right)\right\} \end{aligned} \tag{5.85}$$

Finally, using the above the plastic multiplier can be expressed as;

$$\dot{\lambda} = F_0(\dot{\varepsilon}_v-\dot{\varepsilon}_v^t)+F_1(\dot{\varepsilon}_q-\dot{\varepsilon}_q^t)+F_2\dot{\theta}+F_3 \tag{5.86}$$

where

$$F_0 = \chi Kf_p$$

$$F_1 = \chi 3Gf_q$$

$$F_2 = \chi\big(f_{p_c'}(p_c')_{\theta}-2K\beta_s f_p\big)$$

$$F_3 = f_{p_c'}(p_c')_{t_v}(\dot{t_v})$$

and

$$\frac{1}{\chi} = K{f_p}^2+3G{f_q}^2-f_{p_c'}(p_c')_{\varepsilon_v^p}f_p$$

In terms strain rate tensor components, the deviatoric (distortional) strain rate can be written as (Wood, 1991).

$$\dot{\varepsilon}_q = \frac{1}{3}\sqrt{2\left[\big(\dot{\varepsilon}_{yy}-\dot{\varepsilon}_{zz}\big)+(\dot{\varepsilon}_{zz}-\dot{\varepsilon}_{xx})+\big(\dot{\varepsilon}_{zz}-\dot{\varepsilon}_{yy}\big)+3\big(\dot{\gamma}_{xy}^2+\dot{\gamma}_{yz}^2+\dot{\gamma}_{xz}^2\big)\right]} \tag{5.87}$$

and the total volumetric strain rate can be written as

$$\dot{\varepsilon}_v = \dot{\varepsilon}_{xx}+\dot{\varepsilon}_{yy}+\dot{\varepsilon}_{zz} \tag{5.88}$$

As mentioned in Section 5.9, due to plane strain conditions $\dot{\varepsilon}_{yy} = \dot{\gamma}_{zy} = \dot{\gamma}_{yz} = 0$. Moreover, one dimensional assumption, as shown in Figure 52, implies $\dot{\varepsilon}_{xx} = 0$. Therefore, the deviatoric strain is reduced to

$$\dot{\varepsilon}_q = \frac{1}{3}\sqrt{4\dot{\varepsilon}_v^2 + 3\dot{\gamma}_{xz}^2} \qquad 5.89$$

Taking the square of both sides gives

$$\dot{\varepsilon}_q^2 = \frac{1}{9}(4\dot{\varepsilon}_v^2 + 3\dot{\gamma}_{xz}^2) \qquad 5.90$$

The total volumetric strain could be decomposed in to elastic, plastic and time dependent parts (Section 5.2). However, in this context it is assumed that the total elastic strain is negligible. Therefore, Equation 5.90 can be written as

$$\dot{\varepsilon}_q^2 = \frac{1}{9}\left(4\left(\dot{\varepsilon}_v^p + \dot{\varepsilon}_v^t\right)^2 + 3\dot{\gamma}_{xz}^2\right) \qquad 5.91$$

From the associative flow rule, the ratio K_q between the volumetric plastic strain rate and the distortional plastic strain rate can be written as

$$K_q = \frac{\dot{\varepsilon}_v^p}{\dot{\varepsilon}_q^p} = \frac{\left(\frac{\partial f}{\partial p'}\right)}{\left(\frac{\partial f}{\partial q}\right)} = \frac{M^2(2p' - p_c')}{2q} \qquad 5.92$$

Substituting Equation 5.92 into 5.91 gives

$$\dot{\varepsilon}_q^2 = \frac{1}{9}\left(4\left(K_q\dot{\varepsilon}_q^p + \dot{\varepsilon}_v^t\right)^2 + 3\dot{\gamma}_{xz}^2\right) \qquad 5.93$$

and $\dot{\varepsilon}_q^p = \dot{\varepsilon}_q - \dot{\varepsilon}_q^t$. Therefore, Equation 5.93 can be written as,

$$\dot{\varepsilon}_q^2 = \frac{1}{9}\left(4\left(K_q\left(\dot{\varepsilon}_q - \dot{\varepsilon}_q^t\right) + \dot{\varepsilon}_v^t\right)^2 + 3\dot{\gamma}_{xz}^2\right) \qquad 5.94$$

$\dot{\varepsilon}_q$ can be derived by solving the quadratic Equation 5.94 and it is given as;

$$\dot{\varepsilon}_q = \frac{-\frac{8}{9}A_qK_q \pm \sqrt{\frac{64}{81}A_q^2K_q^2 - 4\left(\frac{4}{9}K_q^2 - 1\right)\left(\frac{4}{9}A_q^2 + \frac{1}{3}\dot{\gamma}_{xz}^2\right)}}{-2\left(\frac{4}{9}K_q^2 - 1\right)} \qquad 5.95$$

where $A_q = \dot{\varepsilon}_v^t - K_q\dot{\varepsilon}_q^t$. One solution of Equation 5.95 is negative. Therefore, the positive solution has been taken into consideration as the total distortional strain should be a positive.

$\dot{\gamma}_{xz} = \frac{\partial v_x}{\partial z}$ and $v_x = v(z,t)$ is the velocity within the shear band in the direction of movement. A linear profile of $v(z,t)$ within the shear band was assumed as shown in Figure 52 in line with Vardoulakis (2002a). So that,

$$v(z,t) = \left(\frac{z}{Z_b}\right) v_d(t) \tag{5.96}$$

where $v_d(t)$ is the velocity at the top of the shear band i.e. the velocity of the sliding mass and Z_b is the thickness of shear band. Finally, the deviatoric strain rate becomes as a function of the velocity of the sliding mass as follows;

$$\dot{\varepsilon}_q = \frac{-\frac{8}{9}A_q K_q \pm \sqrt{\frac{64}{81}A_q^2 K_q^2 - 4\left(\frac{4}{9}K_q^2 - 1\right)\left(\frac{4}{9}A_q^2 + \frac{v_d^2}{3Z_b^2}\right)}}{-2\left(\frac{4}{9}K_q^2 - 1\right)}$$

5.10.3 Final form of heat equation

The final form of the heat equation can be written as follows. This is done by adopting dissipation due to the effect of both creep and plastic deformations. From Equations 5.62 and 5.63 the complete heat equation can be written as

$$\frac{\partial \theta}{\partial t} = k_m \frac{\partial^2 \theta}{\partial z^2} + \frac{D_p + D_t}{C_f} \tag{5.97}$$

$$D_t = p'\left\{\frac{\psi}{(1+e)t_v}\right\} + q\left\{A \exp \bar{\alpha}\bar{D}\left(\frac{t_{d_i}}{t_d}\right)^m\right\} \tag{5.98}$$

$$D_p = \dot{\lambda}(q^2 + (p'M)^2) \tag{5.99}$$

and

$$\dot{\lambda} = F_0 K_q(\dot{\varepsilon}_q - \dot{\varepsilon}_q^t) + F_1(\dot{\varepsilon}_q - \dot{\varepsilon}_q^t) + F_2\dot{\theta} + F_3 \tag{5.100}$$

Substituting 5.98, 5.99 and 5.100 into 5.97 yields,

$$\frac{\partial \theta}{\partial t} = k_m \frac{\partial^2 \theta}{\partial z^2} + \frac{1}{C_f}\left\{\left((F_0 K_q + F_1)(\dot{\varepsilon}_q - \dot{\varepsilon}_q^t) + F_2\dot{\theta} + F_3\right)(q^2 + (p'M)^2) + p'\left(\frac{\psi}{(1+e)t_v}\right) + q\left(A \exp \bar{\alpha}\bar{D}\left(\frac{t_{d_i}}{t_d}\right)^m\right)\right\} \tag{5.101}$$

Collecting temperature rate terms gives

$$\begin{aligned}\frac{\partial\theta}{\partial t}\left(1-\frac{F_2}{C_f}(q^2+(p'M)^2)\right) &\\ &= k_m\frac{\partial^2\theta}{\partial z^2}\\ &\quad+\frac{1}{C_f}\Big\{\big((F_0K_q+F_1)(\dot{\varepsilon}_q-\dot{\varepsilon}_q^t)+F_3\big)(q^2+(p'M)^2)\\ &\quad+p'\left(\frac{\psi}{(1+e)t_v}\right)+q\left(A\exp\bar{\alpha}\bar{D}\left(\frac{t_{d_i}}{t_d}\right)^m\right)\Big\}\end{aligned}\tag{5.102}$$

Hence, Equation 5.102 can be simplified as;

$$\frac{\partial\theta}{\partial t}=D_i\frac{\partial^2\theta}{\partial z^2}+\frac{1}{B_i}\{C_iA_i+p'\dot{\varepsilon}_v^t+q\dot{\varepsilon}_q^t\}\tag{5.103}$$

where;

$$A_i=(q^2+(p'M)^2)\tag{5.104}$$

$$B_i=C_f-F_2(q^2+(p'M)^2)\tag{5.105}$$

$$D_i=\frac{k_mC_f}{\big(C_f-F_2(q^2+(p'M)^2)\big)}\tag{5.106}$$

$$C_i=\big((F_0K_q+F_1)(\dot{\varepsilon}_q-\dot{\varepsilon}_q^t)+F_3\big)\tag{5.107}$$

5.11 Pore pressure equation

The pore pressure equation gives the excess pore pressure inside the shear band and its surroundings. The same equation given in section 3.3 is used here, i.e.

$$\frac{\partial p}{\partial t}=\frac{\partial}{\partial z}\left(c_v\frac{\partial p}{\partial z}\right)+\lambda_m\frac{\partial\theta}{\partial t}\tag{5.108}$$

where c_v and λ_m are the consolidation and pressurization coefficients respectively. These two parameters were discussed in detail in Sections 3.3.1 and 3.3.2 respectively.

5.12 Landslide model assumptions

According to the constitutive model presented here in this chapter, when a critical state is reached, the creep law becomes redundant as the soil fails. Therefore, at critical state, Equation 5.41 will take the form of Cecinato’s thermo elasto-plastic relationship (Equation 2.43) as described in Section 2.3.4 (i.e. the stress relaxation term $\dot{\boldsymbol{\sigma}}^{\boldsymbol{t}}$, in Equation 5.41 will equal zero). Moreover, hardening with respect to time will also cease to be relevant so that, the model is time independent when a critical state is reached. When the stress state lies inside the yield locus, on the other hand, only creep deformation is expected to occur. Thermo-plastic and creep deformation are expected to occur when the stress state is on the yield locus as well, but not at critical state.

It is reasonable to assume here that the stress state will lie inside the yield locus while a landslide is in the creep phase and will reach a critical state during the collapse stage.

The relationship for the volumetric creep strain rate was derived using the secondary compression theory which predicts that the rate of volumetric deformation reduces with time (Equation 5.51).

In the landslide model presented here it is assumed that by the time slide movement was initiated volumetric creep rate has already become negligible. Therefore, in this analysis, only the shear creep deformation of the slip zone is considered. On this basis, the time dependency of the size of the yield locus can also be ignored.

With the assumptions stated above, the movement of a landslide is treated as two decoupled processes as follows;

- Movement during creep stage
- Movement during the catastrophic phase

The envisaged transition between these two processes can be qualitatively described as follows;

Due to heat dissipation, the yield locus shrinks according to the hardening law proposed by Laloui and Francois (2009). As a result, the stress state may eventually lie on the yield locus. Once this happens the landslide enters into a catastrophic phase. Furthermore, for simplicity, it is assumed that when the stress states reaches on the yield locus this occurs at a critical state.

Therefore, the heat equation takes two different forms, one for each process;

The first form is valid during the creep phase, and it can be written as;

$$\frac{\partial\theta}{\partial t}=k_m\frac{\partial^2\theta}{\partial z^2}+\frac{1}{C_f}\frac{v_t}{Z_b} \qquad 5.109$$

In the above, v_t is the creep velocity of the landslide and Z_b is the thickness of shearband.

The second form is valid during the catastrophic phase. In this case the heat equation will be same as the expression developed by Cecinato (2009). This is appropriate due to the following reasons;

- If the time dependency of the hardening law is ignored, so the constitutive law used here reverts to the one used by Cecinato (2009).
- The assumptions of critical state leads to zero volumetric plastic strain as in Cecinato (2009)

Recalling 3.16, the heat equation can be written as;

$$\frac{\partial\theta}{\partial t} = D_i \frac{\partial^2\theta}{\partial\theta^2} + F_i \frac{v_d(t)}{Z_b} \tag{5.110}$$

The parameters for Equation 5.110 have been defined in Section 3.2.

Similarly two dynamic equations should be proposed depending on the scenarios mentioned above. During the catastrophic phase, the dynamic equation developed in Chapter 3 can be used due the reasons listed above. The dynamic equation during the creep phase will be developed in the following subsection 5.12.1.

5.12.1 The dynamic equation during the creep phase

The Singh-Mitchell creep law provides an expression for the axial strain rate in undrained triaxial conditions (Equation 5.47);

$$\dot{\varepsilon}_a^t = A\exp(\bar{\alpha}\bar{D})\left(\frac{t_0}{t}\right)^m \tag{5.111}$$

$\bar{D}$ is a measure of stress level, which is given by;

$$\bar{D} = \frac{q}{q_{ult}} \tag{5.112}$$

q is the applied deviatoric stress, and q_{ult} is the ultimate or failure strength. Due to the assumption of undrained triaxial conditions, the shear creep strain rate can be written as;

$$\dot{\gamma}^t = \frac{3}{2}\dot{\varepsilon}_a^t \tag{5.113}$$

Substituting Equation 5.113 into 5.111 gives;

$$\dot{\gamma}^t = \frac{3}{2}A\exp(\bar{\alpha}\bar{D})\left(\frac{t_0}{t}\right)^m \tag{5.114}$$

Also, in undrained conditions, $q = 2\tau$ and $q_{ult} = 2\tau_{ult}$. So that, Equation 5.114 becomes,

$$\dot{\gamma}^t = \frac{3}{2} A \exp\left(\bar{\alpha}\left(\frac{\tau}{\tau_{ult}}\right)\right)\left(\frac{t_0}{t}\right)^m \tag{5.115}$$

where τ is the applied shear stress on the top of the shear band and $\tau_{ult}$is the ultimate shear strength. By assuming a linear velocity profile inside the shear band, the shear strain rate can be written as;

$$\dot{\gamma}^t = \frac{v_t}{Z_b} \tag{5.116}$$

Solving Equation 5.115 for the shear stress ,τ, gives;

$$\tau = \left\{\ln\left[\frac{2}{3}\frac{v_t}{AZ_b}\left(\frac{t}{t_0}\right)^m\right]\right\}\frac{\tau_{ult}}{\bar{\alpha}} \tag{5.117}$$

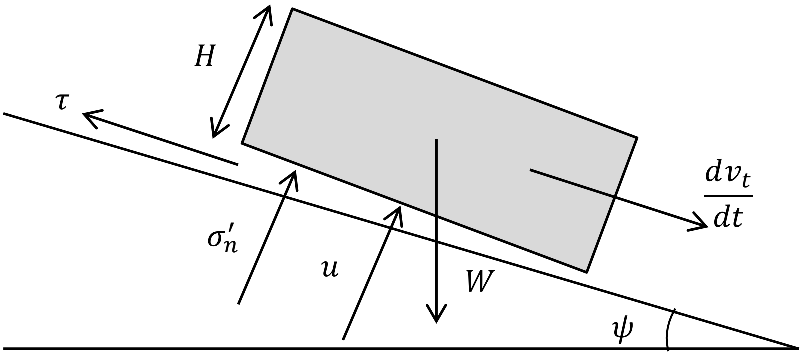

Figure 148: Schematic diagram of block on infinite slope

For simplicity, a block sliding on an infinite slope is assumed to derive the dynamic equation. With reference to Figure 148, the dynamics of the block can be written as;

$$\frac{dv_t}{dt} = g\left(\sin\psi - \frac{\tau}{\gamma_e H}\right) \tag{5.118}$$

where ψ is the slope angle, H is the block thickness, γ_e is the effective density of the soils $(\gamma_s - \gamma_w)$ and is described in Section 4.6.3, and τ is the shear stress acting on the block.

Substituting Equation 5.117 into 5.118 gives the final dynamic equation as;

$$\frac{dv_t}{dt} + \frac{g}{\gamma_e H}\frac{\tau_{ult}}{\bar{\alpha}}\ln\left[\frac{2}{3}\frac{v_t}{AZ_b}\left(\frac{t}{t_0}\right)^m\right] - \sin\psi = 0 \tag{5.119}$$

5.12.2 Stress state assumptions

The next task is to define the necessary stress components, such as the mean effective stress $p'$and deviatoric stress q, as functions of the effective normal stress σ'_n acting on the slip plane. σ'_n can be calculated using the weight of the sliding mass and the seepage conditions.

As described in Section 5.12, during the creep phase, the stress state is inside the yield locus. However, during the collapse phase, the stress state reaches a critical state at which stage, the stress ratio is;

$$\frac{q}{p'} = M \tag{5.120}$$

Generally, it can be argued that some thermal pressurization is expected to be present during creep. However, it was simpler to assume that pressurisation during the time frame of creep was negligible, and consider that the stress ratio $q/p' = M$ throughout the creeping process. The analyses presented in later Section 5.15.1 confirmed that this was reasonable assumption. It is also a conservative one, as pressurisation would decrease effective stress and therefore the production of heat in the shear band.

Hook's law written in terms of the Young's modulus E and Poisson's ratio υ gives:

$$\begin{aligned} \varepsilon_{xx} &= \frac{1}{E}\left(\sigma'_{xx} - \upsilon\sigma'_{yy} - \upsilon\sigma'_{zz}\right) \\ \varepsilon_{yy} &= \frac{1}{E}\left(\sigma'_{yy} - \upsilon\sigma'_{zz} - \upsilon\sigma'_{xx}\right) \\ \varepsilon_{zz} &= \frac{1}{E}\left(\sigma'_{zz} - \upsilon\sigma'_{xx} - \upsilon\sigma'_{yy}\right) \end{aligned} \tag{5.121}$$

If the axes given in Figure 52 are considered, due to oedometric conditions, $\varepsilon_{xx} = \varepsilon_{yy} = 0$, from Equation 5.121 it is written as,

$$\begin{aligned} \sigma'_{xx} &= \upsilon\left(\sigma'_{yy} + \sigma'_{zz}\right) \\ \sigma'_{yy} &= \upsilon(\sigma'_{xx} + \sigma'_{zz}) \end{aligned} \tag{5.122}$$

Equation 5.122 gives;

$$\sigma'_{xx} = \sigma'_{yy} = \frac{\upsilon}{1-\upsilon}\sigma'_{zz} \tag{5.123}$$

Substituting Equation 5.123 into the definition of the mean effective stress gives

$$p' = \frac{1}{3}\left(\sigma'_{xx} + \sigma'_{yy} + \sigma'_{zz}\right) = \frac{\sigma'_n}{3}\left(\frac{1+\upsilon}{1-\upsilon}\right) \tag{5.124}$$

where σ'_n is the normal stress on the slip plane which is equal to σ'_{zz}.

Next, the initial effective preconsolidation pressure should be defined in terms of the normal effective stress σ_n'. In Modified Cam-Clay, if the stress state (p_0', q_0) is on the yield locus, the initial effective preconsolidation pressure can be written as;

$$p_{c0}' = \frac{q_0^2}{p_0' M^2} + p_0' \qquad 5.125$$

where p_0' & q_0 are the intial values of p' & q respectively, which can be determined from σ_{n0}'.Using the expressions of p' and q, the preconsolidation stress can be calculated using Equation 5.125.

As discussed in Section 5.12, at the start of the simulation, the stress state should be inside the yield locus. Therefore, it is assumed that the initial preconsolidation stress is 0.01% bigger than the value given by Equation 5.125. Hence, the actual initial preconsolidation stress p_{c0}' can be written as

$$p_{c0}' = 1.0001 \times \left(\frac{q_0^2}{p_0' M^2} + p_0' \right) \qquad 5.126$$

Expression 5.126 is used as the reference preconsolidation p_{c0T0}' in Equation 5.18

5.13 Parameter selection

For the stage of catastrophic sliding, the same parameters given in Section 3.4.2 and Table 2 are used. Values for the creep parameters were selected in-line with Borja and Kavazanjian (1985). Brief descriptions of each parameter are given below.

According to Equation 5.114, the shear strain rate decreases with time assuming other parameters remain constant. A and $\bar{\alpha}$ are material creep parameters, obtained from creep tests that are linked to the shear strain rate at $t = t_0$ and, with reference to Equation 5.116, the initial velocity of the sliding mass. The parameters A, $\bar{\alpha}$ and t_0 are chosen as $3.5 \times 10^{-5}/min$, 4.45 and 1min respectively, in-line with Borja and Kavazanjian (1985). τ_{ult} is calculated as;

$$\tau_{ult} = \sigma_{n0}' \tan(\varphi_{peak}) \qquad 5.127$$

where φ_{peak} is the initial peak friction angle, material taken as $30°$ for the Vaiont clay (Vardoulakis, 2002a). The last creep parameter m was taken as a two-branch function as described in Section 5.8.2. The pressurization coefficient is taken as $0.012\ \mathrm{MPa/°C}$.

5.14 Numerical implementation

Two sets of landslide equations are developed to describe the creep and catastrophic phase separately. Analyses are first started using the equations corresponding to the creep phase. The equations describing the catastrophic phase are used, once the stress state reaches critical state. Simulations of the catastrophic phase have been carried out already in Chapter 3. Therefore, only the creep phase is considered here. The simulations were run to the point where the stress state reaches critical state. The total duration of the creep phase will be referred to hereafter as “time to catastrophic phase t_c”. The landslide equations for the creep phase can be summarised as;

$$\begin{aligned}
&\frac{\partial p}{\partial t} = \frac{\partial}{\partial z}\left(c_v \frac{\partial p}{\partial z}\right) + \lambda_m \frac{\partial \theta}{\partial t} \\
&\frac{\partial \theta}{\partial t} = k_m \frac{\partial^2 \theta}{\partial z^2} + \frac{1}{C_f}\frac{v_t}{Z_b} \\
&\frac{dv_d}{dt} + \frac{g}{\gamma_e H}\frac{\tau_{ult}}{\bar{\alpha}} ln\left[\frac{2}{3}\frac{v_t}{AZ_b}\left(\frac{t}{t_0}\right)^m\right] - sin\,\psi = 0
\end{aligned} \qquad 5.128$$

The above set of equations is solved numerically using a backward time-centred space finite difference scheme. The solution of the system of finite difference equations is not straight forward; it is a non-linear system and hence an iterative procedure with an appropriate initial guess needs to be employed. MATLAB numerical software was used to solve the non-linear equations using an in-built algorithm fsolve. The initial guess used is the solution of the previous time step, or the initial conditions for the first time step.

The time step was chosen as 10 sec. The analysis starts at $t = t_0$, where $t_0 = 60\ sec$ the reference time.

The initial and boundary conditions for heat and pore water pressure equations are;

$$\begin{aligned}
&u(z, t_0) = 0; \qquad \theta(z, t_0) = \theta_{ref} = 12°\text{C}; \\
&u(\pm\infty, t > t_0) = 0; \quad \theta(\pm\infty, t > t_0) = \theta_{ref} = 12°\text{C}
\end{aligned} \qquad 5.129$$

The initial condition for the dynamic equation is calculated from the shear creep equation by applying $t = t_0$, resulting to $2.6 \times 10^{-5} m/s$.

5.15 Numerical results

5.15.1 Results for the base line case

First, an analysis was carried out with the parameters given in Section 5.13. Hereafter, this will be referred to as the base line model. The evolution of temperature at the middle of the shear band and temperature isochrones within the shear band and its surroundings (0-1000sec) are presented in Figure 149 and Figure 150 respectively. The maximum temperature rise is found as $0.085°\mathrm{C}$ which is negligible. The pore water pressure at the middle of the shear band and the respective isochrones are shown in Figure 151 and Figure 152. Excess pore pressure rose to 6kPa during the period of temperature rise. When the temperature started to drop, the excess pore pressure became negative due to cooling of the shear band. Once the temperature stabilized to its initial magnitude of $12°\mathrm{C}$, the excess pore pressure dropped back to zero.

The velocity and displacement plots are given in Figure 153 and Figure 154 respectively. Velocity drops from $2.6 \times 10^{-5} m/s$ to zero and 13.5 mm of displacement is attained during the time period of 10000 sec.

In this base line case, the model did not reach catastrophic phase as energy dissipation and heat production are low. As a result, the stress state remained inside the elastic region and only creep deformation occurred. For the slide to reach a catastrophic phase, heat dissipation inside the shear band should increase. This is possible if the initial velocity of the slide increases. To this end, the creep parameter A is increased by 10 times. The results are presented in the following subsection.

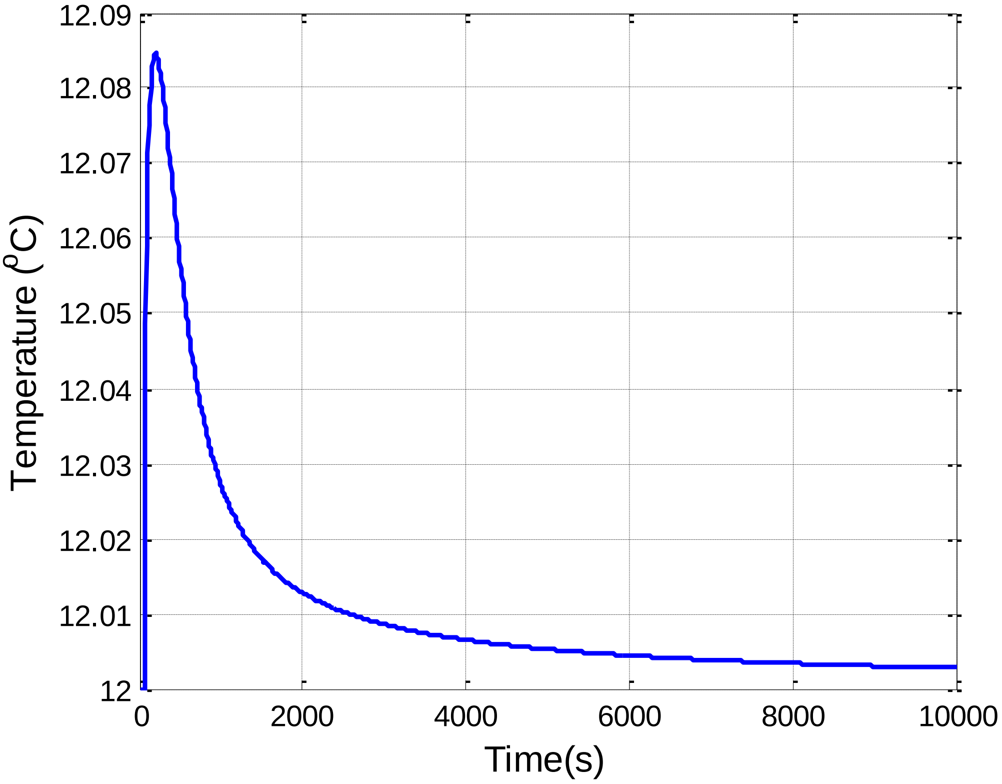

Figure 149: Temperature at the mid of the shear band (base line case)

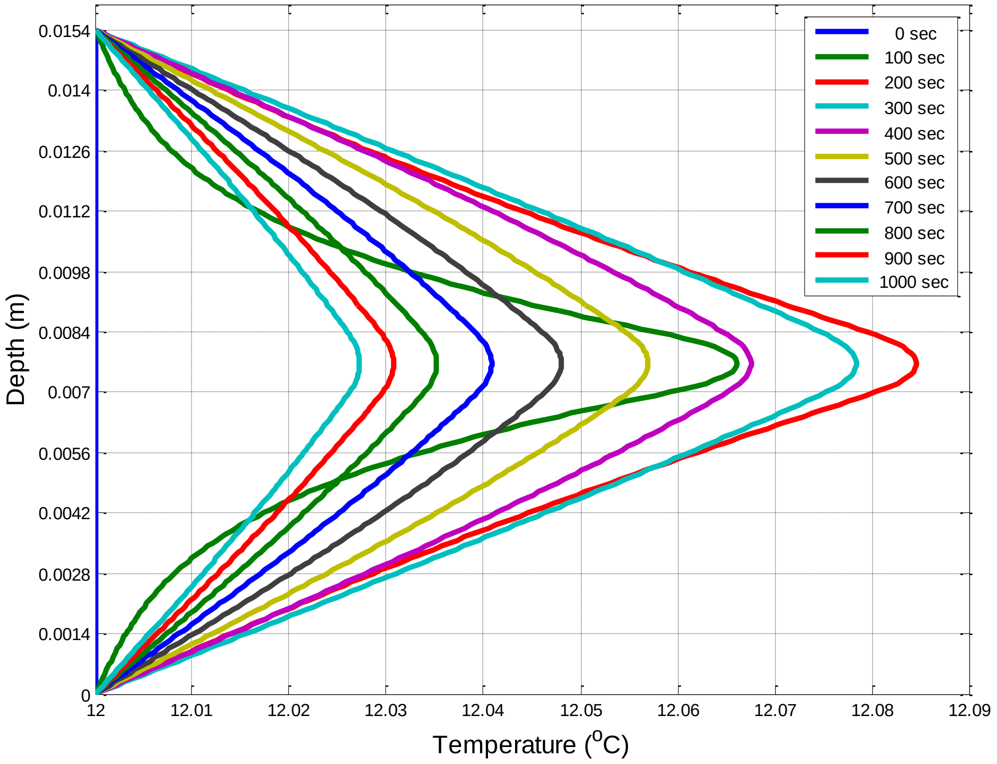

Figure 150: Temperature isochrones within the shear band and its surroundings (base line case)

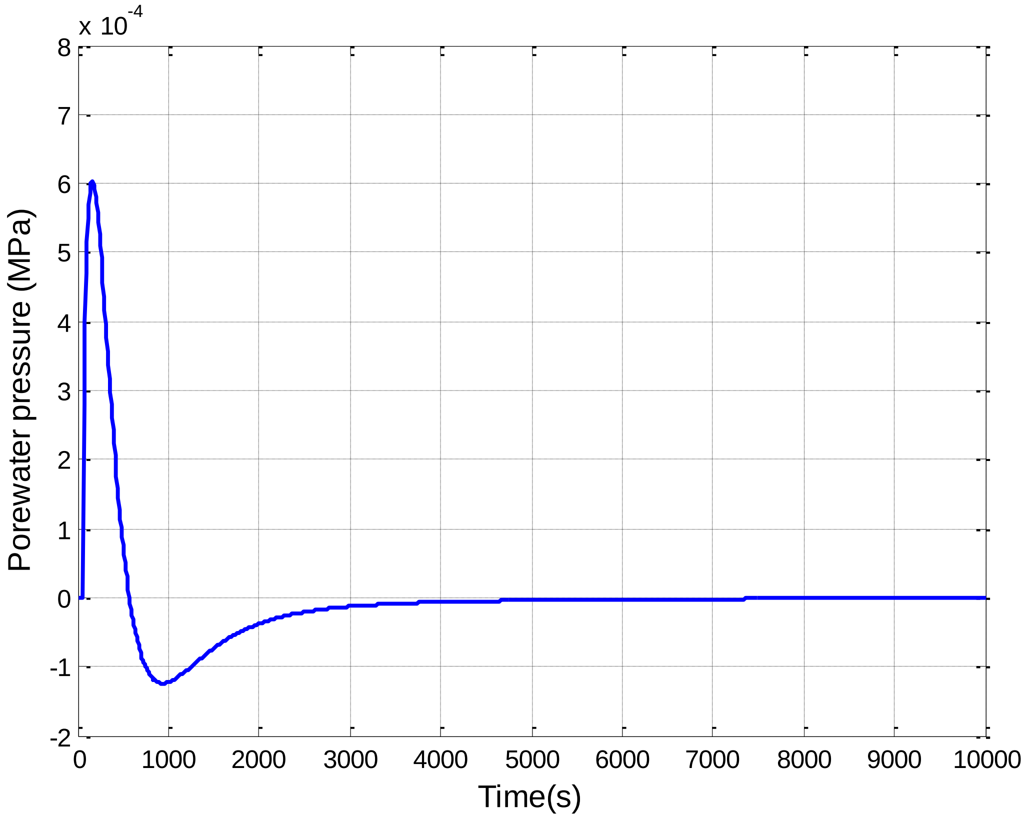

Figure 151: Pore water pressure at the mid of the shear band (base line case)

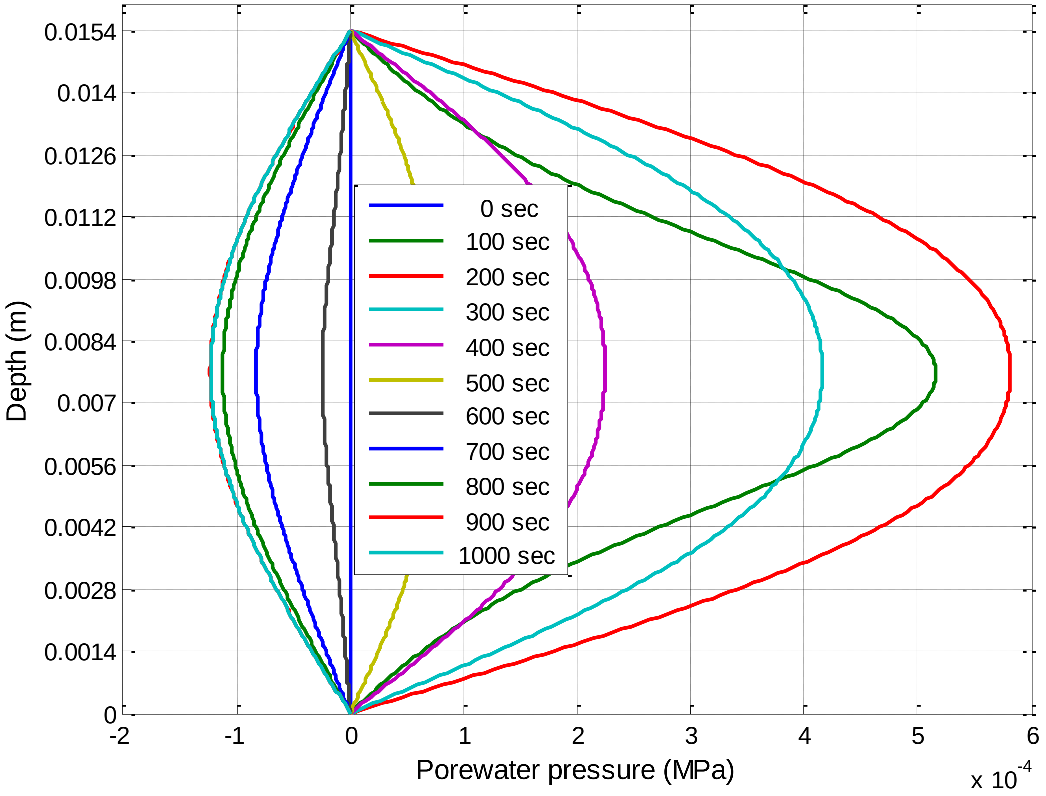

Figure 152: Pore water pressure isochrones within the shear band and its surroundings (base line case)

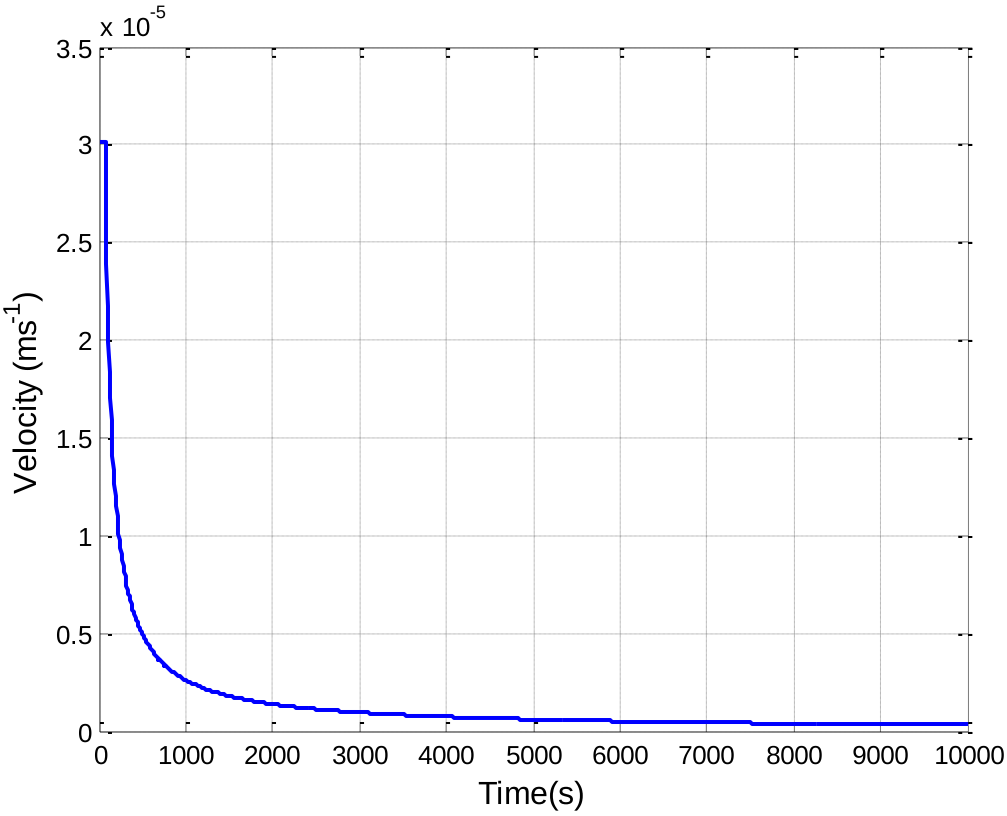

Figure 153: Velocity of the slide (base line case)

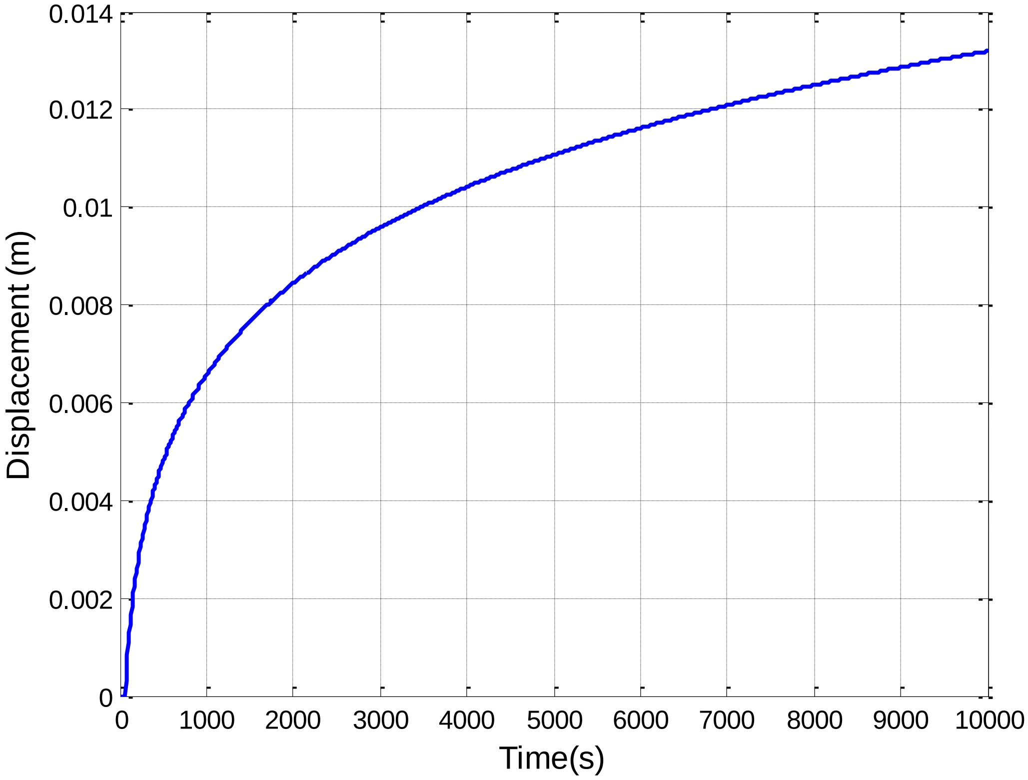

Figure 154: Displacement of the slide (base line case)

5.15.2 Results for higher initial slide velocity

In this section, the results are presented for an initial velocity 10 times higher than that of the assumed base line case (Section 5.15.1).

In this case the temperature reached to $12.85℃$ at 200 sec before dropping as shown in Figure 155 and Figure 156. Also the excess pore pressure peaked to $600\ kpa$ at 165 sec then dropped to zero. The temperature and pore pressure rise were nearly 100 times greater than the base line case due to higher energy dissipation. The velocity and displacement plots are given in Figure 159 and Figure 160 respectively. The slide velocity decreased from $3 \times 10^{-4} m/s$ to $5 \times 10^{-5} m/s$ after 500 sec.

In this case, during the creep phase the slide travelled 48mm before the collapse phase, which was reached after 500 sec. This is well after temperature and excess pore water pressure peak which my appear odd but can be explained thus; when temperature increases the yield locus shrinks, while effective stress reduces due to heating. The yield locus also shrinks due to the development of strain and thermal softening. In contrast, when temperature reduces the yield locus expands, while effective stress increases due to cooling. Therefore, it is possible that the stress state may touch the yield locus (failing point) during the decreasing phase of temperature and pore water pressure, if the rate of change of stress is higher than the rate of change in the size of the yield locus.

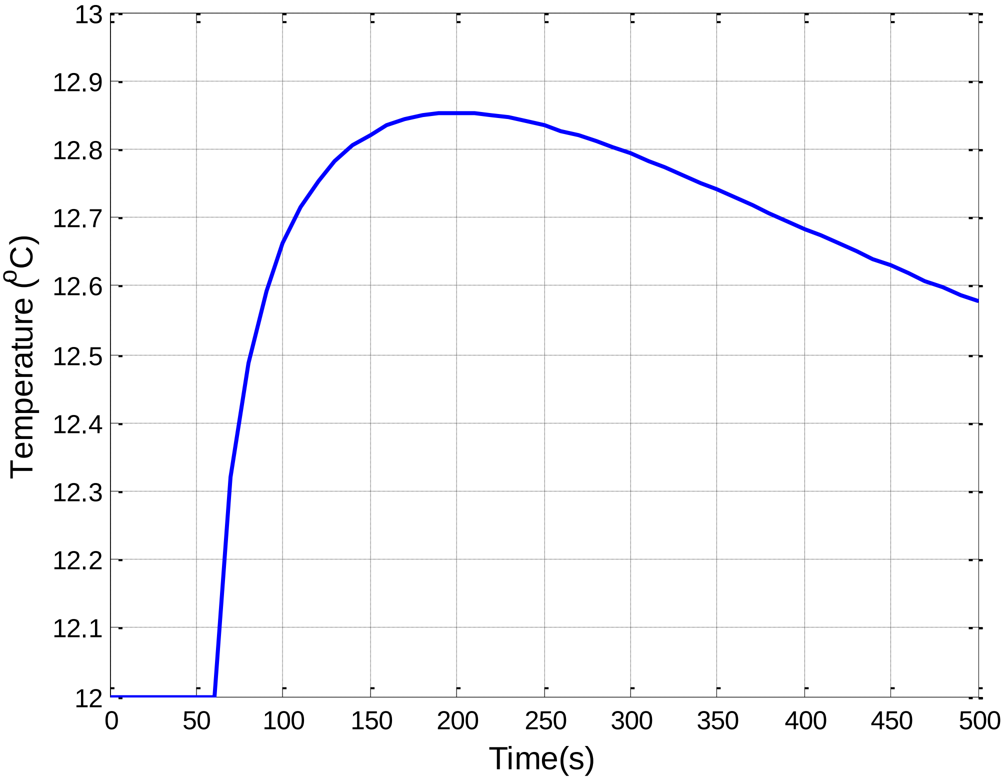

Figure 155: Temperature at the mid of the shear band (A=3.5 x 10^{-4}/min)

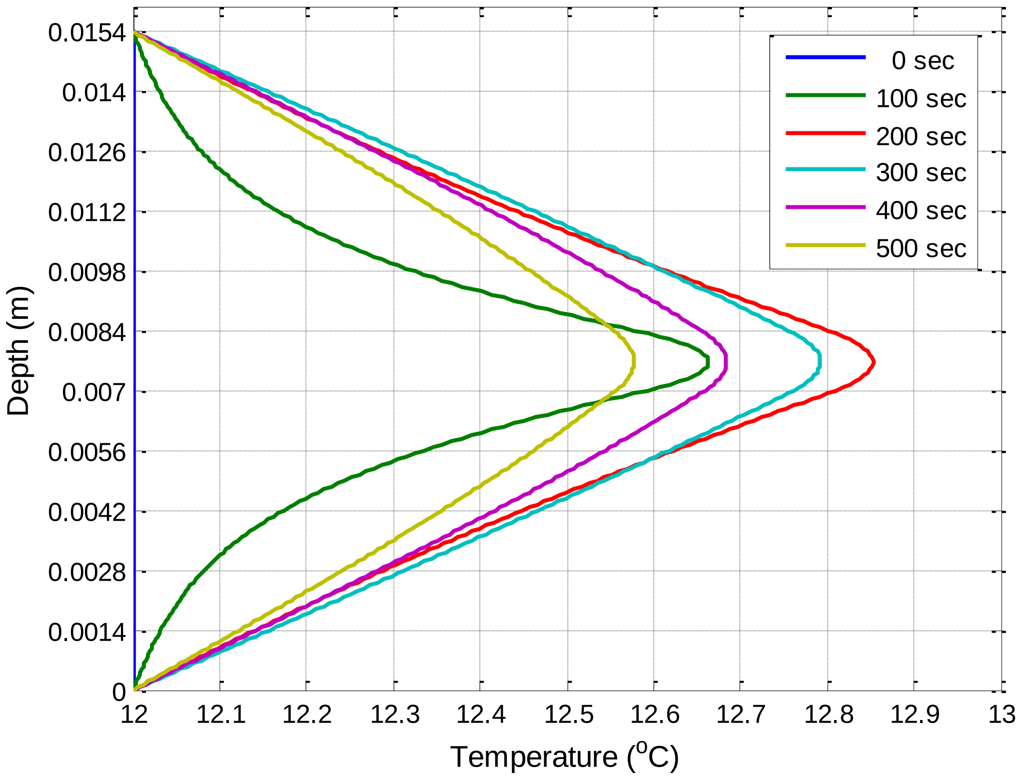

Figure 156: Temperature isochrones within the shear band and surroundings (A=3.5 x 10^{-4}/min)

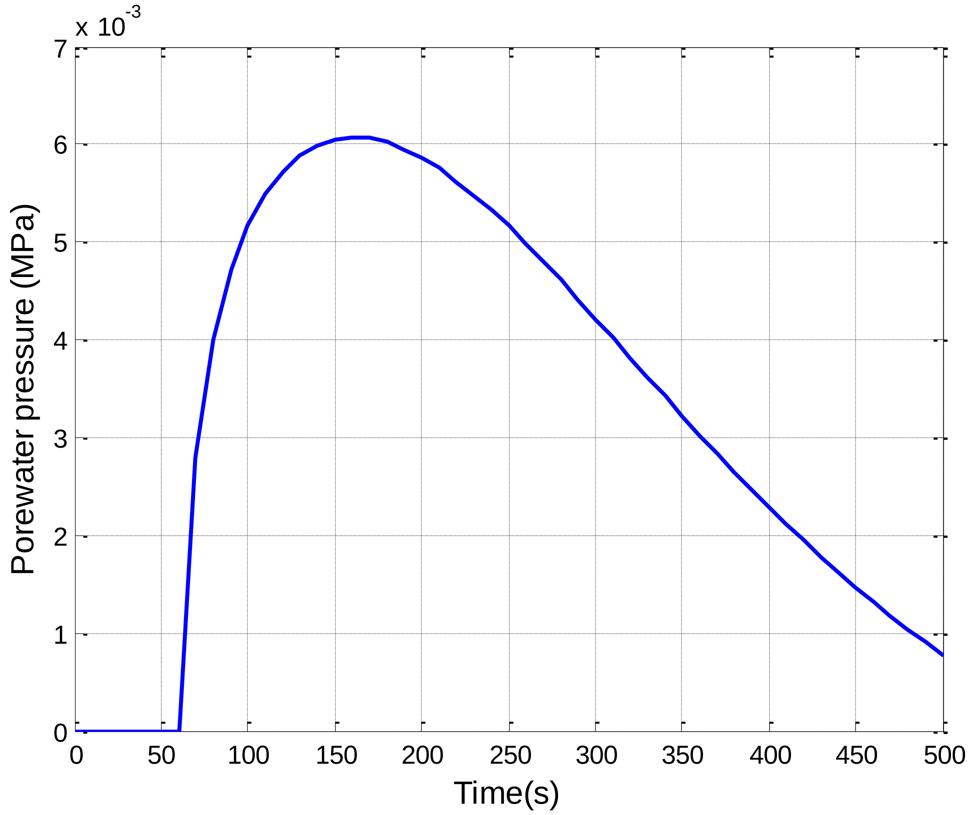

Figure 157: Pore water pressure at the mid of the shear band (A=3.5 x 10^{-4}/min)

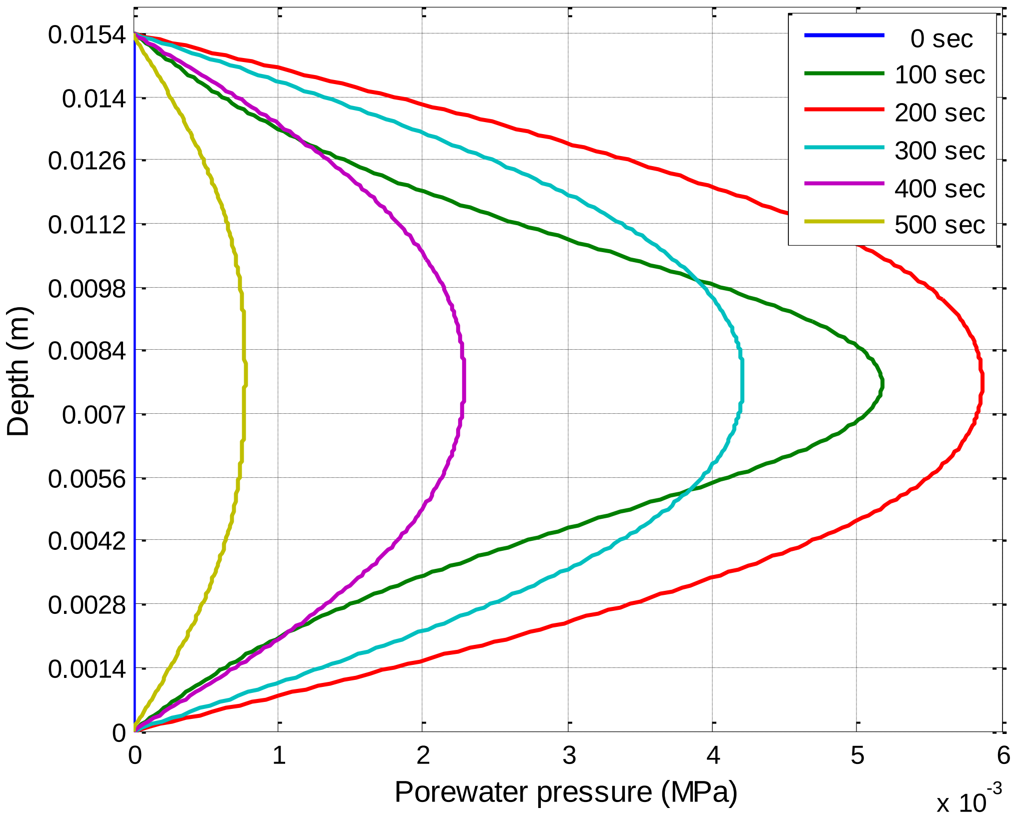

Figure 158: Pore water pressure isochrones within the shear band and its surroundings (A=3.5x10^{-4} /min)

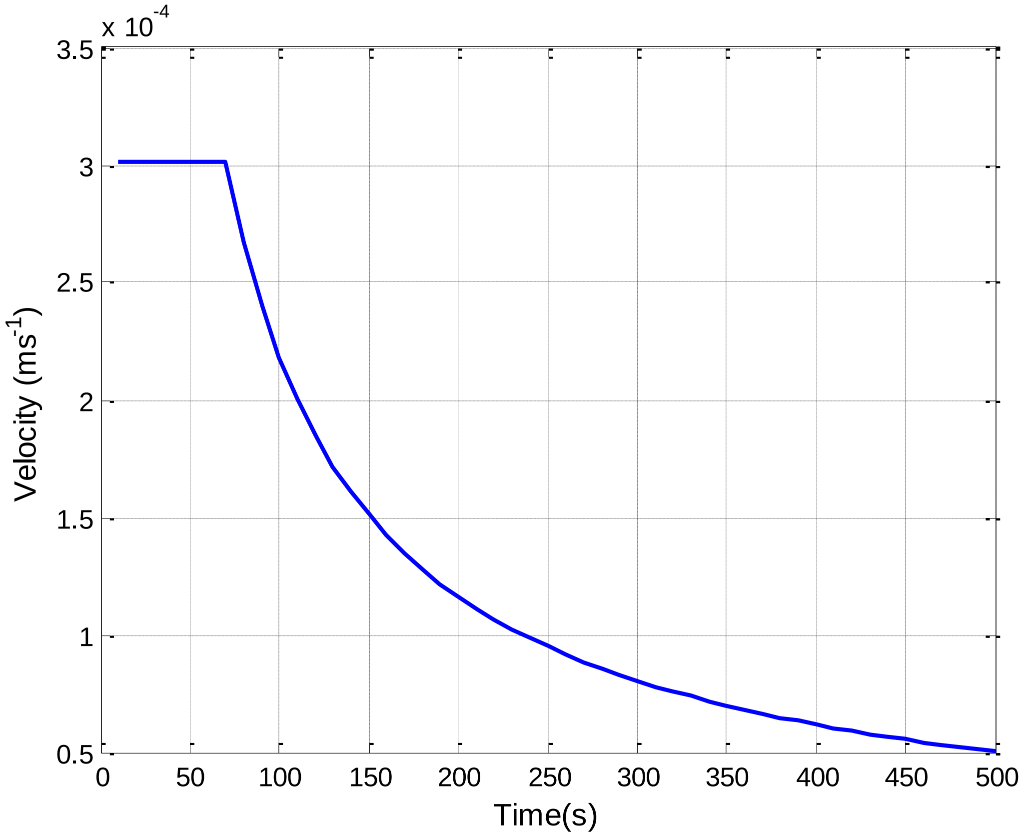

Figure 159: Velocity of the slide (A=3.5 x 10^{-4} /min)

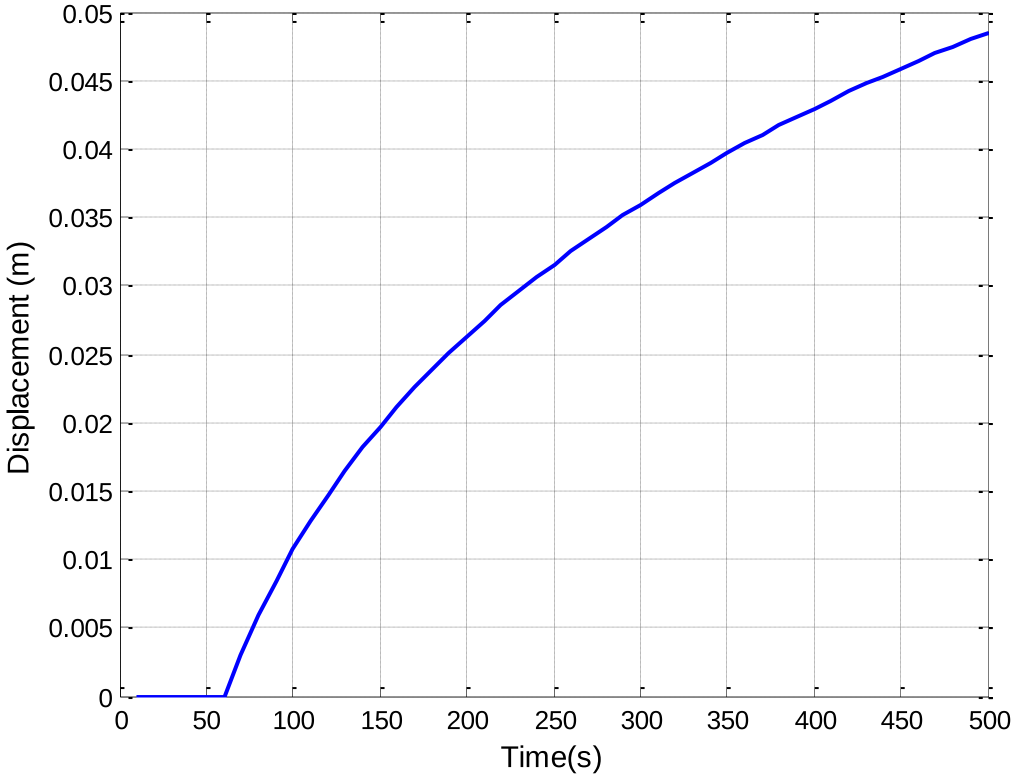

Figure 160: Displacement of the slide (A=3.5 x 10^{-4}/min)

Subsequently, similar analysis with the larger size of model thickness $(51 \times Z_b)$ was carried out. With larger model thickness, the temperature reached to 12.90℃ at 300 sec and remains same till 350 sec at which the catastrophic phase is reached as shown in Figure 161 and Figure 162. Also the excess pore pressure peaked to 650 kPa at 235 sec before dropping (Figure 163 and Figure 164). The velocity and displacement plots are given in Figure 165 and Figure 166 respectively. The slide velocity decreased from $3 \times 10^{-4} m/s$ to $7.5 \times 10^{-5} m/s$ after 350 sec.

In this case, a catastrophic phase was reached after 350 sec which is even sooner than with thinner model thickness. During the creep phase the slide travelled 40 mm before the collapse phase.

Overall, the analysis with higher initial velocity successfully modelled the transition between the creep and the catastrophic phase of a landslide. However, the longest duration of creep movement was predicted to be 500 sec, which is much less than the timescales observed in real landslide cases (e.g. 3 years for Vaiont (Müller, 1964, Müller, 1968)) .

In the following, an attempt is made to increase the duration of the creep phase t_c.

The heat and pore water pressure equations are one-dimensional diffusion-generation equations. The general form of the dimensionless time factor , T_v, for such equations, is given by (Powrie, 2013);

$$T_v = \frac{Y_i t}{Z_b^2} \tag{5.130}$$

where Y_i is the thermal diffusivity κ_m for heat diffusion problems or the consolidation coefficient c_v for consolidation problems. t is the time and Z_b is the thickness of the shear band.

The progress of this process is measured by the time factor T_v. To increase the actual time to which any given time factor corresponds to, either the thickness of the shear band, Z_b can be increased or the thermal diffusivity of the soil water mixture κ_m can be decreased. However, the thicker the shear band the higher the initial velocity (Equation 5.116), therefore t_c will further reduce due to higher heat dissipation. Therefore, in the following subsection analyses are carried out with lower value of thermal diffusivity (κ_m) for the soil-water mixture and with $11 \times Z_b$ of model thickness, to investigate its effect in t_c.

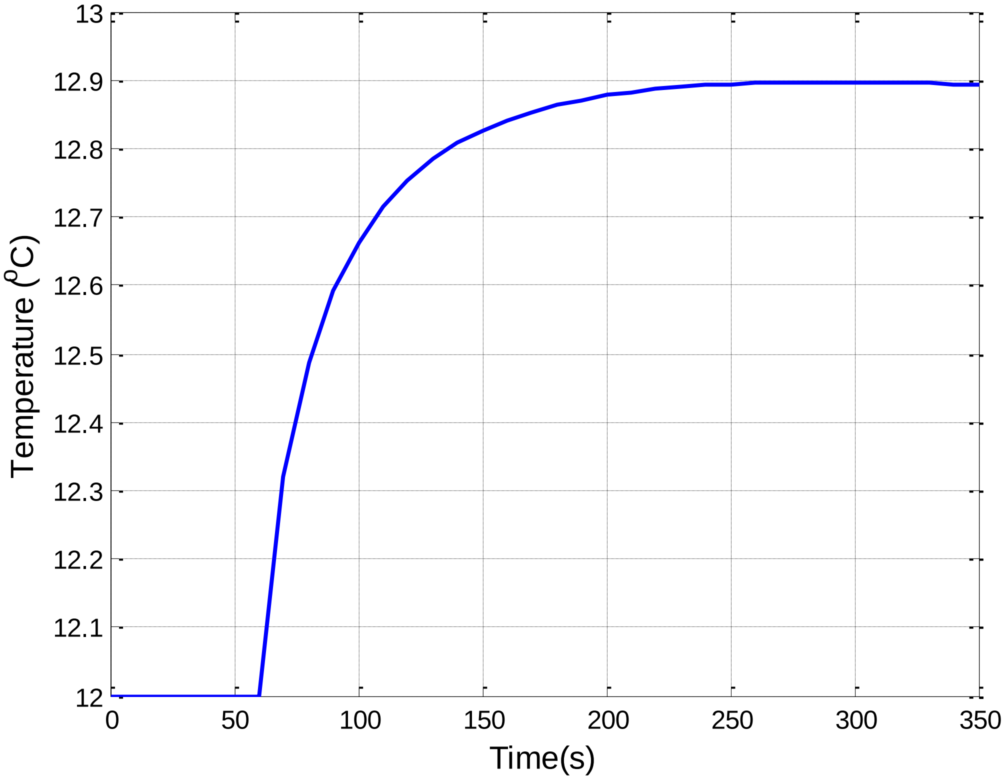

Figure 161: Temperature at the mid of the shear band (A=3.5 x 10^{-4}/min, model thickness $= 51 \times Z_b$)

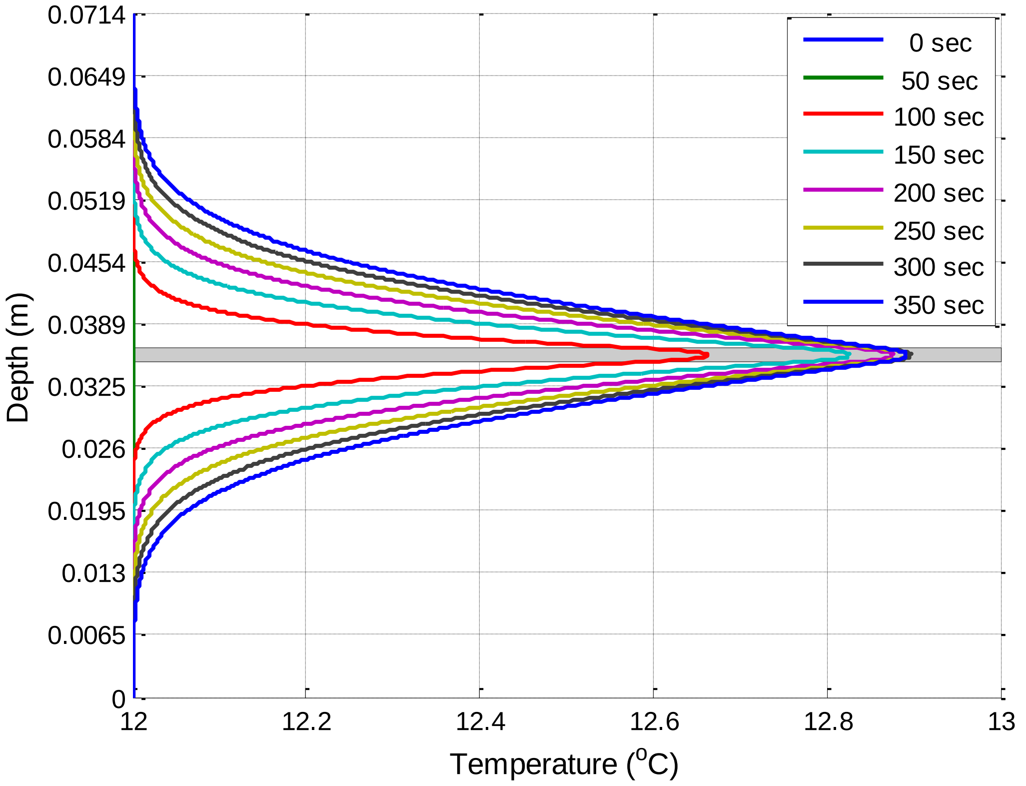

Figure 162: Temperature isochrones within the shear band and surroundings (A=3.5 x 10^{-4}/min, model thickness $= 51 \times Z_b$)

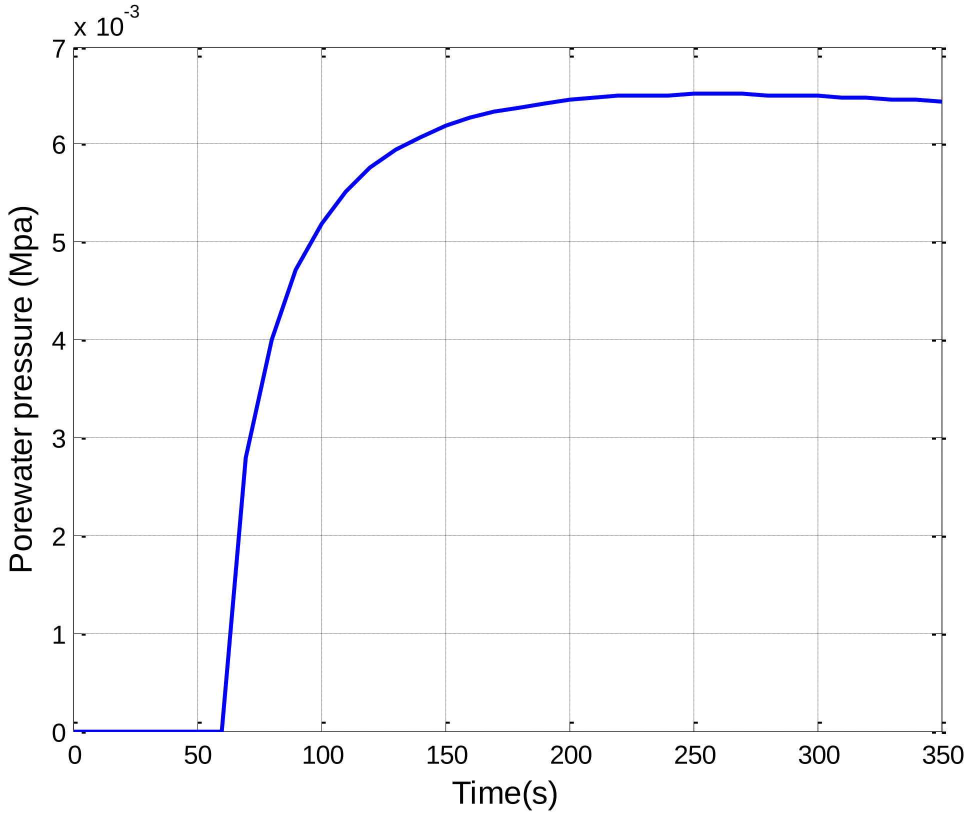

Figure 163: Pore water pressure at the mid of the shear band (A=3.5 x 10^{-4}/min, model thickness $= 51 \times Z_b$)

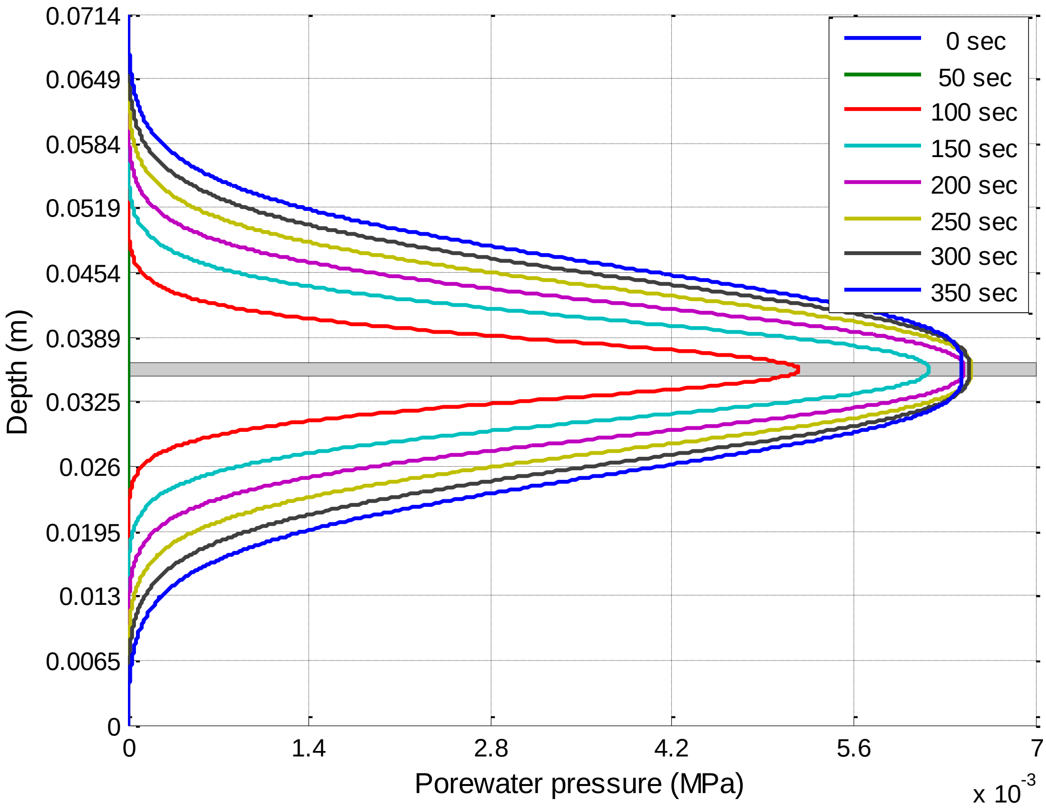

Figure 164: Pore water pressure isochrones within the shear band and its surroundings (A=3.5x10^{-4} /min, model thickness $= 51 \times Z_b$)

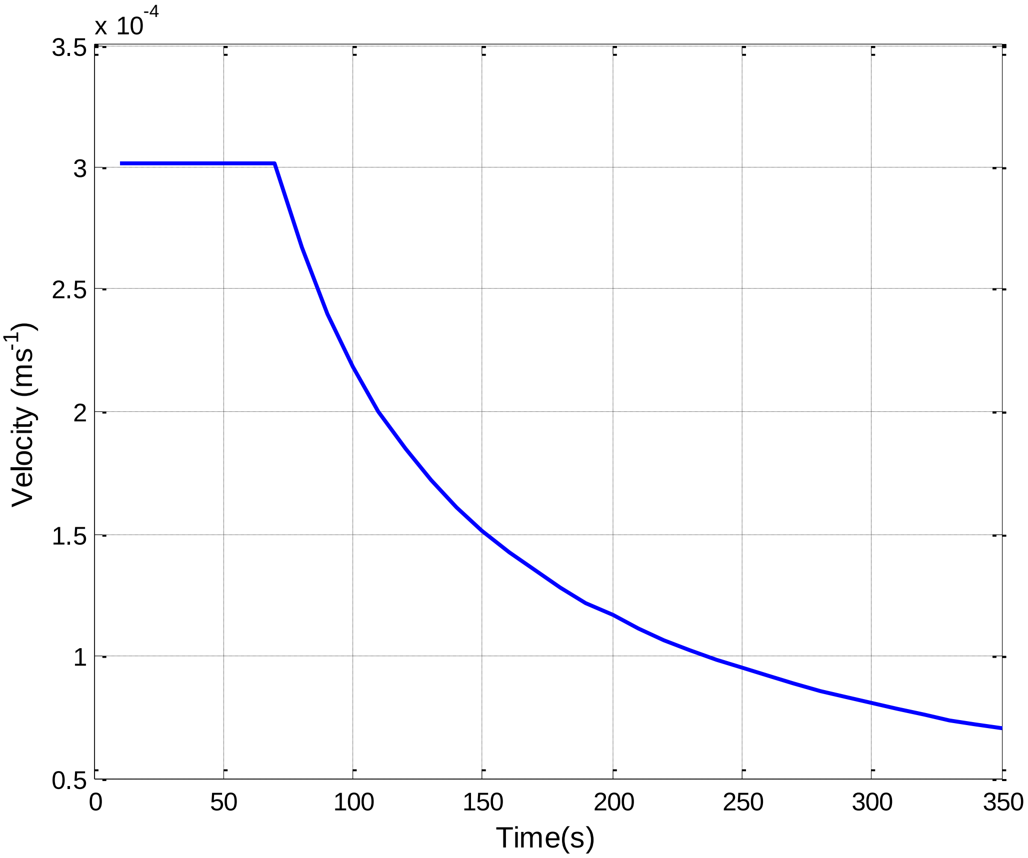

Figure 165: Velocity of the slide (A=3.5 x 10^{-4} /min, model thickness = $51 \times Z_b$)

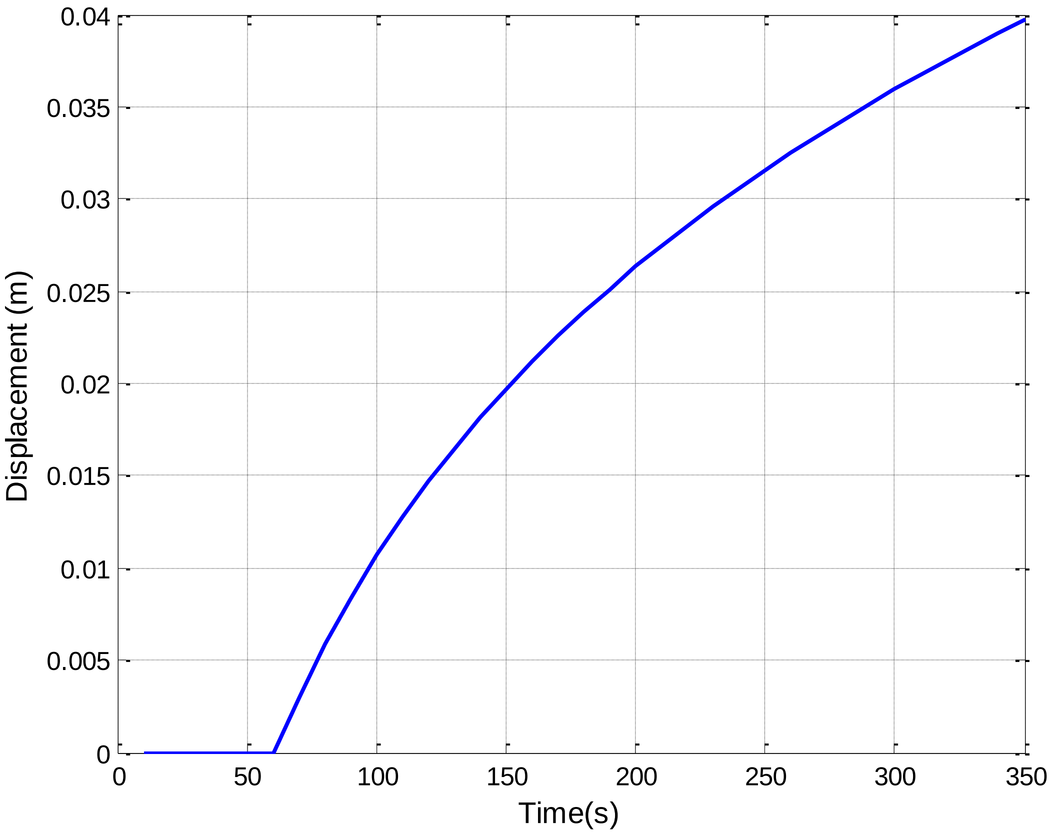

Figure 166: Displacement of the slide (A=3.5 x 10^{-4}/min, model thickness = $51 \times Z_b$)

5.15.3 Results for different values of the thermal diffusivity

In this section the results are presented for different values of thermal diffusivity for the soil-water mixture. Originally $\kappa_m = 1.45 \times 10^{-7} m^2 s^{-1}$was used in-line with Vardoulakis (2002a). Here, analyses are carried out after decreasing the original thermal diffusivity by factors of 0.5 and 0.1 (i.e. $\kappa_m = 7.25 \times 10^{-8}$& $1.45 \times 10^{-8}\ m^2 s^{-1}$). The results show that, all these analyses predict a catastrophic phase. The plots up to the point where the landslide enters a catastrophic phase are presented in this section.

The plot of temperature at the middle of the shear band is given Figure 167. It can be clearly seen that higher thermal dissipation occurs for smaller values of thermal diffusivity of the soils-water mixture. The excess pore water pressure shows similar behaviour as seen in Figure 168. The velocity and displacement plots are shown in Figure 169 and Figure 170. It can be clearly seen that the velocity and displacement of slide are very close for different values of κ_m. Overall, the "time to catastrophic phase t_c" increased from 500 sec to 930 sec when κ_m decreased by a factor of 0.1.

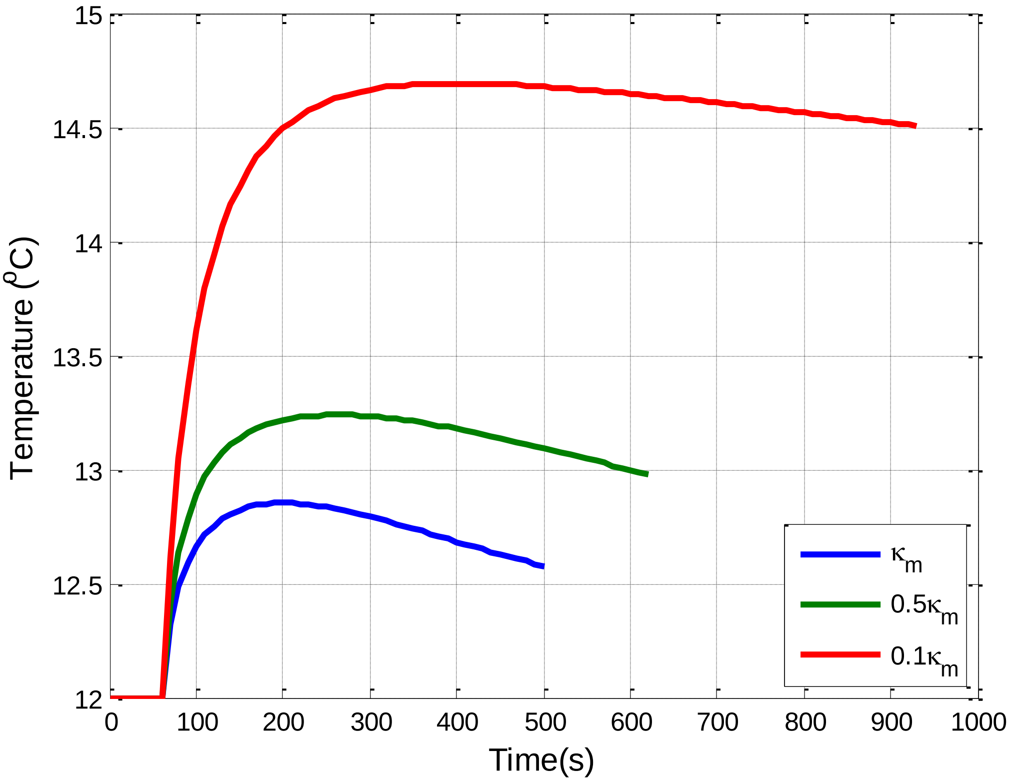

Figure 167: Temperature at the mid of the shear band (different κ_m)

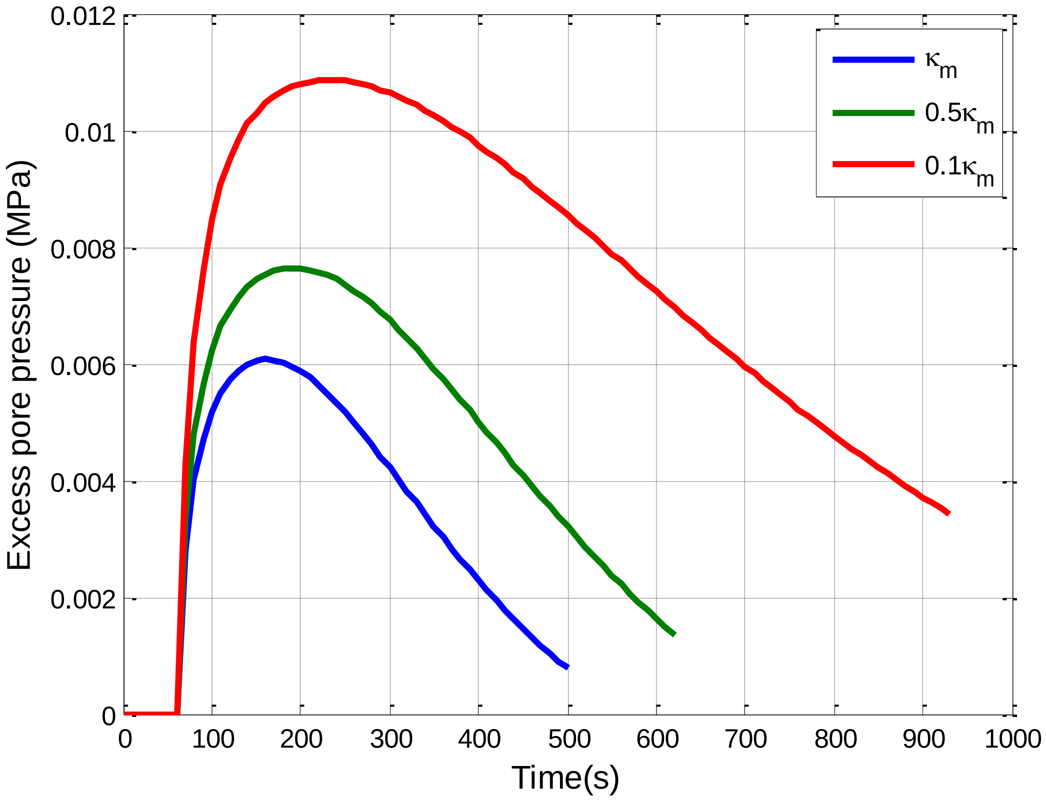

Figure 168: Excess pore pressure at the mid of the shear band (different κ_m)

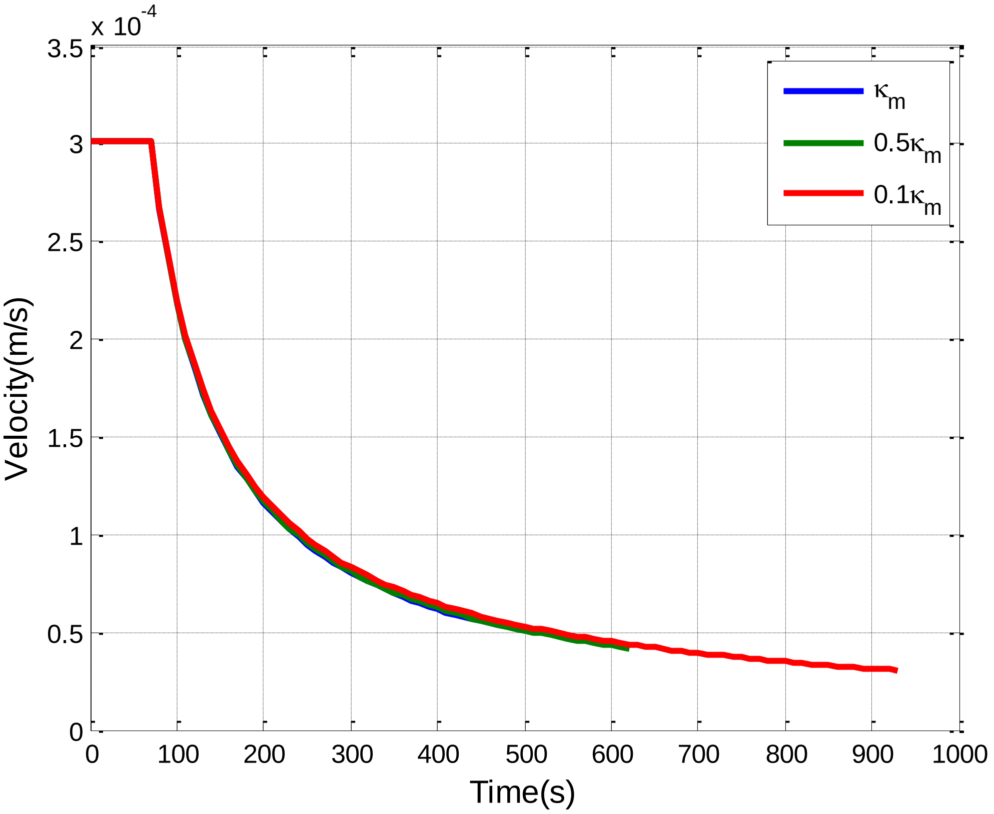

Figure 169: Velocity of the slide (different κ_m)

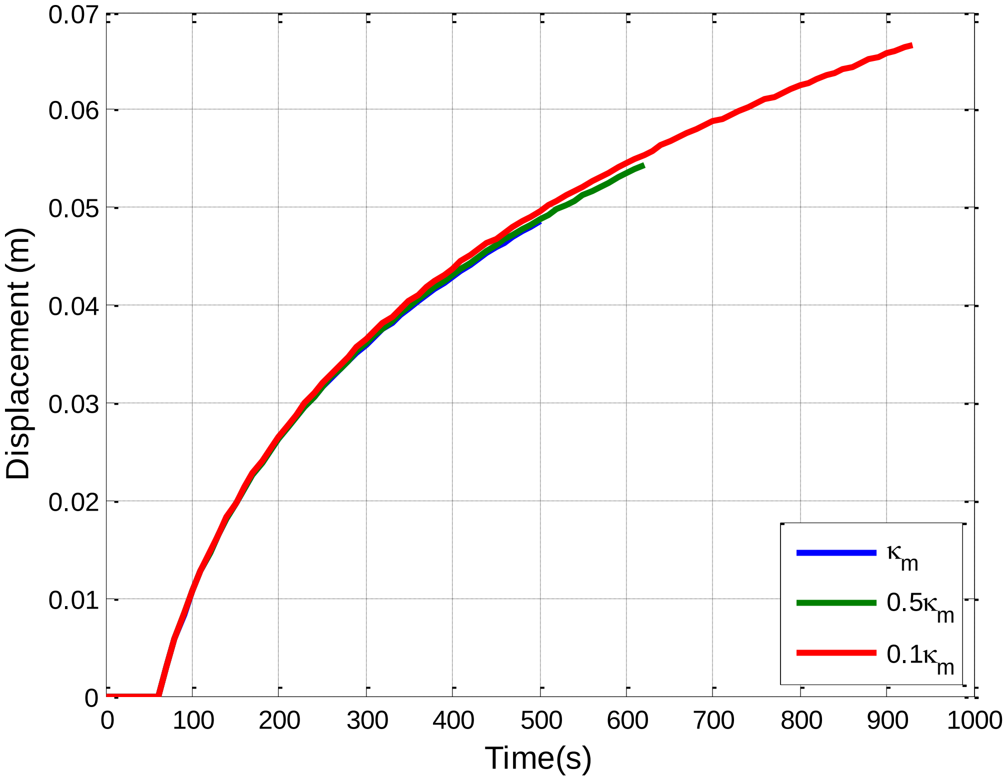

Figure 170: Displacement of the slide (different κ_m)

5.16 Discussion

In this chapter, a new thermo-poro-mechanical landslide model was developed using a refined constitutive model that includes temperature and time effects.

The new constitutive model was developed by combining Borja's model for time dependent behaviour (Borja and Kavazanjian, 1985) and Laloui's model for the thermo-plasticity of soils (Laloui and Francois, 2009). The new constitutive model offers a possible framework for describing the transition between creep and catastrophic failure of a landslide.

First, this model was used in an attempt to back analyse the Vaiont case history. Analysis using the parameters obtained from Vardoulakis (2002a) and Borja and Kavazanjian (1985) showed that a catastrophic phase was not predicted for Vaiont. This is due to the underlying expression for the creep strain rate being a power law, and therefore predicting a strain rate that decreases with time. Thus, energy dissipation also decreases with time. Therefore, if the model does not enter into a catastrophic phase relatively early, the slide will creep continuously and come to rest due to declining heat dissipation. Furthermore, Singh-Mitchell parameters were chosen from Borja and Kavazanjian (1985) however, these parameter values specific to the Vaiont material are not available in the literature.

Moreover, the changes in reservoir level elevation and significant precipitation during the phase were not included in this model.

Subsequently, model behaviour was investigated by varying the initial velocity of the slide and the thermal diffusivity of the soil-water mixture. It was found that the time to catastrophic failure,t_c increases for decreasing thermal diffusivity of the soil-water mixture and decreases for increasing initial slide velocity.

The expression for thermal diffusivity of the soil-water mixture of a soil is given as (Vardoulakis, 2002a):

$$\kappa_m = \frac{k_{Fm}}{(\rho C)_m} \tag{5.131}$$

where k_{Fm} and $(\rho C)_m$ are Fourier's thermal conductivity and the specific heat of the soil-water mixture respectively. k_{Fm} is written as

$$k_{Fm} = (1-n)k_{Fs} + nk_{Fw} \tag{5.132}$$

where n is the porosity of the soil and k_{Fs} and k_{Fw} are Fourier's thermal conductivity of the soil granules and water respectively. Vardoulakis assumed the porosity of the soil as 0.18, which implies $\kappa_m = 1.45 \times 10^{-7} m^2 s^{-1}$. Maintaining k_{Fs} and k_{Fw} unchanged, a reduction of κ_m by a factor of 10 implies a porosity of $-2.68 < 0$, which is physically impossible.

On the other hand, maintaining the porosity unchanged at $n = 0.18$, a reduction of κ_m by a factor of 10 implies reduced values for either k_{Fs} or k_{Fw} or both. However, the thermal conductivity of water k_{Fw} has a well-defined value of $1.2 \times 10^{-3}\ cal/(cm\ s\ ℃)$ (Vardoulakis, 2002a). The value of k_{Fs} then needs to be decreased to $-1.5 \times 10^{-4}\ cal/(cm\ s\ ℃) < 0$, which is again physically impossible.

Even with this unrealistic reduction of κ_m, however, the longest possible time at which transition to catastrophic is predicted is nearly 930sec. This is still very short compared to the field observations. Therefore, additional mechanisms need to be invoked to explain the duration of the creep phase.

Chapter 6: A thermo-poro-mechanical landslide model using viscoplasticity of soil

6.1 Introduction

In this chapter, a thermo-poro-mechanical landslide model using the concept of viscoplasticity is developed. Viscoplasticity also referred to as Perzyna's overstress theory, is widely used to explain the time dependent behaviour of soils by many authors (Adachi and Oka, 1982, Adachi et al., 1990, Fusao et al., 1994, Kimoto et al., Kimoto et al., 2004, Oka et al., 1995). However, viscoplasticity was developed for isothermal conditions. In this chapter, first a new constitutive model is developed by combining viscoplasticity with Laloui's thermal hardening relationship. The background viscoplastic model used is the one proposed by Oka and co-workers (Adachi and Oka, 1982, Adachi et al., 1990, Fusao et al., 1994, Kimoto et al., 2013, Kimoto et al., 2004, Oka et al., 1995, Oka et al., 2002). Subsequently, the landslide model is modified to take in to account this constitutive assumption.

6.2 The proposed thermo-viscoplastic constitutive model

6.2.1 General formulation

As described in Section 2.4.9, the key assumption in Perzyna's viscoplasticity is that elastic strains are time independent and inelastic (viscous) strains are time dependent. Therefore the total strain can be written as;

$$\dot{\varepsilon}_{ij} = \dot{\varepsilon}_{ij}^{e} + \dot{\varepsilon}_{ij}^{vp} \tag{6.1}$$

The elastic strain rate is given by Hooke's law as follows (Kimoto et al., 2004);

$$\dot{\varepsilon}_{ij}^{e} = \frac{1}{2G}\dot{S}_{ij} + \frac{\kappa}{3(1+e_0)p'}\dot{p}' \tag{6.2}$$

where, S_{ij} is the deviatoric stress state tensor, p' is the mean effective stress, κ is the slope of unloading-reloading line (URL), G is the elastic shear modulus and e_0 is the void ratio.

6.2.2 Yield functions

In viscoplasticity theory, two yield functions are introduced.

The first yield function is called static yield function f_y and is equivalent to yield locus of elasto-plasticity. If the stress point lies inside the static yield locus, elastic deformation takes place. In contrast to elasto-plastic theory, the stress states are allowed to go outside the static yield locus and then the viscoplastic strains occur $\left(\varepsilon_{ij}^{vp}\right)$.

The second yield function is called viscoplastic potential or overstress function $\left(f_p\right)$ which passes through the current stress state, if it is outside the yield locus.

Kimoto et al. (2004) suggested static yield locus using original Cam Clay yield locus as follows;

$$f_y = \bar{\eta}_0 + M^* ln \left(\frac{p'}{p'_{cy}}\right) \qquad 6.3$$

where $\bar{\eta}_0$ is the relative stress ratio defined by;

$$\bar{\eta}_0 = \sqrt{\left(\eta_{ij} - \eta_{ij,0}\right)\left(\eta_{ij} - \eta_{ij,0}\right)} \qquad 6.4$$

in which, η_{ij} is the stress ration tensor given as S_{ij}/p' and subscripts 0 denotes the initial state before the deformation occurs and M^* is the stress ratio at critical state (i.e. $\varepsilon_v^{vp} = 0$) . p'_{cy} is the hardening/softening parameter that determines the size of the static yield locus.

Similarly, Kimoto et al. (2004) suggested viscoplastic potential using original cam clay yield locus as follows;

$$f_p = \bar{\eta}_0 + M^* ln \left(\frac{p'}{p'_{cp}}\right) \qquad 6.5$$

where p'_{cp} determines the size of visco plastic potential.

However, it is replaced with normalized modified Cam-Clay for easier numerical implementation due its smooth character. The static yield locus becomes;

$$f_y = \frac{q^2 - M^2 p'\left(p'_{cy} - p\right)}{p'^2} \qquad 6.6$$

In the above, p' and q denote the effective mean and deviatoric stress, M is the critical state parameter and viscoplastic potential becomes

$$f_p = \frac{q^2 - M^2 p'\left(p'_{cp} - p\right)}{p'^2} \qquad 6.7$$

6.2.3 Hardening law

As described in Section 6.2.2, the hardening/softening parameter contained in the expression of the static yield locus (6.6) determines the size of the locus. It depends on the volumetric viscoplastic strain as follows;

$$p'_{cy} = p'_{cy0} \exp\left(\tilde{\beta}\varepsilon_v^{vp}\right) \tag{6.8}$$

To introduce the temperature dependence, the above expression is modified as proposed by Laloui and Cekerevac (2003) and Laloui and Francois (2009) for elasto-plasticity (See also Section 2.3.3).

$$p'_{cy} = p'_{cy0} \exp\left(\tilde{\beta}\varepsilon_v^{vp}\right) \left\{1 - \gamma \log\left(\frac{\theta}{\theta_0}\right)\right\} \tag{6.9}$$

In the above, γ is a material parameter that determines rate of thermal collapse of the yield locus, θ_0 is the reference temperature measured in ℃ and p'_{cy0} is the reference preconsolidation pressure when $\varepsilon_v^{vp} = 0$ and $\theta = \theta_0$. From the above relationship, the size of the static yield locus depends on both viscoplastic strain and temperature.

6.2.4 Final form of constitutive relationship

The viscoplastic strain can be written as follows based on Perzyna's overstress theory Kimoto et al. (2004);

$$\dot{\varepsilon}_{ij}^{vp} = \gamma\langle\Phi(f_y)\rangle \frac{\partial f_p}{\partial \sigma'_{ij}} \tag{6.10}$$

where the symbol $\langle\,.\,\rangle$ is defined as

$$\langle\Phi(f_y)\rangle = \begin{cases} \Phi(f_y) & f_y > 0 \\ 0 & f_y \leq 0 \end{cases} \tag{6.11}$$

$f_y = 0$ and $f_p = 0$ denote the static yield locus and viscoplastic potential function respectively. Φ is a function that determines the rate sensitivity of the material. Based on experimental results, Kimoto et al. (2004) defined the material function Φ as follows.

$$\gamma\Phi(f_y) = C'p \exp(m'f_y) \tag{6.12}$$

where C' and m' are viscoplastic parameters determined from experiments. Substituting the expression for the static yield function (Equation 6.6) into Equation 6.12 gives;

$$\gamma\Phi(f_y) = C'p \exp\left[m'\left\{\frac{q^2 - M^2 p'\left(p'_{cy} - p\right)}{p'^2}\right\}\right] \tag{6.13}$$

Substituting Equation 6.12 into Equation 6.10 gives the viscoplastic strain as

$$\dot{\varepsilon}_{ij}^{vp} = C'p \exp\left[m'\left\{\frac{q^2 - M^2 p'(p'_{cy} - p)}{p'^2}\right\}\right]\frac{\partial f_p}{\partial \sigma'_{ij}} \tag{6.14}$$

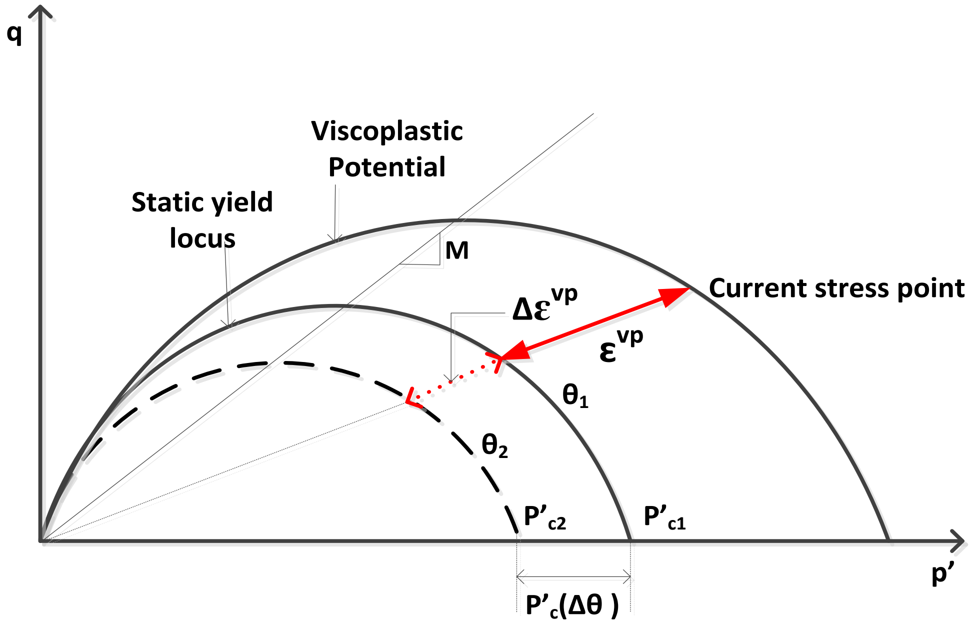

Figure 171: Schematic description of thermo-viscoplastic potential and static yield locus including thermal effects

6.3 Proposed landslide equations

As discussed in Section 2.4.9, the magnitude of the viscoplastic strain rate is determined by the overstress function, which is the difference between the static yield locus and the current stress state as shown in Figure 171. However, the size of the static yield locus is now also dependent on temperature. Therefore, it can be expected that, due to contraction of the static yield locus with temperature, the viscoplastic strain rate will increase as temperature increases. Therefore, due to the influence of temperature, it may be possible to model the transition behaviour between the creep and collapse phases of a landslide. In the following, landslide model equations including the new thermo-viscoplastic constitutive model are developed. Validation through back analysis of the Vaiont case is attempted.

6.3.1 Heat equation

The heat equation provides the temperature variation and evolution inside the shear band with time and consists of a heat diffusion equation with a dissipation term. It is written as

$$\frac{\partial \theta}{\partial t} = k_m \frac{\partial^2 \theta}{\partial z^2} + \frac{D_{vp}}{C_f} \tag{6.15}$$

in which, k_m is thermal diffusivity of soil-water mixture and C_f is the thermal constant. The heat dissipation term, D_{vp} in Equation 6.15, is derived in the following using the proposed viscoplastic law. The volumetric viscoplastic strain in the shear zone of a landslide is assumed negligible compared to the shear part, therefore in this framework, the governing equations are derived using the viscoplastic shear strain only.

Shear heat dissipation (D_{vp}) in terms of shear viscoplastic strain can be written as;

$$D_{vp} = \tau\dot{\gamma}^{vp} \tag{6.16}$$

In the above, τ is the effective shear stress applied on the shear band and $\dot{\gamma}^{vp}$ is the shear viscoplastic strain. From the definition given in Equation 6.14, $\dot{\gamma}^{vp}$ can be written as;

$$\dot{\gamma}^{vp} = C'p\exp\left[m'\left\{\frac{q^2 - M^2p'\left(p'_{cy} - p\right)}{p'^2}\right\}\right]\frac{\partial f_p}{\partial \tau} \tag{6.17}$$

By using chain rule, the derivative of the static yield locus can be written as

$$\frac{\partial f_p}{\partial \tau} = \frac{\partial f_p}{\partial p}\frac{\partial p}{\partial \tau} + \frac{\partial f_p}{\partial q}\frac{\partial q}{\partial \tau} \tag{6.18}$$

The derivatives in the above equation can be written as;

$$\frac{\partial f_p}{\partial p} = -\frac{2q^2}{p^3} + \frac{M^2p'_{cp}}{(p')^2} \tag{6.19}$$

$$\frac{\partial p}{\partial \tau} = 0 \tag{6.20}$$

$$\frac{\partial f_p}{\partial q} = \frac{2q}{p^2} \tag{6.21}$$

$$\frac{\partial q}{\partial \tau} = \frac{3\tau}{q} \tag{6.22}$$

So that, $\frac{\partial f_p}{\partial \tau}$ becomes;

$$\frac{\partial f_p}{\partial \tau} = \frac{6\tau}{(p')^2} \tag{6.23}$$

Substituting 6.23 onto, 6.16 results the heat dissipation as;

$$D_{vp} = \tau C'p\exp\left[m'\left\{\frac{q^2 - M^2p'\left(p'_{cy} - p\right)}{p'^2}\right\}\right]\frac{6\tau}{(p')^2} \tag{6.24}$$

After substituting Equation 6.24 into 6.15, the final form of the heat equation becomes;

$$\frac{\partial \theta}{\partial t} = k_m\frac{\partial^2 \theta}{\partial z^2} + \frac{1}{C_f}\frac{6\tau^2}{(p')^2}C'p\exp\left[m'\left\{\frac{q^2 - M^2p'\left(p'_{cy} - p\right)}{p'^2}\right\}\right] \tag{6.25}$$

6.3.2 Pore pressure equation

The pore pressure equation gives the excess pore pressure inside the shear band and its surroundings and is the same one used in Chapter 3 (Sections 3.3).

$$\frac{\partial p}{\partial t} = \frac{\partial}{\partial z}\left(c_v \frac{\partial p}{\partial z}\right) + \lambda_m \frac{\partial \theta}{\partial t} \tag{6.26}$$

In the above, c_v and λ_m are the consolidation and pressurization coefficients as discussed in sections 3.3.1 and 3.3.2 respectively.

6.3.3 Dynamic equation

In this section, a dynamic equation is derived that describes the velocity of landslide and is consistent with thermo-viscoplastic theory. For simplicity, the landslide is modelled as a block on infinite slope. With reference to Figure 172, the dynamic equation for the sliding mass can be written as,

$$\frac{dv_v}{dt} = g\left(\sin\psi - \frac{\tau}{\gamma_e H}\right) \tag{6.27}$$

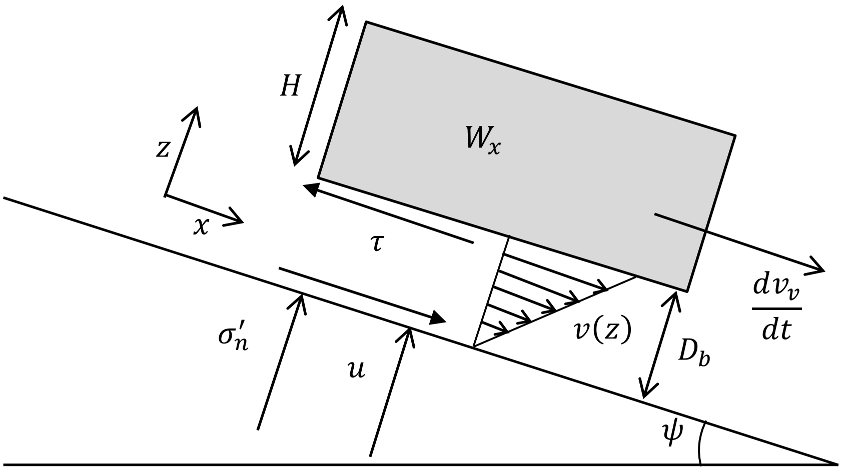

Figure 172: Schematic diagram of block on infinite slope and deforming slip band

where, v_v is the velocity of the slide, H is the block thickness, γ_e is the effective density of the soils $(\gamma_s - \gamma_w)$ and ψ is the slope angle. The shear stress τ inside the slip band is assumed constant. From equations 6.17 and 6.23, the viscoplastic shear strain rate can be written as;

$$\dot{\gamma}^{vp} = C'p' \exp\left[m'\left\{\frac{q^2 - M^2 p'\left(p'_{cy} - p\right)}{p'^2}\right\}\right]\frac{6\tau}{(p')^2} \tag{6.28}$$

Assuming a linear velocity profile inside the shear band, the velocity of the sliding mass can be written as;

$$v_v = Z_b C' p' \exp\left[m' \left\{\frac{q^2 - M^2 p'\left(p'_{cy} - p\right)}{(p')^2}\right\}\right] \frac{6\tau}{(p')^2} \qquad 6.29$$

where Z_b is the thickness of the shearband. Solving Equation 6.28 for the shear stress τ gives:

$$\tau = \frac{(p')^2}{6 Z_b C' p'} \exp\left[-m' \left\{\frac{q^2 - M^2 p'\left(p'_{cy} - p\right)}{(p')^2}\right\}\right] v_v \qquad 6.30$$

Substituting Equation 6.30 into 6.27 yields the final dynamic equation as;

$$\frac{dv_v}{dt} + \frac{g}{\gamma_e H} \frac{(p')^2}{6 Z_b C' p'} \exp\left[-m' \left\{\frac{q^2 - M^2 p'\left(p'_{cy} - p\right)}{(p')^2}\right\}\right] v_v - g \sin(\psi) = 0 \qquad 6.31$$

or

$$\frac{dv_v}{dt} + \mu_v \, v_v - g \sin(\psi) = 0 \qquad 6.32$$

where

$$\mu_v = \frac{q (p')^2}{6 \gamma_e H D_b C' p'} \exp\left[-m' \left\{\frac{q^2 - M^2 p'\left(p'_{cy} - p\right)}{(p')^2}\right\}\right] \qquad 6.33$$

can be thought of as an equivalent stress-dependent viscosity of the material inside the shear band. $\gamma_e H$ is the effective weight per unit area, and this can be written as

$$\gamma_e H = \frac{\sigma'_{n0}}{\cos \psi} \qquad 6.34$$

where σ'_{n0} is the initial effective normal stress acting on the slide. The expressions for stress components p' and q can be derived in terms of effective normal stress σ'_n from Equations 5.124 and 5.120 respectively.

6.4 Numerical implementation

Equation 6.25 is the final heat equation without dynamic effects of slide. Also, the dynamic equation was derived consistent with thermo viscoplastic constitutive theory as in section 6.3.3. Including dynamics of the slide, the heat equation can be written as;

$$\frac{\partial\theta}{\partial t} = k_m \frac{\partial^2\theta}{\partial z^2} + \frac{1}{C_f}\frac{\tau v_v}{Z_b} \qquad 6.35$$

In the above, v_v is the sliding velocity (derived in section 6.3.3), Z_b is the thickness of the shearband.

The complete set of landslide equations are now derived which includes heat, pore pressure and dynamic equation. To simulate the time evolution of temperature, pore pressure and slide velocity, the landslide equations were integrated numerically by using a BTCS scheme. The BTCS is an unconditionally stable numerical scheme; here, time steps ranging between 10 sec to 5 hours are used to perform the analysis.

The solution of the system of finite difference equations is not straight forward; it is a non-linear system and hence an iterative procedure with an appropriate initial guess needs to be employed. MATLAB numerical software was used to solve the non-linear equations using an in-built algorithm fsolve. The initial guess used is the solution of the previous time step, or the initial conditions for the first time step.

The discretisation of governing Equations 6.35 and 6.26 is done along the line with Section 3.4.1 and the initial and boundary conditions were taken as;

$$\begin{aligned} &\theta(\pm\alpha, t) = \theta_{ref} = 12.5℃ \\ &\theta(z, 0) = \theta_{ref} = 12.5℃ \\ &u(\pm\alpha, t) = 0 \\ &u(z, 0) = 0 \end{aligned} \qquad 6.36$$

The 1-D spatial domain is set to 21 times the thickness of the shear band. It is also assumed that the initial slide acceleration is zero. Therefore, from Equation 6.31, the slide velocity with zero acceleration can be written as;

$$v_v = \exp\left[m'\left\{\frac{q^2 - M^2 p'\left(p'_{cy} - p\right)}{(p')^2}\right\}\right]\frac{6Z_b C' p'}{(p')^2}\gamma_e H \sin(\psi) \qquad 6.37$$

The initial velocity v_{v0} can be obtained by applying the initial stress conditions in Equation 6.37; its value depends on the parameters C', m' and Z_b.

6.4.1 Parameter selection

The initial values for stress components (p'_0 and q_o) were calculated using Hooke's law and with the assumption of oedometric condition as described in Section 5.12.2. The resultant p'_0 and q_o are functions of the initial normal effective stress ($\sigma'_{n0} = 2.38\text{MPa}$).

The thickness of the shear band is chosen as 1.4 mm as in previous models (Chapter 3, 4 and 5). The critical state parameter M is taken as 0.657 for the static yield locus as well as the viscoplastic potential. The corresponding friction angle is 22.3° which is the incipient failure angle of the shear band material reported in Vardoulakis (2002a). Finally, p'_{cy0} represents the initial size of the static yield locus. It also represents the reference preconsolidation pressure in Laloui's hardening relationship. Here, it is assumed that $p'_{cy} = 1.6p'_{cp}$, where p'_{cp} is the size the viscoplastic potential which can be calculated from the current stress state components p'_0, q_o and the critical state parameter M. Laloui's thermo-plasticity parameter γ is taken as 0.5×10^{-2}. The remaining parameters are taken from Table 2.

In addition to general parameters described above, there are new parameters that should be defined for viscoplastic theory.

Parameters C' and m' can be determined experimentally. Different authors reported different values, ranging between $10^{-13}/s$ and $10^{-8}/s$ for C' and between 18.5 and 28.2 for m' (Kimoto et al., 2004, Oka et al., 2002). However these values were calibrated to fit specific experimental data sets. In the model presented here, C' and m' are linked to the initial velocity of the landslide. If a landslide is modelled from a time instant where the slide has a particular velocity, the viscoplastic parameters C' and m' need to be consistent with that velocity.

As described in Section 2.2.3, the Vaiont slide was creeping with velocity between 1-10 mm/day over the period between December 1959 and July 1963 before catastrophic failure, as shown in Figure 7 (Müller, 1964). For the first analysis using this model, the parameters C' and m' were calibrated to match an initial velocity of 2.2 mm/day as follows;

$C' = 10^{-8}/s$

$m' = 18.5$

These values fall within the range suggested by Kimoto et al. (2004) and Oka et al. (2002). In addition, parameters M, p'_0, q_0, Z_b and p'_{cy} also influence the initial slide velocity as given in Equation 6.37.

6.5 Numerical results

In this section the numerical results are presented. First a simulation is carried out with parameter values consistent with the Vaiont slide, to be used as a base-line case. Subsequently, the assumed initial velocity of the slide is increased to investigate the behaviour of the model. Finally, the material softening reported in Tika and Hutchinson (1999) is included to examine the thermal dependency of the model.

6.5.1 Results for the base line case

The viscoplastic parameters C' and m'were calibrated to match an initial velocity of 2.2 mm/day as detailed in section 6.4.1. The entire spatial domain was divided in to 200 grid points and temperature and pore pressure were computed at the each grid point. For this baseline case, the analysis modelled 10000 sec using 50 sec time steps.

The time evolution of temperature at the middle of the shear band is given in Figure 173. Figure 174 presents temperature isochrones across the shear band and its surroundings. The pore pressure isochrones and the time evolution of pore pressure at the middle of the shear band are shown in Figure 175 and Figure 176 respectively. The maximum temperature rise predicted was as 1×10^{-4}℃, which is practically zero, and so is the maximum predicted excess pore pressure (6.5×10^{-2}Pa dropping to zero after 8000 sec). The velocity plot of Figure 177 shows that, the block is predicted to reach a steady state of creep immediately at 2.2 mm/day; this is in the range of realistic velocities for a creeping slide of Vaiont (Müller, 1964). The displacement plot Figure 178 shows that, the slide reaches to a displacement of 0.25 mm over a period 1×10^{4} sec. As slide reaches to a steady state velocity, the displacement is expected to increase linearly with time as shown.

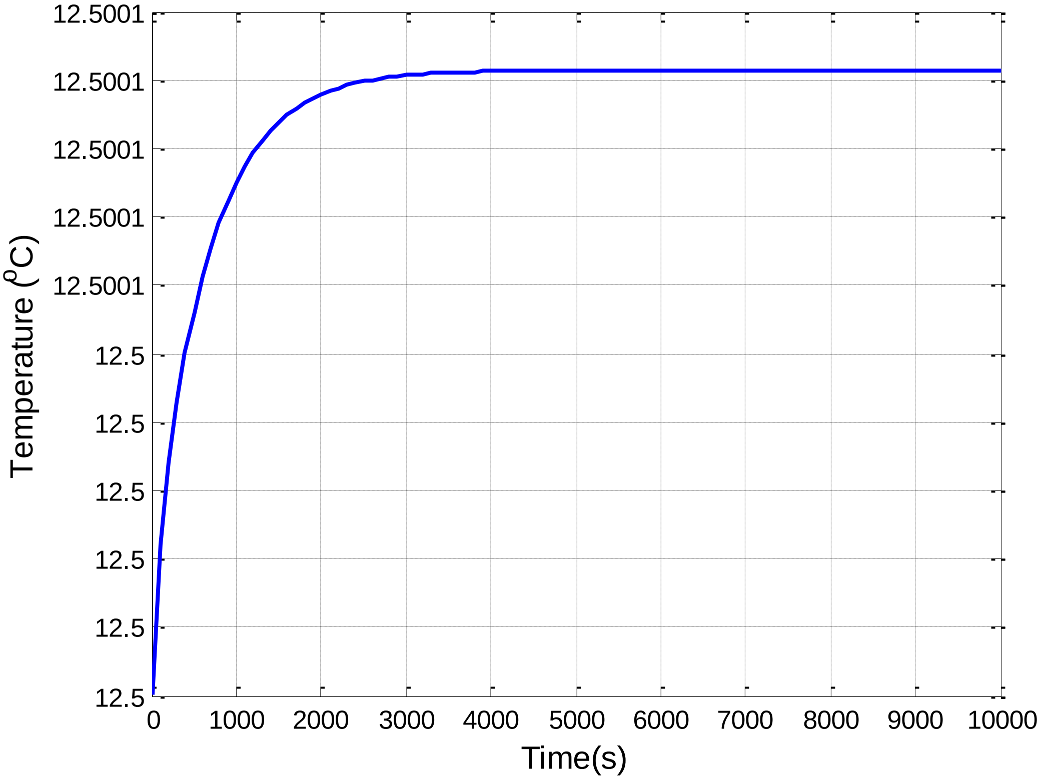

Figure 173: Temperature at the mid of the shear band (base line case)

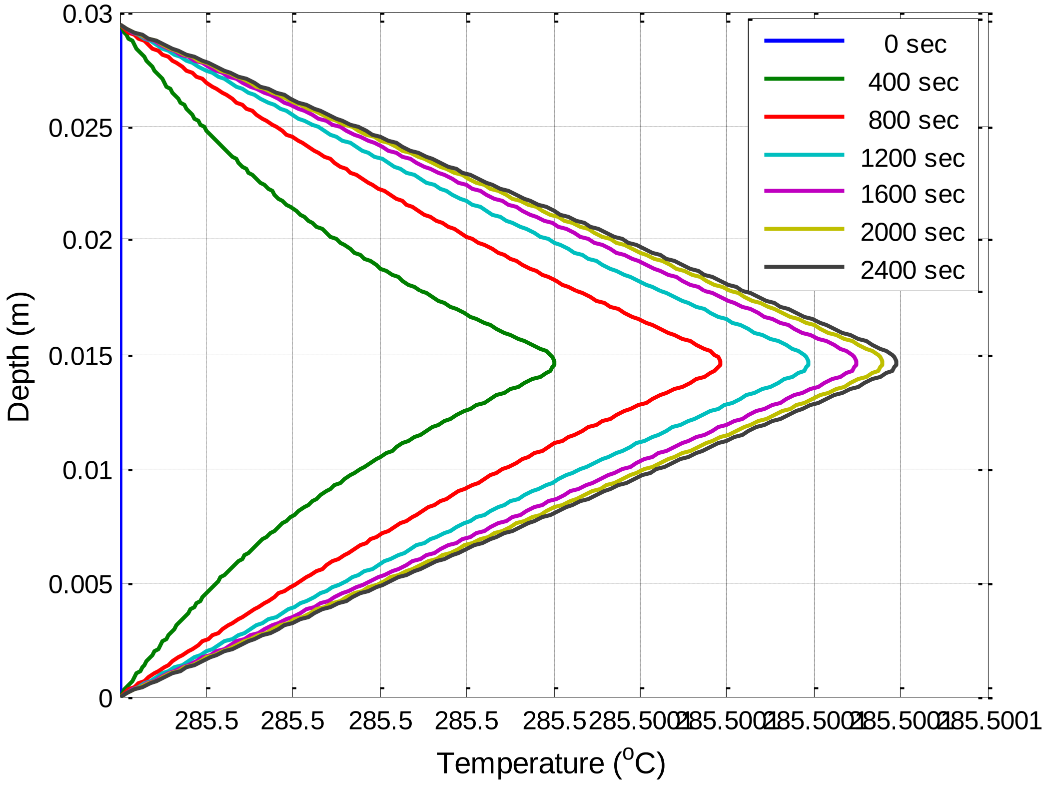

Figure 174: Temperature isochrones within the shear band and its surroundings (base line case)

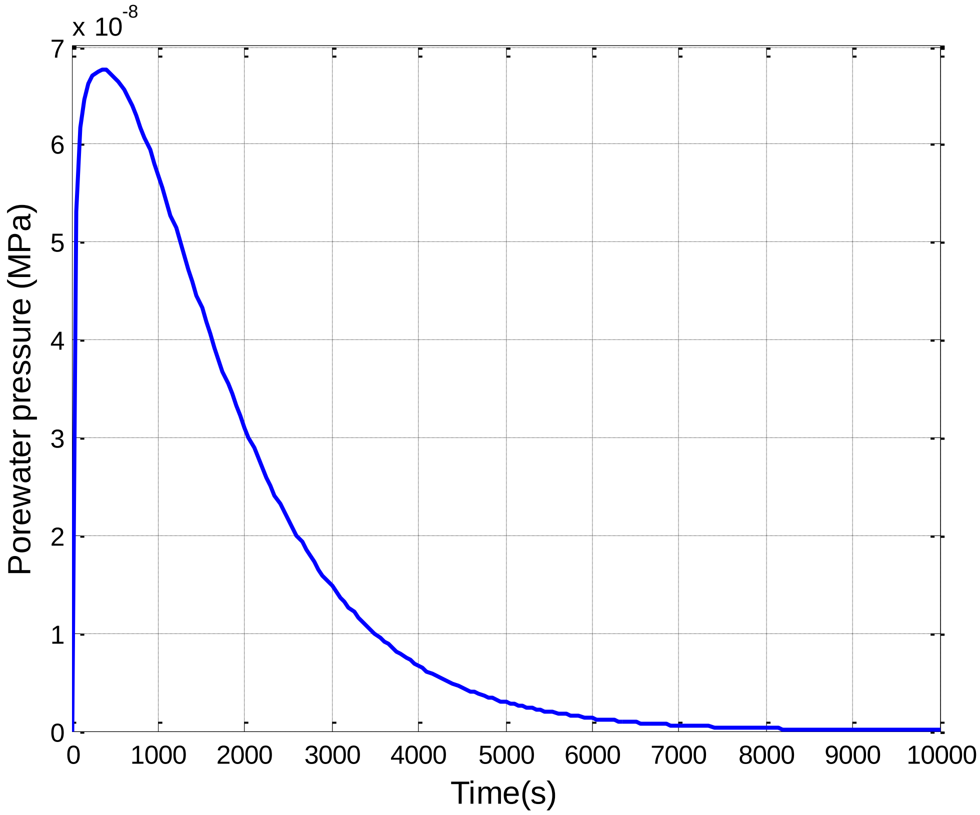

Figure 175: Pore water pressure at the mid of the shear band (base line case)

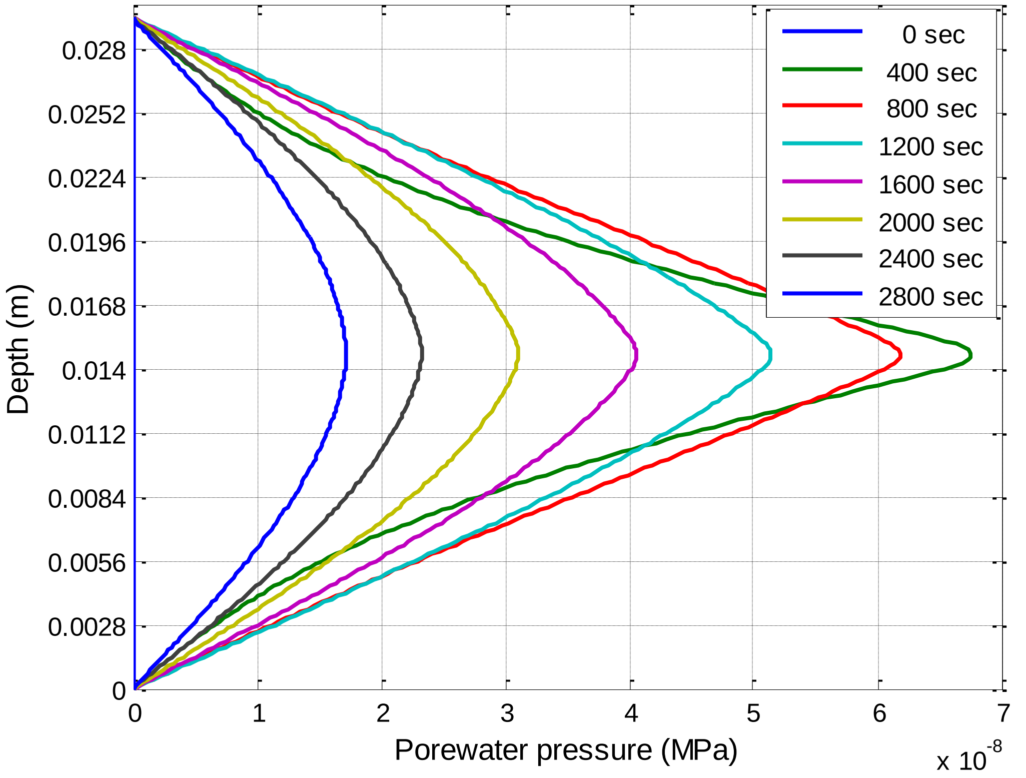

Figure 176: Pore water pressure isochrones within the shear band and its surroundings (base line case)

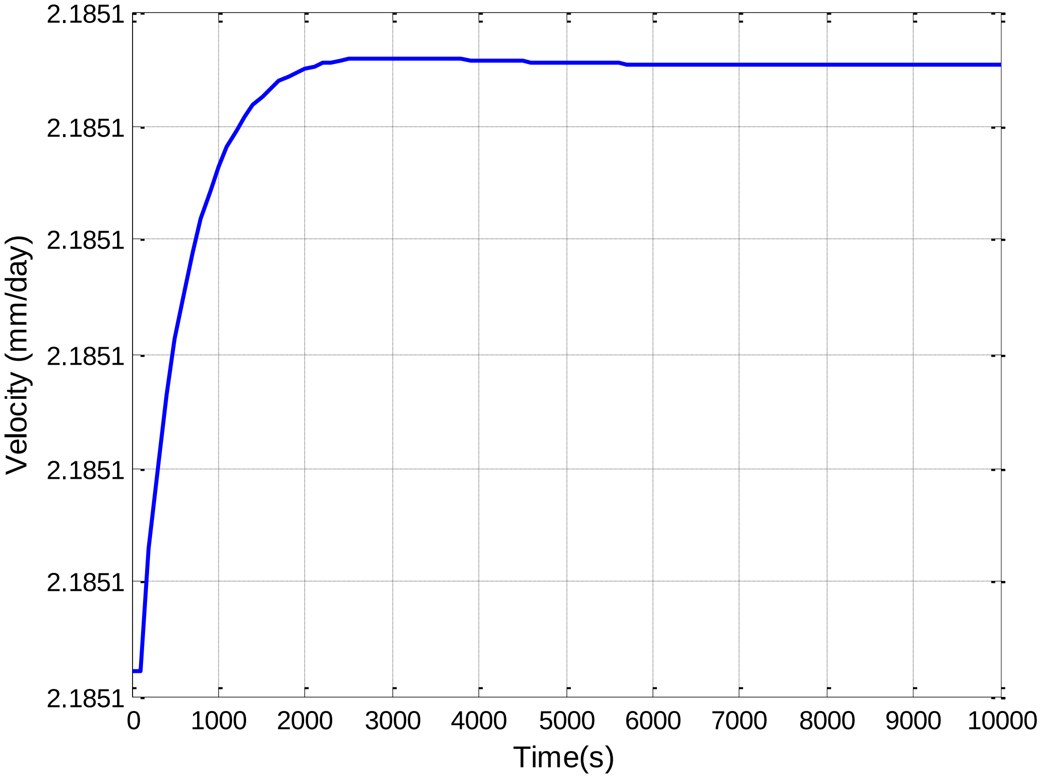

Figure 177: Velocity of the slide (base line case)

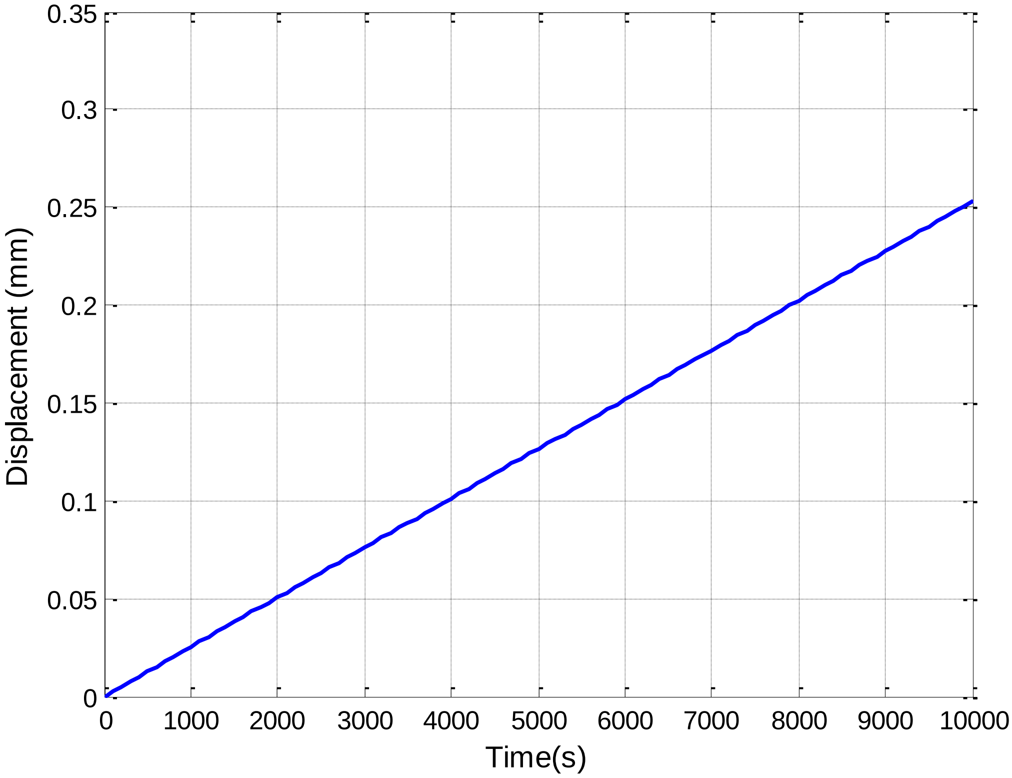

Figure 178: Plot of slide displacement (base line case)

6.5.2 Effect of different initial velocity

The results presented for the base line case clearly show that temperature did not play an important role on the failure of the landslide. This is due to the negligible energy dissipation inside the shear band. Also, the slide was predicted to reach a steady state of creep immediately.

To investigate possibility of capturing a transition from creep to a catastrophic phase the viscoplastic parameter C' was varied; this meant a different initial velocity, consistent with Equation 6.37. Here, the initial velocities were increased up to 10,000 times by increasing the viscoplastic parameter accordingly. The temperature at the middle of the shear band for a range of initial velocities is presented in Figure 179. The corresponding pore pressure at the middle of the shear band for a range of initial velocities is presented in Figure 180. And the corresponding velocity and displacement plots are presented in Figure 181 and Figure 182. It can be clearly seen that, for the parameters used here, the model does not reaches a catastrophic phase even with high initial velocity. In the creep phase temperature effects are not predicted to be important, even with extremely higher initial velocities such as 10,000 times the Vaiont slide creep velocity (i.e. 0.25 mm/sec). This particular initial velocity predicted the catastrophic phase in the models presented in Chapters 4 and 5. However, using viscoplastic theory, frictional heating on its own is not predicted to cause catastrophic collapse of the slope.

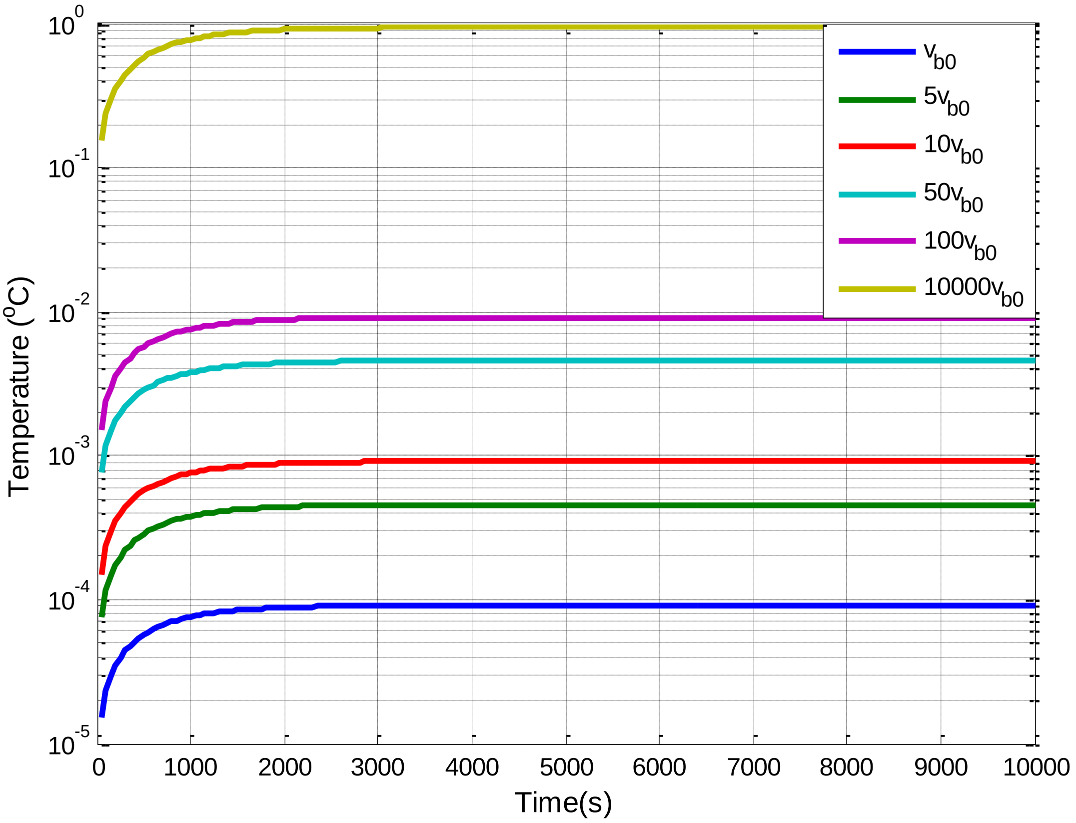

Figure 179: Temperature at the mid of the shear band (different initial velocities)

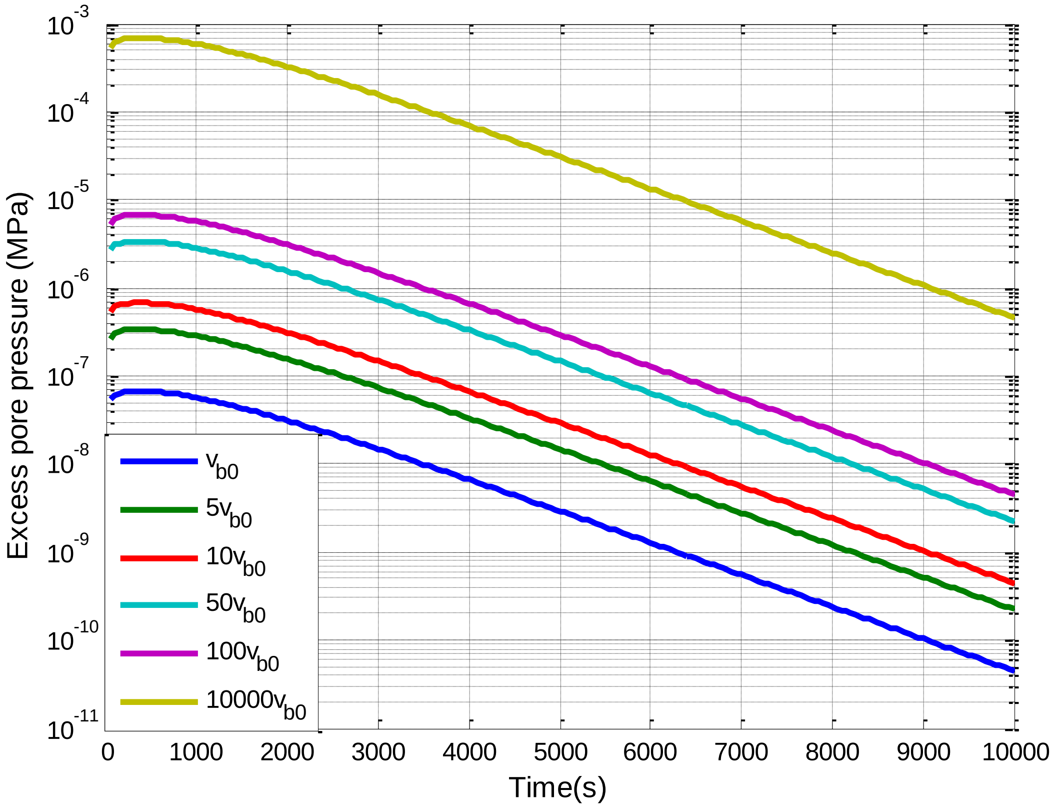

Figure 180: Pore water pressure at the mid of the shear band (different initial velocities)

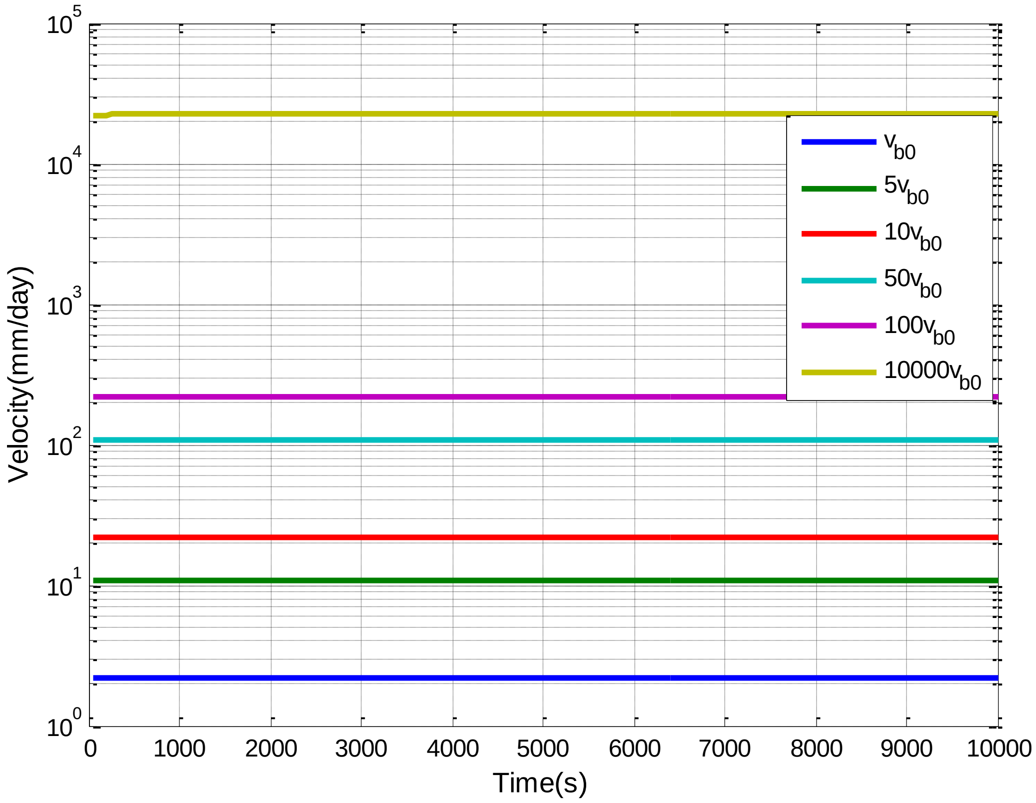

Figure 181: Velocity of the slide (different initial velocities)

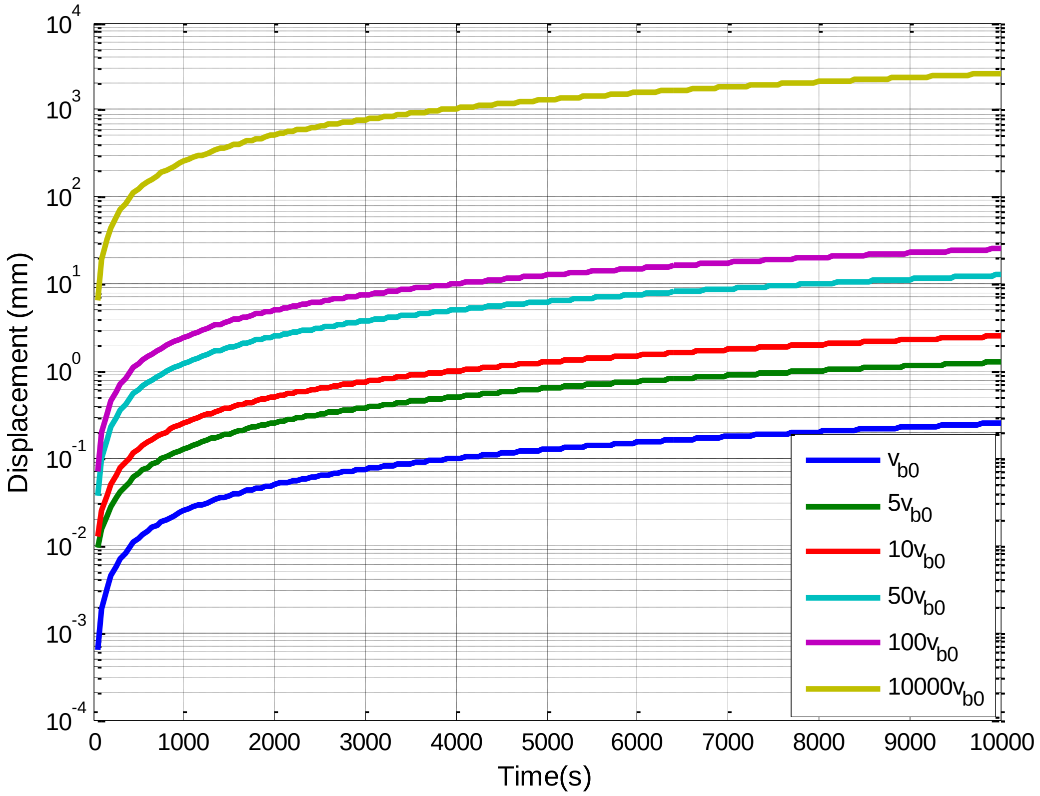

Figure 182: Displacement of the slide (different initial velocities)

6.5.3 Effects of friction softening

In Section 6.5.2, it was seen that high initial velocity is not predicted to be sufficient to trigger a catastrophic phase. Material softening is now included, to investigate how this may affect model behaviour. The numerical results presented here are for the baseline case with the addition of frictional softening.

Material friction softening is only applied to the static yield locus f_y; the critical state parameter for viscoplastic potential f_p was assumed constant throughout the shearing process. As described in Section 2.2.5, the strain, strain rate and temperature dependence of friction angle can be written as Equation 2.70;

$$M(\dot{\gamma},\ddot{\gamma},\theta) = \widehat{M}(\dot{\gamma},\ddot{\gamma}) - \tilde{g}(\theta - \theta_{ref}) \qquad 6.38$$

The thermal friction sensitivity parameter $\tilde{g}$ is taken as 10^{-2} in line with Cecinato (2009).

The time evolution of temperature at the middle of the shear band is given in Figure 183. This plot is obtained by using a time step of 4.8 hours. An initial step increase (4.5×10^{-4} °C) is observed in temperature within the first time step.

To investigate whether this step increase is part of the solution or an artefact of the numerical scheme, the time step was further reduced to 20 sec and an analysis was performed for the first 10,000 sec. From the temperature plot of Figure 184 it can be clearly seen what appears as a step increase in Figure 183 is in fact a smooth increase over the first few thousand seconds and is therefore not an artefact.

Figure 184 presents the evolution of temperature at the middle of the shear band for first 10,000 sec. The pore water pressure plots for 40 days and for first 10000 sec are shown in Figure 186 and Figure 187 respectively. The temperature and pore water pressure isochrones within the shear band and its surroundings are shown in Figure 185 and Figure 188 respectively. The total temperature rise 1.44×10^{-3}°C at 40 days is practically zero and so is the maximum excess pore pressure (3.25×10^{-1}Pa dropping to zero after 8000 sec).

The velocity plot Figure 189 shows that, after an initial acceleration, the block velocity levels off and reaches a steady state of creep at 7.45 mm/day; this is still within the range of realistic velocities for a creeping slide such as Vaiont (Müller, 1964) (Figure 7) . The displacement plot Figure 190 shows that the slide reaches a displacement of 270 mm over a period 40 days. As slide reaches to a steady state a velocity, the displacement is expected to increase linearly with time. The friction softening did not play a significant role for the first 10,000 sec, because the results presented here are very close to the baseline case.

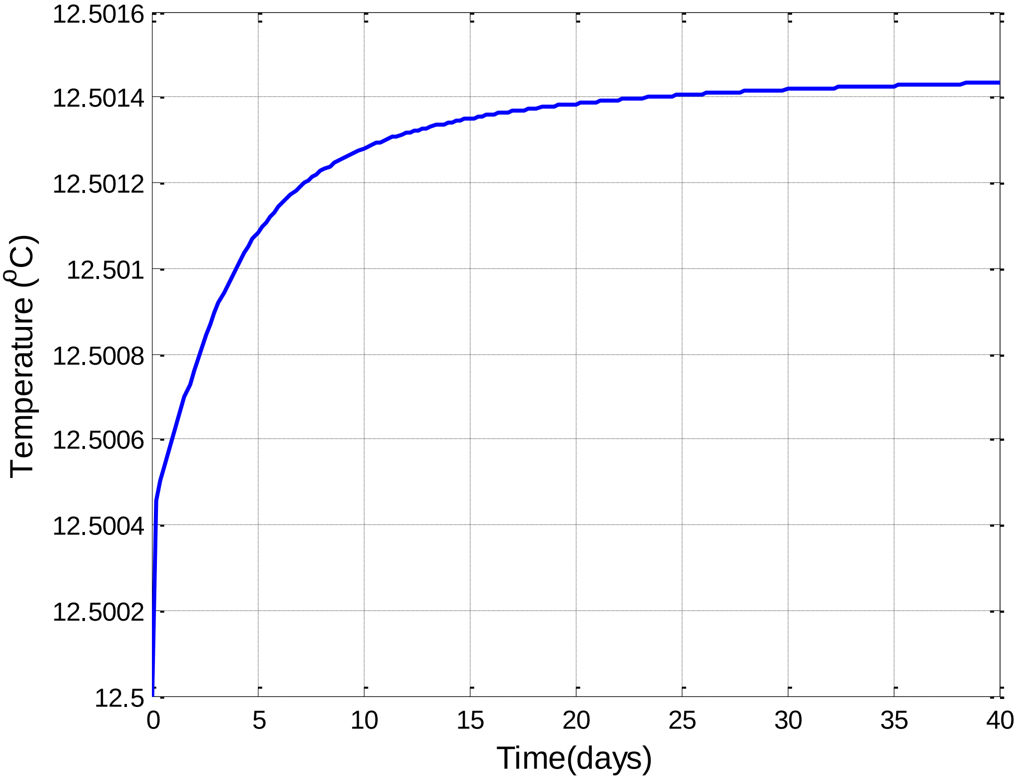

Figure 183: Temperature at the mid of the shear band (with friction softening)

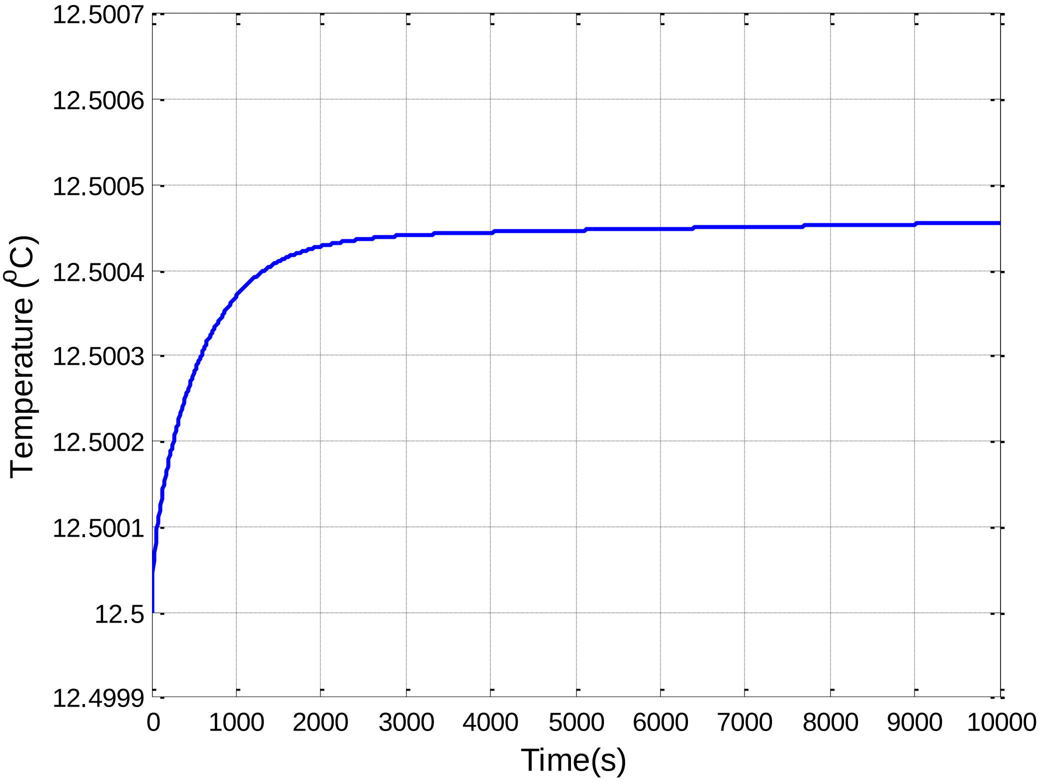

Figure 184: Temperature at the mid of the shear band (with friction softening, 0-10000 sec)

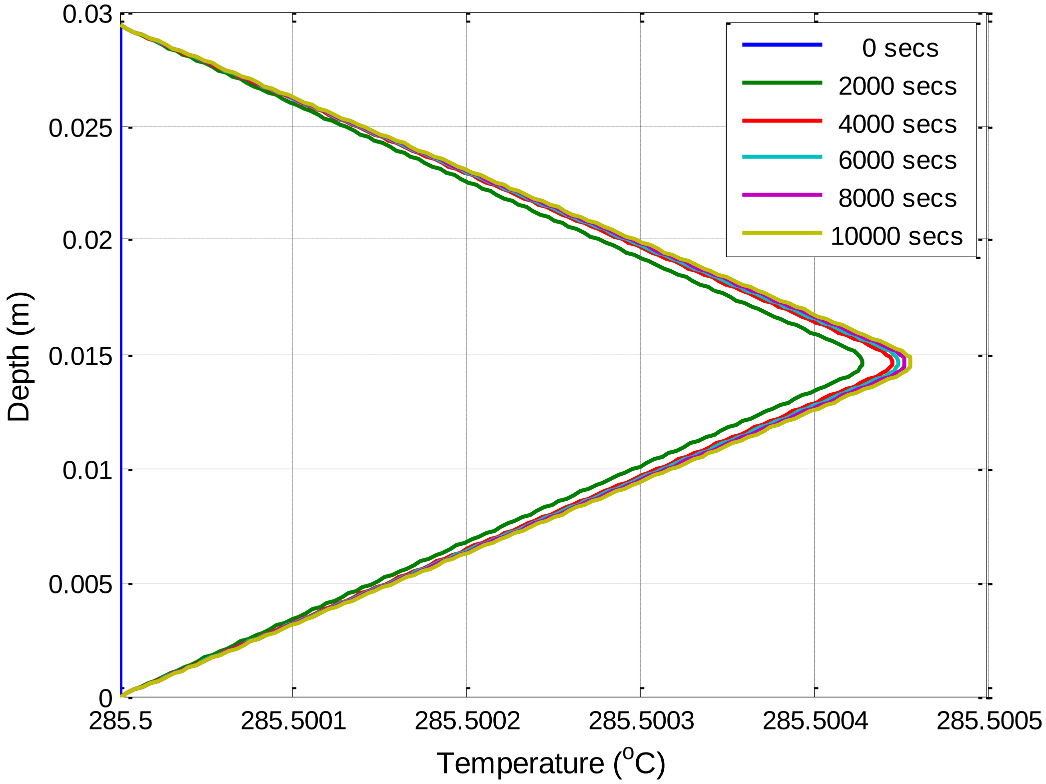

Figure 185: Temperature isochrones within the shear band and its surroundings (with friction softening)

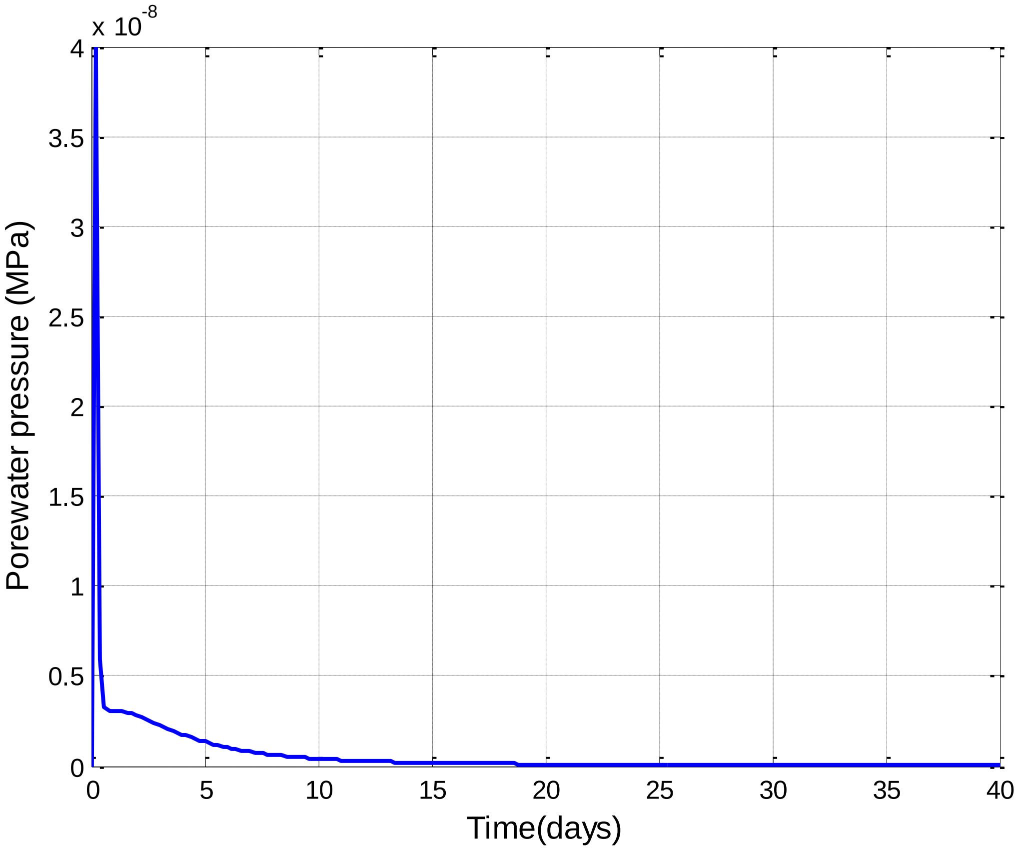

Figure 186: Excess pore water pressure at the middle of the shear band (with friction softening)

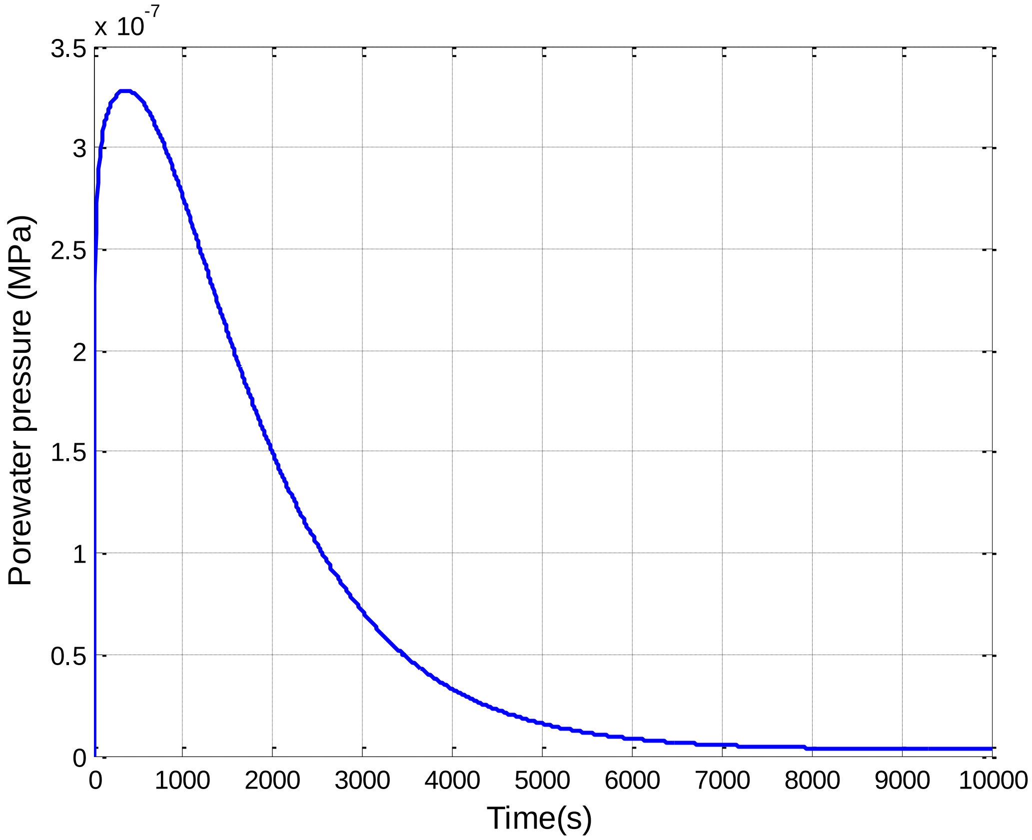

Figure 187: Excess pore water pressure at the middle of the shear band (with friction softening, 0-10000 sec)

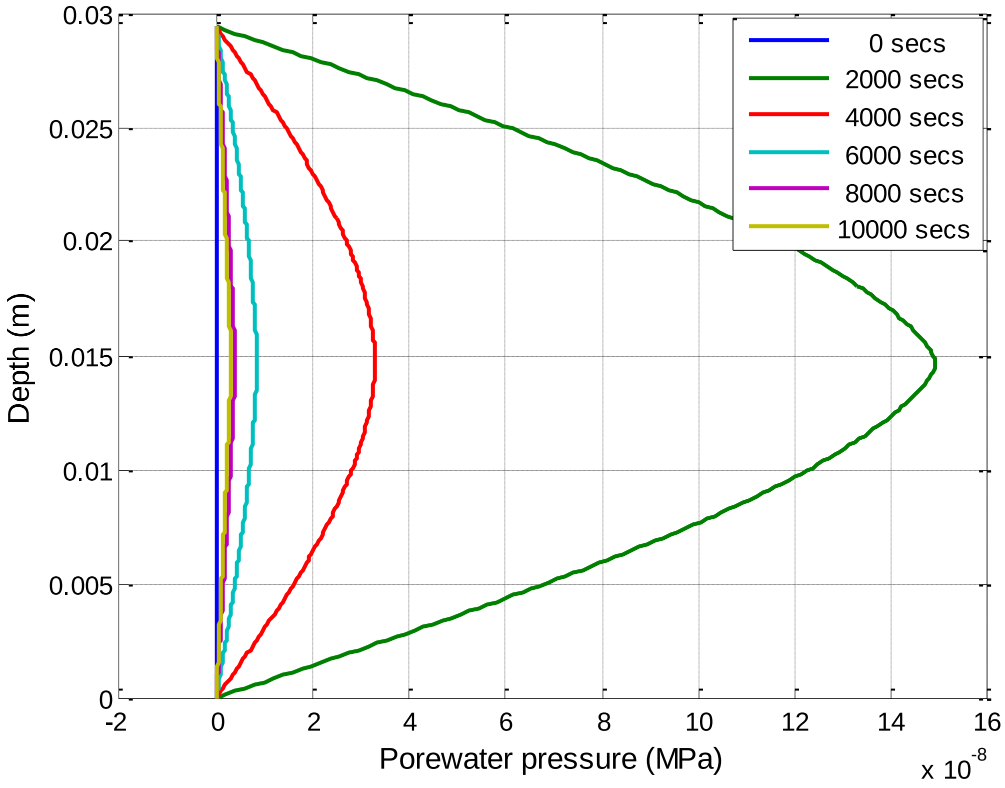

Figure 188: Excess porewater pressure isochrones within the shear band and its surroundings (with friction softening)

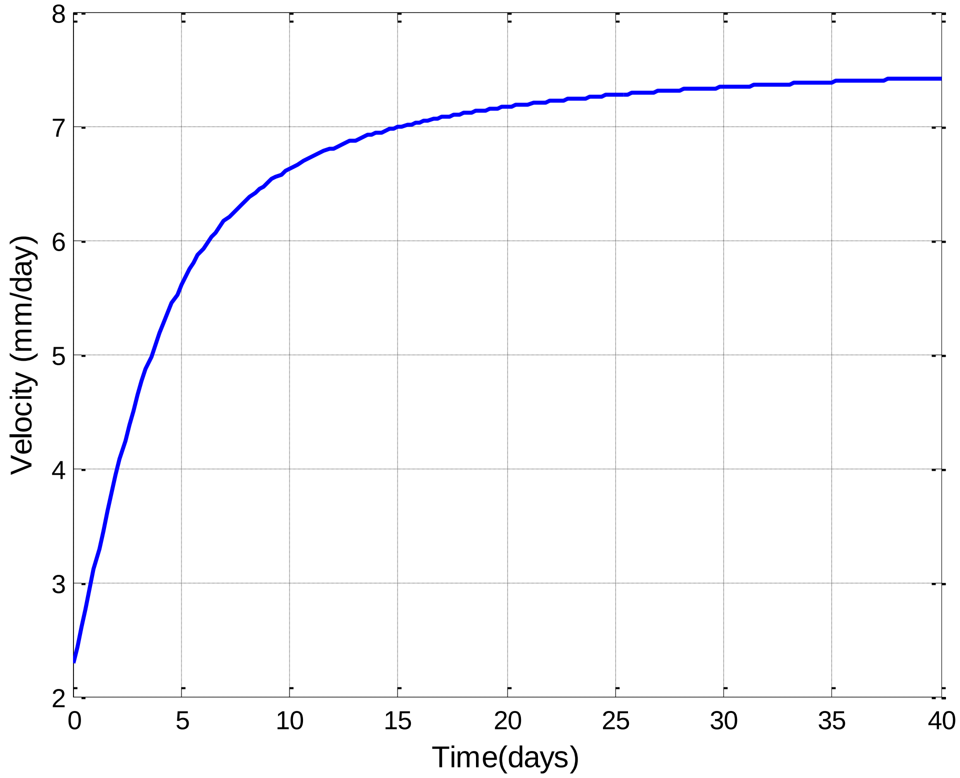

Figure 189: Velocity of the slide (with friction softening)

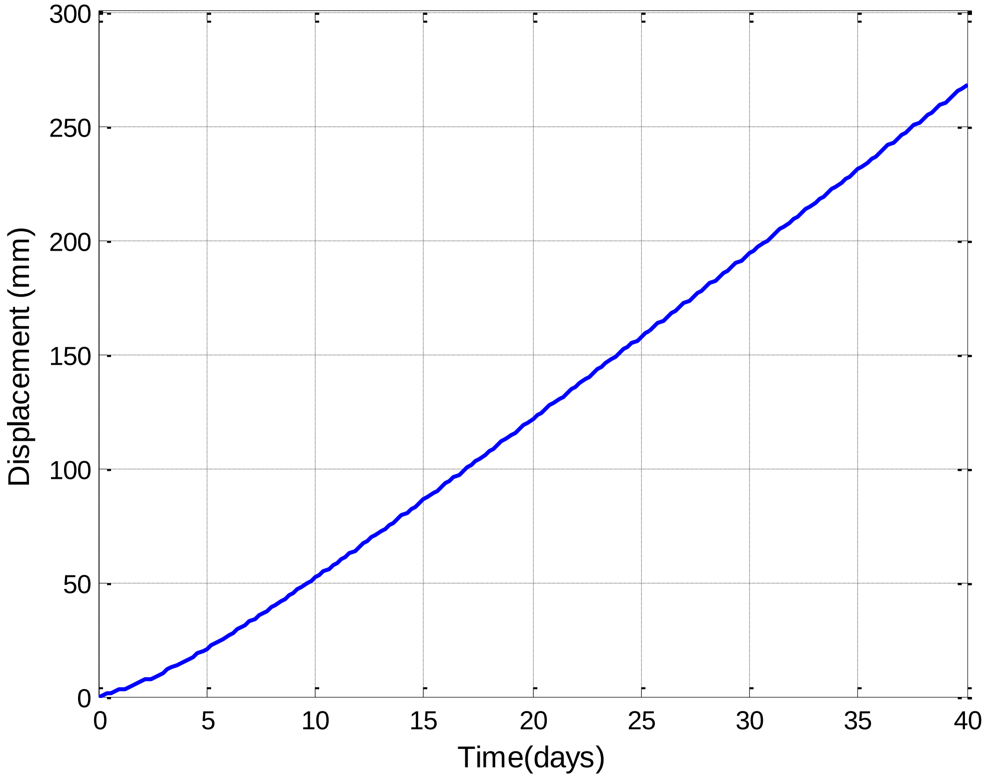

Figure 190: Displacement of the slide (with friction softening)

6.6 Discussion

The results presented show that the developed model does not predict a catastrophic phase in the range of cases considered. In the creep phase temperature effects are of low importance, as energy dissipation and heat production are low.

For the case of Vaiont, the model does not predict catastrophic phase. Furthermore, the analyses with higher initial velocity show that the effects of temperature are not important, even with extremely higher initial velocities such as 10,000 times the Vaiont slide creep velocity (i.e. 0.25 mm/sec). It is worth noting that an initial velocity of 0.25mm/sec led to a catastrophic phase according to both models presented in Chapters 4 and 5. As mentioned in previous chapters, water level changes and precipitation were not included in this model either.

The inclusion of friction softening leads to increase in velocity due to depletion of shear strength but with comparatively slow rate. However a catastrophic phase is not reached, due to the low slide velocity it takes as long as 40 days for the friction angle to drop its residual value.

Therefore, using the thermo-visco-plastic model developed here, frictional heating on its own is not predicted to cause the collapse of a slope; other external actions such as dynamic loading or increase of pore water pressure due to external factors need to be invoked to push the over the threshold and lead to catastrophic failure.

Chapter 7: Conclusions and recommendations

7.1 General conclusions

In this research, the importance of frictional heating on the development of landslides was investigated. In particular, the prediction of the transition between the creeping phase and the final collapse of a landslide was attempted. The general conclusions are:

- A wide range of in-situ conditions and parameters that are relevant for terrestrial landslides were identified and existing models for large scale landslides were critically reviewed. Also a critical review of the Vaiont case history is carried out which is used to back analyse the proposed models in this thesis.
  It was found that, in each model reviewed, either the collapse phase or the creeping regime was considered. Only one model was found that considers the transition between the creeping phase and the final collapse of a landslide (Veveakis et al, 2007) assuming balancing mechanisms of strain rate hardening and thermoplastic softening. However, the assumptions made in this model are not relevant in general for all landslides. Therefore, a comprehensive model covering all aspects of material behaviour at all stages of a landslide is still lacking.
- A comprehensive review of existing models for thermo-plasticity of soils and creep of soils were carried out. It was found that creep models were proposed for isothermal conditions, whereas thermo-plasticity models do not consider creep. A material model considering both creep and temperature dependent soil behaviour is still lacking. However, to model the thermo mechanics of a creeping landslide, it is expected that the constitutive relation for the material should contain combined effects of temperature and creep. A new constitutive model incorporating these effects would facilitate the predictions of the transition between the creeping phase and the final collapse a landslide.
- The driving moment changes while a landslide mass rotates about the centre of the slip circle. This particular aspect was not investigated in the model developed by Cecinato (2009). The dynamic equation was modified from Cecinato (2009) by

incorporating the change in net driving moment. The model was discretised using an implicit finite difference scheme, and validated successfully by back-analysing a real landslide case.

It was found that the refined model gave different predictions for the slide's acceleration and velocity which however were only marginally so in the time window of realistic run-out distances. Moreover, bigger failure mass accelerates faster than of smaller because the net effective driving force is greater in bigger rotational slide

- By using rate process theory, a transition between creep and catastrophic failure of a landslide can be explained. The results show that, for a given modelled spatial domain, a threshold initial velocity separates the creep and collapse regimes, beyond which frictional heating leads to the final failure. Thermal effects will exacerbate slope failure once the threshold velocity is exceeded.

  The extent of the modelled spatial domain plays a dominant role on the failure of a landslide. The larger the domain, the more likely the model is to predict the catastrophic failure. For an infinite upper and lower boundary, the model is expected to predict catastrophic failure irrespective of the value of initial velocity. Moreover, the results were found to be sensitive to the values of the rate process parameters, especially the number of inter-particle bonds and the activation energy.

- It is possible to develop a material model that includes the effects of creep and temperature by combining Borja's creep model and Laloui's thermo-plasticity of soils. This material model was introduced to a landslide model to predict the creep as well as the catastrophic failure of a landslide and was able to predict the transition between the creep and catastrophic phases.

  Prediction of Vaiont's both creep and collapse phases is not possible using this model. However, it predicted a transition between creep and catastrophic failure of landslides with initial velocity higher than observed creep velocities in a typical large scale landslides. Nevertheless, the predicted duration of the creep phase is very short compared to typical field observation.

- It is possible to develop a thermo-visco-plastic constitutive relation for soils by combining Perzyna's viscoplastic model and Laloui's thermoplastic model. A landslide model was then developed using this combined thermo-visco-plastic model. For the case of Vaiont, collapse due to thermal pressurization is impossible in this model because of the extremely low slide velocity predicted during the creep phase, which leads to insignificant heat production inside the shearband.

Moreover, unlike other models the viscoplastic model did not predict a collapse phase for high initial velocities.

- In general, all models developed here based on rate process theory, Borja’s creep model and viscoplastic theory show that frictional heating on its own is not predicted to cause the collapse of a slope. It is not expected that thermal creep is likely dominate in large rapid landsides; other external actions, such as dynamic loading or pore pressure increase, need to be invoked to predict the final collapse. Therefore, heating will not make the slope collapse but may make the event more catastrophic if the slope does collapse. Also these models are limited due to lack of data available for the respective constitutive parameters, which are not routinely measured or reported in the literature for different soils.

7.2 Recommendations for further research

One of the barriers encountered in this thesis was scarcity or even lack of data for the model parameters (i.e. rate process, viscoplastic and Borja’s creep equation parameters). An experimental research could be carried out to obtain realistic values for relevant parameters to improve predictions.

The models developed in this thesis were used in an attempt to back analyse the Vaiont case landslide. However, none of them predicted the complete landslide history, at least partially due to the other external factors present such as water level changes and rainfall. Therefore, the models could be validated using case studies of other large scale landslides available in the literature to assess their suitability. Other well documented landslides are the Jiufengeshan slide; occurred in 1999, killed 2000 people, the La Clapière landslide; occurred in 1987 and the Ok Ma dam landslide occurred in 1984. None, however, is as well documented as Vaiont.

In reality, slip zones develop progressively and their direction is influenced by in-situ conditions (i.e. stress distributions), and external factors (i.e. earthquakes and rainfall). Modelling of crack propagation can also be included to model the initiation and growth of the shear band. This would enable predictions of the effect of frictional heating on the progressive development of landslides.

References

Adachi, T. & Oka, F. (1982). Constitutive equations for normally consolidated clay based on elasto-viscoplasticity. *Soils and Foundations,* 22**,** 57-70.

Adachi, T., Oka, F. & Mimura, M. (1990). Elasto-Viscoplastic Constitutive Equations for Clay and Its Application to Consolidation Analysis. *Journal of Engineering Materials and Technology,* 112**,** 202-209.

Alonso, E. E., Pinyol, N. & Puzrin, A. M. (2010). *Geomechanics of Failures. Advanced Topics*, Springer Verlag.

Andersland, O. & Douglas, A. (1970). Soil deformation rates and activation energies. *Geotechnique,* 20**,** 1-16.

Anderson, D. L. (1980). An earthquake induced heat mechanism to explain the loss of strength of large rock and earth slides. *International Conference on Engineering for Protection from natural disasters,,* Bangkok.

Augustesen, A., Liingaard, M. & Lade, P. V. (2004). Evaluation of Time-Dependent Behavior of Soils. *International Journal of Geomechanics,* 4**,** 137-156.

Baldi, G., Hueckel, T. & Pellegrini, R. (1988). Thermal volume changes of the mineral–water system in low-porosity clay soils. *Canadian Geotechnical Journal,* 25**,** 807-825.

Bishop, A. W. (1966). The Strength of Soils as Engineering Materials. *Géotechnique,* 16**,** 91-130.

Bjerrum, L. (1967). Engineering geology of Norwegian normally-consolidated marine clays as related to settlements of buildings. *Geotechnique,* 17(2)**,** 83-119.

Bjerrum, L. (1973). Problems of soil mechanics and construction on soft clays and structurally unstable soils (collapsible, expansive and others) *Proc. 8 th Int. Conf Soil Mech. Found. Engng,* Moscow, 111-159.

Borja, R. I. & Kavazanjian, E. (1985). A Constitutive Model for the Stress-Strain-Time Behaviour of 'Wet' Clays. *Geotechnique,* 35**,** 283-298.

Campanella, R. G. & Mitchell, J. K. (1968). Influence of temperature variations on soil behavior. *ASCE Journal of Soil Mechanics & Foundations Div,* Vol 94**,** 709-734.

Cecinato, F. (2009). *The role of frictional heating in the development of catastrophic landslides.* Thesis (PhD), University of Southampton,.

Cecinato, F. & Zervos, A. (2008). Thermo-mechanical modelling of catastrophic landslides. *16th Conference of the Association of Computational Mechanics in Engineering,* Newcastle, UK.

Cecinato, F. & Zervos, A. (2012). Influence of thermomechanics in the catastrophic collapse of planar landslides. *Canadian Geotechnical Journal,* 49**,** 207-225.

Cecinato, F., Zervos, A. & Veveakis, E. (2011). A thermo-mechanical model for the catastrophic collapse of large landslides. *International Journal for Numerical and Analytical Methods in Geomechanics*.

Cecinato, F., Zervos, A., Veveakis, E. & Vardoulakis, I. (2008) Numerical modelling of the thermo-mechanical behaviour of soils in catastrophic landslides. *In:* Proceedings of the Tenth International Symposium on Landslides and Engineered Slopes 2008 China.

Chang, K.-J., Taboada, A. & Chan, Y.-C. (2005a). Geological and morphological study of the Jiufengershan landslide triggered by the Chi-Chi Taiwan earthquake. *Geomorphology,* 71**,** 293-309.

Chang, K.-J., Taboada, A., Lin, M.-L. & Chen, R.-F. (2005b). Analysis of landsliding by earthquake shaking using a block-on-slope thermo-mechanical model: Example of Jiufengershan landslide, central Taiwan. *Engineering Geology,* 80**,** 151-163.

Christensen, R. W. & Wu, T. H. (1964). Analysis of clay deformation as a rate process. *Journal of the Soil Mechanics and Foundations Division, ASCE,* 90**,** 125-157.

Cruden, D. M. & Varnes, D. J. (1996). Landslide types and processes. *In: Turner A.K.; Shuster R.L. (eds) Landslides: Investigation and Mitigation. Transp Res Board,* 247**,** 36-75.

Cui, Y. J., Sultan, N. & Delage, P. (2000). A thermomechanical model for saturated clays. *Canadian Geotechnical Journal,* 37**,** 607-620.

De Blasio, F. V. & Elverhoi, A. (2008). A model for frictional melt production beneath large rock avalanches. *J. Geophys. Research-Earth Surface,* 113.

Delage, P., Sultan , N. & Cui, Y. J. (2000). On the thermal consolidation of Boom clay. *Canadian Geotechnical Journal,* 37**,** 343-354.

Di Benedetto, H., Tatsuoka, F. & Ishihara, M. (2002). Time-dependent shear deformation characteristics of sand and their constitutive modelling. *Soils and Foundations,* 42**,** 1-22.

Dikau, R. (1996). *Landslide Recognition: Identification, Movement and Causes : Report No. 1 of the European Commission Environment Programme, Contract No. Ev5v-Ct94-0454,* Commission of the European Communities, Wiley.

Eriksson, L. (1989) Temperature effects on consolidation properties of sulphide clays. *In*, 1989. Taylor and Francis Group.

Erismann, T. (1979). Mechanisms of large landslides. *Rock Mechanics and Rock Engineering,* 12**,** 15-46.

Erlandsson, R., Hadziioannou, G., Mate, C. M., Mcclelland, G. M. & Chiang, S. (1988). Atomic scale friction between the muscovite mica cleavage plane and a tungsten tip. *The Journal of Chemical Physics*, 89**,** 5190-5193.

Eyring, H. (1936). Viscosity, Plasticity, and Diffusion as Examples of Absolute Reaction Rates. *The Journal of Chemical Physics,* 4**,** 283-291.

Feda, J. (1989). Interpretation of creep of soils by rate process theory. *Geotechnique,* 39**,** 667-677.

Fox, P. J. & Edil, T. B. (1996). Effects of stress and temperature on secondary compression of peat. *Canadian Geotechnical Journal,* 33**,** 405-415.

Fusao, O., Adachi, T. & Yashima, A. (1994). Instability of an elasto-viscoplastic constitutive model for clay and strain localization. *Mechanics of Materials,* 18**,** 119-129.

Gaziev, E. (1984). Study of the Usoy landslide in Pamir. *In: Proc. 4th International Symposium on Landslides,* Toronto, 511–515.

Ghabezloo, S. & Sulem, J. (2009). Stress dependent thermal pressurization of a fluid-saturated rock. *Rock Mechanics and Rock Engineering,* 42**,** 1-24.

Goren, L. & Aharonov, E. (2007). Long runout landslides: The role of frictional heating and hydraulic diffusivity. *Geophys. Res. Lett.,* 34**,** L07301.

Goren, L. & Aharonov, E. (2009). On the stability of landslides: A thermo-poro-elastic approach. *Earth and Planetary Science Letters,* 277**,** 365-372.

Habib, P. (1975). Production of gaseous pore pressure during rock slides. *Rock Mechanics and Rock Engineering,* 7**,** 193-197.

Hendron, A. & Patton, F. (1985). The Vaiont slide, a geotechnical analysis based on new geologic observations of the failure surface, Technical Report GL-85-5. Washington, DC: Department of the Army US Corps of Engineers.

Hueckel, T. & Baldi, G. (1990). Thermoplasticity of Saturated Clays: Experimental Constitutive Study. *Journal of Geotechnical Engineering,* 116**,** 1778-1796.

Hueckel, T. & Borsetto, M. (1990). Thermoplasticity of Saturated Soils and Shales: Constitutive Equations. *Journal of Geotechnical Engineering,* 116**,** 1765-1777.

Hueckel, T. & Peano, A. (1987). Some geotechnical aspects of radioactive waste isolation in continental clays. *Comput. Geotech.,* 3**,** 157-182.

Hueckel, T. & Pellegrini, R. (1991). Thermoplastic modeling of undrained failure of saturated clay due to heating. *Soils Foundations,* 31**,** 1-16.

Hungr, O., Evans, S., Bovis, M. & Hutchinson, J. (2001). A review of the classification of landslides of the flow type. *Environmental & Engineering Geoscience,* 7**,** 221-238.

Hutchinson, J. (1989) General report: morphological and geotechnical parameters of landslides in relation to geology and hydrogeology: Proc 5th International Symposium on Landslides, Lausanne, 10–15 July 1988V1, P3–35. Publ Rotterdam: AA Balkema, 1988. *In:* International Journal of Rock Mechanics and Mining Sciences & Geomechanics Abstracts, 1989. Pergamon, 88.

Hyde, A. F. L. & Brown, S. F. (1976). The plastic deformation of a silty clay under creep and repeated loading. *Géotechnique,* 26**,** 173-184.

Johnson, K. L. (1987). *Contact Mechanics,* Cambridge University Press.

Kavazanjian, E. & Mitchell, J. K. (1977). A general stress-strain-time formulation for soils. *Ninth International Conference on Soil Mechanics and Foundation Engineering,* Tokyo, Japan, 113-120.

Kimoto, S., Khan, B., Mirjalili, M. & Oka, F. (2013). A Cyclic Elasto-Viscoplastic Constitutive Model for Clay Considering the Nonlinear Kinematic Hardening Rules and the Structural Degradation. *International Journal of Geomechanics,* 0**,** null.

Kimoto, S., Oka, F. & Higo, Y. (2004). Strain localization analysis of elasto-viscoplastic soil considering structural degradation. *Computer Methods in Applied Mechanics and Engineering,* 193**,** 2845-2866.

Kuhn, M. R. & Mitchell, J. K. (1993). New Perspectives on Soil Creep. *Journal of Geotechnical Engineering,* 119**,** 507-524.

Kuwano, R. & Jardine, R. J. (2002). On measuring creep behaviour in granular materials through triaxial testing. *Canadian Geotechnical Journal,* 39**,** 1061-1074.

Kwok, C. Y. & Bolton, M. (2010). DEM simulations of thermally activated creep in soils. *Geotechnique,* 60**,** 425-433.

Laloui, L. (2001). Thermo-mechanical behaviour of soils. *Revue Française de Génie Civil,* 5**,** 809-843.

Laloui, L. & Cekerevac, C. (2003). Thermo-plasticity of clays:: An isotropic yield mechanism. *Comput. Geotech.,* 30**,** 649-660.

Laloui, L. & Cekerevac, C. (2008). Numerical simulation of the non-isothermal mechanical behaviour of soils. *Comput. Geotech.,* 35**,** 729-745.

Laloui, L. & Francois, B. (2009). ACMEG-T: Soil Thermoplasticity Model. *Journal of Engineering Mechanics,* 135**,** 932-944.

Laloui, L., Leroueil, S. & Chalindar, S. (2008). Modelling the combined effect of strain rate and temperature on one-dimensional compression of soils. *Canadian Geotechnical Journal,* 45**,** 1765-1777.

Leroueil, S., Kabbaj, M., Tavenas, F. & Bouchard, R. (1985). Stress-Strain-Strain Rate Relation for the Compressibility of Sensitive Natural Clays. *Geotechnique,* 35**,** 159-180.

Leroueil, S., Marques, S. & Esther, M. (1996) Importance of strain rate and temperature effects in geotechnical engineering. *In:* Measuring and Modeling Time Dependent Soil Behavior, Geotechnical Special Publication No. 61, 1996. ASCE, 1-60.

Lo, K. (1961). Secondary compression of clays. *Journal of the Soil Mechanics and Foundations Division, ASCE,* 87**,** 61-87.

Mase, G. E. (1970). *Schaum's Outline of Theory and Problems of Continuum Mechanics,* McGraw-Hill.

Mateši , L. & Vucetic, M. (2003). Strain-rate effect on soil secant shear modulus at small cyclic strains. *Journal of geotechnical and geoenvironmental engineering,* 129**,** 536.

Mesri, G. (1973). Coefficent of secondary compression. *Journal of Soil Mechanics & Foundations Div,* 99.

Mitchell, J., Campanella, R. & Singh, A. (1968). Soil creep as a rate process. *Journal of Soil Mechanics & Foundations Div,* Vol 94**,** 709-734.

Mitchell, J. K. (1964). Shearing Resistance of Soils as a Rate Process *ASCE Journal of Soil Mechanics & Foundations Div,* Vol 90**,** 29-61.

Mitchell, J. K. & Campanella, R. G. (1964) Creep studies on saturated clays. *In:* ASTM-NRC of Canada, Symposium of Laboratory Shear Testing of Soils, 1964 Ottawa, Canada.: ASTM International, 90-103.

Mitchell, J. K., Singh, A. & Campanella, R. G. (1969). *Bonding, effective stresses, and strength of soils,* University of California, Institute of Transportation and Traffic Engineering, Soil Mechanics and Bituminous Materials Research Laboratory.

Mitchell, J. K. & Soga, K. (2005). *Fundamentals of soil behavior,* John Wiley & Sons.

Modaressi, H. & Laloui, L. (1997). A thermo-viscoplastic constitutive model for clays. *International Journal for Numerical and Analytical Methods in Geomechanics,* 21**,** 313-335.

Morgenstern, N. & Tchalenko, J. (1967). Microscopic structures in kaolin subjected to direct shear. *Geotechnique,* 17**,** 309-328.

Müller, L. (1964). *The rock slide in the Vajont Valley,* Springer-Verlag.

Müller, L. (1968). New considerations on the Vaiont slide. *Rock Mechanics & Engineering Geology.*

Murayama, S., Michihiro, K. & Sakagami, T. (1984). Creep characteristics of sand. *Soils and foundations,* 24.

Murayama, S. & Shibata, T. (1958). On the Rheological Characters of Clay Part 1. *Bulletins-Disaster Prevention Research Institute, Kyoto University,* 26**,** 1-43.

Oka, F., Adachi, T. & Yashima, A. (1995). A strain localization analysis using a viscoplastic softening model for clay. *International Journal of Plasticity,* 11**,** 523-545.

Oka, F., Higo, Y. & Kimoto, S. (2002). Effect of dilatancy on the strain localization of water-saturated elasto-viscoplastic soil. *International Journal of Solids and Structures,* 39**,** 3625-3647.

Olszak, W. & Perzyna, P. (1966a). The constitutive equations of the flow theory for a non-stationary yield condition. *In:* GÖRTLER, H. (ed.) *Applied Mechanics.* Springer Berlin Heidelberg.

Olszak, W. & Perzyna, P. (1966b). On Elastic/Visco-Plastic Soils. *In:* KRAVTCHENKO, J. & SIRIEYS, P. (eds.) *Rheology and Soil Mechanics / Rhéologie et Mécanique des Sols.* Springer Berlin Heidelberg.

Perzyna, P. (1962a). *The Constitutive Equations for Rate Sensitive Plastic Materials,* Brown University. Division of Applied Mathematics

United States. Office of Naval Research, Defense Technical Information Center.

Perzyna, P. (1962b). *The study of the dynamic behavior of rate sensitive plastic materials,* BROWN UNIV PROVIDENCE RI DIV OF APPLIED MATHEMATICS.

Perzyna, P. (1966). Fundamental Problems in Viscoplasticity. *Advances in applied mechanics,* 9**,** 243.

Pinyol, N. M. & Alonso, E. E. (2010). Criteria for rapid sliding II.: Thermo-hydro-mechanical and scale effects in Vaiont case. *Engineering Geology,* 114**,** 211-227.

Powrie, W. (2013). *Soil Mechanics: Concepts and Applications, Third Edition,* Taylor & Francis.

Puzrin, A., Saurer, E. & Germanovich, L. (2010). A dynamic solution of the shear band propagation in submerged landslides. *Granular Matter,* 12**,** 253-265.

Puzrin, A. M. & Germanovich, L. N. (2005). The growth of shear bands in the catastrophic failure of soils. *Proceedings of the Royal Society A: Mathematical, Physical and Engineering Science,* 461**,** 1199-1228.

Puzrin, A. M. & Schmid, A. (2011). Progressive failure of a constrained creeping landslide. *Proceedings of the Royal Society A: Mathematical, Physical and Engineering Science*.

Puzrin, A. M. & Sterba, I. (2006). Inverse long-term stability analysis of a constrained landslide. *Geotechnique,* 56**,** 483-489.

Rice, J. R. (2006). Heating and weakening of faults during earthquake slip. *Journal of Geophysical Research: Solid Earth,* 111**,** B05311.

Robinet, J. C., Rahbaoui, A., Plas, F. & Lebon, P. (1996). A constitutive thermomechanical model for saturated clays. *Engineering Geology,* 41**,** 145-169.

Roscoe, K. & Burland, J. (1968). On the generalized stress-strain behaviour of wet clay. *Engineering plasticity, Cambridge University Press,* 3**,** 539-609.

Schrefler, B. & Sanavia, L. 2005. Finite element analysis of strain localization in multiphase materials.

Semenza, E. & Ghirotti, M. (2000). History of the 1963 Vaiont slide: the importance of geological factors. *Bulletin of Engineering Geology and the Environment,* 59**,** 87-97.

Sidle, R. C. & Ochiai, H. (2006). *Landslides: Processes, Prediction, and Land Use,* Washington, DC, AGU.

Singh, A. & Mitchell, J. (1968). General Stress-Strain-Time Function For Soils. *ASCE Journal of Soil Mechanics & Foundations Div,* Vol 94**,** 21-46.

Smith, R. E. & Wahls, H. E. (1969). Consolidation under constant rates of strain. *ASCE Journal of Soil Mechanics & Foundations Div,* Vol 95**,** PP 519-539.

Sulem, J., Lazar, P. & Vardoulakis, I. (2007). Thermo-poro-mechanical properties of clayey gouge and application to rapid fault shearing. *International Journal for Numerical and Analytical Methods in Geomechanics,* 31**,** 523-540.

Sultan, N., Delage, P. & Cui, Y. J. (2002). Temperature effects on the volume change behaviour of Boom clay. *Engineering Geology,* 64**,** 135-145.

Taylor, D. W. (1948). Fundamentals of Soil Mechanics. *Soil Science,* 66**,** 161.

Ter-Stepanian, G. (1975). Creep of a clay during shear and its rheological model. *Geotechnique,* 25**,** 299-320.

Tika, T. (1989). *The effect of rate of shear on the residual strength of soil.* Ph. D. Dissertation, University of London (Imperial college of Science and Technology).

Tika, T., Vaughan, P. & Lemos, L. (1996). Fast shearing of pre-existing shear zones in soil. *Geotechnique,* 46**,** 197-233.

Tika, T. E. & Hutchinson, J. (1999). Ring shear tests on soil from the Vaiont landslide slip surface. *Geotechnique,* 49**,** 59-74.

Towhata, I., Kuntiwattanaku, P., Seko, I. & Ohishi, K. (1993). Volume change of clays induced by heating as observed in consolidation tests. *Soils and Foundations,* 33**,** 170-183.

Vaid, Y. P. & Campanella, R. G. (1977). Time-dependent behavior of undisturbed clay. *Journal of the Geotechnical Engineering Division,* 103**,** 693-709.

Vardoulakis, I. (2000). Catastrophic landslides due to frictional heating of the failure plane. *Mechanics of Cohesive-frictional Materials,* 5**,** 443-467.

Vardoulakis, I. (2002a). Dynamic thermo-poro-mechanical analysis of catastrophic landslides. *Geotechnique,* 52**,** 157-171.

Vardoulakis, I. (2002b). Steady shear and thermal run-away in clayey gouges. *International Journal of Solids and Structures,* 39**,** 3831-3844.

Varnes, D. J. (1978). Slope movement types and processes. *Transportation Research Board Special Report*.

Veveakis, E., Vardoulakis, I. & Di Toro, G. (2007). Thermoporomechanics of creeping landslides: The 1963 Vaiont slide, northern Italy. *J. Geophys. Res.,* 112**,** F03026.

Voight, B. & Faust, C. (1982). Frictional heat and strength loss in some rapid landslides. *Geotechnique,* 32**,** 43-54.

Wibberley, C. a. J. & Shimamoto, T. (2005). Earthquake slip weakening and asperities explained by thermal pressurization. *Nature,* 436**,** 689-692.

Wissa, A., Christian, J. T., Davis, E. H. & Heiberg, S. (1971). Consolidation at constant rate of strain. *Journal of Soil Mechanics & Foundations Div,* Vol 97**,** pp 1393-1413.

Wood, D. M. (1991). *Soil Behaviour and Critical State Soil Mechanics,* Cambridge University Press.

Yang, W. Y., Cao, W., Chung, T. S. & Morris, J. (2005). *Applied Numerical Methods Using MATLAB*, John Wiley & Sons.

Zwillinger, D. (2002). *CRC Standard Mathematical Tables and Formulae, 31st Edition,* Taylor & Francis.